UNIVERSITY OF SOUTHAMPTON

Investigations on Turbulence in Low Pressure Turbines based on Direct Numerical Simulations

by

Richard Pichler

A thesis submitted in partial fulfillment for the degree of Doctor of Philosophy

in the

Faculty of Engineering and Environment

Aerodynamic and Flight Mechanics

March 2016

UNIVERSITY OF SOUTHAMPTON

ABSTRACT

FACULTY OF ENGINEERING AND ENVIRONMENT
Aerodynamic and Flight Mechanics

Doctor of Philosophy

by Richard Pichler

To date no generally accepted prediction method is available for a low pressure turbine designer. Detailed information about the flow field that can be used to improve turbulence models is difficult to obtain from experiments. Direct numerical simulations (DNS), capable of delivering that information, have been published and showed the ability of this method to accurately predict the flow field. However, in these previous studies detailed turbulence information was not published and to date detailed information about turbulence in LPT flows is missing.

In this work compressible DNS were conducted and turbulence was investigated in detail. First a method was developed that enables large scale numerical simulations of low pressure turbines on state of the art high performance computers. Particular emphasis was put on boundary conditions with respect to reflections and an efficient way of generating inlet turbulence. To allow for efficient computation the computational performance was examined and optimized and showed good scaling up to large numbers of cores and GPUs, allowing the exploitation of large parallel computing systems.

A grid convergence study is presented showing that while large scales are grid converged at similar resolutions to previously published work, convergence of quantities related to fine scales required a substantially higher resolution than published work. Budgets of the transport equations of Favre averaged momentum, total energy and TKE are presented in the vortex shedding region, the developed wake and the blade boundary layer. These are useful for turbulence modellers to understand the accuracy of a particular turbulence model. Energy transport mechanisms were discussed to provide an understanding of the important mechanisms and their variation with Reynolds number. Finally a local assessment of linear eddy-viscosity models was presented where a turbulence model based on an optimized turbulence viscosity was compared to the standard k-ϵ model. It was found that in the vortex shedding region there was scope for improvement of the k-ϵ model. However, the remaining modelling error of the optimized model was large highlighting the limitation of linear eddy viscosity models. Further, regions with large errors in the turbulence model were identified close to leading and trailing edge.

Contents

List of Figures

List of Tables

Nomenclature

Arabic Letters

variable	name
$\mathcal{C}_1$	turbulent transport of TKE
$\mathcal{C}_2$	pressure diffusion of TKE
$\mathcal{C}_3$	molecular diffusion of TKE
c	speed of sound
c_v	heat coefficient at constant volume
c_p	heat coefficient at constant pressure, blade pressure coefficient
c_{sut}	Sutherland constant
c_{th}	thermal constant
c_μ	coefficient of $k\epsilon$ model
e	internal energy
$e_{t,kin}$	transport of kinetic energy
$e_{t,h}$	transport of enthalpy
$e_{t,\widetilde{u}}$	molecular stress work
$e_{t,\tau}$	RS Work
$e_{t,u''}$	Favre diffusion
$e_{t,\widetilde{T}}$	mean heat flux
$e_{t,T''}$	Favre heat flux
$e_{t,h''}$	turbulent heat flux
E	energy/velocity spectrum
F	Interface normal flux
$\vec{f}$,$\vec{g}$,$\vec{h}$	flux vectors
h	enthalpy
J	Jacobian determinant of grid
K_{in}	factor of characteristic boundary condition
k	turbulence kinetic energy, wave number
$\vec{L}$	transport term in characteristic governing equations
Ma	Mach number
p	pressure
$\mathcal{P}$	production of Reynolds stress/TKE
q	quantity
$\vec{Q}$	characteristic solution vector
$\vec{q}$	solution vector, heat transfer
Pr	Prandtl number

Re	Reynolds number
$\mathcal{R}$	pressure work (TKE and Reynolds stress equation)
S_{ij}	strain rate tensor component
t_{ij}	viscous stress tensor component
T	Temperature
t	time
$\mathcal{V}$	viscous work (TKE and Reynolds stress equation)
u_i	velocity vector component
x_i	spatial coordinate

Greek Letters

variable	**name**
β	wave number of inlet turbulence, local flow angle
δ_{ij}	Kronecker Delta
η	coordinate in computational space
ϵ	dissipation rate
γ	ratio of specific heats
χ	modelling error in energy due to Reynolds stress
μ	molecular viscosity
μ_t	turbulence viscosity
ω	wake loss
Π	pressure dilatation (TKE and Reynolds stress equation)
ρ	density
σ_{in}	factor used for characteristic boundary conditions
σ_k	coefficient of gradient diffusion model
τ_{ij}	Reynolds stress component
τ_w	wall shear stress
ξ	coordinate in computational space, error in the divergence of the Reynolds stress
ζ	second viscosity, Reynolds stress modelling error

Abbreviations

BC	boundary condition
BL	boundary layer
CBC	characteristic boundary condition
DNS	direct numerical simulation
HiPSTAR	high performance solver for turbulence and aeroacoustic research
KH	Kelvin - Helmholtz
LES	large eddy simulation
LPT	low pressure turbine
MPI	message passing interface
RANS	Reynolds averaged Navier Stokes
RS	Reynolds stress
RHS	right hand side
TKE	turbulence kinetic energy

Subscripts and Superscripts

variable	**name**
b	Boussinesq model
$char$	characteristic
$diff$	diffusion term
gd	gradient diffusion
i, j, k	components of tensors and vectors with range 1 to 3
is	isentropic reference value
n	normal
ns	Navier Stokes
ref	reference value
rms	root mean square
sh	shear
sp	sponge
t	stagnation
v	viscous
∞	reference value
τ	optimized for minimum error in Reynolds stress
$\tilde{q}$	Favre average of q
$\overline{q}$	Reynolds average of q
$'$	Reynolds fluctuation
$''$	Favre fluctuation q
$*$	inverse grid metric
$+$	nondimensional wall unit

Acknowledgements

While I conducted this work the continuous interaction with the group in Southampton was of great help. In particular my supervisor, but also the rest of the HIPSTAR users and fellow PHD students as well as research stuff always had on open ear when I came with questions.

My work was sponsored by General Electric and I am gratefull for the permission to publish my research in this thesis as well as other publications. I also would like to thank my main contact at GE for their guidance on how to make the research more relevant for engine manufacturers.

Ein besonderer Dank gilt meine Eltern, die mich von früher Kindheit an unterstüzt haben und mir eine Ausbildung hin zu einem akademischen Abschluss ermöglichten.

UNIVERSITY OF Southampton

Academic Thesis: Declaration Of Authorship

I, Richard Pichler ,

declare that this thesis and the work presented in it are my own and has been generated by me as the result of my own original research.

Thesis Title: Investigations on Turbulence in Low Pressure Turbines based on Direct Numerical Simulation

I confirm that:

1. This work was done wholly or mainly while in candidature for a research degree at this University;
2. Where any part of this thesis has previously been submitted for a degree or any other qualification at this University or any other institution, this has been clearly stated;
3. Where I have consulted the published work of others, this is always clearly attributed;
4. Where I have quoted from the work of others, the source is always given. With the exception of such quotations, this thesis is entirely my own work;
5. I have acknowledged all main sources of help;
6. Where the thesis is based on work done by myself jointly with others, I have made clear exactly what was done by others and what I have contributed myself;
7. Either none of this work has been published before submission, or parts of this work have been published as: [please list references below]:
   - Sandberg et al.(2015)
   - Michelassi et al. (2015)
   - Pichler et al. (2015)

Signed: .....

Date:

The declaration is signed in the printed version available at the Univeristy of Southampton

Chapter 1

Introduction and Background

1.1 Motivation

Lowering the fuel consumption of aircraft is one of the key targets in aircraft design to both decrease the operational cost and to fulfil environmental regulations. Reducing the fuel consumption can be achieved by various means and one among them is the reduction of the specific fuel consumption (sfc) of the engines. In general, during design different engine concepts are rated according to defined performance parameters. These performance parameters have to be obtained from the engine and several of them depend on flow field variables. Therefore the flow field is generally either measured or predicted using computations. Several numerical approaches tremendously decrease cost with respect to experiments. However, to date the accuracy of numerical methods is still insufficient for general turbine flows as stated by Denton (2004):

> "Turbine design is a complex process which is far from being an exact science. Much of the literature on the subject is specific to one manufacturer's range of machines and may not apply to other types of design. Published work almost inevitably tries to give the impression that all is understood and predictable. The reader is warned not to be taken in by these claims, the real flow is almost infinitely complex and we are still far from being able to predict the fine details of the flow even over a turbine blade in a cascade."

Similar to many other engineering fluid mechanics problems, one main issue responsible for the inaccuracy of predictive methods comes to mind immediately. A set of governing equations was developed more than 100 years ago and is known to represent the physics for various flows. However, to date no analytical solution for general problems has been found. Numerical approximations of the governing equations for many engineering applications (without any further modelling) are currently not practicable since

the computational power is not sufficient. To overcome this limitation additional modelling is applied to reduce the computational cost or some sort of correlation is used. Correlations predict a value based on a database of experiments and their accuracy for different designs is unclear. Further modelling on the other hand yields problems if the modelling assumptions are not valid. Even though a fair amount of research has been published, universally accepted models or correlations are still missing. Improving the understanding of the flow processes and physics is expected to aid the improvement of currently used design tools.

In order to enhance the physical understanding of flows through turbomachines numerical simulations are conducted. Numerical simulations are used since the entire three dimensional unsteady flow field is accessible, which in case of experiments is not generally the case. The flow field information can be used to understand flow physics and investigate the problems of current modelling approaches. Since the flow field through a turbomachine is comprised of several sections that are fundamentally different, it generally is broken down into smaller parts. In this work the low pressure turbine (LPT) is investigated. The reason for this choice is that the Reynolds number in the LPT is comparably small (Tucker, 2011), having two important consequences. Firstly, as the cost of direct numerical simulations (DNS) increases with Reynolds number only DNS of low to moderate Reynolds number flows, as present in an LPT, are feasible (cf. section 1.2.2). Further, at lower Reynolds number the boundary layer (BL) remains laminar for a longer proportion of the blade surface. This is an issues since laminar BLs are known to be more prone to separation than turbulent BL under adverse pressure gradients. Hence, if the BL remains laminar in the adverse pressure gradient region at the suction side the flow might separate which often has a significant influence on performance.

The main idea of this work is to understand the limitation of linear eddy viscosity RANS models for flow predictions of the LPT with the aid of DNS and the numerical algorithm is presented in chapter 2. Owing to the high cost of DNS computational performance is assessed and where necessary improved which is done in chapter 3. Therefore first a high accuracy dataset has to be provided which requires a thorough validation conducted in chapter 4. Since a DNS solution provides the full three dimensional time resolved flow field a deep insight into the flow physics can be gained. Therefore the created dataset is investigated and presented in 5. By comparing turbulence models with the DNS dataset their limitations can be assessed and in chapter 6. Finally the conclusions are drawn in chapter 7 followed by suggestions for future research.

1.2 Modelling of the Flow through an LPT

1.2.1 Governing Equations

For most engineering air flows it is considered that the physics can be represented by a set of conservation laws defined in the following. Assuming that the smallest scales of the fluid motion are significantly greater than scales of molecular motion (being valid for LPT flows as considered here) the flow can be treated as a continuum. Considering an infinitesimally small control volume in that continuum, the conservation laws take the form presented in this section. The representation in dimensional form can be found, for example, in (Wilcox, 1998, p. 174).

Throughout this text the Einsteinian summation convention (summation over repeated indices) will be used if not stated differently. Further, if not stated differently all variables are used in nondimensional form. In appendix A the relationship between dimensional and nondimensional variables as used in this work is presented.

First some general assumptions are stated. The molecular viscosity is computed using Sutherland's law given by (nondimensional form)

$$\mu = \frac{T^{\frac{3}{2}}\,(1 + c_{sut})}{T + c_{sut}}, \tag{1.1}$$

where c_{sut} is the nondimensional Sutherland reference temperature which is set to 0.3686 (Schlichting, 1979) based on a reference temperature of 300K and for mono-atomic gases the second viscosity is defined as

$$\zeta = -\frac{2}{3}\mu, \tag{1.2}$$

which is generally used for air (Wilcox, 1998). The strain rate tensor is defined as

$$S_{ij} = \frac{1}{2}\left[\frac{\partial u_i}{\partial x_j} + \frac{\partial u_j}{\partial x_i}\right], \tag{1.3}$$

where u_i and x_i are the velocity components and the spatial directions. The fluid is assumed to be Newtonian and thus the molecular stress and strain are related using

$$t_{ij} = 2\mu S_{ij} + \zeta \frac{\partial u_k}{\partial x_k}\delta_{ij}. \tag{1.4}$$

Further, the fluid is assumed to be ideal and thus the ideal equation of state in nondimensional form can be used. It is given by

$$p = \frac{\rho T}{\gamma Ma_\infty^2}, \tag{1.5}$$

where p, ρ, T,γ and Ma_∞ are pressure, density, temperature, ratio of specific heats and reference Mach number (see below), respectively. Assuming a perfectly caloric gas,

specific energy e and specific enthalpy h can be related to temperature as

$$e = c_v T \quad \text{and} \quad h = c_p T, \tag{1.6}$$

where c_v and c_p are heat coefficients at constant volume and constant pressure change, respectively. Using the Fourier law the heat flux vector is given by

$$q_i = \frac{-\mu}{(\gamma - 1)\, Re_\infty Pr_\infty Ma_\infty^2} \frac{\partial T}{\partial x_j} \,. \tag{1.7}$$

The process of nondimensionalization (further details in appendix A) introduces reference Reynolds, Mach and Prandtl number into the set of governing equations given by

$$Re_\infty = \frac{\rho_\infty U_\infty L_\infty}{\mu_\infty} \quad \text{and} \quad Ma_\infty = \frac{U_\infty}{\sqrt{(\gamma - 1)\, c_p T_\infty}} \quad \text{and} \quad Pr_\infty = \frac{c_{p,\infty} \mu_\infty}{\kappa_\infty} \,. \tag{1.8}$$

Conservation of Mass The first conservation law is the conservation of mass (also called continuity equation), given by

$$\frac{\partial \rho}{\partial t} + \frac{\partial}{\partial x_i} (\rho u_i) = 0. \tag{1.9}$$

The continuity equation conserves the mass in the control volume, i.e. mass can neither be generated nor destroyed inside the volume.

Conservation of Momentum The second conservation law is obtained from Newtons second law and it is often referred to as the Navier-Stokes equations. It is a vector equation with one component for each spatial dimension i and it is given by (neglecting surface, gravitational and other volume forces)

$$\frac{\partial}{\partial t} (\rho u_i) + \frac{\partial}{\partial x_j} (\rho u_j u_i) = -\frac{\partial p}{\partial x_i} + \frac{1}{Re_\infty} \frac{\partial}{\partial x_j} (t_{ji}) \,. \tag{1.10}$$

Conservation of Energy Finally the conservation of energy completes the set of governing equations. It represents the first law of thermodynamics and is given by (here the total energy form is chosen)

$$\begin{aligned} &\frac{\partial}{\partial t} \left[\rho \left(e + \frac{1}{2} u_i u_i \right) \right] + \frac{\partial}{\partial x_j} \left[\rho u_j \left(h + \frac{1}{2} u_i u_i \right) \right] \\ &= \frac{1}{Re_\infty} \frac{\partial}{\partial x_j} (u_i t_{ij}) + \frac{1}{(\gamma - 1)\, Re_\infty Pr_\infty Ma_\infty^2} \frac{\partial}{\partial x_j} \left(\mu \frac{\partial T}{\partial x_j} \right). \end{aligned} \tag{1.11}$$

The three conservation laws result in a system of five coupled partial differential equations, and along with the equation of state a closed system is obtained which is called

set of governing equations in the following. Since no analytical solution for complex problems in general and for an LPT passage in particular has been found to date, another method has to be applied to obtain the flow field. One frequently used method is to numerically approximate the governing equations as discussed in the following.

1.2.2 Numerical Modelling Strategies

First three basically different approaches are reviewed to present their advantages and disadvantages and to show the sort of modelling being applied for each method in order to briefly point out the improvement potential and how this study can help.

Direct Numerical Simulation (DNS): The set of governing equations is comprised of five coupled partial differential equations and one additional equation to close the system as explained in section 1.2.1. Numerical methods have been developed that can be used to directly approximate this set of equations. In theory this is a straight forward process. However, it requires that all flow structures (i.e small to large in space and short to long in time) have to be resolved which turns out to not be achievable for many cases because of the prohibitive computational cost. Using the Reynolds number of the large scales given by

$$Re_L = \frac{\rho\sqrt{k}L}{\mu}, \tag{1.12}$$

where k, L and μ are the specific turbulence kinetic energy, characteristic length of the largest structures (e.g. turbulent length scale) and the kinematic viscosity, it can be shown that for homogeneous isotropic turbulence (HIT) the computational cost scales as (Pope, 2000, p. 186 and 347)

$$N^3 \sim Re_L^{9/4} \quad \text{and} \quad N_t \sim Re_L^{1/2}\,, \tag{1.13}$$

where N is the number of grid points in one spatial direction and N_t is the number of times steps required for DNS. Altogether the computational cost therefore scales with Re_L^3 not taking numerical stability constraints into account yet. Hence, the computational cost strongly depends upon the Reynolds number of the flow. Such a clear scaling relation is not available for an LPT case for various reasons. In contrast to HIT it cannot be assumed that turbulence is in quasi-equilibrium, i.e. that turbulence is generated at the large scales at the same rate as it is dissipated at the smallest scales. Also the turbulence is not homogeneous and isotropic (c.f Stieger & Hodson (2005)). Further, the flow is wall bounded and thus transition occurs in the boundary layers and the structures close to the wall are not of same character as in homogeneous isotropic turbulence. Even though there is no clear relation between Re and the cost, there is a strong dependence on Reynolds number and a rough estimate for the number of cells used versus Re can be found in (Tucker, 2011). Therefore direct numerical simulations have mainly been

performed in regions of turbomachines that are relatively small or for model problems (Tucker, 2011). Since the LPT is the region where the Reynolds number in the engine is lowest, most DNSs treating real geometry cases to date have been conducted in the LPT. However, using DNS to perform design computations of turbomachines is still not feasible to date, such that cheaper approaches have to be used.

Reynolds averaged Navier Stokes (RANS) simulations: In order to limit cost Reynolds averaged or Favre averaged solutions can be considered which are presented in the following. First, only flow having a constant time mean (ergodic) are discussed allowing one to use time averages instead of ensemble averages. For incompressible cases the well known Reynolds decomposition is applied where the flow quantities are separated into a mean part and a turbulent fluctuation

$$q(t) = \overline{q} + q^{'}(t)\,. \tag{1.14}$$

If Reynolds decomposed variables are substituted into the compressible Navier Stokes equations and the Reynolds averaging procedure is applied, additional terms compared to the incompressible case would arise. Therefore rather than decomposing the variables using Reynolds averages, Favré averages, being defined as (Wilcox, 1998)

$$\tilde{q} = \frac{1}{\overline{\rho}} \lim_{T\to\infty} \frac{1}{T} \int_t^{t+T} \rho(\mathbf{x},\tau) q(\mathbf{x},\tau) d\tau = \frac{\overline{\rho u}}{\overline{\rho}} \tag{1.15}$$

are used for velocity, energy, enthalpy and temperature. Favre decompositions of these variables are defined by

$$q_i(t) = \widetilde{q_i} + q_i^{''}(t)\,, \tag{1.16}$$

where the Favre mean is denoted by a tilde and the Favre fluctuation by the double prime. The derivation of the compressible RANS equations can be found in (Wilcox, 1998, p. 172ff) and here only the resulting set of equations is given in the notation used in this work. The Favre averaged continuity equation is given by

$$\frac{\partial \overline{\rho}}{\partial t} + \frac{\partial \overline{\rho}\widetilde{u_j}}{\partial x_j} = 0, \tag{1.17}$$

the Favre averaged momentum equation yields

$$\frac{\partial\left(\overline{\rho}\widetilde{u_i}\right)}{\partial t} + \frac{\partial\left(\overline{\rho}\widetilde{u_j}\widetilde{u_i}\right)}{\partial x_j} + \frac{\partial\left(\overline{\rho u_j^{''} u_i^{''}}\right)}{\partial x_j} = -\frac{\partial \overline{p}}{\partial x_i} + \frac{\partial t_{ij}\left(\widetilde{u}\right)}{\partial x_j}, \tag{1.18}$$

and the Favre averaged energy equation is given by

$$\frac{\partial}{\partial t}\left[\overline{\rho}\widetilde{e}+\frac{1}{2}\overline{\rho}\widetilde{u}_i\widetilde{u}_i+\overline{\rho}k\right]+\frac{\partial}{\partial x_j}\left[\overline{\rho}\widetilde{u}_j\widetilde{h}+\overline{\rho}\widetilde{u}_j\frac{1}{2}\widetilde{u}_i\widetilde{u}_i+\overline{\rho}\widetilde{u}_jk\right]=\frac{\partial}{\partial x_j}\left[\widetilde{u}_it_{ij}\left(\widetilde{u}\right)+\widetilde{u}_i\tau_{ij}\right]+$$
$$+\frac{\partial}{\partial x_j}\left(c_{th}\mu\frac{\partial\widetilde{T}}{\partial x_j}\right)+\frac{\partial}{\partial x_j}\left(c_{th}\mu\frac{\partial\overline{T''}}{\partial x_j}-\overline{\rho u_j''h''}\right)+$$
$$+\frac{\partial}{\partial x_j}\left[\overline{u_i''t_{ij}\left(u''\right)}-\overline{\rho u_j''\frac{1}{2}u_i''u_i''}\right]+\frac{\partial}{\partial x_j}\left[\overline{u_i''}t_{ij}\left(\widetilde{u}\right)+\widetilde{u}_it_{ij}\left(\overline{u''}\right)\right] \tag{1.19}$$

where the constants for the heat flux are summarized as

$$c_{th}=\frac{1}{\left(\gamma-1\right)Re_\infty Pr_\infty Ma_\infty^2}. \tag{1.20}$$

In this set of equations the only assumption is that $\overline{\mu}=\mu$ such that additional terms appear as compared to the notation in Wilcox (1998). The compressible RANS equations are solved for the mean values and, therefore, terms depending on the fluctuations (indicated in blue) cannot be simulated. The so called Reynolds stress tensor appearing in both the momentum and energy transport equation, being generally defined as

$$\tau_{ij}=-\overline{\rho u_i''u_j''}\,, \tag{1.21}$$

depends on fluctuations and in order to solve the equations it has to be modelled. Further, also terms depending on the turbulent kinetic energy k as well as the terms

$$\frac{\partial}{\partial x_j}\left[\overline{u_i''t_{ij}\left(u''\right)}-\overline{\rho u_j''\frac{1}{2}u_i''u_i''}\right], \tag{1.22}$$

the thermodynamic fluctuations

$$\frac{\partial}{\partial x_j}\left(\frac{1}{\left(\gamma-1\right)Re_\infty Pr_\infty Ma_\infty^2}\mu\frac{\partial\overline{T''}}{\partial x_j}-\overline{\rho u_j''h''}\right) \tag{1.23}$$

and the terms depending on the time mean of the Favre velocity fluctuations

$$\frac{\partial}{\partial x_j}\left[\overline{u_i''}t_{ij}\left(\widetilde{u}\right)+\widetilde{u}_it_{ij}\left(\overline{u''}\right)\right] \tag{1.24}$$

only appearing in the energy equation depend on fluctuations and have to be modelled. These terms govern the contribution of turbulent kinetic energy to mean total energy. Even though terms depending on fluctuations might not be of interest for the designer in terms of rating the performance, they represent the influence the fluctuations have on the mean. Hence, if they are not modelled appropriately, the mean is probably also affected. Significant effort has been made to develop turbulence models to date but none of them is accepted as universal, i.e. gives correct results for at least a wide range of flows.

Large Eddy Simulation (LES): In between DNS and RANS in terms of modelling fidelity level and computational cost, so called large eddy simulations (LES) have been developed. Rather than modelling all turbulent fluctuations (RANS), or resolving all (DNS), the larger scales are resolved and the smaller ones are modelled. Most of the turbulence kinetic energy is contained in the larger scales (Pope, 2000) and thus resolved. Hence the contribution of the modelled part is smaller. Further, it is widely assumed that the smallest scales in non-wall-bounded flows are uniform and thus easier to model.

In order to perform LES the governing equations are filtered. This filtering procedure, similar to RANS, introduces a subgrid stress term, but in case of LES this term is considerably smaller than in RANS since it only accounts for the smallest scales. Different models exist, but in general the smallest scales are filtered (dissipated) and the filter strength depends on the grid size. Particularly for non wall-bounded flows this is an attractive alternative. For wall bounded flows, though, the smallest scales close to the wall are important. However, these are filtered out in case of LES if the grid is too coarse to resolve them. Considering transition, the smallest scales are the onset of transition, but if not resolved this might delay transition. Since the correct simulation of transition is crucial for this study, a DNS-like resolution has to be used close to the wall, even if an LES is performed. Therefore, close to the wall the potential saving of computational time is limited. In the wake, though, LES is expected to still enable computational cost reduction at reasonable accuracy even if the smallest scales are modelled. Thus LES with DNS-like resolution close to the wall should allow for cheaper simulations but still is expected to yield accurate results. Michelassi *et al.* (2003) performed a comparison of incompressible LES and DNS and found reasonable agreement for well resolved cases.

Concluding remarks: Other methods (e.g. potential methods, boundary layer methods, throughflow methods,..) are available and used to solve the flow through turbomachines but even though cheaper, these methods in general rely on further modelling and/or correlations. Among these methods RANS has the lowest level of modelling, such that the focus in this study is on RANS even though conclusions drawn on general physical mechanisms might help to improve other methods as well. The choice of RANS for the base test model is also related to their increased usage due to risen computational power in the recent years. Modelling assumptions used for RANS simulations are based on the fluctuating flow content, in particular correlations of them. Hence, wherever in the flow there are fluctuations these terms might be non-zero and a model has to predict them appropriately. Therefore, the literature review in the following will focus on presenting the flow environment focusing on the identification of regions where fluctuations arise in an LPT flow. This includes virtually all non-laminar flow regions, most namely transitional and turbulent regions, but also acoustic waves.

1.3 Current Understanding of the Flow through Low Pressure Turbines

1.3.1 Domain under consideration:

In common aircraft engines in the LPT the flow coming from the high pressure turbine is expanded and the work obtained is used to power the fan and the first compressor stages. Given the varying operating conditions during each flight the LPT operates through a range of Reynolds and Mach numbers. The actual flow in a real low pressure turbine is complex and in order to focus on certain aspects and make DNS simulations affordable some general assumption used are stated before the review of current understanding is conducted.

In general the rotational motion of the rotor plays an important role in the flow through a turbomachine. Important phenomena particularly concerning the boundary layer and loss development can also be investigated using a so called cascade model as used in wind tunnel experiments where only one blade row is investigated and the blades are unwrapped (Hodson, 2004). If the blade sections are constant along the span this case is called a linear cascade.

In a turbomachine as well as in cascade wind tunnel experiments the flow is confined to a certain span by so called endwalls. At these endwalls boundary layers (BL) develop that interact with the flow (and BL) about the blade. These endwall flows by themselves have been an intensive research area (Denton, 1993) since additional losses are caused there that can contribute for as much as a third of the overall loss (Denton, 2004). Considering that for high aspect ratio blades as used in LPTs the majority of the losses arise from the midspan region (Hodson & Howell, 2005), this flow sufficiently far away from these endwalls in a linear cascade is considered. Therefore the endwall boundary layers are not required to be resolved which significantly reduces computational cost. Further, this allows one to separate the effects of endwall and blade BLs and so called quasi two dimensional flow can be investigated. In order to obtain quasi two dimensional flow conditions in experiments often BL suction is used, to counteract the blockage by the endwalls.

For eddy-resolving numerical studies, simplified configurations have been developed (Wu & Durbin, 2001*b*; Wissink, 2003; Medic & Sharma, 2012) in order to reduce computational cost. A linear cascade with periodic boundaries in the span is used, where the flow has no mean gradients in the spanwise directions (quasi two dimensional). This configuration is expected to represent the flow configuration in a blade-to-blade surface (or surface of revolution, pitchwise-streamwise surface, cf. figure 1.1) of linear cascades well.

The LPT is comprised of several stages, each stage consisting of a stator and a rotor. Rotor rows are turning in the circumferential (pitchwise) direction and stator rows are steady with respect to the engine casing. Hence rotor and stator rows have a relative velocity. First an isolated stage (i.e. a stator with a downstream rotor) with uniform inflow to the stage is considered. Then some conclusions for multi-stage configurations are drawn.

1.3.2 Stator-Rotor interaction

In the following discussion the engine casing will be assumed to be at rest. In figure 1.1 the schematics of the stator-rotor interaction for a single stage of an LPT are shown. The horizontal and vertical directions are the streamwise and pitchwise directions, respectively. Since a linear cascade is considered the spanwise direction normal to the plane presented is uniform. On the streamwise axis three positions are indicated labelled P_0,

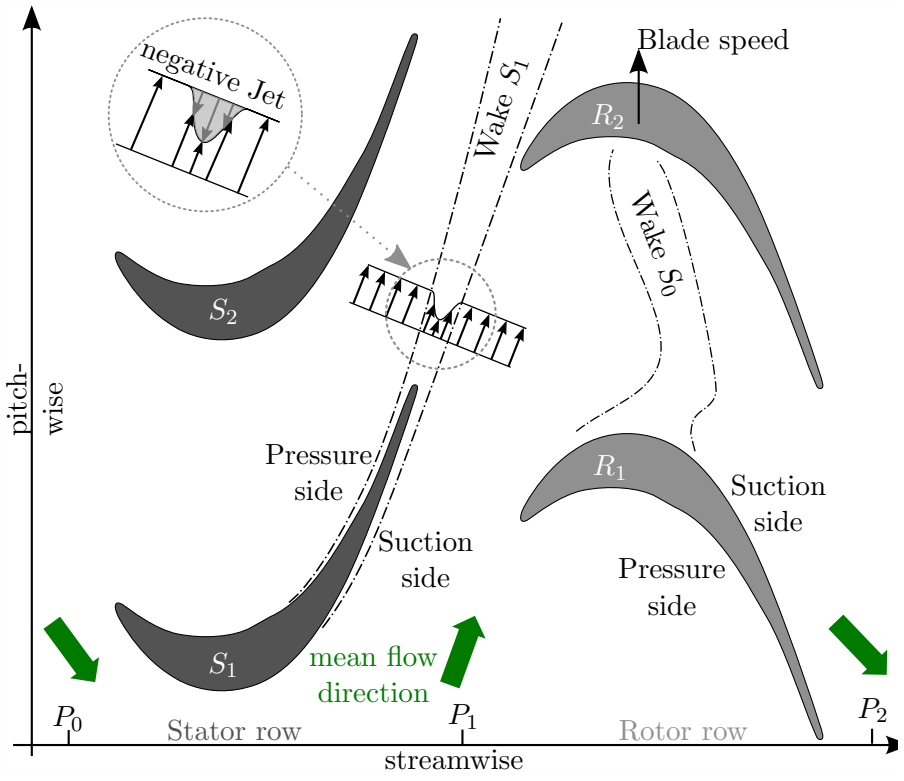

FIGURE 1.1: Stator-Rotor interaction based on Coull & Hodson (2011)

P_1 and P_2, where P_0 is the stage inlet position and P_2 is the stage outlet position. Position P_1 is located such that it is downstream of the stator row and upstream of the rotor row. The mean flow direction at each position is indicated by the green block arrows. Since a single stage with uniform inflow is considered the mean flow at P_0 is uniform across the pitch.

The most important unsteady effects due to rotor stator interaction arise due to wakes of upstream rows and potential effects of both upstream and downstream rows, where the wake effects are generally assumed to dominate (Hodson & Howell, 2005). However, since boundary layers are close to separation, minor potential effects might have a considerable influence and thus cannot be neglected. Since the impact of wakes in general is considered to be of higher importance, most of the research is concerned with it. In the following the current understanding on the unsteady environment will be presented. In the setup presented in figure 1.1 the stator only experiences potential flow effects and the rotor experiences both wakes and potential flow effects.

Each of the blades generates a potential field around it and thus non-uniform profiles in the pitchwise direction. Due to the relative motion this means that each blade experiences time varying flow variables upstream of the rotor and downstream of the stator. This so called potential flow effect has been investigated using quasisteady methods (Mills, 1996; Parker, 1968; Parker & Watson, 1972) or fully unsteady approaches (Giesing, 1968) based on inviscid potential flow theories. These studies showed that if blades are in close vicinity potential flow effects cannot be neglected. However, the rapid decay of potential flow effects with distance also meant that only rows immediately upstream or downstream can have a significant effect. Parker (1968) conducted an experimental study of a single stage compressor where the axial gap between rotor and stator could be varied to understand the accuracy of the potential flow theory. He found that quasisteady potential flow investigations of blade row interaction as conducted by him are "an adequate basis for estimating the relative amplitudes of excitation to be expected from alternative designs but are not yet adequate for predicting absolute values".

Since viscous effects are often considered as more important the majority of research investigated viscous affects and in particular the interaction of wakes with the downstream blade row. Dring *et al.* (1982) conducted an experimental study of a test engine (incorporating both potential and viscous effects) first looking at unsteady pressures at several positions around the blade and downstream of it. Their configuration was one single stage where the row spacing could be varied and thus the influence of the row spacing could be investigated. The influence of the row spacing on the effect of the axial spacing was found to scale with the wake decay for the respective axial gap between the rows indicating that the unsteady effects are mainly governed by the wakes in their configuration. In the following the wake interaction process is discussed related to the generation process, the subsequent convection and distortion process and the interaction with the downstream blade.

Wake generation: The flow approaches the stator blade and has to pass around it. This yields a net reduction of area and a boundary layer developing from the stagnation point close to the blade leading edge on both suction and pressure sides. At the trailing

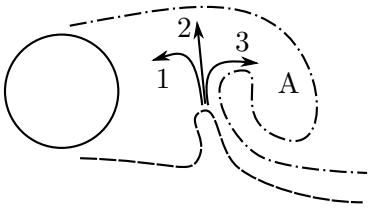

FIGURE 1.2: Vortex shedding formation region according to Gerrard (1966)

edge the boundary layers of the suction and pressure sides merge, resulting in a region of reduced momentum. Additionally, the blunt trailing edge also often leads to vortex shedding. Combined, these two effects comprise the so called wake region, being characterised by a smaller velocity and a generally higher turbulence level compared to the flow in the freestream away from the blades. Vortex shedding is of particular interest for the performance of the blade since it is directly related to the base pressure, which has an impact on losses (Denton, 1993).

Behind bluff bodies vortex shedding occurs which was first studied by Kàrmàn (an English translation can be found inKármán (2013)) using stability analysis. For cylinders several studies have been published validating the orginal theory and studied regarding various aspects. A similar form of vortex shedding is observed behind other bluff bodies including turbine blades. In order to understand the influence of the shape of the body and the trailing edge several studies have been performed. Motivated by water turbine vibrations, Heskestad & Olberts (1960) compared the vortex shedding frequency and intensity of a flat plate with reactangular, triangular, beveled and grooved trailing edges in a water tunnel. They concluded that the Strouhal number as well as the intensity varied for different trailing edge geometries. Further, they discuss the influence a laminar or turbulent upstream boundary layer as well as the ratio of the boundary layer thickness to the trailing edge thickness on the vortex shedding strength. Toebes & Eagleson (1961) performed similar experiments and highlighted the influence of the trailing edge geometry. In particular they investigated the range where the vortex shedding frequency was close to the natural frequency of the blade causing severe structural vibrations, motivating the need of accurate vortex shedding predictions.

Gerrard (1966) focuses on the vortex formation region of a cylinder which qualitatively is also expected to occur for trailing edge flows. In figure 1.2 one instant of the vortex shedding cycle of flow past a cylinder is sketched. The wake center line is the horizontal axis and the shear layers on either side of the cylinder are illustrated with the dashed and the dash-dotted line both with opposite circulation. The already generated vortex around point A draws the shear layer from the opposite side of the cylinder towards the wake center line and across it along the three indicated lines. One part of the shear layer turns towards the trailing edge and creates a reverse flow as indicated by arrow one. The most downstream part is entrained by the already existing vortex as indicated

by arrow 3 and the middle part is transported across the wake center axis such that a similar vortex but of opposite direction as around point A will be created which in turn will induce a vortex similar to the one around point A and so on.

In order to understand the influence of the shape of the bluff body Okajima (1982, 1990) studied the flow around a flat plate with rectangular leading edge (LE) and trailing edge (TE) (rectangular planform). In particular the influence of the ratio of chord to thickness (variation between 0.5 and 8) on the flow structures and the Reynolds number impact (variation between 70 and 20,000 based on thickness and free-stream quantities) on the flow patterns and Strouhal number was investigated. For smaller chord to thickness ratios below one they found a clear coupling between the LE and TE dynamics similar to what has been observed for cylinders. With an increasing chord to thickness ratio this coupling is less significant. The boundary layer that separates at the rectangular leading edge and reattaches before the trailing edge is reached. Beyond a certain chord to thickness ratio the TE vortex shedding seems to be independent of the direct potential interaction and the vortex shedding is mostly influenced by the boundary layers at the trailing edge.

Conducting a numerical simulation of a rectangular trailing edge and applying the Orr-Sommerfeld equation, Hannemann & Oertel (1989) concluded that the reverse flow region directly downstream of the trailing edge resulted in a local absolute instability and caused the vortex shedding process. Downstream of the reverse flow region the wake is locally convectively unstable.

Based on a similar geometry Yao *et al.* (2001) conduct direct numerical simulations of a similar configuration. Using pressure isosurfaces they illustrate the large scale Karman vortices and plotting iso surfaces of the second invariant of the velocity gradient tensor they visualize the fine scale turbulent vortices presenting the interaction of both.

Cicatelli & Sieverding (1997) conducted experiments of a turbine blade where the pressure probe at the trailing edge could be rotated allowing for a high spatial resolution of the unsteady pressure measurements. They concluded that the rms of the pressure reached up to 8% with respect to the downstream dynamic head. Further, they did split the signal into a random and periodic signal and found that the periodic pressure rms was up to 3% with respect to the downstream dynamic head.

This unsteady wake region can be averaged in time yielding a pitchwise varying velocity profile downstream of the stator which is steady in the absolute frame of reference. Since the rotor passes at a non-zero blade speed it experiences an unsteady inflow. To transform between absolute and relative frame of reference, velocity triangles are used, as depicted in figure 1.3. Following Coull & Hodson (2011), the velocity triangles for the freestream and the minimum velocity in the wake are plotted. In the absolute frame of reference a pure velocity deficit Δc between the free-stream absolute velocity c_F and the wake absolute velocity c_W is obtained. This phenomenon is often referred to as negative

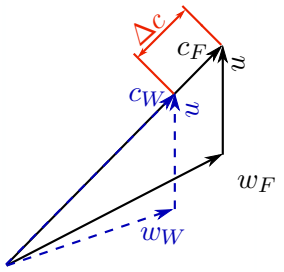

FIGURE 1.3: Velocity triangles of wake (blue-dashed), free-stream (black-solid) and velocity deficit of wake (red) (Coull & Hodson, 2011)

jet according to Meyer (1958) who used potential flow theory to model the convection of the velocity deficit (negative jet). Focusing again at the velocity triangle it is obvious that no angle variation is apparent in the absolute frame of reference. The relative velocities are obtained as the vector difference of absolute velocity and blade speed u. Since the velocity triangles are at the same radius and same rotor (i.e. same rotor speed), the blade speed is the same. This transformation results in a reduced velocity and in an angle change in the relative frame of reference. Both triangles presented in figure 1.3 represent the extrema during each cycle. Hence, even though the wake leads to a pure reduction in velocity magnitude in the stator frame of reference, both a variation of angle and magnitude occurs in the rotor frame of reference which also manifests itself in the mean quantity. Therefore, in order to compare the characteristics of a rotor blade subjected to clean inflow with upstream wakes at same mean inlet angle, the inlet angle of the free stream for both cases has to be different.

Wake convection and distortion: A wake develops downstream of each stator as presented for stators S_1 and S_0 in figure 1.1 (in this figure just wakes affecting the passage S_1, S_2, R_1 and R_2 are shown). Stator S_0 is located at stator pitch below S_1, but not shown in the figure. As illustrated in figure 1.1 the rotors move at blade speed u upwards and first the rotor R_2 will enter the wake of stator S_1 and thus clip it. Once rotor R_1 passes through the wake of the stator S_1, the wake is confined between the rotor blades similar to the wake of stator S_0 as illustrated in figure 1.1. As this wake is convected downstream it interacts with the flow field about the rotor. Smith (1966) describes this interaction using transport considerations and the chopping of the wake at the rotor leading edges. Since the transport on either side of the blade is different they do not merge again at the trailing edge of the rotor. While convected through the stage the flow within the wake region and the flow outside do different amounts of work.

Instantaneous snapshots give an understanding of the flow condition at a particular timestep, but in order to draw general conclusions, mean quantities are often considered. A pure time mean in this case would wash out the effect of the wake and just the mean influence of the wake can be investigated. However, the effect of the wake at particular

positions within the rotor is of interest as well and thus a different way of averaging is used. Since the wakes are steady in the mean and the rotor passes by at constant speed, a periodic inflow is apparent at the inlet. Hence, the flow can be averaged at certain positions of the wake with respect to the rotor blade (i.e phases). This procedure is called phase averaging and is generally performed at various wake positions, so that the mean influence of the wake on the rotor flow can be investigated. Binder *et al.* (1985) used Laser 2 Focus velocimetry to record the convection and distortion of wakes through a one stage axial compressor using phase averages and reported mean flow results as well as turbulence intensities. They showed that while the wakes (identified as regions of elevated turbulence intensities with respect to the rest of the flow) are convected through the following blade row, their turbulence intensity increases. This does not happen in the region between two wakes that initially have lower turbulent intensity compared to the wake. Even though the spatial resolution is coarse the wakes are clearly obvious in the phase averages presented. Also they reported that for a phase with higher turbulence intensity (wake passing) the phase locked mean outlet angle is higher compared to a phase with lower turbulence intensity (no wake) indicating that the presence of wakes leads to higher turning.

Additionally, several authors use a so called perturbation velocity defined as (Stieger & Hodson, 2005)

$$\langle U_p^* \rangle = \langle U^* \rangle - \overline{U^*} \,, \tag{1.25}$$

where anglebrackets denote a phase average and the overline denotes a time average. This perturbation velocity shows the difference of the current phase with respect to the time mean at this position (similar to the definition of the negative jet). Considering perturbation velocity, it can be seen that in the wake the "negative jet points towards its source" (Stieger & Hodson, 2005), thus away from the pressure side and towards the suction side, as illustrated in figure 1.4 by the single arrows.

Wu & Durbin (2001*b*), who performed a DNS of the T106A LPT-profile, reported on the "distorted migrating wakes" and their straining in LPTs. During its downstream convection the wake is subjected to the flow field. They used the principal axis of the strain rate tensor to identify the compression and stretching of the flow field and its impact on several quantities in the wake. They found that compression and stretching of the wake occurred along different axes close to the pressure side and the suction side as shown in figure 1.4 by the double arrows. Close to the suction side the wake is stretched in a direction normal to the wake and compression occurs in a direction along the wake, whereas close to the pressure side the opposite occurs. According to Rogers (2002), the development of wake width, velocity deficit and turbulent fluctuations depends on the global strain field. For the area close to the pressure side the strain field yields a reduction in all three quantities, whereas these quantities grow close to the suction side. Hence, after the wake is split by the blade leading edge it develops differently for the suction and the pressure side. Further, the study compared the deformation of the wake

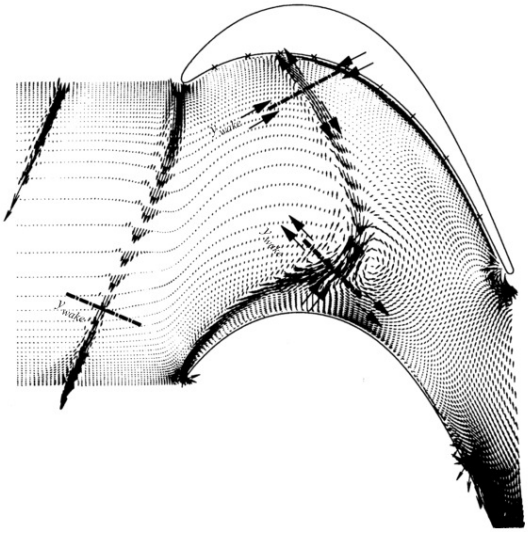

FIGURE 1.4: Perturbation velocity at one phase throughout the cycle, double arrows indicate compression and stretching of the wake close to suction and pressure side (from Wu & Durbin (2001*b*))

with a pure material transport of particles through the passage. It was found that both are similar and thus that "the irrotational base flow velocity field dominates the wake deformation process".

Stieger & Hodson (2005) presented results from two dimensional laser Doppler anemometry, given in figure 1.5. Turbulence kinetic energy is plotted at various phase averaged times t/τ_0, showing the position of the turbulent wake in contrast to the clean flow between the wakes (i.e low turbulence level). This illustrates how the wake is distorted while it is convected downstream. In figure 1.5 (c) and (d) perturbation velocity vectors are shown. Looking at the bow of the wake in figure 1.5 (d) it can be seen that there appear to be two counter-rotating vortices (one downstream and one upstream of the wake) even though they concluded that those are artefacts of the plotting perturbation velocity given that the free-stream is irrotational. Similar to Binder *et al.* (1985), Stieger & Hodson (2005) reported an increase in turbulent kinetic energy in the wake which they attributed to production of turbulent kinetic energy resulting from the Reynolds stresses being subjected to strain.

As the wake passes through the rotor passage it also interacts with the blade surfaces and their boundary layers. Wu & Durbin (2001*b*) found that while the wake convects downstream, the upper part aligns with the pressure side. This was illustrated by using the λ_2 criterion as defined by Jeong & Hussain (1995) to identify the vortex cores as presented in figure 1.6. Three wakes can be seen, with wake 3 just entering the rotor and wake one leaving it. The vortical structures in wake 3 are not oriented in one particular direction but due to the convection process explained earlier the upper part of the wake is strained and vortical structures eventually align with the pressure side (wake 1). This means that close to the leading edge just the uppermost part of the wake interacts with

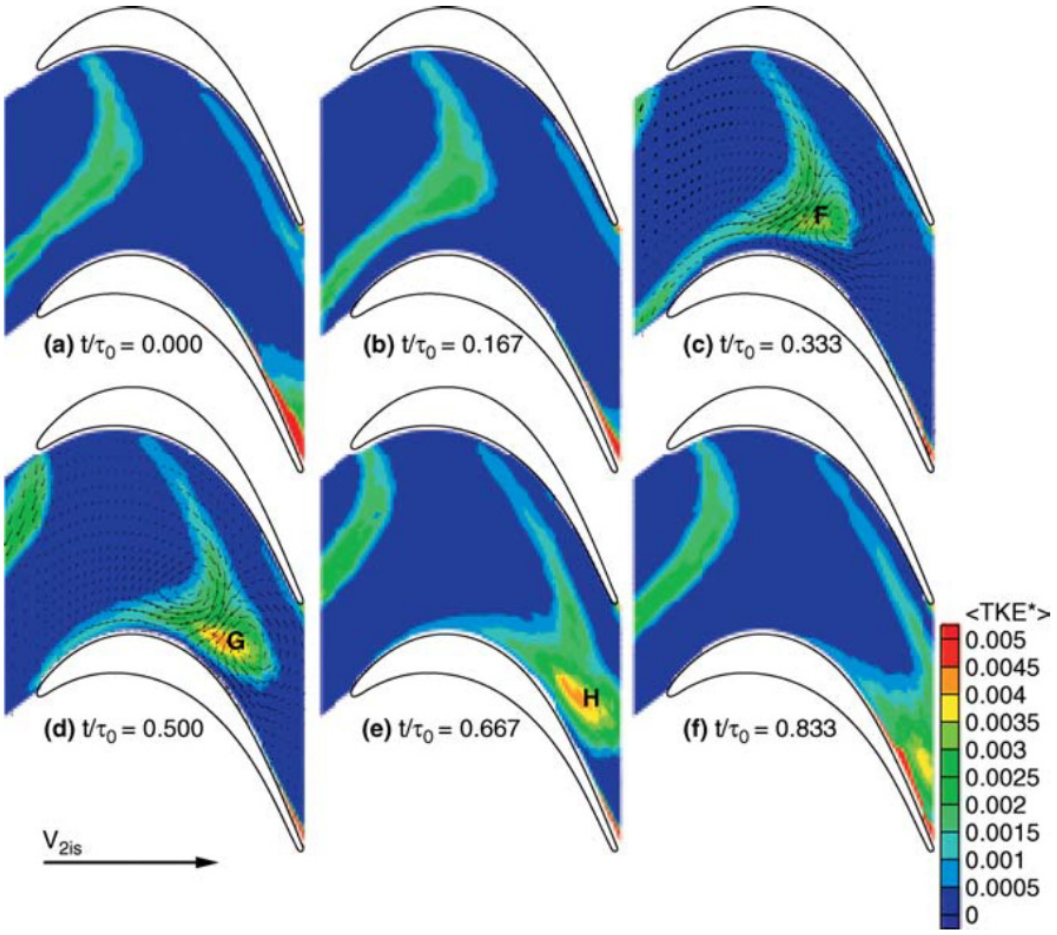

FIGURE 1.5: Turbulent kinetic energy at several phases (Stieger & Hodson, 2005)

the pressure side, but since further downstream the wake aligns with the pressure side, the leg from the bow to the uppermost part interacts with the pressure side. Hence, the wake affected region close to the leading edge during the interval between two wakes is small, but regions further downstream are almost under constant influence of the wakes. At the wall the flow has to stagnate and this induces a counter rotating vortex. Close to the leading edge the wakes are only interacting with the surface for a smaller fraction of time and thus vortical structures are only apparent for a small fraction around the time while the wake passes. Further downstream, though, the wake is interacting with the pressure side boundary layer for the majority of the time and the vortical structures are almost always there. The vortex alignment process identified by Wu & Durbin (2001*b*) was confirmed by Michelassi *et al.* (2003) for a lower Reynolds number case. However, in this case the wake passing period was higher and thus the pressure side was constantly subjected to the wake structures. While the vortices approximate the wall they reduce in size and induce turbulent structures at the wall.

Since the velocity in the wake region is smaller than in the background flow while the wake is transported through the downstream stage it is moved towards the suction side. Looking at figure 1.5 it is obvious that the high turbulent intensity region is closer to

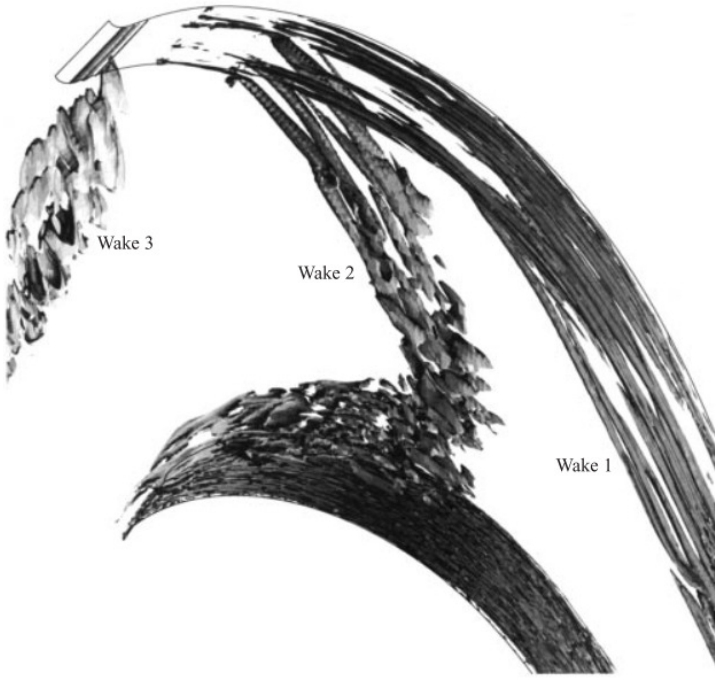

FIGURE 1.6: Vortex structures in wake identified by $\lambda_2 < 0$ from Wu & Durbin (2001*b*)

the suction side, thus the interaction of the wake with the suction side boundary layer might be more important.

Multi-stage environment: So far only one single isolated stage has been considered. General aircraft engine LPTs, though, consist of several stages. Hence, in general the flow approaching the stator is not uniform but disturbed by an upstream row (except for the first stage, but this generally doesn't see a clean inflow either). Thus the stator as well experiences a wake that travels at blade speed and similar effects to the ones described above will occur.

Further, the wake is generally not mixed out when it leaves the downstream blade row, such that it also affects rows further downstream. This process is less investigated compared to stator-rotor interaction in terms of detailed measurements in the blade row. Even though it is important, in this work only the interaction of one stator and one rotor is considered, thus this multi-stage effect is not discussed further. Considering that the flow mechanisms driving the development of the fluctuations are similar, conclusions from a single stage configuration are also expected to improve multistage simulations.

Concluding remarks: As mentioned in the previous section, the focus in this work is on the modelling of fluctuations. Considering the configuration presented in figure 1.1 if there is no background (freestream) turbulence at the inlet, fluctuations are confined to the transitional and turbulent parts of the boundary layers and the wake regions of both blades. In general, upstream of the stator there are further devices leading to

turbulence at the inlet. For these cases fluctuations are present in most of the flow field where the regions can be classified as transitional and turbulent flows. In the following the understanding of transition and turbulence as present in LPTs is presented.

1.3.3 Transition

Transition plays a major role in LPT design and the reasons are outlined following Hodson & Howell (2005), who presented design considerations for current LPTs indicating the importance of the state of the suction side boundary layer. The suction side boundary layer contributes approximately 60% of the total losses. In general the efficiency of the blades is high and thus optimization focuses on maintaining the efficiency (or even accept minor drops) while increasing the loading per blade and thus fewer blades are required per stage. This leads to a reduction in weight and also production cost. Higher loading, though, means that the flow might separate, which significantly increases losses. This is particularly an issue, since the isentropic Reynolds number (based on chord and isentropic exit velocity) is comparably low, between 100,000 and 250,000 at cruise (Coull *et al.*, 2010). Therefore, the boundary layer remains laminar over a long proportion of the chord and is more prone to separation. In fact, current designs typically feature a laminar separation with detached transition and turbulent reattachment, a so called short laminar separation bubble.

Therefore transition plays a major role in the determination of losses and the blade row performance. The blades are generally subjected to turbulent inflow and unsteady wake passing with both effects promoting transition. It also turns out that considering the unsteadiness during design, blades with increased lift (high lift and ultra high lift LPTs) can be constructed with similar losses to the datum where unsteadiness reducing the separation is not considered.

Hence, transition in LPTs has been an intense field of research. Several studies have been performed and different transition mechanisms have been found. A comprehensive study to identify transition mechanisms in turbomachines has been performed by Halstead *et al.* (1997*a*). According to them transition can be classified into "natural transition", "bypass transition" and "separated transition". Due to the unsteady environment natural transition is less important in turbomachines (Hodson & Howell, 2005). Bypass transition occurs if a boundary layer is subjected to freestream turbulence. Klebanoff *et al.* (1962) identified turbulent spots in such an environment in their experiments of zero pressure gradient flat plate boundary layers. Considering LPTs these spots have been observed as well but in general their occurrence is delayed to higher momentum thickness Reynolds number (Mayle & Dullenkopf, 1991). If the blade loading is sufficiently high the boundary layer might separate before natural or bypass transition occurs. In this case additionally an inflectional stability arises and can lead to transition. This phenomenon has been observed in LPT studies, particularly for high

and ultra high lift devices (Halstead *et al.*, 1997*b*; Hodson & Howell, 2005; Stieger & Hodson, 2005).

Coull & Hodson (2011) conducted a systematic study to identify the various transition mechanisms which they summarized as various "routes to transition" in figure 1.7 giving a more detailed picture as outlined by Halstead *et al.* (1997*a*). Considering the various sources that promote transition, the "routes to transition" observed for each source are illustrated. Grey indicates that this mechanism was not observed in that study. As a

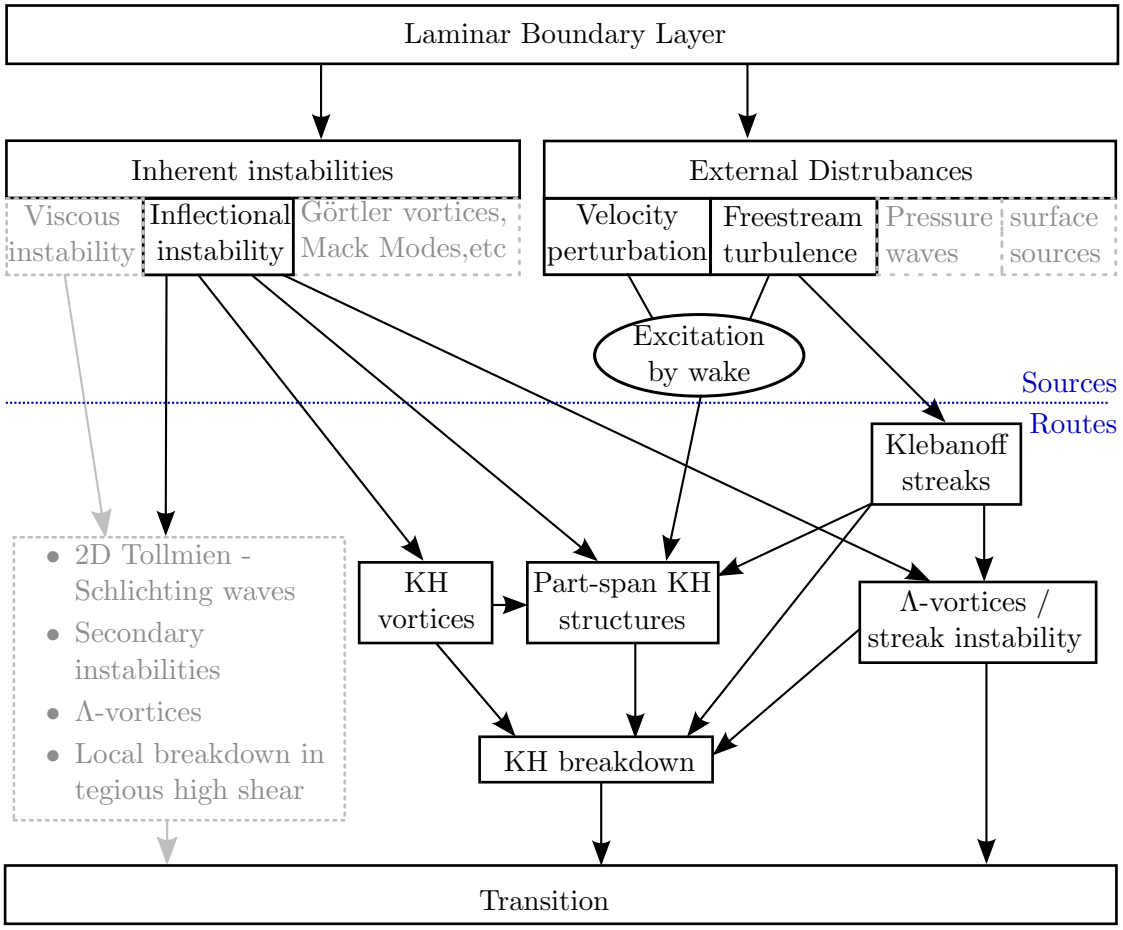

FIGURE 1.7: "Routes to Transition" as defined in Coull & Hodson (2011)

flow passes over a surface disturbances arise (sources) in the initially laminar boundary layer. Sources for these disturbances in general are either due to the flow in the boundary layer itself (i.e. inherent instabilities) or caused by the exterior (external disturbances). These disturbances grow (routes) and eventually transition starts.

Sources: In terms of inherent instability one can distinguish between viscous instability, inflectional instability (i.e. due to an inflection point in the wall normal velocity profile) and other inherent instabilities, in this context most notably Görtler vortices that have been found in flow investigations of laminar separation bubbles (Marxen *et al.*, 2009).

External disturbances might arise from velocity perturbations, freestream turbulence, pressure waves and disturbances that originate from the blade surface (like roughness) or flow control at the blade surface. In this work surface roughness is not considered and flow control is not investigated.

Considering the flow through a real LPT, a coupled process of the various sources leads to transition but the contribution of each source is different. In experiments and numerical investigations it is often tried to understand the influence of unsteadiness. Thus often a clean case (i.e. no inlet unsteadiness) is compared to either a case with free stream turbulence, incoming wakes (i.e. velocity deficit) or a combination of both.

Steps: The above disturbances might be amplified and depending on the contribution of the single sources various "routes to transition" (Coull & Hodson, 2011) have been identified by several authors. The contribution does not just vary from one case considered to another, but also changes throughout the wake passing cycle. In fact, the mechanisms coloured in black were all found throughout one wake passing cycle. However, several of those routes have similar "steps" represented by the boxes in figure 1.7 and before the routes are discussed these steps are briefly introduced.

- **Natural Transition:** Natural transition is hardly apparent in LPTs due to the high disturbance level environment. Nevertheless, it is briefly reviewed. These can be explained from stability theory (Schlichting, 1979). First two-dimensional Tollmien-Schlichting waves are observed which then break down into three-dimensional structures due to secondary instabilities. These then develop into Λ-shaped structures that then lead to turbulent spots which eventually merge into fully turbulent flow. In case of high freestream turbulence level the first stages might be bypassed. This process is called bypass transition.
- **Klebanoff streaks:** Free stream turbulence interacts with the boundary layer and induces "streaky structures" (Coull & Hodson, 2011) in it. The mean shear of the boundary layer acts in a way that disturbances of higher frequencies diminish and just lower frequencies interact with the boundary layer. Penetration depth has been shown to decrease with increasing Reynolds number (Jacobs & Durbin, 1998) thus the blade leading edge, where the boundary layer also is thinner, is the main region of interaction.
- **Kelvin-Helmholtz (KH) vortices:** If subjected to a strong adverse pressure gradient, the boundary layer will separate before transition. This leads to an inflectional velocity profile and similar to a free shear layer, spanwise-coherent vortices roll up.

- **part-span KH vortices:** If the unstable separation region is subjected to Klebanoff streaks the spanwise extent of KH vorticies might be significantly smaller than in a clean case.
- **Λ vortices and streak instability:** Durbin *et al.* (2009) considered three cases, one with just Tollmien-Schlichting waves, one with just Klebanoff streaks and one with both. They found that if just one of the two sources was considered, then no transition occurred, but if both sources were used then the flow underwent transition.
- **KH vortex breakdown:** KH vortices eventually become unstable and break down, where additional disturbances might promote the breakdown.

As mentioned earlier, in a general case for an LPT at low Reynolds number, inflectional instability as well as velocity perturbations and freestream turbulence combined determine transition. Following Coull & Hodson (2011), the transition process for this general case is explained. In figure 1.8 a space time plot is presented, where the suction

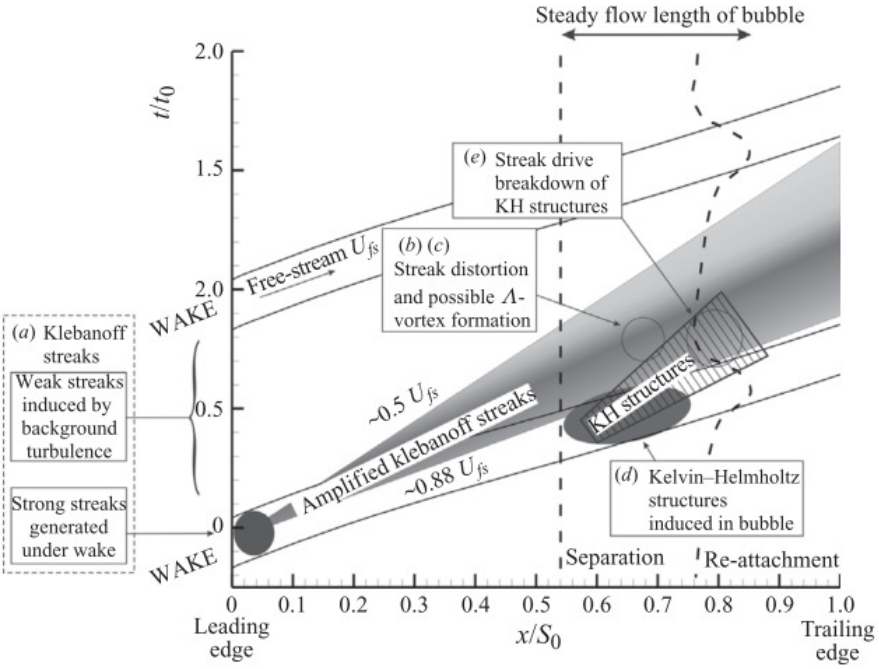

FIGURE 1.8: Tranisition mechanism in a space time plot from Coull & Hodson (2011)

side surface length is plotted along the horizontal axis and two wake cycles are plotted along the vertical axis. A particle moving at free stream velocity would follow the grey solid lines.

Close to the leading edge Klebanoff streaks are induced by both free stream and wake unsteadiness as indicated by (a) in figure 1.8. Since the turbulence intensity in the wake is bigger the Klebanoff streaks induced by the wake are stronger. These streaks convect downstream, as indicated by the grey triangle, at velocities of about 50% to 88%

of the freestream velocity, where the strongest streaks are transported at a velocity of approximately 70%. If the streaks interact with Λ vortices this might lead to transition as explained above.

When the wake passes over the separation bubble the KH vortices start to break down. The stronger Klebanoff streaks (induced by the wake) have not yet arrived since their convection speed is lower than the convection speed of the wakes. Therefore the breakdown seems to be a consequence of the wake convected outside of the BL. However, there are the small Klebanoff streaks induced by the free-stream and the velocity deficit in the wake. But which one or if it is the combination of those two or anything else could to date not be verified.

Once the strong Klebanoff streaks arrive at the KH vortices, they accelerate the breakdown and promote transition. This leads to a smaller bubble extension compared to the steady case. Once the strong streaks have passed, transition and reattachment move further downstream since after the wake has passed a so called calmed region (quiet region), as explained for example in Hodson (2004) appears, being characterised by low levels of disturbances. The vertical dashed lines indicate the length of the bubble and it can be seen that compared to the steady case (denoted by the arrow at the top of the figure) a net reduction of the bubble length is observed, leading to earlier transition.

In the above description the current understanding of how transition is affected by the unsteady environment is given. This is just done for one case and it is obvious that the actual picture will vary from case to case, where important parameters are Reynolds number, freestream turbulence intensity, blade loading, wake passing frequency and others. Any sort of correlation or physical model has to take into account those effects. Coull & Hodson (2012) tested current transition models and found for the best model a mean error of about 7% (even though most of the experiments used moving bars, rather than an actual upstream blade).

1.3.4 Turbulence and Reynolds stress modelling

The turbulent regions of the flow are confined to the wall boundary layer, the wakes and if background turbulence enters at the inlet also the rest of the domain. Most of the turbulence models are developed under assumptions which in general do not apply to the turbulence present. This is particularly true for the low Reynolds numbers present in LPTs and the vicinity of the trailing edge where vortex shedding occurs.

As mentioned above the Reynolds stress depends on the fluctuations and using an appropriate derivation (as presented in appendix B.1) a transport equation for each the

Reynolds stress component can be derived (Adumitroaie *et al.*, 1999)

$$\begin{aligned}\frac{\partial \tau_{ij}}{\partial t}+\frac{\partial \tau_{ij}\widetilde{u_k}}{\partial x_k} = & \underbrace{-\tau_{ik}\frac{\partial \widetilde{u_j}}{\partial x_k}-\tau_{jk}\frac{\partial \widetilde{u_i}}{\partial x_k}}_{-P_{ij}}+\underbrace{\frac{\partial \overline{\rho u_i'' u_j'' u_k''}}{\partial x_k}}_{-T_{1,ij}} \\ & \underbrace{+\overline{u_i''}\frac{\partial \overline{p}}{\partial x_j}+\overline{u_j''}\frac{\partial \overline{p}}{\partial x_i}}_{-R_{ij}}+\underbrace{\overline{\frac{\partial u_i'' p'}{\partial x_j}}+\overline{\frac{\partial u_j'' p'}{\partial x_i}}}_{-T_{2,ij}}\underbrace{-\overline{p'\frac{\partial u_i''}{\partial x_j}}-\overline{p'\frac{\partial u_j''}{\partial x_i}}}_{-\Pi_{ij}} \\ & \underbrace{-\overline{u_j''}\frac{\partial t_{ik}(\widetilde{u})}{\partial x_k}-\overline{u_i''}\frac{\partial t_{jk}(\widetilde{u})}{\partial x_k}}_{-\mathcal{V}_{ij}}\underbrace{-\frac{\partial}{\partial x_k}\overline{u_j'' t_{ik}(u'')}-\frac{\partial}{\partial x_k}\overline{u_i'' t_{jk}(u'')}}_{-T_{3,ij}} \\ & \underbrace{+\overline{t_{jk}(u'')\frac{\partial u_i''}{\partial x_k}}+\overline{t_{ik}(u'')\frac{\partial u_j''}{\partial x_k}}}_{-\overline{\rho}\epsilon_{ij}}\end{aligned} \tag{1.26}$$

On the left hand side are the time derivatives of the Reynolds stress components and their transport. The right hand side is comprised of the production term $\mathcal{P}_{ij}$, viscous acceleration $\mathcal{V}_{ij}$, pressure acceleration R_{ij}, pressure strain covariance Π_{ij}, dissipation $\overline{\rho}\epsilon_{ij}$ and turbulent transports $T_{k,ij}$. This transport equation shows the terms contributing to the development of the fluctuations. It introduces further unknowns and thus cannot be solved unless additional modelling is applied. Modelling of the Reynolds stress transport equation is even more advanced compared to the modelling of the Reynolds stresses and to date no model being universal and numerically robust is known. Therefore, first the well known class of eddy viscosity models is introduced. This class is wide spread and the k-ϵ, the k-ω and their derivatives are among them.

1.3.4.1 Linear eddy viscosity model

The Reynolds stress defined previously as

$$\tau_{ij} = -\overline{\rho u_i'' u_j''} \tag{1.27}$$

is a symmetric second-order tensor. Due to an analogy with the molecular transport being modelled as molecular stress it is called Reynolds stress (more details in Wilcox (1998)) which was first discussed by Boussinesq (1877). In fact, this analogy is the basis of a class of turbulence models using a closure of the form

$$\tau_{b,ij} = \underbrace{2\mu_t\left[\widetilde{S}_{ij}-\frac{1}{3}\widetilde{S}_{ii}\,\delta_{ij}\right]}_{\text{anisotropic}}-\underbrace{\frac{2}{3}\overline{\rho}k\delta_{ij}}_{\text{isotropic}} \tag{1.28}$$

(often called Boussinesq approximation), where $\tau_{b,ij}$, $\widetilde{S}_{ij}$, μ_t, and k are the mean Reynolds stress tensor, the mean strain tensor, the turbulent viscosity and the turbulent kinetic

energy (TKE), respectively. Models of that class are often called eddy or turbulent viscosity models. The Boussinesq approximation is comprised of two terms, the first relating the anisotropic part of the Reynolds stress tensor with the strain, and the second part stating that the isotropic part is governed by the TKE. Many turbulence models are based on the Boussinesq approximation but to date none of them has been identified as the "best". It is thus of interest to comment on the validity of the Boussinesq approximation in general and thus cover all turbulence models based on it. This requires the recognition of parts that are universal for all turbulence models called "inherent assumptions" and parts specific to each model being called "specific assumptions" (Pope, 2000). General statements can only be made for the inherent assumption. Taking a look at the isotropic part first it is obvious that the crucial bit is to get the TKE correct which is entirely governed by the specific turbulence model and thus is a specific assumption. Focusing on the anisotropic part it can be seen that a linear coupling of Reynolds stress and strain is enforced (multiplying a scalar with a matrix yields another matrix that is only scaled). This immediately shows that the Boussinesq approximation requires the two tensors to be aligned which is an inherent assumption and due to this linearity the models are often referred to as linear turbulence models. This inherent assumption is implicitly coupled with the specific assumption of the actual value of turbulent viscosity being supported by the particular turbulence model.

Looking through literature several studies can be found that show that the Boussinesq approximation fails in terms of the alignment (both general studies (Pope, 2000) and LPT studies (Stieger & Hodson, 2005)). However, models based on the Boussinesq approximation are still widely used which on the one hand is due to their stability and availability in commercial codes but also due to the fact that for many flows they give reasonable accuracy at reasonable cost. Schmitt (2007) concludes that even though the Boussinesq approximation fails and has huge impact on the Reynolds stress (second order moment) the mean (first order moment) might not be affected in the same way. Hence, if the target of the study is to find mean quantities a different measure has to be found to define the validity of the Boussinesq approximation. Therefore, purely quantifying the error with respect to the accuracy of the Reynolds stress might not be enough.

Turbulence viscosity as such is a model parameter and not a flow quantity. Since the linear alignment assumption for the Boussinesq approximation fails for various flows it is not possible to find a scalar that can multiply the anisotropic strain such that it matches the Reynolds stress simulated from DNS. However, as discussed by Muldoon & Acharya (2006) a turbulence viscosity can be computed that minimizes the error in the Reynolds stress. For brevity first the anisotropic strain is defined as

$$\widetilde{S}^*_{ij} = \widetilde{S}_{ij} - \frac{1}{3}\widetilde{S}_{kk}\delta_{ij} \tag{1.29}$$

and the anisotropic Reynolds stress is summarized as

$$\widetilde{\tau}_{ij}^{*} = \widetilde{\tau}_{ij} + \frac{2}{3}\overline{\rho}k\delta_{ij}, \tag{1.30}$$

where in the following quantities indicated with a * are anisotropic quantities. The error between the modelled and simulated stress is represented by

$$\zeta_{\tau} = \left|\left|\tau_{ij}^{*} - \tau_{b,ij}^{*}\right|\right|, \tag{1.31}$$

where the Frobenious norm of the tensor is used to obtain a scalar. By substituting the Boussinesq approximation the error takes the form

$$\zeta_{\tau} = \left|\left|\tau_{ij}^{*} - 2\mu_t\widetilde{S}_{ij}^{*}\right|\right|. \tag{1.32}$$

Since ζ_{τ} is positive the minimum of ζ_{τ} and ζ_{τ}^2 are the same such that the minimum of ζ_{τ} can be computed from

$$\frac{\partial\zeta_{\tau}^2}{\partial\mu_t} = 0 \tag{1.33}$$

where using ζ_{τ}^2 simplifies the algebra which evaluates to (not using the Einstein summation over repeated indices)

$$\mu_{t,\tau} = \frac{1}{2}\frac{\sum_{k=1}^{3}\sum_{l=1}^{3}\widetilde{S}_{kl}^{*}\tau_{kl}^{*}}{\sum_{k=1}^{3}\sum_{l=1}^{3}\widetilde{S}_{kl}^{*2}}. \tag{1.34}$$

It is interesting to note that the nominator of $\mu_{t,\tau}$ represents the inner product of the two tensors which can be interpreted as alignment that is used by Schmitt (2007) to define a validity measure for the alignment assumption of the Boussinesq approximation. For similar reasons the same equation for μ_t has been developed by Spalart *et al.* (2014).

1.3.4.2 Turbulence Kinetic Energy Transport Equation Budget

Commenting on the validity of the Boussinesq class turbulence models thus only allows for testing of the linear stress-strain relationship. However, many frequently used turbulence models also use the transport equation for turbulent kinetic energy (TKE) to obtain the isotropic part and also as one of the variables to determine the turbulent viscosity. The transport equation of turbulent kinetic energy is given by

$$\begin{aligned}\frac{\partial\left(\overline{\rho}k\right)}{\partial t} + \frac{\partial\left(\overline{\rho}\widetilde{u}_j k\right)}{\partial x_j} =& \tau_{ij}\frac{\partial\widetilde{u}_i}{\partial x_j} - \overline{t_{ij}\left(u''\right)\frac{\partial u_i''}{\partial x_j}} + \overline{p'\frac{\partial u_i''}{\partial x_i}} + \overline{u_i''}\left(\frac{\partial t_{ij}\left(\widetilde{u}\right)}{\partial x_j} - \frac{\partial\overline{p}}{\partial x_i}\right) \\ &- \frac{\partial}{\partial x_j}\left[\overline{\frac{\rho u_i'' u_i'' u_j''}{2}} + \overline{p' u_i''}\delta_{ij} - \overline{t_{ij}\left(u''\right)u_i''}\right]\end{aligned} \tag{1.35}$$

In this equation there are several new terms depending on the fluctuations that have to be modelled. Using eddy resolving simulations and some experimental measurement methods it is possible to obtain data to test these approximations. Collecting all terms of the TKE transport equation allows for thorough comparison of turbulence models. Since the flow through turbomachines is compressible, the compressible budget should be used, which from experimental work is difficult to obtain.

TKE transport equation budgets have been reported for various flows, but here the focus is on LPT and thus studies close to real engine conditions are of interest. Stieger & Hodson (2005) reported incompressible TKE (cf. figure 1.5) and anisotropy of the compressible flow field. They found that significant TKE production arises away from the wall boundary layers at the bow of the wake (cf. figure 1.5). A similar study was conducted by Bijak-Bartosik *et al.* (2009) who also looked at production of TKE and confirmed the findings of Stieger & Hodson (2005) for a different geometry.

Laurent *et al.* (2011) looked at full budgets of TKE for a flat plate subjected to a first favourable and then adverse pressure gradient boundary layer, leading to a separation bubble. In this study, however, no real LPT was considered and thus the wake mixing and the far downstream behaviour is expected to be different.

Gao *et al.* (1997) reported Reynolds stress and dissipation budgets for a flat plate with a rectangular trailing edge. Similarly Yao *et al.* (2001); Thomas *et al.* (2003) reported TKE budgets for a similar flat plate trailing edge and discussed the energy transfer. In a follow on paper Yao *et al.* (2002) compared results from URANS with their DNS data and revealed substantial differences with respect to DNS data. For example the vortex shedding frequency was twice as high as for DNS and significant differences in the terms of the TKE transport they compared were reported.

If URANS is used the major assumption is that the averaging interval is such that the turbulence fluctuations are averaged, but the mean flow variations are simulated. This requires that the time scales of the mean flow have to be considerably larger than those of the turbulent fluctuations (aka. spectral gap). Considering the LPT this seems like an attractive approach since the unsteadiness due to wakes of the upstream row considerably changes the mean flow as discussed above. On the other had for LPT simulations it is in doubt if a spectral gap exists (Tucker, 2011), particularly with respect to vortex shedding.

1.4 High Fidelity Simulations of Low Pressure Turbines

In section 1.2.2 the various modelling approaches were presented. Since all the flow features are of interest in this work they have to be resolved and cannot be modelled and therefore RANS cannot be used. LES might help to decrease cost of the simulations,

but it is not clear if the modelled turbulence affects the results. Hence, first DNS will be used to obtain results and later it can be tested if LES gives reasonable agreement with DNS. If feasible, subsequent studies can be conducted using LES.

Previously in this chapter the current understanding of the flow field through an LPT was presented. The understanding to date is limited and eddy resolving simulations can help to shed light onto some of the areas not yet fully understood. Several studies using eddy resolving simulations of LPTs have been performed and reported to this day. Those are reviewed in the following with an eye on resolution and particularly whether they show sufficient proof of sufficient resolution.

Before literature is reviewed general consideration on the accuracy of simulations are presented that will be used to draw conclusions on the grid requirements. Simulations are numerical approximations of the governing model. Therefore, errors can either result from an invalid model or occur due to the approximation. For DNS the model is comprised of conservation of mass, momentum and energy as presented above which has been used in many studies and concluded to be adequate for simulations as carried out in this work. For LES in addition the LES model has to be valid which is less clear and, therefore, initially DNS will be conducted as already mentioned. Since for DNS only errors due to the numerical approximation are of relevance these are discussed in the following.

Numerical approximations of the governing equations are achieved by discretizing in space and time. Methods are mostly classified according to their underlying principle into finite difference methods, finite volume methods, spectral methods and finite element methods (in particular spectral element methods) (Ferziger, 1998). DNS of LPTs have been conducted using spectral element methods by Hillewaert *et al.* (2014). However, their study did not consider free-stream turbulence allowing for a significantly coarser resolution in the free-stream. Therefore those are not included into the following discussion. For finite difference, finite volume and spectral methods guidelines exist of how the resolutions compare to each other.

For finite difference methods as used in this work the differential operators in the governing equations (eqns (1.9)-(1.11)) are replaced using finite difference approximations. Using a well known error analysis based on Taylor series expansion the error can be understood. Mostly this analysis is performed on equidistant curvilinear grids and leads to a classification based on the order of the method (Ferziger, 1998). In addition also dissipation errors, dispersion errors and coupled errors between different derivatives occur. Finally, in order to discretize real LPT geometries curvilinear meshes are used which add errors due to stretching and skewness of the grid as examined by You *et al.* (2006). The complete picture prevents a direct analysis of the error but some general well known guidelines can be summarized that reduce the error of the simulation:

- increased resolution

- higher order method
- reduced skewness

As mentioned a direct analysis is not possible and therefore published studies are presented in light of these parameters table 1.1. In addition first the Reynolds number (Re) is listed since as explained earlier the computational cost strongly depends on it. Then spanwise extent based on the true chord length (Δz) is listed. In all these studies a homogeneous-uniform grid in the spanwise direction was used and the blade-to-blade plane normal to was meshed with a curvilinear grid with clustering of the points close to the blade for the cases with real geometry. Wu *et al.* (1999) considered a flat plate where a rectangular grid with points clustering towards the blade was use. In the table n_p represents the number of points in the blade to blade plane and n_{sp} the points in the spanwise direction. The resulting number of points in the full domain is given as n_{tot}. In the next column the scheme is presented followed by the near wall resolution, where available.

Even though the boundary layers are transitional for many flows the well known non-dimensional wall scaling in plus units is often used. For fully turbulent channel flow DNS guideline values for the wall spacing are summarized for various studies in Lee & Moser (2014) where convergence of the turbulence kinetic energy budgets (which are one of the targets of this study) was shown. For the streamwise spacing x^+ generally values between 5 to 15 are used, for the wall normal spacing y^+ values of 0.01 to 0.5 are common and for the spanwise spacing the values range between 3 and 7. Comparing these values with the values summarized in the table 1.1 it can be seen that the guideline values are generally significantly finer. This is probably because the boundary layers for LPT flows are hardly turbulent but since neither of the studies has proven grid convergence of fine scale turbulence quantities like the TKE transport equation budgets these values should be taken with care.

Paper	$Re[k]$	Δz	n_p	n_{sp}	n_{tot}	scheme	x^+,y^+,z^+
Wu *et al.* (1999)	-	0.2	410,000	128	52M	FV	24,*,11
Wu & Durbin (2001*b*)	-	0.15	440,000	129	57M	FV	-
Wissink (2003)	60	0.2	263,640	64	16M	2^{nd} FV	-
Kalitzin *et al.* (2003)	200	0.15	665,281	129	57M	FV	28,2.3,19
Wissink & Rodi (2006)	100	0.2	-	-	93.4M	2^{nd} FV	25,1.7,15

TABLE 1.1: Grid characteristics of published eddy-resolving LPT simulations

The major focus of high fidelity simulations studies of LPTs in the past was on presenting the capability of them to correctly predict the flow and report flow physics that are difficult to obtain from experiments. Most studies used a comparison with experiments in terms of blade pressure distribution (Wu & Durbin, 2001*b*; Wissink, 2003; Wissink & Rodi, 2006) and mean wake loss (Wissink, 2003; Michelassi *et al.*, 2003) for validation of their simulation. Wu *et al.* (1999) also showed the level of grid convergence they

achieved for the Reynolds stress. In light of the findings these studies reported, which are mostly based on qualitative assessment of flow features, this is considered to be sufficient. Since all quantities used for validation are governed by the mean flow field or quantities depending on the large scales (Pope, 2000) they do not validate the fine scale turbulence characteristics. Since those are expected to have an influence on turbulence budgets these guideslines might not be sufficient. On the other hand the numerical scheme used in this work is of higher order than the schemes employed in the presented studies such that a coarser resolution should be sufficient.

The flow physics reported by these studies have already been discussed above and in the following a brief history of these simulations is presented and how their focus was reflected by the resolution of the grid they used. The first study investigating the influence of incoming wakes on a separated/transitional boundary layer was conducted by Wu *et al.* (1999). In order to limit computational cost a flat plate boundary layer was considered where wakes shed from moving bars where introduced in terms of the mean flow field of a fully developed bar wake using the inlet boundary condition. In a subsequent study Wu & Durbin (2001*b*) were the first to perform incompressible DNS on a real geometry cascade. The focus in this study was the transport of the wake through the downstream blade row. Hence, the resolution of the wall was not considered as important as long as the potential flow through the blade row was correctly simulated.

Wissink (2003) and Michelassi *et al.* (2003) performed incompressible large eddy simulation LES and incompressible DNS of the T106A profile and compared the results to see how LES performs compared to DNS and they found that if the LES is sufficiently well resolved, the overall picture is good and just the small scales are not resolved (as expected). LES was a factor of 10 cheaper, compared to DNS. Similar to Wu & Durbin (2001*a*) they introduced the wake velocity deficit and the elevated free stream turbulence inside the wake to mimic wakes. In a similar study (Kalitzin *et al.*, 2003) presented instantaneous flow physics observed in the LPT with a particular focus on the interaction of the wake injected at the inlet with the blade and the turbulent structures that are seen present in the boundary layer close to the blade surface. For these studies an adequate wall resolution is required to correctly represent the mean flow field.

Matsuura (2006) was the first to conducted *compressible* LES. Comparing two different levels of inlet turbulence they investigated the influence of inlet disturbance on the suction side separation. Since these where compressible simulations they could discuss how acoustic pressure waves originating from the trailing edge interact with the separation bubble and the neighbouring blade on the same blade row.

Sarkar (2007, 2008, 2009) conducted a series of LES studies where the influence of structure size on transition was investigated. In order to model the structure size the wake shed by bars computed either in 3D or 2D where the latter remained more coherent. The wakes generated by a precursor simulation where then injected into the domain

of the low pressure turbine and it was found that the structure size has a significant influence on the blade aerodynamics. It was pointed out that most of the experiments considering detailed flow investigations were conducted with simulating the upstream blade by a bar. However, the influence of using a bar rather than an upstream blade was not investigated in detail yet.

In addition several LES studies have been performed, mostly focusing on the potential of LES to correctly obtain the mean flow field. Mittal & Venkatasubramanian (2001) conducted LES of an LPT and investigated the flow structures. Luo *et al.* (2009) conducted LES of an LPT with a focus on passive control realized by a groove. Jimbo & Biswas (2010) focused on the LES model contribution and control of the separation bubble at the suction side of an LPT. Medic & Sharma (2012) conducted a series of LES studies at different Reynolds numbers and compared them to experiments. They found that particularly at low Reynolds number they had a severe deviation from measurements.

1.5 Research Questions

The current understanding of the flow through LPTs has been discussed above to outline the challenges prediction tools face. In particular the unsteady environment due to the relative motion of rotor and stator is a challenge for RANS and URANS models. A large number of papers showing the importance of unsteady effects is available, but the number of detailed studies that can be directly translated to aid RANS modellers is limited. Therefore, in this study the focus is on a particular geometry and a small number of different cases making it possible to investigate in detail the influence of inlet background turbulence level and Reynolds number.

It has been thoroughly discussed that the wake shed by one blade is subsequently mixed and distorted by the downstream blade row and then interacts by various means with the downstream blade row, triggering transition. Transition significantly influences the wake of the downstream blade and every step has to be accounted for correctly by an accurate prediction tool. With respect to Favre averaged prediction tools, in general, the wake generation and distortion process is mainly modelled through the RANS model with a separate transition model in place capturing the transition process. In this work the focus is on the RANS model such that in particular wake generation, mixing and distortion are of particular interest.

In the following, the central research questions are stated:

1. **Developing a compressible DNS method for LPTs:** Before compressible DNS can be performed a numerical tool has to be developed. Therefore, current methods using various state of the art components and new developments are presented in chapter 2.

2. **Performance optimization of the numerical method:** Given that DNS is computationally expensive it is of paramount importance to have a solver that can exploit large computing systems and the latest architectures. Developments in this regard are discussed in chapter 3.

3. **Validation of the setup:** Previous studies have focussed on the validation of mean flow results which do not directly validate the accurate representation of the small scale flow features. Since those are of interest in this study, conclusions from these works cannot be used without further validation in this work. A thorough validation is presented in chapter 4.

4. **Turbulence kinetic energy budgets:** Similar to Stieger & Hodson (2005), Bijak-Bartosik *et al.* (2009) and Wu & Durbin (2001*b*) who collected certain terms of the budgets, here a record of the full budgets of compressible LPT cases is presented to allow turbulence modellers to quantitatively compare new models (cf. section 1.2.2). Further, this allows to investigate the importance of the various mechanisms similar to Thomas *et al.* (2003). This is discussed in chapter 5.

5. **Test commonly assumed turbulence modelling assumptions:** Turbulence modelling assumptions such as the Boussinesq approximation are widely used but their validity is expected not to hold for LPT flows. The data obtained here can be used to understand to which degree these assumptions are valid for LPT simulations and where the problem zones are. This is presented in chapter 6.

6. **Test the performance of linear turbulence models:** A commonly used assumption in many works is based on the linear eddy viscosity assumption. As discussed above an "optimum" turbulence viscosity can be extracted from DNS results allowing one to understand the improvement potential of common physical models.

Chapter 2

Numerical Method and Data Analysis

2.1 Numerical Approach Used

In section 1.2.2 it is concluded that for the first simulations DNS will be used to prevent uncertainties of turbulence modelling. The numerical methods used for the results obtained to this stage are presented in the following. Before the numerical approach is presented, the equations are rewritten for convenience. Looking at the three conservation laws it can be seen that each equation has a similar structure in terms of a time derivative, first order spatial derivatives in each direction and a source vector of similar form in terms of the flow variables. Hence, the five equations can be written as one vector equation as follows

$$\frac{\partial \vec{q}}{\partial t} + \frac{\partial \vec{f}}{\partial x_1} + \frac{\partial \vec{g}}{\partial x_2} + \frac{\partial \vec{h}}{\partial x_3} = \vec{S}\,, \tag{2.1}$$

with the conservative state vector $\vec{q}$ defined as

$$\vec{q} = [\rho, \rho u_1, \rho u_2, \rho u_3, \rho e_t]^T\,, \tag{2.2}$$

the fluxes $\vec{f}$,$\vec{g}$,$\vec{h}$ defined as

$$\begin{aligned} \vec{f} &= \left[\rho u_1, \rho u_1^2 + p, \rho u_1 u_2, \rho u_1 u_3, u_1\left(\rho e_t + p\right)\right]^T \\ \vec{g} &= \left[\rho u_2, \rho u_1 u_2, \rho u_2^2 + p, \rho u_2 u_3, u_2\left(\rho e_t + p\right)\right]^T \\ \vec{h} &= \left[\rho u_3, \rho u_1 u_3, \rho u_2 u_3, \rho u_3^2 + p, u_3\left(\rho e_t + p\right)\right]^T \end{aligned} \tag{2.3}$$

and the viscous source vector $\vec{S}$ given as

$$\vec{S} = \frac{\partial \vec{f_v}}{\partial x_1} + \frac{\partial \vec{g_v}}{\partial x_2} + \frac{\partial \vec{h_v}}{\partial x_3} \,. \tag{2.4}$$

The viscous fluxes $\vec{f_v}$,$\vec{g_v}$,$\vec{h_v}$ are defined as

$$\begin{aligned} \vec{f_v} &= [0, t_{11}, t_{12}, t_{13}, u_1 t_{11} + u_2 t_{12} + u_3 t_{13} - q_x]^T \\ \vec{g_v} &= [0, t_{12}, t_{22}, t_{23}, u_1 t_{12} + u_2 t_{22} + u_3 t_{23} - q_y]^T \\ \vec{h_v} &= [0, t_{13}, t_{23}, t_{33}, u_1 t_{13} + u_2 t_{23} + u_3 t_{33} - q_z]^T \,. \end{aligned} \tag{2.5}$$

In the above equations e_t is the total energy defined as

$$e_t = e(T) + \frac{1}{2} u_i u_i \tag{2.6}$$

Bringing the conservation laws in this form allows one to develop one numerical configuration that can be used for all components of the vector equation and thus in the following a numerical system is developed for equation 2.1. In this work a combination of a spectral method and finite differences is used to discretize the equations. The discretization schemes used in this work require a uniform orthogonal grid. Since a real LPT geometry is used, uniform, orthogonal, equidistant grids are not practical. In order to allow for more complex curvilinear grids a coordinate transformation, presented in the following, is used.

2.1.1 Generalized Coordinates

For simulations of more complex geometries like LPTs, non-uniform non-Cartesian grids are used. In this work linear cascade flow is simulated allowing for the use of spanwise uniform grids for simulation at the midplane where the flow is assumed to quasi two-dimensional. Hence just the blade to blade plane, i.e. spatial directions x_1 and x_2, has to be transformed from the curvilinear space representing the physical domain to an equidistant orthogonal mathematical domain represented by ξ and η where the discretization is applied. The transformation can be written as

$$\begin{aligned} \xi &= \xi\,(x_1, x_2) \\ \eta &= \eta\,(x_1, x_2) \\ x_3 &= x_3 \end{aligned} \tag{2.7}$$

In terms of derivatives in mathematical and physical space the following relation holds (Anderson, 1995, p. 168ff)

$$\begin{aligned}\frac{\partial}{\partial x_1} &= \frac{1}{|J|}\left[\frac{\partial x_2}{\partial \eta}\frac{\partial}{\partial \xi} - \frac{\partial x_2}{\partial \xi}\frac{\partial}{\partial \eta}\right] = x^*_{2,\eta}\frac{\partial}{\partial \xi} - x^*_{2,\xi}\frac{\partial}{\partial \eta} \\ \frac{\partial}{\partial x_2} &= \frac{1}{|J|}\left[\frac{\partial x_1}{\partial \xi}\frac{\partial}{\partial \eta} - \frac{\partial x_1}{\partial \eta}\frac{\partial}{\partial \xi}\right] = x^*_{1,\xi}\frac{\partial}{\partial \eta} - x^*_{1,\eta}\frac{\partial}{\partial \xi}\,,\end{aligned} \tag{2.8}$$

with

$$x^*_{1,\xi} = \frac{1}{|J|}\frac{\partial x_1}{\partial \xi},\quad x^*_{1,\eta} = \frac{1}{|J|}\frac{\partial x_1}{\partial \eta},\quad x^*_{2,\xi} = \frac{1}{|J|}\frac{\partial x_2}{\partial \xi},\quad x^*_{2,\eta} = \frac{1}{|J|}\frac{\partial x_2}{\partial \eta}\,, \tag{2.9}$$

and the Jacobian determinant

$$|J| = \begin{vmatrix} \frac{\partial x_1}{\partial \xi} & \frac{\partial x_1}{\partial \eta} & 0 \\ \frac{\partial x_2}{\partial \xi} & \frac{\partial x_2}{\partial \eta} & 0 \\ 0 & 0 & 1 \end{vmatrix} \tag{2.10}$$

Using this transformation the NS equations can be written in generalized form

$$\frac{\partial \vec{q}}{\partial t} + \left[x^*_{2,\eta}\frac{\partial \vec{f}}{\partial \xi} - x^*_{2,\xi}\frac{\partial \vec{f}}{\partial \eta}\right] + \left[x^*_{1,\xi}\frac{\partial \vec{g}}{\partial \eta} - x^*_{1,\eta}\frac{\partial \vec{g}}{\partial \xi}\right] + \frac{\partial \vec{h}}{\partial x_3} = \vec{S_g}\,, \tag{2.11}$$

with the source vector in generalized form

$$\vec{S_g} = \left[x^*_{2,\eta}\frac{\partial \vec{f_v}}{\partial \xi} - x^*_{2,\xi}\frac{\partial \vec{f_v}}{\partial \eta}\right] + \left[x^*_{1,\xi}\frac{\partial \vec{g_v}}{\partial \eta} - x^*_{1,\eta}\frac{\partial \vec{g_v}}{\partial \xi}\right] + \frac{\partial \vec{h_v}}{\partial x_3}\,. \tag{2.12}$$

2.1.2 Discretization

The discretization methods are presented along with considerations why these particular ones are used. Generally speaking, for DNS the main problem is the computational cost. DNS simulations are generally conducted on high performance computing (HPC) facilities which allow for running in parallel on many thousands of cores. The trend in HPC development tends towards less cache and RAM per CPU and thus methods requiring less memory might be faster even though they might need more floating point operations. Hence, the two key restrictions for the development of the numerical methods and code are scalability (performance of the methods on high core counts) and low memory requirement of the methods. In fact, in general it is considered that methods with lower memory requirement and sligthly more floating point operations are beneficial. The methods used in this work have been selected on this bases. For the temporal discretization a low memory five-step fourth-order stability-enhanced Runge Kutta scheme developed by Kennedy *et al.* (2000) is used. Additional stability enhancement is achieved by the use of a so called skew-symmetric splitting (Kennedy & Gruber, 2008) of the set of governing equations.

For spatial discretization of the blade to blade plane a compact difference scheme by Kim & Sandberg (2012) is used. Compact difference schemes in contrast to standard differences also use the first derivative of the neighbouring points to compute the first derivative and thus the system is implicit (requires a linear algebraic system to be solved). This is more computationally expensive than in case of standard difference schemes but it also has a higher accuracy, i.e. fewer points have to be used for the same flow problem. The particular method used here further has been optimized for small dissipation and dispersion error which in light of long run times is of paramount importance. Overall there generally is a saving in computational time in case of compact differences. In order to simplify parallelization boundary stencils are used allowing that the linear algebraic system for each processor just contains points of this processor so that it can be solved separately for each processor.

In the spanwise direction a spectral discretization using Fourier transformation is applied. This implies that only spanwise periodic simulations can be performed with this approach. The Fourier transform is conducted using the FFTW algorithm (Frigo & Johnson (2011)).

2.1.3 Characteristic Form of the Governing Equations

The set of governing equations can be transformed to a characteristic form allowing one to understand the direction of transport of information under certain assumptions that are presented in the following. At boundaries and interfaces the transport direction can be used to identify which information has to be prescribed or is transported.

Quasilinear Form

Before the governing equations can be transformed to characteristic space, in an intermediate step they are transformed to a quasilinear form, from which then the characteristic form is obtained. A quasilinear form is a form where the highest derivatives just occur in linear form and for the set of governing equation it takes the form

$$\frac{\partial \vec{U}}{\partial t} + \underline{\tilde{A}}\frac{\partial \vec{U}}{\partial \xi} + \underline{\tilde{B}}\frac{\partial \vec{U}}{\partial \eta} + \underline{\tilde{C}}\frac{\partial \vec{U}}{\partial x_3} = \vec{S}_g \ . \tag{2.13}$$

For $\vec{U}$ various choices are applicable and in this derivation the conservative state vector $\vec{q}$ as given in (2.2) is used such that the quasilinear equations are of the form

$$\frac{\partial \vec{q}}{\partial t} + \underline{A}\frac{\partial \vec{q}}{\partial \xi} + \underline{B}\frac{\partial \vec{q}}{\partial \eta} + \underline{C}\frac{\partial \vec{q}}{\partial x_3} = \vec{S}_g \ , \tag{2.14}$$

where the matrices $\underline{A}$, $\underline{B}$ and $\underline{C}$ are obtained for the current set of governing equations using the chain rule and factoring out $\frac{\partial \vec{q}}{\partial \xi}$, $\frac{\partial \vec{q}}{\partial \eta}$ and $\frac{\partial \vec{q}}{\partial x_3}$. This operation leads to the

quasilinear form given by

$$\frac{\partial \vec{q}}{\partial t} + \underbrace{\left[x^*_{2,\eta}\frac{\partial \vec{f}}{\partial \vec{q}} - x^*_{1,\eta}\frac{\partial \vec{g}}{\partial \vec{q}}\right]}_{\underline{A}}\frac{\partial \vec{q}}{\partial \xi} + \underbrace{\left[x^*_{1,\xi}\frac{\partial \vec{g}}{\partial \vec{q}} - x^*_{2,\xi}\frac{\partial \vec{f}}{\partial \vec{q}}\right]}_{\underline{B}}\frac{\partial \vec{q}}{\partial \eta} + \underbrace{\frac{\partial \vec{h}}{\partial \vec{q}}}_{\underline{C}}\frac{\partial \vec{q}}{\partial x_3} = \vec{S}_g \, . \tag{2.15}$$

Characteristic Form

In this section the characteristic form of the set of governing equation is derived and the transformation to and from the generalized quasilinear form is shown. The derivation is done for the ξ-direction only, but the derivation for the other directions are straight forward. The starting point is the set of governing equations in generalized quasilinear form (2.14). If the solution of this equation at a ξ boundary is to be obtained, the numerical derivatives with respect to ξ have to be obtained using one sided stencils. One sided stencils in contrast to central schemes just use the information from one side and if this does not coincide with the propagation direction of the information then the system might not be stable. The transport direction of the governing equations can be found in the characteristic space.

Characteristic form in this context means that the equations are transformed in a way that the derivatives with respect to one direction (here ξ) of one component of the vector equation does not appear in the other components, i.e. the components of the vector are independent in terms of the derivatives with respect to the ξ direction and thus can be treated separately. Before the transformation is performed the derivatives with respect to the η and x_3 directions are added to the extended source vector since they are not required in this transformation, giving

$$\frac{\partial \vec{q}}{\partial t} + \underline{A}\frac{\partial \vec{q}}{\partial \xi} = \vec{S}_g - \underline{B}\frac{\partial \vec{q}}{\partial \eta} - \underline{C}\frac{\partial \vec{q}}{\partial x_3} = \vec{S}_{char} \, . \tag{2.16}$$

In order to make the ξ-derivatives of the vector components independent and thus obtain the characteristic form, matrix $\underline{A}$ has to be diagonalized as $\underline{A} = \underline{P}\,\underline{\Lambda}\,\underline{P}^{-1}$ and both sides are left multiplied by $\underline{P}^{-1}$, yielding

$$\underline{P}^{-1}\frac{\partial \vec{q}}{\partial t} + \underline{\Lambda}\,\underline{P}^{-1}\frac{\partial \vec{q}}{\partial \xi} = \underline{P}^{-1}\vec{S}_{char} \, , \tag{2.17}$$

where the diagonal matrix takes the following form

$$\underline{\Lambda} = \mathrm{diag}\left[U, U, U, U + c\sqrt{\xi^2_{x1} + \xi^2_{x2}}, U - c\sqrt{\xi^2_{x1} + \xi^2_{x2}}\right] \tag{2.18}$$

with

$$U = \xi_{x1}u_1 + \xi_{x2}u_2. \tag{2.19}$$

Finally defining $\delta\vec{Q} = \underline{P}^{-1}\delta\vec{q}$ (Thompson, 1987) the characteristic form is obtained as

$$\frac{\partial\vec{Q}}{\partial t} + \underline{\Lambda}\frac{\partial\vec{Q}}{\partial\xi} = \underline{P}\vec{S}_{char} \,. \tag{2.20}$$

This equation has the form of a multicomponent one-dimensional convection equation, where the i-th component of $\vec{Q}$ is transported at velocity Λ_{ii}. For convection equations it is known that the solution depends on the upstream behaviour only. The convection direction is therefore given by the sign of Λ and at the boundary it is determined if information is transported out of the domain or into it. Hence, if information is transported out of the domain the information from inside the domain can be used. But if the quantity is transported into the domain, the information has to come from outside and thus has to be prescribed.

Next the influence of the right hand side onto the transport direction is investigated in order to understand if it can be neglected for these considerations. Looking at the extended source vector given by

$$\vec{S}_{char} = \underbrace{\left[x^*_{2,\eta}\frac{\partial\vec{f_v}}{\partial\xi} - x^*_{2,\xi}\frac{\partial\vec{f_v}}{\partial\eta}\right] + \left[x^*_{1,\xi}\frac{\partial\vec{g_v}}{\partial\eta} - x^*_{1,\eta}\frac{\partial\vec{g_v}}{\partial\xi}\right] + \frac{\partial\vec{h_v}}{\partial x_3}}_{\text{viscous terms}} - \underbrace{\underline{B}\frac{\partial\vec{q}}{\partial\eta} - \underline{C}\frac{\partial\vec{q}}{\partial x_3}}_{\text{flux terms}} \,, \tag{2.21}$$

the following conclusions can be drawn:

- viscous terms: these are of dissipative nature which primarily affects the magnitude but not the direction of the transport
- flux terms: these are the flux terms in the other directions and thus the transport in ξ is not affected by those as they are in the plane of interest

Hence, it is reasonable to assume that the transport direction is not significantly altered by both viscous terms and flux terms in interface direction.

2.2 Initial and Boundary Condition

In order to solve the system of governing equations initial and boundary conditions are required. Since the simulation has a time mean, the initial condition is of lesser importance since, if reasonably chosen, after a transient all solutions are expected to end at the same state. A better initial guess will lead to a shorter transient, though. The initial condition used in this study computes the total energy at the inlet and sets it in the whole flow field. Velocity magnitude and angle are set to unity and the value for the angle depends on the streamwise position. From the inlet to the leading edge the angle is gradually varied from the prescribed value at the inlet to the angle of the camber

line at the leading edge along the whole pitch. Throughout the blade it is varied with the camber line angle at the streamwise position and at the trailing edge and downstream the angle of the camberline at the trailing edge is used. Towards the blade the velocity is linearly decreased from one to 0 over the last 30 cells. The density is set to unity at the inlet and change accordingly for points where the velocity magnitude is smaller (close to the blade). This highly approximate initialization is first converged in two dimensions and the results are used as the initial condition for the three dimensional simulation without any spanwise variation.

Computational expenses of simulations increase with bigger domains. This is especially true for DNS for which in the case that turbulence is present in the whole domain it has to be resolved requiring a fine resolution also in the far field. Therefore it is desirable to decrease the domain as much as possible. At these domain boundaries, though, the governing equations can't be solved since they depend upon the flow outside of the domain under consideration. Hence, the physical information has to be prescribed in form of boundary conditions (BCs) and thus has to be available. Therefore in general the domain has to extend to a so called free stream or far field state. The optimum inlet and outlet boundary positions are thus as close as possible to the area of interest (blade in this case) but still at a position such that prescribing the "free stream" value does not affect the simulations. This distance was tested using two-dimensional simulations considering they are cheaper and generate more coherent vortices. These in general are a bigger challenge to BCs.

Additionally the values at walls have to be prescribed because the fluid is interacting with a solid and this is not captured by the equations. The statements so far are both true for analytical and numerical considerations. In order to apply boundary conditions to simulations though, they have to be discretized at the boundary. In the following the different types of BCs used for the simulations are discussed.

In figure 2.1 the BC setup used in the blade to blade plane is presented. The BCs can

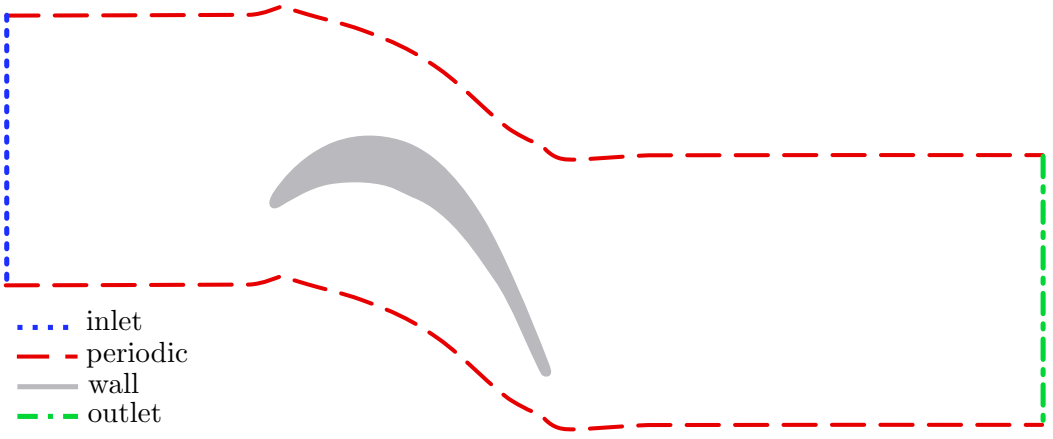

FIGURE 2.1: Boundary Condition setup in blade to blade plane

be classified in inlet, outlet, periodic and wall BCs which are discussed separately below.

Considering an infinite series of blades in the pitchwise direction and assuming that the variations in pitchwise direction are small with respect to the pitch, periodic BCs can be used in the pitchwise direction.

In the spanwise direction (i.e. perpendicular to the blade to blade plane), considering that LPT blades in general have a high aspect ratio (blade height over chord), it is assumed that the flow at mid-height is quasi two-dimensional and thus is considered suitable for using periodic BC in the span. Here a Fourier discretization is used in spanwise direction that is intrinsically periodic. The spanwise extent has to be chosen such that the biggest flow structures fit well within the domain. This is determined later in a grid convergence study.

Wall

Two types of wall boundary conditions are used where the difference is in the specification of temperature. In both cases the no-slip condition requiring all velocity components u_i to be zero (Dirichlet type condition) is used. In case of an isothermal wall the temperature at the wall is set and has to be provided as an input (Dirichlet type condition). For the adiabatic wall the temperature is computed considering that the heat flux in wall normal direction, given by

$$q_n = \frac{-\mu}{(\gamma - 1)\, Re_\infty Pr_\infty Ma_\infty^2} \frac{\partial T}{\partial n} \tag{2.22}$$

where n denotes the wall normal direction, is zero. If viscosity is assumed to be constant (which is reasonable since it only depends on temperature) the fraction ahead of the wall normal temperature gradient is a non-zero constant and also the wall normal temperature gradient has to be zero(von Neuman type condition). In both cases density at the wall is computed to satisfy mass conservation given by equation 1.9.

Inlet

In contrast to the wall boundary that is part of the domain by nature, the inlet as well as the outlet boundaries are artefacts of an artificial truncation in order to limit the extent of the domain used in the simulations. The actual position has to be chosen such that it has no significant influence on the area of interest (see chapter 4). In the case of the simulations considered in this work the domain is truncated at points where the flow has a constant time mean that is assumed to be uniform across the boundary itself (i.e. spatially uniform). These simulations are subsonic in the whole domain and thus only subsonic boundary conditions at the inlet are considered.

Using a characteristic transformation it was shown (2.1.3) that the transport of information for three variables is at flow velocity, for one variable at flow velocity plus speed

of sound and for one variable at flow velocity minus speed of sound. This shows that for a subsonic inlet one characteristic is leaving the domain and has to be obtained from within the domain, whereas four variables are transported into the domain and thus have to be prescribed. For these four variable the physical values have to be obtained. In this work the four values prescribed are the three velocity components $u_i(t)$ and the density. The target of this study is to conduct simulations to represent the flow through an LPT. Generally the LPT experiences high background turbulence levels having a significant influence on the flow and thus turbulence has to be injected into the domain. This generates the question of how to specify a turbulent signal. In this work two synthetic methods to generate a turbulent inflow signal are used that are explained in the following.

2.2.1 Inlet turbulence generation methods

To study the sensitivity of linear turbine cascade flow to inflow turbulence, a turbulent inflow generation technique is required. Experimental studies mostly provide turbulent intensities and some also give length scales. In general, only these two parameters are available from real turbomachinery data as well. Thus the turbulence generation method has to allow one to adjust these parameters to mimic both experiments and real turbomachinery flow. A quantitative description of turbulence in experiments has been reported by, e.g., Michalek *et al.* (2012). In addition to the turbulence intensities they also quantified the homogeneity to be $\overline{u^2}/\overline{v^2} = 1.2$. Also they reported length scales to be slightly above 10% of the chord length which might require spanwise domain sizes in excess of what is required to resolve the actual flow about a blade. Therefore, a value of about 5% is targeted in this study.

Various methods to generate turbulence have been proposed and were reviewed by Tabor & Baba-Ahmadi (2010). Two main methods have evolved: ones that read in turbulence data (file-IO heavy), and another group that synthetically generates turbulence. IO heavy methods generally are a bottleneck in terms of computational efficiency and thus first a synthetic turbulence generation method was used.

Digital filtering The synthetic turbulence generation method used (referred to as "digital filtering") is based on a method developed by Klein *et al.* (2003). A Gaussian random number distribution is generated in a three dimensional box and in order to obtain turbulent characteristics it is filtered by means of a digital filter to obtain coherent structures present in real turbulence. This method is expensive and Xie & Castro (2008) suggested to use a correlation in the streamwise direction and thus the filtering is just applied in a two dimensional plane normal to the boundary. Since the earlier mentioned methods are for incompressible flows the extension to compressible flows by Touber & Sandham (2009) is used in this work. The result of this method is a time-dependent

velocity signal that has a length scale and energy spectra of homogeneous isotropic turbulent flow. However, a certain streamwise length is required for a turbulent flow to develop. This method is known for small development length but the cost of this method depends on the size of the filter length squared. The size of the filter is given by the number of grid points used per length scales so that particularly for fine grids or bigger length scales even the optimized two dimensional version is expensive. In fact, the cost of a turbulent simulation at desired conditions (i.e. large turbulence length scales) yields a 30% increase in cost compared to one without. For LPT simulations an inlet domain length of at least 80% chord is required to obtain the correct potential flow, thus a simple method, based on harmonic waves at a few discrete wave numbers, can be considered despite possibly requiring a longer development length for the turbulence than more sophisticated, but more expensive, methods.

Discrete waves Perturbations are introduced in the three velocity components at the inlet using a sum of n discrete waves of the form

$$\begin{aligned} u'(n,t,y,z) &= c_1(n)\sin\left[f\left(n,t\right)\right]\cos\left[g\left(n,t,y\right)\right]\cos\left[h\left(n,t,z\right)\right] \\ v'(n,t,y,z) &= c_2(n)\cos\left[f\left(n,t\right)\right]\sin\left[g\left(n,t,y\right)\right]\cos\left[h\left(n,t,z\right)\right] \\ w'(n,t,y,z) &= c_3(n)\cos\left[f\left(n,t\right)\right]\cos\left[g\left(n,t,y\right)\right]\sin\left[h\left(n,t,z\right)\right]. \end{aligned} \tag{2.23}$$

The arguments of the harmonic functions in time t (and through convection in the streamwise direction x), the pitchwise y and spanwise z directions are given by

$$\begin{aligned} f(t,n) &= \beta_1(n)t + \varphi_1(n) \\ g(t,y,n) &= \beta_2(n)(y - \dot{\phi}_2(n)t) + \varphi_2(n) \\ h(t,z,n) &= \beta_3(n)(z - \dot{\phi}_3(n)t) + \varphi_3(n). \end{aligned} \tag{2.24}$$

Each of the parameters in equations 2.24 and 2.25 allow fine-tuning of the inlet perturbations to obtain a turbulence target state. The time and length scales can be adjusted using the frequencies $\beta_1(n)$ and the wave numbers $\beta_2(n)$ and $\beta_3(n)$. The computational domain is periodic in the pitchwise and spanwise directions requiring that the wave numbers have to be chosen such that the perturbations satisfy the same constraint. This is realized by requiring

$$\beta_{2,3}(n) = 2\pi\frac{k_{2,3}(n)}{p_{2,3}}, \tag{2.25}$$

where p_2 and p_3 are the pitchwise and spanwise length, respectively, and $k_{2,3}$ are integers. Note that the spanwise and pitchwise wave numbers are in general not the same. This limitation does not apply to $\beta_1(n)$. Different orientations of the inlet structures can be achieved by adjusting $\dot{\phi}_i(n)$. Finally a phase shift can be specified using $\varphi_i(n)$. The turbulence intensities are adjusted using the coefficients c_i independently for each direction. In an exhaustive preliminary study, it was found that good results were

obtained using a total of 16 waves, based on four different wave number combinations j. The wave numbers for each j are given in the left part of table 2.1. Each wave in each of the wave number combinations j is shifted by one fourth of a period and the corresponding $\varphi_i(m)$ are given in the right part of table 2.1.

j	β_1	k_2	k_3	m	ϕ_2	ϕ_3
1	10.90	4	1	1	0	u
2	17.35	7	3	2	$2v$	$-u$
3	27.03	13	5	3	0	u
4	41.54	17	7	4	$2v$	$-u$

TABLE 2.1: Turbulence generation parameters

An instantaneous snapshot of the turbulence generated in this way is presented in figure 2.2 (a), where the Q-criterion was used to visualize the turbulent structures. The green arrow indicates the mean inlet flow direction and the blue surface denotes the blade surface. The visualized structures appear three-dimensional and random as expected for a turbulent flow. At closer inspection, a pattern of reoccurring structures can be observed in the pitchwise direction. However, the distance between them is sufficiently large (one third of the pitch) that they are not expected to affect the transition behaviour on the blade that is governed by interaction with structures of the size of a few boundary layer thicknesses. To get a more quantitative understanding of the behavior

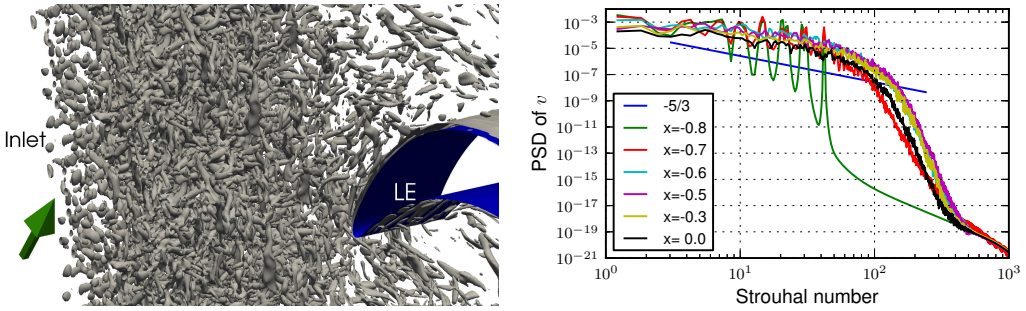

(a) (b)

FIGURE 2.2: (a) Structures generated using the presented Discrete Wave method visualized using the q-criterion at a level of 50. (b) Time Spectra at various Streamwise positions given in the Legend of the Figure.

of the background turbulence, a precursor simulation of a rectangular box representing only the inlet region of an LPT cascade set-up were conducted, extending from $x = -0.8$ to $x = 1$, where the leading edge of a blade would be located at $x = 0$. Time-spectra of the pitchwise velocity component at different streamwise positions are plotted in figure 2.2 (b). At the inlet ($x = -0.8$), as expected peaks at the introduced wave numbers (given in table 2.1) are observed. First the small scales develop (high frequencies) and already at 20% chord downstream of the inlet a broadband signal characteristic of a fully turbulent flow is present. Peaks at the injected frequencies are still visible but the gaps are quickly filled and at half a chord length from the inlet the peaks are hardly

distinguishable and the spectrum follows the $-5/3$ law. As simulations in the current study have an inlet length of at least 80% chord, well developed turbulence will therefore be 'seen' by the blade. Using an autocorrelation function of the time signal and Taylors frozen turbulence assumption, the length scale of the turbulence impacting on the blade has been estimated to be about 5%. Hence, the required characteristics of the background turbulence, both intensity and length scale, can be obtained using this method.

Using a different set of parameters a divergence free turbulence can be generated and thus no acoustic disturbances are injected. Setting $\dot{\phi}_i = 0$ and using the fact that the divergence of the velocity has to be zero yields

$$c_1\beta_1 + c_2\beta_2 + c_3\beta_3 = 0, \tag{2.26}$$

a divergence free signal can be obtained. Considering that c_i and β_i represent intensity and length scales this additional constraint, in general, restricts the turbulence from being isotropic. Using the earlier presented parameters leads to density fluctuations in the inlet region of less than 0.1% so that considering the severe restrictions of the divergence free method this approach was not used.

2.2.2 Boundary Conditions for Compressible Simulations

For compressible simulations acoustic waves are present and if those reach boundaries, this can lead to spurious reflections if not treated properly. Several methods have been developed to deal with this problem. In this work the two types fixed inlet with a sponge and characteristics based BCs are used and briefly presented in the following. Both have to allow for the specification of inlet turbulence.

Characteristic Boundaries In section 2.1.3 the characteristic transformation has been explained. Before discussing characteristic boundary conditions (CBCs), as generally done in literature, the vector $\vec{L_\xi}$, defined as

$$\vec{L_\xi} = \underline{P}^{-1}\frac{\partial \vec{q}}{\partial \xi}\,, \tag{2.27}$$

is used to rewrite (2.17) as

$$\underline{P}^{-1}\frac{\partial \vec{Q}}{\partial t} + \underline{\Lambda}\vec{L_\xi} = \underline{P}^{-1}\vec{S}_{char} \tag{2.28}$$

As mentioned in section 2.1.3 the term replaced by $\vec{L_\xi}$ in (2.17) is the convection term depending on upstream information. In order to specify the boundary this vector has to be specified. If a component of $\vec{L_\xi}$ leaves the domain the information at the boundary

can be obtained from inside. In this case nothing is done with this component. On the contrary for components entering the domain the value has to be specified using physical information from outside. Generally this information is not available and has to be approximated. It should be noted that to this stage no simplification has been performed apart from discretizing the viscous term with one sided stencils. In order to find $\vec{L_\xi}$, Poinsot & Lele (1992) introduced the so called local one dimensional inviscid assumption. If just boundary-normal and inviscid terms are kept and everything else is neglected then the following can be derived (here in the notation of Kim & Lee (2000) since this notation is used in this work)

$$\frac{\partial \rho}{\partial t} + L_1 + \frac{\rho}{2c}\left(L_4 + L_5\right) = 0 \tag{2.29}$$

$$\frac{\partial p}{\partial t} + \frac{\rho c}{2}\left(L_4 + L_5\right) = 0 \tag{2.30}$$

$$\frac{\partial w}{\partial t} + L_2 = 0 \tag{2.31}$$

$$\frac{\partial}{\partial t}\left(x^*_{1,\eta} u - x^*_{2,\eta} v\right) + L_3 = 0 \tag{2.32}$$

$$\frac{\partial}{\partial t}\left(x^*_{1,\eta} u + x^*_{2,\eta} v\right) + \frac{1}{2}\left(L_4 - L_5\right) = 0. \tag{2.33}$$

Even though the above equations can be derived for conservative quantities as well, the representation here is based on the primitive variables (u_i, p and ρ) since these are more commonly prescribed (Kim & Lee, 2000). The above equations state the relation of the components of $\vec{L}$ with the time derivative of the primitive variables. These relations will be used to specify BCs in the following.

Poinsot & Lele (1992) conclude that the LODI assumption is valid for high Reynolds numbers, because viscous terms are less important and from results they obtained they state that good agreement is also found for lower Reynolds number cases. More recently, in Granet *et al.* (2010) it was concluded that particularly at the outlet inclusion of traversal terms (i.e. flux terms in the boundary plane) might allow for a shorter domain and thus reduced computational cost. Originally this specification method for CBCs has been developed for turbulence-free (clean) inlets (Poinsot & Lele, 1992; Kim & Lee, 2000). Therefore the target value is a constant and generally a far upstream (inlet) or far downstream (outlet) value is used. Considering variable q_i the correction mechanism is of the from

$$L_i = K\left(q_i - q_{i,\infty}\right) \tag{2.34}$$

where K,q_i and $q_{i,\infty}$ are a constant, the current value at the boundary and the target value. The constant generally used is

$$K = \sigma\left(1 - M^2_{max}\right)\frac{c}{L_{ref}}\,, \tag{2.35}$$

where σ, M, c and L_{ref} are a forcing factor, maximum Mach number, speed of sound and a reference length. The forcing factor σ in general is set to 0.25 (Rudy & Strikwerda, 1980). For a clean inlet this method works well but for a turbulent inlet it has to be extended, which is presented next.

The relation of the time derivative and the desired flux derivative normal to the boundary is given in equations 2.29 to 2.33. Earlier it was explained how the time dependent velocity inlet signal is obtained and thus the derivative with respect to the time can be computed and prescribed. Guezennec & Poinsot (2009) developed an enhanced method that, while injecting the correct vorticity based turbulence signal, reduces injected acoustic noise based on a low Mach number expansion initially developed by Prosser (2005). This method however, does not correct any mean drift and thus cannot be used right away.

The method used here is a combination of the approaches by Kim & Lee (2000) and Guezennec & Poinsot (2009). The target value $u_{i,\infty}$ in equation 2.34 is replaced by the instantaneous turbulent velocity. The conditions for each component of $\vec{L}$ are thus as follows

$$\begin{aligned} L_1 &= 0.0 \\ L_2 &= K_{in}\frac{u_3 - u_{3,t}}{2} - \frac{\partial u_{3,t}}{\partial t} \\ L_3 &= K_{in}\frac{u_2 - u_{2,t}}{2} - \frac{\partial u_{2,t}}{\partial t} \\ L_4 &= K_{in}\left(u_1 - u_{1,t}\right) - \frac{\partial u_{1,t}}{\partial t} \\ L_5 &= L_{5,inside} + \frac{\partial u_{1,t}}{\partial t}\ . \end{aligned} \tag{2.36}$$

Setting $L_1 = 0.0$ implies that the density is computed from an isentropic condition. Components L_2, L_3 and L_4 maintain the mean of the velocities (first term) and introduce the different turbulence velocity signals (second term). L_5 is different to the other components since it generally leaves (subsonic inlet) the domain and thus according to the theory does not have to be specified. In case of injection of a turbulent signal, though, the outgoing value $L_{5,inside}$ (computed from inside) is corrected to minimize reflections. For the constant K_{in}, a forcing σ_{in} has to be used (c.f. equation 2.35).

To general choice for $\sigma_{in} = 0.25$ results in a drift of the mean flow which is too high to be accepted. Therefore two additional values of 1 and 4 have been tested and the results are presented in section 4.

Sponge The second type of boundary condition that was used is a fixed inlet where a so called sponge is used to damp out the fluctuations approaching the inlet in order to

prevent reflections at the inlet. The fluctuations of a variable are damped using

$$q_{sp}\left(\vec{x},t\right) = q_{ns}\left(\vec{x},t\right) - c_{sp} f_{sp}\left(x_1\right)\left(q_{ns}\left(\vec{x},t\right) - q_{ref}\left(\vec{x},t\right)\right), \tag{2.37}$$

where $q_{ns}\left(\vec{x},t\right)$, $q_{ref}\left(\vec{x},t\right)$, c_{sp} and $f_{sp}\left(x_1\right)$ are the solution of the governing equations, the reference value of the variable, the sponge strength and the strength function

$$f_{sp}\left(x_1\right) = \frac{1}{2}\left(1 + \cos\left(2\pi \frac{x_s - x_1}{x_s - x_e}\right)\right), \tag{2.38}$$

depending on the boundary normal distance x_1 being unity at x_s and zero at x_e. The reference value for the clean case is the BC value at the inlet. For cases with background turbulence the situation is less straight forward. Using the inlet BC values as in the clean case leads to a rapid decay of the imposed turbulence. Therefore, the reference values at each point are computed using Taylors frozen turbulence assumptions. The same approach as used at the inlet (see section 2.2.1) is applied where the arguments of the harmonic functions are replaced with

$$\begin{aligned} f(t,n) &= \beta_1(n)\left(t - \Delta t\right) + \varphi_1(n) \\ g(t,y,n) &= \beta_2(n)(y + \Delta y - \dot{\phi}_2(n)\left(t - \Delta t\right)) + \varphi_2(n) \\ h(t,z,n) &= \beta_3(n)(z + \Delta z - \dot{\phi}_3(n)\left(t - \Delta t\right)) + \varphi_3(n). \end{aligned} \tag{2.39}$$

The differences in time and location t_0, Δy and Δz are computed assuming pure convection (Taylors frozen turbulence assumption) such that the turbulence signal at the location under consideration is the one generated at the injection time at the inlet. Hence, the differences take the form

$$\begin{aligned} \Delta t &= \frac{x - x_{inlet}}{\overline{u}_1} \\ \Delta y &= -\overline{u}_2 \Delta t \\ \Delta z &= -\overline{u}_3 \Delta t \end{aligned} \tag{2.40}$$

where u_3 is zero in the simulations carried out here.

Outlet

At the outlet a zonal CBC is used. The difference of a zonal CBC to regular CBC is that the treatment is not only applied to the last point but also to a certain number of points, where a ramping function between zero at the first point in the zone and 1 at the outlet is multiplied to the correction term similar to the sponge zone. At an outflow (subsonic case) the flow leaves the domain and thus components L_1 to L_4 are computed from inside. In case of strong vortices passing through the outlet that changes the instantaneous flow direction such that flow enters (i.e. locally reverse flow),

the corresponding component of $\vec{L}$ is set to 0, meaning that the amplitude of the variable does not change with respect to time. L_5 generally enters and thus has to be specified. It is used to keep the outlet pressure at the target value using a condition similar to the inlet (but now for the pressure), given by

$$L_5 = K_{out} \frac{p - p_\infty}{\rho c} \tag{2.41}$$

with

$$K_{out} = \sigma_{out} \left(1 - M_{ref}^2\right) \frac{c}{l} \tag{2.42}$$

According to the literature σ_{out} is set to 0.25 (Kim & Lee, 2000).

2.3 Characteristic Interface Conditions

Multi block grids are used to allow for higher flexibility in grid generation. Between these blocks there are interfaces and in classical approaches the numerical schemes are applied across these boundaries and thus grids, in particular the metric terms, have to be smooth across them. Kim & Lee (2003) developed an approach where a characteristic treatment like introduced in section 2.1.3 for boundaries is applied at interfaces. The characteristic form given by (2.20) is rewritten as

$$\frac{\partial \vec{Q}}{\partial t} + \vec{F} = \vec{S}_{c,t} \ , \tag{2.43}$$

such that the interface normal flux is defined as $\vec{F}$ and the extended source term is written as $\vec{S}_{c,t}$. Further in the following an interface between a block "right" denoted by "R" and a block "left" denoted by "L" is considered.

The method for interfaces works as follows. Like in the case of boundaries for each block the value at the interface is obtained using one sided finite-difference stencils. But in contrast to boundaries at the interface the information from both sides is available. At the interface the variables have to match and this should be true for all times, thus also the time derivatives have to match and looking at (2.43)

$$\vec{F}^L - \vec{S}_{c,t}^L = \vec{F}^R - \vec{S}_{c,t}^R \tag{2.44}$$

has to hold for the left and right side of the interface. As explained in section 2.1.3, the one sided stencil only can be used if the points used for the determination of the interface value are located upstream. Since this is an interface as long as there is a non-zero velocity the flow has to leave one domain and enter the other. Points used for the determination of the interface normal derivative can be used. If the flow enters the domain the one sided stencil at the interface cannot be used, as the propagation

direction is opposed. The value can be computed from (2.44) as given by

$$F_i^L = F_i^R - S_{c,t,i}^R + S_{c,t,i}^L \,, \tag{2.45}$$

if the flow moves from the right to the left and by

$$F_i^R = F_i^L - S_{c,t,i}^L + S_{c,t,i}^R \tag{2.46}$$

in the other case. Hence, in this way at the interface one sided stencils can be used and thus non-continuous grids across interfaces can be considered.

2.4 Grid Generation

The discretized solution procedure is applied on a grid. In case of finite differences, structured grids are used that are generally less flexible compared to unstructured grids, but generally allow for lower computational costs. For the highest possible accuracy the grid should be uniform and orthogonal. For flows like homogeneous isotropic turbulence such a grid can be used. For more complex flows, though, this might result in using grid points in regions where they are not required in order to resolve the flow phenomena, or might not be possible due to the geometry within the domain. In an LPT cascade generally the grid spacing close to the blade (i.e. wall) has to be fine in order to resolve the wall structures. The grid away from the wall depends on the incoming flow turbulence level, or the turbulent breakdown downstream of the blade.

Further, the blade has finite thickness leading and trailing edges of circular form and thus an O-type grid is used allowing for orthogonal wall next cells along the whole blade surface. On the other hand the domain is periodic in the pitchwise direction and thus an H-type grid should be used for that. Thus the grid linking at the interface between O-Grid and H-grid is distorted (i.e. non-orthogonal). For distorted grids with non-uniform spacing the accuracy is best if these changes occur gradually and thus methods have been developed to generate such grids. The grid generation used here is based on a method the proposed by Gross & Fasel (2008) who developed grids particularly suited for cascade simulations, with some modifications to better resolve the far-field.

Grid topology

Gross & Fasel (2008) used an O-type grid about the blade to allow for good resolution close to the wall and an H-type grid to allow for pitchwise periodicity. The topology is presented in figure 2.3. Since the grid is periodic in the pitchwise direction just one periodic section is drawn and the uppermost and lowest lines denote a periodic boundary. The number associated with each block is given by the black number in this figure. It

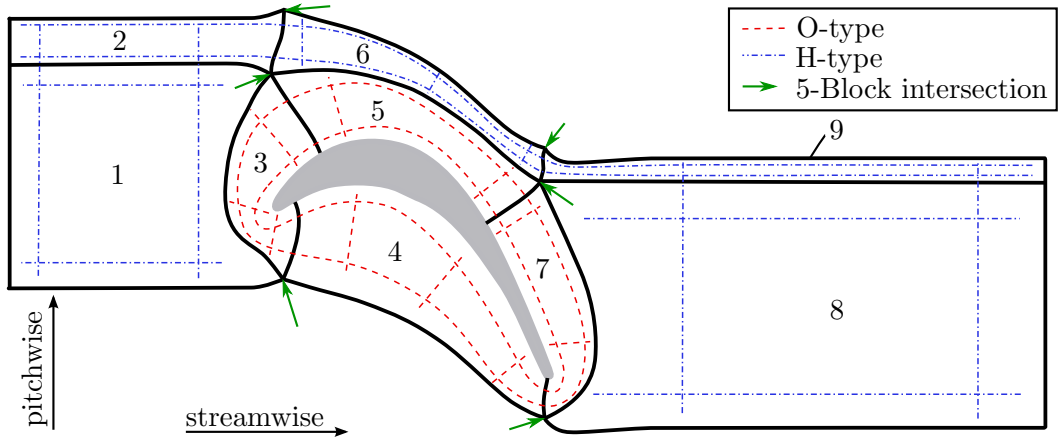

FIGURE 2.3: Grid Topology as suggested by Gross & Fasel (2008)

consists of an O-type section comprised of blocks 3,4,5 and 7 (indicated by the red dashed lines) and of an H-type section comprised of the other blocks (indicated by the blue dash-dotted lines). At the points indicated by arrows, five blocks intersect. At these points the cells cannot be orthogonal but have a maximum angle of $360 \div 5 = 72$ degrees. Since the uppermost and lowest line are periodic four of these five-block points exist.

Grid generation method

The method used is based on the solution of the Poisson equation. As described in section 1.2.2 the physical grid (x_1, x_2) is mapped onto a mathematical grid (ξ, η) as

$$x_1 = x_1(\xi, \eta) \quad \text{and} \quad x_2 = x_2(\xi, \eta)\ . \tag{2.47}$$

Smooth grids are obtained by defining the Poission equations as

$$\frac{\partial^2 \xi}{\partial x_1^2} + \frac{\partial^2 \xi}{\partial x_2^2} = \tilde{P}(\xi, \eta) \tag{2.48}$$

$$\frac{\partial^2 \eta}{\partial x_1^2} + \frac{\partial^2 \eta}{\partial x_2^2} = \tilde{Q}(\xi, \eta)\ , \tag{2.49}$$

where $\tilde{P}(\xi, \eta)$ and $\tilde{Q}(\xi, \eta)$ are forcing parameters that can be used to cluster the grids in certain areas. If these forcing functions are set to zero, then uniform grids will be obtained. Using this set of equations very smooth grids can be obtained (Thompson *et al.*, 1999).

Equations (2.48) and (2.49) are solved using a numerical algorithm. The functions $\xi(x_1, x_2)$ and $\eta(x_1, x_2)$ are not known, only their inverse functions are given numerically

and thus first the system is transformed, following Gross & Fasel (2008), to

$$\alpha\frac{\partial^2 x_1}{\partial\xi^2} - 2\beta\frac{\partial^2 x_1}{\partial\xi\partial\eta} + \gamma\frac{\partial^2 x_1}{\partial\eta^2} = -J^2\left(x_{1,\xi}\tilde{P}(\xi,\eta) + x_{1,\eta}\tilde{Q}(\xi,\eta)\right) \tag{2.50}$$

$$\alpha\frac{\partial^2 x_2}{\partial\xi^2} - 2\beta\frac{\partial^2 x_2}{\partial\xi\partial\eta} + \gamma\frac{\partial^2 x_2}{\partial\eta^2} = -J^2\left(x_{2,\xi}\tilde{P}(\xi,\eta) + x_{2,\eta}\tilde{Q}(\xi,\eta)\right)\ , \tag{2.51}$$

with

$$\alpha = x_{1,\eta}^2 + x_{2,\eta}^2\ ,\ \beta = x_{1,\xi}x_{1,\eta} - x_{,2\xi}x_{2,\eta}\ ,\ \gamma = x_{1,\xi}^2 + x_{2,\xi}^2 \tag{2.52}$$

and the Jacobian

$$J = x_{1,\xi}x_{2,\eta} - x_{1,\eta}x_{2,\xi}\ . \tag{2.53}$$

Equations (2.50) and (2.51) are discretized using central differences and the evolving system is then solved using a Gauss-Seidel algorithm. At the wall an orthogonal condition is used, such that grid-orthogonality at the wall is ensured. This is done by computing the point at a wall by intersecting the spline defined by wall points with the line through the wall next point (computed by the Poisson algorithm) and being normal to the wall. At inlet and outlet a derivative boundary condition is used, where the points are free to move in the pitchwise (x_2) direction and the streamwise (x_1) direction is fixed. Using the information of the neighbouring block a smooth grid is guaranteed across block interfaces. At points close to the five-block points this leads to problems and a different method has to be used that is explained later in this section.

In the above method forcing functions have been introduced. These functions were defined in a sense that they depend on both the ξ and the η directions. However, since Gross & Fasel (2008) used these functions to cluster grid points along block interfaces at constant rates they defined them in a way that $P(\xi)$ and $Q(\eta)$ were used to cluster points along ξ-lines and η-lines, respectively. Those functions were defined as

$$P(\xi) = \frac{\alpha}{J^2}\Phi(\xi) \tag{2.54}$$

$$Q(\eta) = \frac{\gamma}{J^2}\Psi(\eta)\ . \tag{2.55}$$

The strength of the clustering was obtained from

$$\Phi(\xi) = -A\ \mathrm{sgn}(\xi - \xi_i)\exp\left(-B|\xi - \xi_i|\right) \tag{2.56}$$

$$\Psi(\xi) = -C\ \mathrm{sgn}(\eta - \eta_i)\exp\left(-D|\eta - \eta_i|\right)\ , \tag{2.57}$$

where A,B,C and D where constants (specified by the user) and ξ_i and η_i are the ξ and η value about which the clustering was performed. Constants A and C defined the strength of the clustering and B and D defined the decay with respect to the index difference, i.e. how fast the forcing reduces the further the point is away from the point about which the clustering was defined.

Grids obtained using this method initially showed two major problems:

- wall next cell height: Clustering as introduced by (2.56) and (2.57) does only allow for specification of one constant per block. At the blade this meant that in order to sufficiently cluster points at all locations the constant had to be set in a way that some regions where significantly over resolved. When performing DNS on such a grid though the time step has to be reduced due to stability issues. Therefore the constant is now specified for each cell separately such that all wall nearest cells have the same height. This is done automatically by targeting a prescribed height for the first cell next to the blade.

- 5-block corners: the original method Gross & Fasel (2008) showed severe grid distortions at 5-block corners as presented for one of the corners in figure 2.4 (a), where the red arrows indicate the corner. The adjacent cells are severely distorted and cannot be used as such in a DNS. In the following the method to resolve this issue is presented.

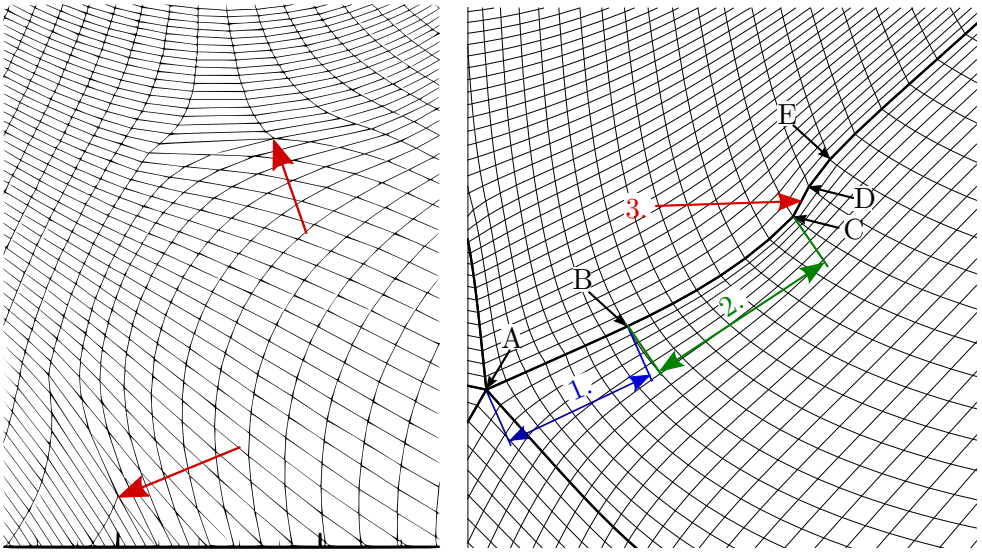

FIGURE 2.4: (a) 5-block points with method suggested by Gross & Fasel (2008); (b) correction of 5-block corners

In order to solve the 5-block point problem the following is done. The goal is to achieve cells that are equally distorted. Since five blocks share this corner point this yields an angle of 72 degrees per block. As mentioned earlier, the highest accuracy is achieved with an orthogonal grid and since this is not possible at those corners it is of interest to move them out of any area where high gradients (e.g. in the wake or close to the wall) are present.

In figure 2.4 (b) the procedure used in the current way is sketched. Block interfaces are the thicker black lines and the thin black lines denote the grid. The corner point, labelled "A" in figure 2.4 (b), is fixed in space and thus can be specified at a position where the mean gradients are benign. In order to obtain a smooth transition to the

grid computed by the Poisson method described earlier, the following three steps are performed (cf. figure 2.4 (b)).

1. The points adjacent to corner point "A" are distributed such that the angle between two block interfaces is 72 degrees. A number of points specified is distributed along a rectilinear line such that for all 5 blocks a star is generated. At the interface under consideration this leads to point "B".

2. From point "B" (the last one specified in 1.) a third order spline is defined in order to change from the slope of the fixed points to the slope computed by the Poisson equation (i.e. slope between points "D" and "E"). Hence, the four conditions for this spline are the position, slope and curvature (being 0) at point "B" and the slope at point "C" (being equal to slope between points "D" and "E").

3. In figure 2.4 (b) the result of this procedure after step 2 can be seen. It yields a smooth change of slope between the two last points of the spline and the first points computed using the Poisson equation (points "D" and "E"). But the slope of the point connecting the Poisson solution and the spline (i.e. points "C" and "D") might be different and this is corrected in the third step. Using the clustering parameters (which in a mathematical sense are forcing parameters), the solution can be smoothed. Since these changes should just affect the solution close to these corners the equations 2.56 and 2.57 are modified to

$$\Phi(\xi,\eta) = -A\,\mathrm{sgn}(\xi-\xi_i)\exp\left(-B_1|\xi-\xi_i|\right)\exp\left(-B_2|\eta-\eta_i|\right) \tag{2.58}$$

$$\Psi(\xi,\eta) = -C\,\mathrm{sgn}(\eta-\eta_i)\exp\left(-D_1|\xi-\xi_i|\right)\exp\left(-D_2|\eta-\eta_i|\right)\,, \tag{2.59}$$

such that a decay along the interface can be specified (i.e. the η-direction for a ξ-interface and the ξ-direction for a η-interface)

Using the method defined above smooth grids can be obtained that have orthogonal cells about the blade as presented in figure 2.5 (a), allowing for good resolution of flow structures at the wall and that have a reasonable grid at the 5-block points as shown in figure 2.5 (b).

2.5 Pre- and Postprocessing to compare with Experiments

Experiments are conducted at a certain set of dimensional physical parameters. To understand the influence of different designs it is of interest to define a set of parameters that allows for comparison, i.e. if theses parameters are the same then the flow is the same. For the LPT case the isentropic Reynolds and isentropic Mach number and the Prandtl number comprise the set of generally used dimensionless parameters. The

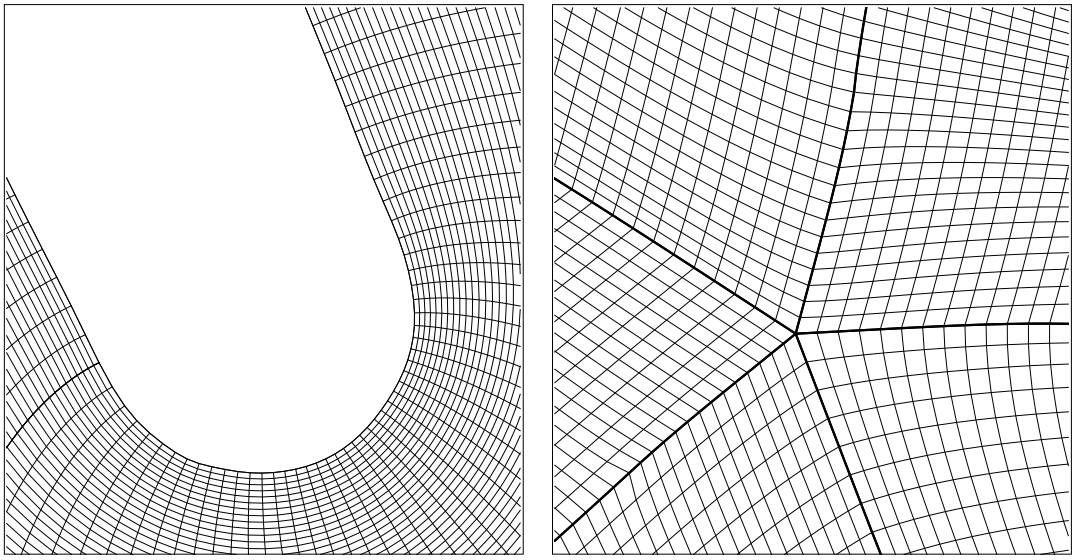

(a) (b)

FIGURE 2.5: final grid: (a) orthogonal cells about blade; (b) 5-block points after special treatment

.

Prandtl number is assumed to be constant for the flow and the other parameters are given by

$$Re_{is} = \frac{\rho_{is} u_{is} c}{\mu_{is}} \tag{2.60}$$

and

$$M_{is} = \sqrt{\left[\left(\frac{p_{t,in}}{p_{s,out}}\right)^{\frac{\gamma-1}{\gamma}} - 1\right] \frac{2}{\gamma - 1}}, \tag{2.61}$$

respectively, where subscripts $_{is}$, $_{in}$ and $_{out}$ denote the isentropic, inlet and outlet value respectively. In the above equation c and μ_{is} are the true chord length and the dynamic viscosity at isentropic temperature. The isentropic condition is a hypothetical state between stagnation quantities at inlet and static quantities at outlet.

For simulations conducted in this work the governing equations are nondimensionalized with Reynolds number, Mach number and Prandtl number as in the experiments but defined using inlet conditions rather than isentropic conditions. Hence, in order to conduct simulations at standard LPT parameters first the relationship between Mach number, Reynolds number and Prandtl number at inlet and isentropic condition have to be defined which is done in the following. The Prandtl number is assumed to be constant and thus is taken from the working medium air and is 0.72. Determining the Reynolds and Mach number is more difficult. From the isentropic condition only stagnation conditions at the inlet are available and therefore a set of static quantities has to be obtained. The static quantities though are part of the solution of the simulations and are iterated. In order to limit the cost the iterations are only performed using two dimensional simulations. To further decrease the cost the initial guess is estimated as

follows. The conservation of mass given by

$$\rho_{in} u_{1,in} = \rho_{out} u_{1,out} \tag{2.62}$$

can be transformed to

$$\rho_{in} \left|\vec{u}_{in}\right| \cos \alpha_{in} = \rho_{out} \left|\vec{u}_{out}\right| \cos \alpha_{out} \tag{2.63}$$

considering velocity triangles. Using isentropic relations the inlet and outlet velocity can be transformed to

$$\left|\vec{u}_{in,out}\right| = M_{in,out} a_{in,out} = M_{in,out} \frac{\sqrt{T_{in,out}}}{M_\infty} \tag{2.64}$$

and considering adiabatic flow between inlet and outlet (after dividing by $\rho_t \sqrt{T_t} M_\infty^{-1}$) yields

$$M_{in} \cos\left(\alpha_{in}\right) \left[1 + \frac{\gamma - 1}{2} M_{in}^2\right]^{-\frac{1+\gamma}{2(\gamma-1)}} = M_{out} \cos\left(\alpha_{out}\right) \left[1 + \frac{\gamma - 1}{2} M_{out}^2\right]^{-\frac{1+\gamma}{2(\gamma-1)}} \tag{2.65}$$

In this equation the inlet flow angle is known and M_{in} is to be obtained. Assuming no losses (which will lead to a slightly too high M_{in}) M_{out} can be replaced with M_{is} and the above equation can be numerically solved for M_{in}. Finally also α_{out} has to be known which is not necessarily reported from experiments and if it is not known the outlet metal angle can be used as a first approximation. Additionally also the reference Reynolds number being defined as

$$Re_\infty = \frac{\rho_{in} u_{in} c}{\mu_\infty} \tag{2.66}$$

needs to be related to the isentropic condition. A similar transformation as done above for the Mach number leads to

$$Re_{in} = \frac{M_{in} \left[1 + \frac{\gamma-1}{2} M_{in}^2\right]^{-\frac{1+\gamma}{2(\gamma-1)}}}{M_{is} \left[1 + \frac{\gamma-1}{2} M_{is}^2\right]^{-\frac{1+\gamma}{2(\gamma-1)}}} Re_{is} \frac{\frac{\left[1+\frac{\gamma-1}{2} M_{is}^2\right]^{-1}}{\left[1+\frac{\gamma-1}{2} M_{is}^2\right]^{-1}+S}}{\frac{\left[1+\frac{\gamma-1}{2} M_{in}^2\right]^{-1}}{\left[1+\frac{\gamma-1}{2} M_{in}^2\right]^{-1}+S}} \tag{2.67}$$

where S is the Sutherlands constant divided by the stagnation temperature at the inlet. Starting with the initial guesses for both M_{in} and Re_{in} the values are iterated until Re_{is} and M_{is} from the two dimensional simulation match the experimental ones. In order to obtain Re_{is} and M_{is} from the simulation first the pitchwise nonuniform profiles have to be appropriately averaged.

2.5.1 Obtaining the integral values from Simulation results

The simulations provide full three-dimensional time varying data to which in general an adequate postprocessing has to be applied to before the results can be used to discuss certain aspects. In general the postprocessing methods will be developed alongside the discussion of the results. Here only the extraction of Re_{is} and M_{is} is discussed. These values depend on time mean quantities appropriately averaged over the pitchwise direction and thus the DNS data has to be averaged first. Since the mean of the flow is uniform in span the averaging is performed both over time and span. Statistics of various mean quantities are recorded while running the simulation for both Reynolds averages (denoted by an overbar) and Favré averages (denoted by a tilde, for more details see section 1.2.1) resulting in two-dimensional mean flow fields. From these the pitchwise profiles are extracted by interpolation along pitchwise orientated lines. Since no instantaneous quantities are used in this section for better readability no bars and tildes are written but all variables are the Favré averaged values in the derivation of the mixed out losses.

In general writing time series of flow field is not feasible since writing the data to disk slows down the simulation significantly (as discussed in chapter 3) and also creates huge data sets. Therefore, statistics are collected on the fly. Considering the rms given by

$$u_{rms} = \frac{1}{n-1}\sum_{i=1}^{n}\left[u(i)-\overline{u}\right], \tag{2.68}$$

this definition cannot be used as is since it requires the time mean of the velocity that is not available when the statistics are collected. In order to obtain quantities depending on the mean flow the following transformation can be used. Starting from the equation

$$\overline{u^2(t)} = \overline{\left(\overline{u}+u'\right)^2} = \overline{u}^2 + \underbrace{2\overline{\overline{u}u'}}_{=0} + \overline{u'^2} \tag{2.69}$$

and rearranging for u' results in

$$\overline{u'^2} = \overline{u^2} - \overline{u}^2. \tag{2.70}$$

Hence, the rms can be computed by collecting $\overline{u^2}$ and $\overline{u}^2$ at runtime and evaluating equation 2.70. A similar transformation can be applied to all terms that are presented in table 2.2.

Mixed-out averaging In order to obtain the pitchwise averaged values mixed-out averaging (Cumpsty & Horlock, 2006) is applied. For this type of averaging it is assumed that a nonuniform profile is a shear layer (i.e. pitchwise velocity gradients) and is subsequently mixed out to a state where a uniform pitchwise veloicty profile is obtained.

It is assumed that this mixing takes place at a pitchwise uniform constant pressure and the area does not change during mixing. Hence, this averaging process also takes into account the mixing losses and thus does ideally not depend on the position at which the profile is extracted. The mean pitch averaged streamwise fluxes for mass ($\mathcal{M}$), momentum ($\mathcal{I}_1$ and $\mathcal{I}_2$) and total energy ($\mathcal{E}$) given by

$$\mathcal{M} = \frac{1}{l_p}\int_{l_p} \rho\left(x_2\right) u_1\left(x_2\right) dx_2 \tag{2.71}$$

$$\mathcal{I}_1 = \frac{1}{l_p}\int_{l_p} \left[\rho\left(x_2\right) u_1^2\left(x_2\right) + p\left(x_2\right)\right] dx_2 \tag{2.72}$$

$$\mathcal{I}_2 = \frac{1}{l_p}\int_{l_p} \rho\left(x_2\right) u_1\left(x_2\right) u_2\left(x_2\right) dx_2 \tag{2.73}$$

$$\mathcal{E} = \frac{1}{l_p}\int_{l_p} u_1\left(x_2\right) \left[\rho\left(x_2\right) e_t\left(x_2\right) + p\left(x_2\right)\right] dx_2 \tag{2.74}$$

are constant for all streamwise positions in the given scenario neglecting the viscous terms. Thus these fluxes would also be apparent when the quantities are completely uniform across the pitch (i.e. mixed out). Hence, they can be written in terms of the mixed out values as

$$\mathcal{M} = \rho_{\mathrm{mix}} u_{1,\mathrm{mix}} \tag{2.75}$$

$$\mathcal{I}_1 = \rho_{\mathrm{mix}} u_{1,\mathrm{mix}}^2 + p_{\mathrm{mix}} \tag{2.76}$$

$$\mathcal{I}_2 = \rho_{\mathrm{mix}} u_{1,\mathrm{mix}} u_{2,\mathrm{mix}} \tag{2.77}$$

$$\mathcal{E} = u_{1,\mathrm{mix}}\left(\rho_{\mathrm{mix}} e_{t,\mathrm{mix}} + p_{\mathrm{mix}}\right), \tag{2.78}$$

where energy and pressure are related by the equation of state

$$\rho_{\mathrm{mix}} e_{\mathrm{mix}} = \frac{p_{\mathrm{mix}}}{\gamma - 1} = \rho_{\mathrm{mix}} e_{t,\mathrm{mix}} - \rho_{\mathrm{mix}} \frac{u_{1,\mathrm{mix}}^2 + u_{2,\mathrm{mix}}^2}{2}, \tag{2.79}$$

giving a system of five unknowns. The solution of this system of equation is given by

$$u_{1,\mathrm{mix}} = \frac{-\frac{\gamma}{\gamma-1}\mathcal{I}_1 + \sqrt{\left(\frac{\gamma}{\gamma-1}\mathcal{I}_1\right)^2 + 2\frac{\gamma+1}{(\gamma-1)}\mathcal{M}\left(\frac{\mathcal{I}_2^2}{2\mathcal{M}} - \mathcal{E}\right)}}{\frac{\gamma+1}{(\gamma-1)}\mathcal{M}} \tag{2.80}$$

$$\rho_{\mathrm{mix}} = \frac{\mathcal{M}}{u_{1,\mathrm{mix}}} \tag{2.81}$$

$$u_{2,\mathrm{mix}} = \frac{\mathcal{I}_2}{\rho_{\mathrm{mix}} u_{1,\mathrm{mix}}} \tag{2.82}$$

$$p_{\mathrm{mix}} = \mathcal{I}_1 - \rho_{\mathrm{mix}} u_{1,\mathrm{mix}} u_{1,\mathrm{mix}}, \tag{2.83}$$

defining the primitive variables of the flow state. Note that the flow through an LPT cascade is considered to be quasi two-dimensional and thus velocity components in the spanwise direction are zero. Using the mixed-out averaged values obtained in this way, Re_{is} and M_{is} can be computed using eqns. 2.60 and 2.61.

2.5.2 Additional variables that have to be computed

The quantities available from the statistical averaging explained above are summarized in table 2.2. In order to compare with experiments and also to get further insight in the physics several additional quantities are used and their relation to other quantities is presented in the following. Since the flow is quasi two-dimensional there is no mean velocity in the spanwise direction and the derivatives of the mean flow variables with respect to the spanwise direction are 0. All of the following equations can be applied to mean as well as instantaneous results. Using the nondimensional relation the speed of sound is computed from

$$a = \sqrt{\gamma \frac{p}{\rho}} \tag{2.84}$$

which together with the local velocity

$$\|\vec{u}\| = \sqrt{u_1^2 + u_2^2} \tag{2.85}$$

leads to the local Mach number

$$M = \frac{\|\vec{u}\|}{a} \,. \tag{2.86}$$

Then total pressure and total temperature follows from the isentropic relation as

$$\frac{p_t}{p} = \left[1 + \frac{\gamma - 1}{2} M^2\right]^{\frac{\gamma}{\gamma - 1}} \tag{2.87}$$

and

$$T_t = T \left[1 + \frac{\gamma - 1}{2} M^2\right] \,. \tag{2.88}$$

The local flow angle is obtained using

$$\beta = \arctan\left(\frac{u_2}{u_1}\right) \tag{2.89}$$

and turbulent intensity is defined as

$$\mathrm{TI} = \sqrt{\frac{u_1^2 + u_2^2 + u_3^2}{3}} \tag{2.90}$$

using the general definition and in order to compare with some experiments also the definition

$$\mathrm{TI}_{exp} = \overline{|\vec{u}|^2} - \overline{|\vec{u}|}^2 \tag{2.91}$$

often reported if single hotwire probes are used. The pressure distribution around the blade is defined as

$$c_p = \frac{p_{bl} - p_{out,is}}{p_{t,in,is} - p_{out,is}} \tag{2.92}$$

where p_{bl} is the local pressure and the wake loss is obtained using

$$\omega = \frac{p_{t,in,is} - p_{t,out}}{p_{t,in,is} - p_{out,is}} \tag{2.93}$$

where $p_{t,out}$ is the pressure at the location considered.

index	**term**	**general form**	**eq.**
1	x	-	-
2	y	-	-
3	$\overline{\rho}$	-	-
4	$\overline{\rho u_1}$	-	-
5	$\overline{\rho u_2}$	-	-
6	$\overline{\rho u_1 u_2}$	-	-
7	$\overline{p}$	-	-
8	$\overline{T}$	-	-
9	$\overline{\rho k}$	-	-
10	$\overline{\rho^{'2}}$	-	-
11	$\overline{\rho u_1^{'} u_1^{'}}$	-	-
12	$\overline{\rho u_2^{'} u_2^{'}}$	-	-
13	$\overline{\rho u_1^{'} u_2^{'}}$	-	-
14	$\overline{\rho T^{'2}}$	-	-
15	$\overline{p^{'2}}$	-	-
16	$\overline{\rho u_3}$	-	-
17	$\overline{\rho u_1 u_3}$	-	-
18	$\overline{\rho u_2 u_3}$	-	-
19	$\overline{\rho u_3^{'} u_3^{'}}$	-	-
20	$\overline{\rho u_1^{'} u_3^{'}}$	-	-
21	$\overline{\rho u_2^{'} u_3^{'}}$	-	-
22	$\widetilde{u_1}$	-	-
23	$\widetilde{u_2}$	-	-
24	$\widetilde{u_3}$	-	-
25	$\overline{u_1}$	-	-
26	$\overline{u_2}$	-	-
27	$\overline{u_3}$	-	-
28	$\overline{u_1^{''}}$	-	-
29	$\overline{u_2^{''}}$	-	-
30	$\overline{u_3^{''}}$	-	-
31	$\frac{\partial \widetilde{u_1}}{\partial x_1}$	$\nabla \vec{\widetilde{u}}$	-
32	$\frac{\partial \widetilde{u_1}}{\partial x_2}$	$\nabla \vec{\widetilde{u}}$	-

Continued on next page

Table 2.2 – continued from previous page

index	term	general form	eq.
33	$\frac{\partial \widetilde{u_1}}{\partial x_3}$	$\nabla \vec{\widetilde{u}}$	-
34	$\frac{\partial \widetilde{u_2}}{\partial x_1}$	$\nabla \vec{\widetilde{u}}$	-
35	$\frac{\partial \widetilde{u_2}}{\partial x_2}$	$\nabla \vec{\widetilde{u}}$	-
36	$\frac{\partial \widetilde{u_2}}{\partial x_3}$	$\nabla \vec{\widetilde{u}}$	-
37	$\frac{\partial \widetilde{u_3}}{\partial x_1}$	$\nabla \vec{\widetilde{u}}$	-
38	$\frac{\partial \widetilde{u_3}}{\partial x_2}$	$\nabla \vec{\widetilde{u}}$	-
39	$\frac{\partial \widetilde{u_3}}{\partial x_3}$	$\nabla \vec{\widetilde{u}}$	-
40	$\frac{\partial \overline{p}}{\partial x_1}$	∇p	-
41	$\frac{\partial \overline{p}}{\partial x_2}$	∇p	-
42	$\frac{\partial \overline{p}}{\partial x_3}$	∇p	-
43	$\frac{\partial \overline{u_1}}{\partial x_1}$	$\nabla \vec{\overline{u}}$	-
44	$\frac{\partial \overline{u_1}}{\partial x_2}$	$\nabla \vec{\overline{u}}$	-
45	$\frac{\partial \overline{u_1}}{\partial x_3}$	$\nabla \vec{\overline{u}}$	-
46	$\frac{\partial \overline{u_2}}{\partial x_1}$	$\nabla \vec{\overline{u}}$	-
47	$\frac{\partial \overline{u_2}}{\partial x_2}$	$\nabla \vec{\overline{u}}$	-
48	$\frac{\partial \overline{u_2}}{\partial x_3}$	$\nabla \vec{\overline{u}}$	-
49	$\frac{\partial \overline{u_3}}{\partial x_1}$	$\nabla \vec{\overline{u}}$	-
50	$\frac{\partial \overline{u_3}}{\partial x_2}$	$\nabla \vec{\overline{u}}$	-
51	$\frac{\partial \overline{u_3}}{\partial x_3}$	$\nabla \vec{\overline{u}}$	-
52	$\frac{\partial \overline{u_1}}{\partial x_1}$	$S(\overline{u})$	-
53	$\frac{1}{2}\left(\frac{\partial \overline{u_1}}{\partial x_2} + \frac{\partial \overline{u_2}}{\partial x_1}\right)$	$S(\overline{u})$	-
54	$\frac{1}{2}\left(\frac{\partial \overline{u_1}}{\partial x_3} + \frac{\partial \overline{u_3}}{\partial x_1}\right)$	$S(\overline{u})$	-
55	$\frac{\partial \overline{u_2}}{\partial x_2}$	$S(\overline{u})$	-
56	$\frac{1}{2}\left(\frac{\partial \overline{u_2}}{\partial x_3} + \frac{\partial \overline{u_3}}{\partial x_2}\right)$	$S(\overline{u})$	-
57	$\frac{\partial \overline{u_3}}{\partial x_3}$	$S(\overline{u})$	-
58	sum of the RHS TKE equation	-	1.35
59	transport term TKE equation	$\sum_{i,j} \frac{\partial(\widetilde{\rho u_j} k)}{\partial x_j}$	1.35
60	TKE production	$\sum_{i,j} \tau_{ij} \frac{\partial \widetilde{u_i}}{\partial x_j}$	1.35
61	TKE dissipation rate	$\sum_{i,j} \overline{t_{ji} \frac{\partial u_i''}{\partial x_j}}$	1.35
62	molecular diffusion	$\sum_{i,j} \frac{\partial}{\partial x_j}\left(\overline{t_{ij}\left(u''\right) u_i''}\right)$	1.35
63	turbulent transport	$-\sum_{i,j} \frac{\partial}{\partial x_j}\left(\overline{\frac{\rho u_i'' u_i'' u_j''}{2}}\right)$	1.35
64	pressure diffusion	$-\sum_{i,j} \frac{\partial}{\partial x_j}\left(\overline{p' u_i''} \delta_{ij}\right)$	1.35
65	pressure work	$\sum_i \overline{u_i''} \frac{\partial P}{\partial x_i}$	1.35

Continued on next page

Table 2.2 – continued from previous page

index	term	general form	eq.
66	pressure dilatation	$\sum_i \overline{p' \frac{\partial u_i''}{\partial x_i}}$	1.35

TABLE 2.2: Output vector as in statistics.F

Chapter 3

Computational and Parallel Performance

As mentioned previously one of the major limits of the usage of DNS is the computational cost. Hence, when conducting DNS it is important to optimize the setup comprised of grid, numerical method and algorithm to minimize cost. In chapter 2 the code used in this work, HiPSTAR, has been described in terms of the algorithms and libraries used. In the following the optimization of the code that is applied to minimize computational expenses for a given grid is discussed and the "optimization" of the grid is performed in chapter 4.

Before the code is discussed a general review and an outlook on near-future architectures is provided to understand certain code-design decisions. This is of particular importance since code optimization and the choice of algorithms strongly depends on the hardware (platform) used. The hardware is steadily improving which allows for increasing complexity in the simulations. Since its market share is too small the main driver is not high performance computing (HPC) and as such not all improvements of the hardware lead to benefits for HPC systems. The trend of a continuous improvement has been recognized by Moore (1965) who predicted that the number of transistors on a single semiconductor chip doubles every two years. Looking at the Top500 (2015) computer list which reflects the advances in HPC systems this trend can be seen. Giles & Reguly (2014) discuss that this advance for many years was mostly related to decrease in time per clock cycle. The reduction in time per clock cycle resulted in a speed-up of application without the requirement to change the underlying code. On the other hand the reduction of time per clock cycle increases the energy consumption significantly and therefore the time per clock cycle has stagnated for several years already. Still additional transistors are added to new chips and those are now used to form multi-core systems on one chip or for additional execution units within each core (Levesque & Wagenbreth, 2011). Another important aspect is that the increase in memory access speed (random

access memory) has been slower than the increase in the speed of the processor. This lead to the development of sophisticated cache systems taking up a substantial part of the chip. For CPUs the cache takes 50% or more of the space on the chip (Giles & Reguly, 2014). Still memory is considered to be the main limitation for many HPC applications (Levesque & Wagenbreth, 2011).

Recently accelerators or graphical processing units (GPUs) entered HPC systems. For those in general more of the chip is used for computational units and less for memory and scheduling. In essence this favours highly vectorizing codes, i.e. where the same operation has to be executed for different data (sinlge instruction multiple data - SIMD). Recently also CPUs have added SIMD features but while CPUs work on two to four data variables simultaneously GPUs work on substantially more. The vector length (number of SIMD instruction that can be executed in one clock cycle in parallel)on an NVIDIA K20x is 32 (TITAN Web Team, 2015).

In general HPC systems are comprised of many equal nodes connected via a fast network. Each node hosts one or more CPUs and the supporting infrastructure like random access memory (RAM), network interface connector etc. Some systems also have one or more accelerators on each node. Given that the RAM is located on each node and can only be directly accessed from the cores on the respective node, these systems are often referred to as *distributed memory* systems, as opposed to *shared memory systems* where each processor can directly access the memory of all other processor. The largest systems of today exceed one million cores (Top500 (2015) list November 2014). In order to exploit these systems a code has to use many cores simultaneously (i.e. run in parallel) therefore has to cope with this distributed memory approach.

While for a long time the applications did speed-up automatically due to the time per clock cycle decrease the recent advances in hardware require adapting the application's code to use the additional hardware features in the evolving architecture. Particularly parallelization of the code and using accelerators requires substantial changes of the code. In the following the code used in this work, HiPSTAR, and its capability to run on these systems is investigated and then its porting to GPUs is presented and the performance is compared to pure CPU systems to understand the potential of GPU systems.

3.1 Code structure of HiPSTAR

As discussed in chapter 2, HiPSTAR is a solver for the unsteady three-dimensional compressible flow equations. In this section the organisation of the code solving these equations on HPC systems is described. The equation that is solved is given by (see

eqns. (2.2) - (2.6)) and summarized as

$$\frac{\partial \vec{q}}{\partial t} + \frac{\partial \vec{f}}{\partial x_1} + \frac{\partial \vec{g}}{\partial x_2} + \frac{\partial \vec{h}}{\partial x_3} = \frac{\partial \vec{f_v}}{\partial x_1} + \frac{\partial \vec{g_v}}{\partial x_2} + \frac{\partial \vec{h_v}}{\partial x_3}. \tag{3.1}$$

Bringing all the spatial derivatives to the right hand side the equation takes the form

$$\frac{\partial \vec{q}}{\partial t} = \underbrace{-\frac{\partial \vec{f}}{\partial x_1} - \frac{\partial \vec{g}}{\partial x_2} - \frac{\partial \vec{h}}{\partial x_3} + \frac{\partial \vec{f_v}}{\partial x_1} + \frac{\partial \vec{g_v}}{\partial x_2} + \frac{\partial \vec{h_v}}{\partial x_3}}_{\mathbf{RHS}}, \tag{3.2}$$

where the right hand side will be referred to as **RHS** in the following. The numerical solution is obtained by disretizing the **RHS** on a spatial grid that has to be sufficiently fine to resolve all structures in the flow. For DNS this mostly results in a large number of grid points where at each point the solution is progressed in time using an explicit Runge-Kutta scheme for numerical time integration

$$\vec{q}|_{n+1} = \vec{q}|_n + \Delta t \sum_{k=1}^{5} b_k \mathbf{RHS}|_n. \tag{3.3}$$

In order to obtain a solution an initial flow field has to be provided as an initial condition.

The large number of grid points required to perform DNS is generally in excess of what is possible to be performed on a single core. In general DNS are therefore performed on massively parallel systems and in order to use such systems the work has to be shared among all processors (parallelization). In HiPSTAR, as in many other flow solvers, this is achieved through a domain decomposition as shown in figure 3.1. The computational region is covered by the grid lines (black lines) where only every fourth grid line is plotted for clarity. The sub-domain enclosed by the red lines are executed in parallel, i.e. simultaneously on different cores. Note that no domain decomposition is applied in the spanwise direction normal to the plane shown in figure 3.1.

A sample domain decomposition is illustrated in figure 3.2(a) where one subdomain is depicted. For simplicity a two dimensional equidistant Cartesian grid is presented but it can be applied to any structured grid. The points represent a subset of the discretized computational domain which is clipped at the dashed rectangle to limit the illustrated extent. All the points within the hatched rectangle are the points this particular subdomain is working, i.e. the solution is progressed in time and is referred to as *base* subdomain in the following. The horizontal axis is the i direction and the vertical axis is the j direction where the lower-left corner is at $(1, 1)$ and the upper-right corner is at (nxp, nyp). Hence the number of points in the base subdomain is given by $nxp \times nyp \times n_{sp}$ where n_{sp} is the number of points in the direction normal to the $i - j$ plane, corresponding to the number of points used for the span of the LPT simulations in this work. The boundaries of the neighbouring subdomains are indicated by the dotted lines, but again those are clipped at the dashed lines to limit the illustrated domain.

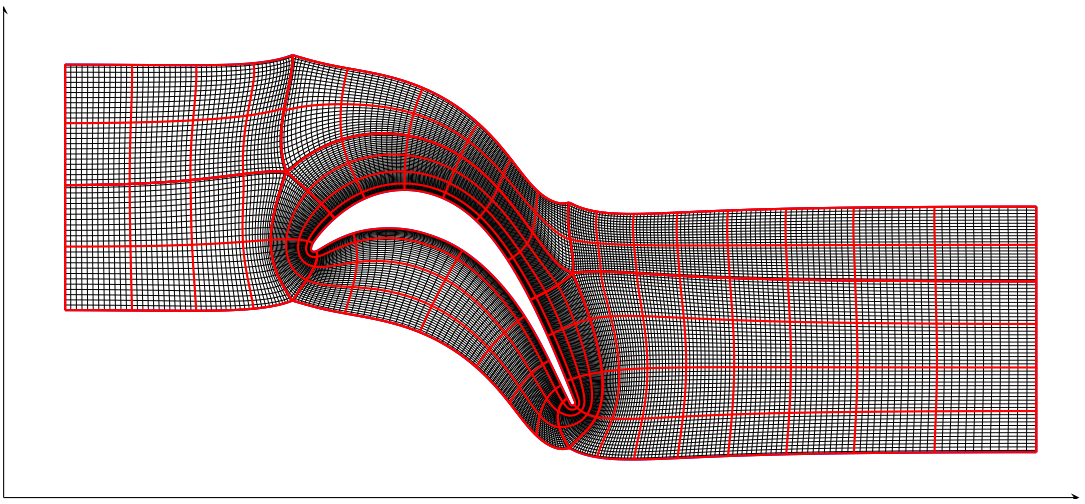

FIGURE 3.1: Domain decompostion for a low pressure turbine DNS

The spatial derivatives in the **RHS** operator require information from the entire spatial domain. Using discrete finite difference operators the data at the points appearing in the stencils (i.e. the points appearing in the finite difference functions (Ferziger, 1998)) is required. Considering a five-point stencil for the point indicated in red the information for the points coloured in orange is required. The points to the left of the point coloured in red are within the same subdomain. The points to the right of the red point are not in the same subdomain and therefore have to be obtained from another subdomain. Considering that the subdomain illustrated in figure 3.2(b) is the subdomain right of the one in subdomain in figure 3.2(a), the postion of the red point would be, as indicated in figure 3.2(b), the first point left outside of the domain. Hence, the points containing the required information for this particular derivative are indicated in green. In addition to finite difference schemes also filters have spatial stencils that reach outside of the subdomain. Hence, in order to obtain the solution for the hatched rectangle figure 3.2(a), information on a larger spatial region is required. Since only one dimensional stencils are used these additional regions, referred to as *halo points* or *halos*, are illustrated with the yellow and blue areas. The width of these domains called xhalo and yhalo can be determined from the particular stencils used.

In HiPSTAR this is realized by launching a separate instance of the program for each subdomain using the message passing interface (MPI) library. Each instance (MPI rank) executes exactly the same program but for a different subdomain, which means that it only can update its own memory and as such variables. As mentioned above each processor requires the information in the base subdomain (solid rectangle) and the halos. In practice, the domain actually allocated by each processor is the region encircled by the dashed rectangle in figure 3.2(a) and will be referred to as *extended subdomain*. Owing to the circumstance that two dimensional arrays have to be rectangular in Fortran, the extended subdomain is slightly bigger than what is required by the subdomain. Still each processor needs to only update the solution in its subdomain and not in the halos,

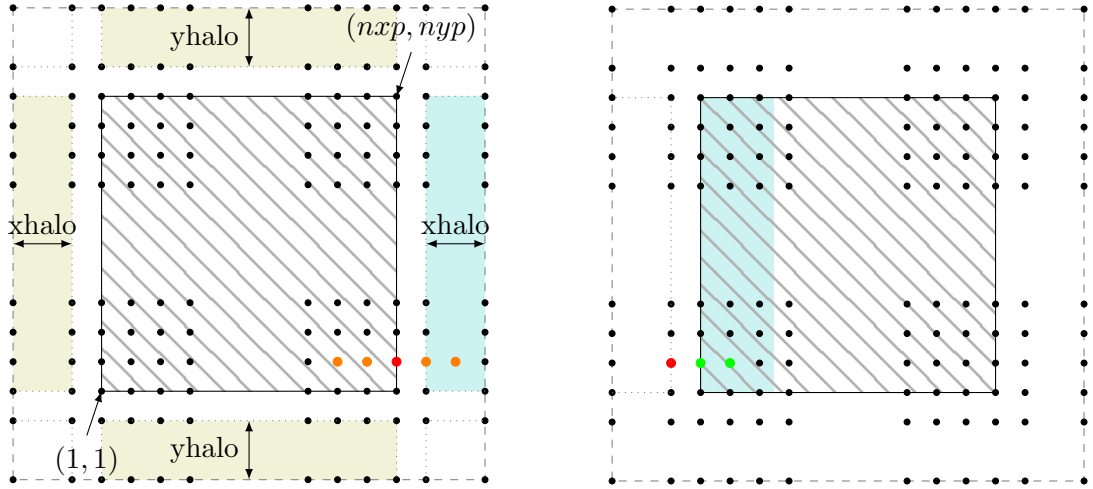

(a) receiving processor (b) sending processor to the right of receiving

FIGURE 3.2: Domain decomposition schematic

where the information might be outdated. If an operation, like a derivative, requires information in the halos this has to be obtained from the subdomain that works on the respective halo region. This is done by an MPI communication realized through library calls and defined here as *swapping*. Since the two communicating subdomains might be on different nodes in the cluster the MPI library issues a network communication that in general is slow with respect to computation.

Considering that current large scale systems have shared memory within each node, one subdomain (or MPI rank) can be computed by various processors using an OpenMP shared memory approach. This is often referred to as hybrid OpenMP/MPI code. As discussed by Levesque & Wagenbreth (2011) the advantage of hybrid approaches is that with respect to MPI-only implementation, higher core counts can be reached since less communication is required. The implementation of hybrid OpenMP/MPI infrastructure in HiPSTAR is discussed in Edwards *et al.* (2010).

The structure of HiPSTAR is illustrated as a flow chart in figure 3.3. First initialization routines are executed that initialize variables, read in the flow field or set up the environment parallel environment. Since they are only executed once at the beginning and even for big cases rarely exceed a minute of the simulation runtime of several hours they are not further discussed. Similar, at the end of the simulation there are some wrap up routines performed once but due to the small fraction of execution time they are not discussed here. The majority of time is spent in the main time loop which will be the focus of the following discussion.

The first step in each timestep is to compute a new inlet turbulence state. As discussed in section 2.2.1 various methods are implemented and in terms of performance a method has been implemented that decreased the generation time significantly (leading to reduction of the runtime by $\approx 30\%$ for large length scales).

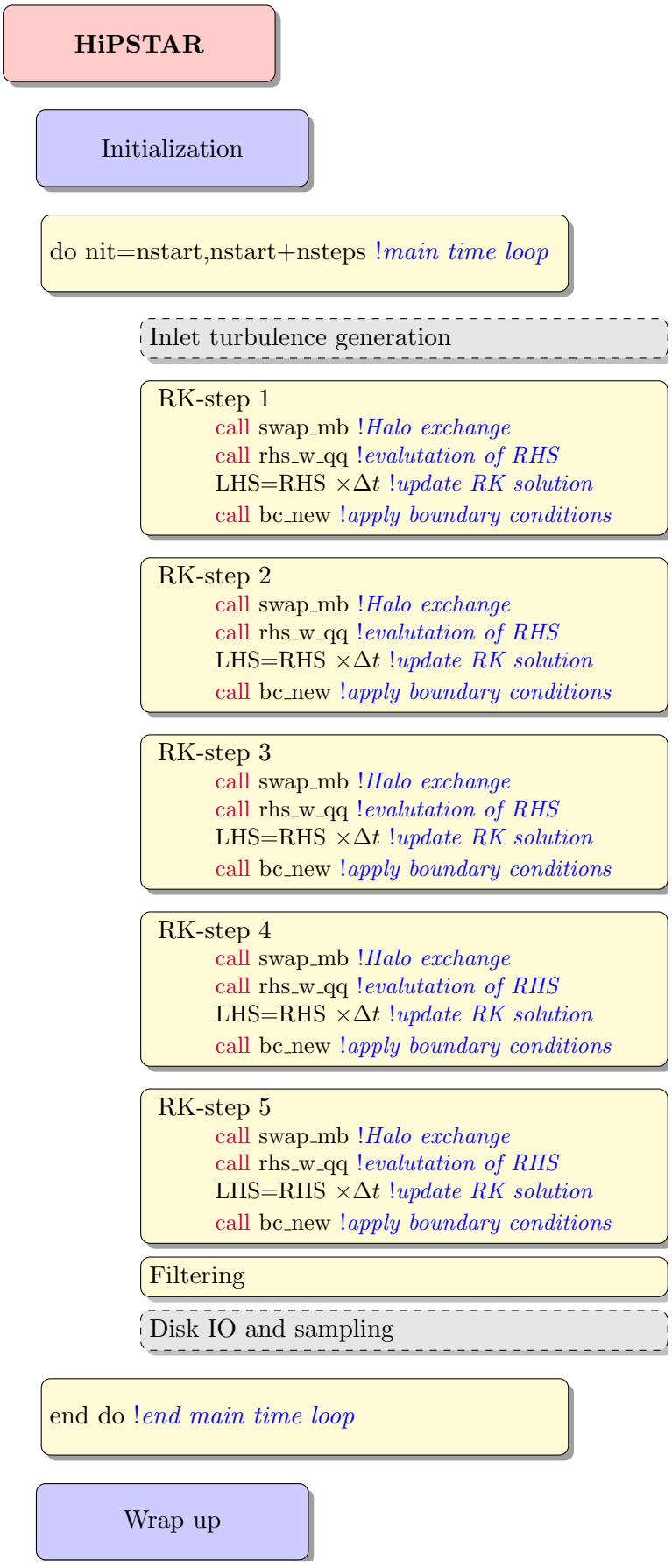

FIGURE 3.3: Flow chart of HiPSTAR

Then the five Runge-Kutta steps are executed. First the halo exchange is performed to update the halos. Then the **RHS** is evaluated using the routine *rhs_w_qq*. Within this routine there are several calls to the Fourier and the derivative routines which are required in order to assemble eqn. (3.3). Several derivatives are required and each of those essentially follows the steps that first the derivative is prepared on the extended subdomain, then the derivative is taken and the result of it is added to the solution vector on the base subdomain. Given the memory bottleneck as discussed earlier the memory footprint is minimized by reusing arrays as much as possible, even at the expense of additional computational cost. Some terms in eqn. (3.3) contain second derivatives of the flow field that are obtained by applying the first order derivative routine twice. Therefore within the **RHS** another halo exchange of the first order derivatives is required. Then the solution is updated and the boundary conditions are reinforced. After the last Runge-Kutta step the solution for the next time step is available and in order to achieve a stable solution numerical oscillations are filtered.

At certain intervals the flow field is recorded to allow for post-processing. Given that file input/output (IO) takes significantly longer than computation and the generated database requires large amounts of diskspace it is tried to minimize it. This is achieved by computing statistics on-the-fly, as explained in 2.5.

The explanation of the code given in this chapter does not represent all details in light of brevity. Rather it was intended to explain the major work flow and concepts. At the start of this work the code was generally working for cascade flows and major work packages in terms of improvement have been the implementation of the sponge routine as well as the implementation of the turbulent inlet. Pure performance optimization was only required for certain routines particular to the cascade case where some MPI routines have been optimized. For example, the grid used for these simulations results in points where five blocks are neighbouring which is ill-defined in a finite difference sense. Hence, an averaging procedure was implemented and optimized. this resulted in a performance improvement between 5% and 10% runtime for small and large parallelizations, respectively.

3.2 Performance of the code on CPU architectures

As mentioned above DNS is often restricted by computational cost. In addition it is important to conduct simulations in a reasonable time (wall time, i.e. the time that passes on a wall-clock). In the following the relationship between wall time and total cost is investigated for the code optimized for this work.

In general the performance of codes is assessed using two forms of scaling tests that are often assessed for parallel programs. The first scaling test is called weak scaling . In this case the work per processor is kept constant while the number of processors is increased.

Hence, the total problem size is increased. This scaling test allows to understand if there is a penalty if problem size and number of cores are increased accordingly. HiPSTAR has generally excellent weak scaling (above 90%) as can be seen for example in Sandberg *et al.* (2015) and, therefore, only the strong scaling potential is investigated in this work.

In case of strong scaling the number of processors is changed for a given testcase (problem size) which leads to a change of the work per processor. If the number of processors is increased a reduction of wall time is anticipated. Ideally the cost of the simulation remains the same if more processors are used, which requires a reduction of wall time at the same factor at which the processor count is increased. For HiPSTAR, as for many similar codes, the reduction of time of the computational work in each subdomain in general reduces at a greater rate as the time spent in MPI communication. Hence, even though the wall time is decreased it does not occur at the ideal rate which results in an increase of the cost of the simulation.

The strong scaling tests on CPUs are performed on the Archer UK supercomputing facility. It hosts a CRAY XC30 with two 12-core Intel Xeon E5-2697 CPU (Ivy Bridge) per node and the nodes are connected using and ARIES interconnect (Archer Web Team, 2015). Performance tests were conducted using the Cray programming environment "PrgEnv-cray/5.1.29" with the Cray compiler environment "cce-8.3.7" and the MPI version "cray-mpich-7.1.1" that has shown best performance among the available compilers and software environments.

A testcase representing a large scale simulation as presented in table 3.1 has been used to understand performance characteristics. The number of points for each block in the i and j directions are nx and ny, respectively. In the last column the number of points in each block is given. The sum of the number of points in the $i-j$ plane for all blocks is 2,793,600. Using 128 Fourier modes in the span wise direction (258 physical collocation points) the total number of points is approximately 720 Million mesh points. In order to achieve perfect load balancing (i.e. each processor gets the same amount of grid points to work) the MPI subdomain decomposition can only be achieved if the subdomain lengths called *nxp* and *nyp* are common divisors of nx and ny for all blocks. In order to obtain the lowest number of MPI subdomains the greatest common divisor, 120, has to be used, resulting in 194 MPI subdomains with nxp and nyp being 120 for all processors in the domain. Using a common divisor of 60 the number of MPI subdomains results in 776 and the smallest subdomains that are considered are achieved by using a common divisor of 30 which results in 3104 MPI subdomains.

Before the parallelizations that are used in this work are presented a naming convention is introduced that will be used throughout this section. For each parallelization the MPI subdomain size is given based on the base subdomain size either as 120^2, 60^2 or 30^2. The number of OpenMP threads is append with "Th" and if hyper-threading is used the parallelization is called "HT". Hence, parallelization "60^2-8Th-HT" refers to a case

Block	nx	ny	# of points
1	720	360	259,200
2	720	480	345,600
3	240	360	86,400
4	240	960	230,400
5	240	960	230,400
6	480	960	460,800
7	240	720	172,800
8	840	720	604,800
9	840	480	403,200
		$\sum$	2,793,600

TABLE 3.1: Number of points in each block for the testcase used for the scaling and performance test on the CPU

with nxp and nyp being 60 (i.e. 776 MPI subdomains) using 8 OpenMP threads and HT. The number of cores for cases not using hyper-threading can be computed using

$$n_c = n_{MPI} \times n_{Th} \tag{3.4}$$

where n_{MPI} is the number of MPI subdomains and n_{Th} is the number of OpenMP threads. For cases employing HT it can be computed using

$$n_{c,HT} = \frac{n_{MPI} \times n_{Th}}{2}.$$

The number of OpenMP threads cannot be chosen freely but according to the following restrictions to maintain good performance. On Archer each node is comprised of two CPUs each with twelve cores and hardware hyper-threading (HT). Each of the two CPUs has its own RAM and even though the RAM of the other CPU can be addressed directly, the memory access takes longer which results in a performance decrease. Hence, the largest shared memory unit existing is accessed by twelve cores with HT disabled or 24 "virtual" cores if HT is enabled. For high performance all OpenMP threads of one MPI subdomain have to access the same shared memory region. In addition, the highest performance is achieved if each OpenMP thread is working on its dedicated core. Hence the product of the number of OpenMP threads and the number of MPI subdomains per node has to equate to 12 (HT disabled) or 24 (HT enabled). Then the number of nodes is obtained by dividing the number of MPI subdomains for the problem by the number of MPI subdomains per node.

In table 3.2 the core counts for all parallelizations used in the following are summarized. Only cases where a core count is reported have been executed. The baseline parallelization selected for referencing is using MPI subdomain 120^2 with no OpenMP parallelization (i.e. 1 OpenMP thread) and HT disabled. Simulations for all parallelizations have been executed for between 20 and 800 timesteps such that the wall time

MPI	OMP Threads - HT disabled					OMP Threads - HT enabled				
	1	2	4	6	12	1-HT	2-HT	4-HT	8-HT	12-HT
120^2	194	388	776	1164	2328	-	194	388	776	1164
60^2	776	-	-	-	9312	388	776	1552	3104	4656
30^2	3104	6208	12416	18624	37248	1552	3104	6208	12416	18624

TABLE 3.2: Core counts for different parallelizations used in this work

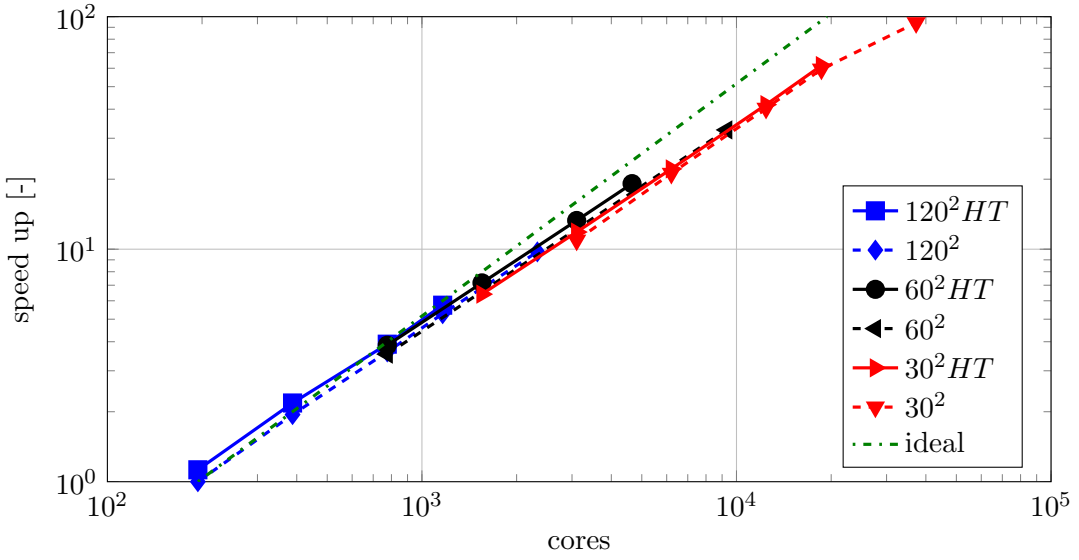

FIGURE 3.4: Strong scaling speed-up on Archer for the MPI/OpenMP CPU version

of each simulation is between 6 and 20 minutes. Then the wall time per time step is computed. The speed-up for each simulation is computed as

$$\text{speed-up} = \frac{\text{wall time per timestep of baseline simulation}}{\text{wall time per timestep of respective simulation}}. \tag{3.5}$$

In order to assess the performance first the speed-up is plotted over the number of cores in figure 3.4. As mentioned above the anticipated speed-up is that the ratio of processors for two parallelizations is inversely proportional to the ratio of time which would result in the *ideal* speed-up curve presented. Note that ideal speed-up is not a limit but chosen such that the cost of the simulation is constant along that line. Parallelizations for which the speed-up is above the ideal line have a reduced overall simulation cost with respect to the simulation and cases that are below it perform worse. The dashed lines represent cases without HT and the cases with HT are plotted using solid lines. One line is plotted for each MPI subdomain size such that along one line only the number of OpenMP threads is varied and the number of threads increases when moving to the right on each line. It can be seen that the dashed lines are always below the solid lines. Therefore, HT is always beneficial. While for smaller core counts the ideal speed-up is almost reached or exceeded if HT is used, for larger core counts the speed-up is not perfect anymore but still acceptable.

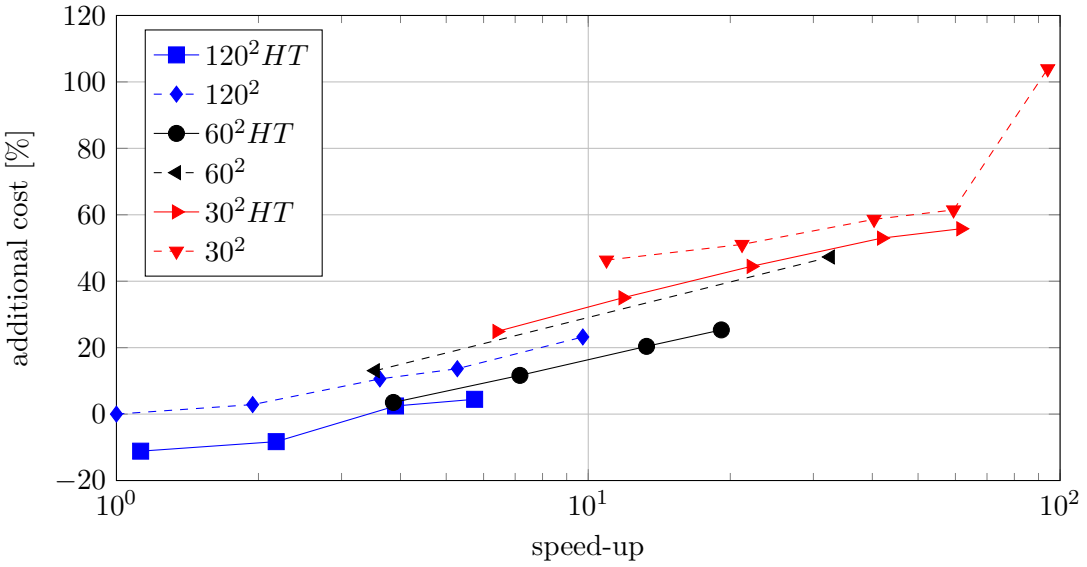

FIGURE 3.5: Additional cost versus speed-up on Archer

As mentioned above when conducting a simulation it is of interest to know what additional cost arises if more cores are used to speed-up the simulation. This can be obtained by looking at figure 3.5 where the additional cost is plotted versus the speed-up. The cost of a simulation is determined by multiplying the cores that are used with the wall time. Using the baseline again as reference the additional cost is obtained by

$$\text{additional cost} = \frac{\text{cost of respective simulation} - \text{cost of baseline simulation}}{\text{cost of baseline simulation}} \tag{3.6}$$

Therefore, the baseline case has zero additional cost and is located at a speed-up of 1. The largest speed-up that is obtained among the cases tested here is approximately 100 and corresponds to the case "30^2-12Th". However, the cost of the simulation doubles with respect to the baseline case. Similarly to figure 3.4, along one line only the number of OpenMP threads is altered and therefore the point next to it on the same line corresponds to the parallelization "30^2-6Th". With respect to all other cases, a tremendous increase in additional cost occurs by switching to 12 OpenMP threads. Such an increase in cost is not apparent for the cases based on MPI subdomains 120^2 and 60^2 when switching from 6 to 12 OpenMP threads. Similar scaling tests for different cases, not presented in this work, reveal that the performance of HiPSTAR drops if the domain size per processor for the LPT cascade cases is below approximately 20,000 to 30,000 points. However, this is not considered a major limitation since large cases that exceed this lower limit still allow for reasonable wall times to finish as will be presented in the following.

The testcase used has a similar size to a production run of an LPT cascade at an isentropic exit Reynolds number of about 100,000, where the dissipation range is fully resolved. The estimates used in this section are based on conclusions of chapter 4.

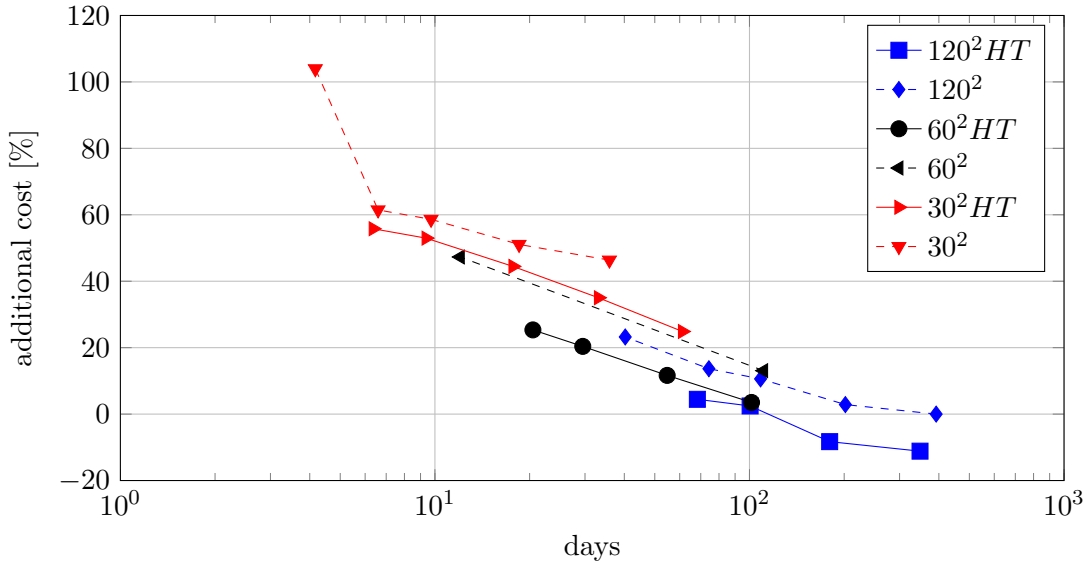

FIGURE 3.6: Approximate simulation wall time considering a simulation with an isentropic exit Reynolds number of 100,000 where the dissipation range is resolved.

To resolve the wall a nondimensional wall resolution, y^+, of less than one has to be achieved for the turbulent regions. For explicit solvers the Courant-Friedrichs-Lewy number should be below one which results in an approximate timestep of 1.5×10^{-5}. For such a simulation approximately 15 flow-through times are required to go through the transient and to achieve statistical convergence for turbulence quantities in the wake region. Hence, the simulation requires about one million timesteps. Using the wall-time per timestep obtained from the testcases presented in this section the wall time for the entire simulation can be estimated. This estimate is plotted with the additional cost arising using the different parallelizations possible in figure 3.6 . Note that this is only the simulation wall time and does not account for queueing. The actual real world time is mostly between a factor of 5 to 10 slower. If the baseline case is considered the actual wall time is approximately 400 days. Considering queueing times a shorter wall time is required. In order to finish the simulation within three month 10 to 15 days of simulation wall time is a safe choice for many clusters. Hence, the best choice seems to be to use any of the cases with an MPI subdomain size of 60^2 and hyperthreading enabled. For this simulation the cost increases by about 15% to 20%. The cost of such a simulation is approximately 1.2 million core hours.

Hence, even though the ideal speed-up is not achieved HiPSTAR on CPUs can be used to conduct DNS of LPT of engine like Reynolds numbers within a reasonable time frame. Note that the simulation considered in this example resolves all scales down to the dissipation range. If dissipation is not of interest the cost can be significantly reduced or larger Reynolds numbers can be considered.

In addition to Archer various other clusters have been used and in table 3.3 the approximate cost of the simulation in terms of core hours of 15 nondimensional time units

grid	Archer	BLUE GENE Q	CRAY XE 6	IRIDIS 4 - Intel XEON
G1	28,000	100,000	60,000	30,000

TABLE 3.3: Core hours for case G1 using different architectures

for grid G1 (defined in chapter 4) on different clusters are compared. In terms of performance the IRIDIS 4 supercomputer in Southampton shows good performance but due to its small size (maximum job size of 512 cores) big cases cannot be finished in a reasonable time. The CRAY XE6 (HeCTOR) is not in service anymore but was used in the initial part of this work. On a core-hour basis the BLUE GENE Q is the slowest architecture, however, in general its hardware cost is cheaper.

3.3 Porting of the code to accelerators (GPUs)

Accelerators (GPUs) work well if a high level of parallelism is available. For example the NVIDIA K20x installed in TITAN at Oakridge national lab and Piz Daint at the CSCS computing facility provides 2688 CUDA cores for single precision operations (TITAN Web Team, 2015). More importantly, for DNS it hosts 896 CUDA cores for double precision that are organised in 14 so called streaming units. Hence, each streaming unit contains 64 CUDA cores. Theoretically the accelerator allows to perform 896 double precision operation per clock cycle, where one clock cycle takes about four times as long as for an Intel XEON CPU. Comparing with a 12-core Intel Xeon E5-2697 CPU (Ivy Bridge with a SIMD length of three (Archer Web Team, 2015)) as used for Archer this would result in about 6 times the number of double precision floating point operations. On the other hand, as mentioned above, memory access is often the limiting factor and additionally for purely sequential code the CPU performance is better. Levesque *et al.* (2012) ported a finite difference flow solver S3d with a combustion model and achieved a speed-up of the GPU version with respect to the CPU version between 2x and 3x on Titan. In HiPSTAR a large part of the code can be parallized on the entire subdomain with a size of $nxp \times nyp \times n_{sp}$. For common simulations this results in more than 100,000 points per MPI rank and therefore it is expected that accelerators can help. In order to understand what performance can be achieved in this work the code was ported to GPU.

The porting was supported by John Levesque and Tom Edwards from the Cray center of Excellence. To understand which routines of the code are computationally heavy, profiling was performed as suggested by Levesque & Wagenbreth (2011). The profiles were obtained using a mesh that was tailored for GPU application in a way that the length of the innermost loop was 64, i.e. twice the minimum vector length and equal to the number of double precision floating points operations per streaming processor unit. As mentioned above the innermost loop length is comprised of the length of the

block	nx	ny	nprocx	nprocy
1	360	240	6	4
2	360	240	6	4
3	240	240	4	4
4	240	480	4	8
5	240	480	4	8
6	240	480	4	8
7	240	360	4	6
8	600	360	10	6
9	600	240	10	4

TABLE 3.4: Grid points per block for testcase used during the porting of HiPSTAR to GPU

subdomain plus the halos, i.e.

$$nxp + 2 \times xhalo \tag{3.7}$$

and xhalo was 2 for the derivative schemes used in this work. Therefore the number of points in the i direction,nxp , was set to 60. The number of points for each block of the mesh for the testcase are summarized in table 3.4 where nx and ny are the number of points in the i and j directions, respectively. The number of processors in the i and j directions are given as nprocx and nprocy such that each subdomain has the correct length. Using 96 modes in the spanwise direction (194 physical points) the number of points for this case yielded approximately 200 million cells which is a medium size production case. Using the decomposition stated in table 3.4 this results in 284 MPI ranks.

If not mentioned differently all the profiles have been generated using the software Cray-PAT and have been obtained on Piz Daint which is an XC30 system. Each node hosts one eight core Intel XEON E5-2670 and one Nvidia Kepler K20x GPU. For both CPU and GPU profiles one MPI rank is placed per node. For the CPU profile eight OpenMP threads are used to fully exploit the cores, resulting in a total of 2,272 cores. Of particular interest is the relative fraction of time spent in the routines to identify the computation hotspots and to decide which routines to initially port to the accelerator. For the profile presented in figure 3.7 the code was instrumented such that all the routines directly called from main time loop (see figure 3.3) were traced. In figure 3.7 (a) the time spent in User routines is compared with time spent in MPI routines and time that is not captured. The latter refers to routines that take less than one percent of the overall simulation and are not presented in this plot. About 12.7% of the time is spent in MPI routines and looking into more detail it can be seen that it is mostly spent in waiting routines. On the one hand an MPI overhead of 12.7% is acceptable and on the other hand cannot be affected directly by porting the code to the accelerators and as such is not discussed further here. Since more than 80% of the time is spent in user routines this is further investigated and in figure 3.7(b) the user routines are further split into all routines called from the main loop. It can be seen that more than 93% of the time is spent in the routine rhs_w_qq, used to assemble the **RHS** and all the routines called

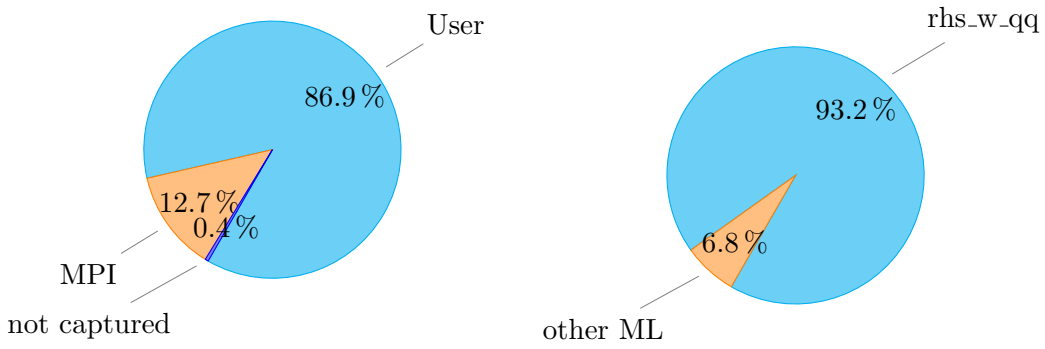

(a) Relative time spent in all routines

(b) relative time spent in User routines

FIGURE 3.7: Profiles of the CPU version

from therein. Less than 7% of the time is spent in all other routines combined. Therefore in the first step all the routines in the rhs_w_qq are ported, which corresponds to less than 30% of the code.

Porting is discussed along with the sample code in listing 3.1. This code essentially loops over the number of iterations, "nit". In each loop iteration the routine swap_mb is called. Then there is a heavily parallel region and at the end the routine bc_new is called. Comparing with the flow chart of HiPSTAR in figure 3.3, it can be seen that this code is a significantly reduced version of HiPSTAR where the main idea of the porting process can be demonstrated. The code that is executed on the accelerator is within lines 5 and 30.

LISTING 3.1: Sample ACC code

```
1  !$acc data create(q)
2        do nit=nstart,nend
3          call swap_mb(q , nvar , kmodw)
4  !$acc update device(q)
5  ! ============ star of accelerator region ====================
6  !$acc parallel loop gang
7          do k=1,kmodw
8  !$acc loop worker
9            do j=1-yhalo,nyp+yhalo
10 !$acc loop vector
11             do i=1-xhalo,nxp+xhalo
12               q(i,j,k,1)= parallel_op
13             end do
14           end do
15         end do
16 !$acc end parallel loop
17 ! there might be other code on accelerator
18
19 !$acc parallel loop gang
20         do k=1,kmodw
21 !$acc loop worker
22           do j=1-yhalo,nyp+yhalo
23 !$acc loop vector
24             do i=1-xhalo,nxp+xhalo
25               q(i,j,k,1)= q(i,j,k,1) + parallel_op
```

```
26              end do
27            end do
28          end do
29 !$acc end parallel loop
30 ! ============= end of accelerator region ===========
31 !acc update self(q)
32
33          call bc_new(q)
34        end do
35 !acc end data
```

Listing 3.1: Sample ACC code

In order to port a code to accelerator supported architectures using OpenACC, directives have to be added to the code. OpenACC directives start with the string "!$acc". A compiler that does not understand ACC directives considers them as comments since they start with an exclamation mark. An OpenACC aware compiler uses the trailing string to execute this work on the accelerator. Essentially porting occurs by performing two steps. First code sections that should be executed on the accelerator have to be labelled. As mentioned above, within HiPSTAR there are various loops that perform one operation for all points in the MPI subdomain (i.e. SIMD) which is implemented using nested loops as indicated in listing 3.1 between lines 7 and 15 as well as lines 20 to 28. Using the "!$acc parallel loop gang" on lines 5 and 18, respectively and the "!$acc end parallel loop" directive the compiler is instructed to generate code that executes these loops on the accelerator. Strictly speaking the "loop gang" is not required and gives the compiler additional information in conjuction with the "!$acc loop vector" directive for the innermost nested loop (lines 10 and 23) and the "!$acc loop worker" directives for lines 8 and 21. As mentioned above, NVIDIA GPUs have 896 CUDA cores for double precision operations that allow for parallel executions. In order to schedule the work efficiently these CUDA cores are grouped at two different levels. The vector, worker and gang statement tell the compiler how this grouping should be performed.

In addition to pointing out the sections of the code that are parallel, in the second step it is important to define memory regions. Both GPU and CPU have their own RAM and can only work if the variables accessed in the loops are resident in their respective RAM. By default OpenACC will always copy the required data to the accelerator when entering a parallel region, then work on it on the accelerator and copy the data back once the parallel region is left. Given that the data transfer between CPU and GPU is slower than RAM access, this mostly turns out as a bottleneck. In order to reduce this slowdown caused by the data copies, memory regions can be defined as done in line 1, where the array q is allocated on the accelerator. The data region ends at line 35 and the array q is deallocated on the accelerator. Hence in this region the array is allocated both in the accelerator and CPU memory. In line 3 the routine swap_mb is called which performs the halo exchange and, as discussed above, it will be left on the CPU and updates the array q in the CPU memory. Hence, before the region executed

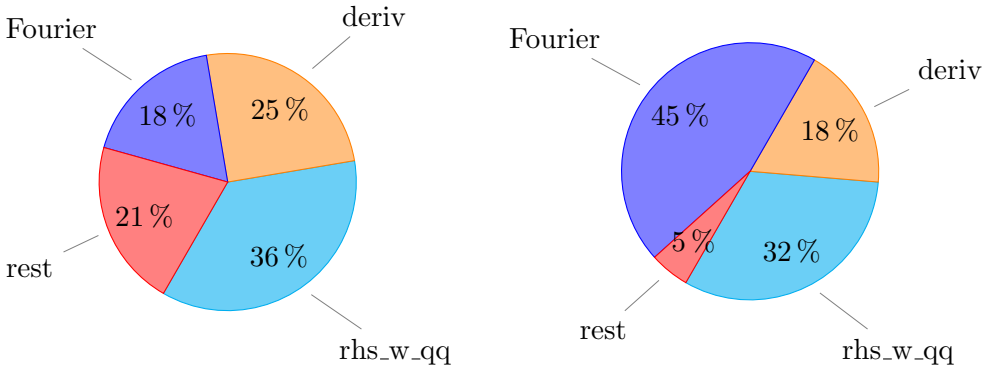

(a) accelerated version (b) CPU version

FIGURE 3.8: Comparions of the User routines relative timing between CPU and accelerated version

on the accelerator is entered, the array has to be updated using the statement on line 4 where "device" refers to the accelerator. At the end of the accelerator region the CPU memory is updated at line 31 where "self" refers to the CPU. Then the routine bc_new is called and executed on the CPU.

With respect to HiPSTAR the porting process is accomplished by porting the **RHS**, i.e. the routine "rhs_w_qq" and all routines called therein. Then the memory regions are defined and the all arrays required both for accelerated routines and the CPU routines are copied to the accelerator before every call to "rhs_w_qq" and copied to the CPU directly afterwards. In total there are five data transfers to the accelerator and five to the CPU for every time step. This was the state the OpenACC accelerated version obtained from CRAY and in the following the performance of this intermediate code version is summarized as a reference.

Comparing the CPU and the accelerated version a speed-up of 1.18x on Titan was achieved for the sample case (i.e. the accelerated version was 1.18 times faster than the CPU version). In order to understand the limitations that prevented better performance, profiles are compared. The profile reveals immediately that about 30% of the total time is spent in data transfer between CPU and accelerator. In order to understand the potential of further improvement, relative timings of User routines on CPU and accelerated version are compared in figure 3.8. Note that these profiles have been created on TITAN using CrayPAT and the routines called in "rhs_w_qq" are collected explicitly in contrast to figure 3.7, because it is of interest to understand how particular routines have profited from the porting and which routines cause problems. All routines that have not been ported are collected in "rest".

It is apparent that the runtime of the code remaining on the CPU has increased considerably from 5% to 21%. On the one hand since a speed-up has been achieved for the accelerated code the relative fraction of time spent increased for the code left on the CPU as it has not seen any speed-up. The far more important contribution, though,

results from a slowdown of the CPU code. As mentioned above the comparison of the CPU and GPU version is performed placing one MPI rank onto every node. For the CPU version OpenMP parallelization is used within each node but not for the GPU version. Hence, using the GPU version the code sections remaining on the CPU loses the OpenMP parallelization meaning that one core has to do the same work as opposed to 16 for the OpenMP version. This results in a significant slowdown and is of particular importance for the filtering routines which have an intermediate computational cost. Using the CPU version with OpenMP, they require about 1.3% of the total runtime but for the accelerated version their contribution to the total runtime increases to about 12%. In addition it can be seen that the Fourier routines show the biggest improvement and the derivative routines and "rhs_w_qq" experience a relative slowdown.

This code version was the starting point for the performance optimization of the accelerated code performed in this work. In order to achieve an improvement, first all routines in the main loop are ported to limit data transfer to places where it cannot be prevented. In addition this means that the filtering routines were also ported, expecting to result in a speed-up of this routine as well. This requires that an additional 30% of the code have to be ported using the same mechanism discussed in step one. In contrast to porting of the computationally heavy routines here most of the routines work on a limited region of the subdomain. Both boundary conditions as well as halo exchange (as discussed above) access memory only on a limited part of the subdomain and therefore the memory access is not continuous. This is a challenge since memory access is considered as one of the major bottlenecks. Hence, even though these routines do not contain a significant computational effort, particular attentions is paid to these routines and in the following the halo exchange is discussed in detail.

The halo exchange affects only a limited part of the domain as indicated by the blue and yellow areas in figure 3.2, which has to be communicated. In order to limit the amount of data that is communicated and to provide a continuous array for the MPI routine, in HiPSTAR these areas are first packed using the algorithm presented in listing 3.2. In particular this algorithm performs the packing of the blue area in figure 3.2(b) but the packing of the other halo regions as well as the unpacking have similar forms.

Listing 3.2: Packing Loop for halo exchange

```
1  !$acc parallel loop private(l)
2            do n=1,nv
3              do k=1,kpoints
4               do j=1-yhalo,nyp+yhalo
5                 do i=1,xhalo
6                    l = i + (j+yhalo-1)*xhalo
7       &             + (k-1)*(nyp+2*yhalo)*xhalo
8       &             + (n-1)*(kpoints)*(nyp+2*yhalo)*xhalo
9                    ahoxm(l) = a(i,j,k,n)
10                enddo
11              enddo
12            enddo
```

```
13          enddo
```

LISTING 3.2: Packing Loop for halo exchange

In order to work with a simplified testcase this code section has been isolated and is repeatedly called to require a sufficient amount of time such that assessing the performance is possible. This *baseline* version already contains an ACC directive that allows for correct execution of the code but the performance is poor. One of the major problems is that xhalo is generally small (in the case discussed here it is two) and the memory access of the innermost dimension is strided. Further, the compiler does not know about the length of the loop and might take inefficient decisions. In particular this test case required more than 1600 seconds to complete. Various versions using different approaches have been tried and the fastest execution was obtained using the code presented in listing 3.3.

LISTING 3.3: Optimized Packing Loop for halo exchange

```
1  !$acc parallel loop private(l) collapse(2)
2           do n=1,nv
3             do k=1,kpoints
4  !$acc loop vector
5              do j=1-yhalo,nyp+yhalo
6  !dir$ unroll
7                do i=1,xhalo
8                   l = i + (j+yhalo-1)*xhalo
9       &            + (k-1)*(nyp+2*yhalo)*xhalo
10      &            + (n-1)*(kpoints)*(nyp+2*yhalo)*xhalo
11                  ahoxm(l) = a(i,j,k,n)
12               enddo
13             enddo
14           enddo
15         enddo
```

LISTING 3.3: Optimized Packing Loop for halo exchange

Using this optimized version, the test code finished in ≈12.1s and resulted in a speed-up of more than 100x. The most significant improvement was achieved by placing the *vector* directive in the j loop and the collapse statement of the outermost loop, reducing the runtime to ≈14.8s. Fine tuning using the unroll directive for Cray compilers resulted in an additional 2.7s reduction of runtime for this test case. Similar tests have been performed for the other halos as well as the boundary conditions and the fastest approach has been implemented into the latest GPU version of HiPSTAR. Even though these routines take significantly less than 1% (1% is the level below which the profiler does not report timings) of the runtime on the CPU, without applying this tuning the performance of the accelerated version is very poor. For the particular test case the runtime of the GPU version of HiPSTAR increased by 7x and was significantly worse than the CPU version. Using the optimized fine-tuned version though, the accelerated version achieved around 1.3x to 1.4x speed-up with respect to the CPU version on Titan.

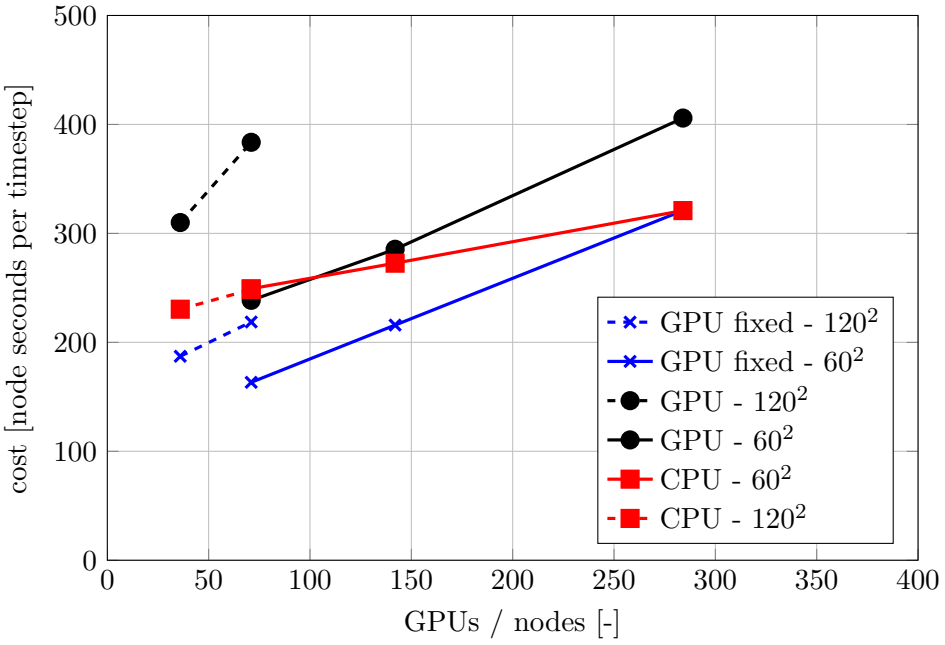

FIGURE 3.9: Cost of simulation using different code versions on Piz Daint

Another important step to improve performance has been to set the number of points in each direction of the subdomain (i.e. nxp, nyp and nzp) as Fortran parameters in the code (i.e. fixing the number of points at compilation time). It seems as if this allows for additional compiler optimization. On the other hand this decreases the flexibility of the code significantly since it requires recompiling if the domain size changes. In figure 3.9 the performance of the code on Piz Daint using the CPU version is compared with the accelerated version with fixed parameters for nxp, nyp and nzp (GPU fixed) and the accelerated version with variable nxp, nyp and nzp. The cost in terms of node seconds per timestep is plotted versus the number of GPUs used. Strong scaling is shown for the testcase summarized in table 3.4, where two different MPI domain decompositions are considered. Using the processor counts given in table 3.4, 284 subdomains (MPI ranks) are obtained, each with nxp as well as nyp being 60. This parallelization is referred to as 60^2. Using half the number of processors in each direction this results in 71 MPI subdomains (MPI ranks) and nxp as well as nyp for each processors is 120. Therefore it is named parallelization 120^2. For both cases the spanwise number of points in each subdomain is 194.

The CPU version is denoted by the red lines in figure 3.9. For the CPU the scaling plots are similar to the plots presented in section 3.2. On the horizontal axis the number of GPUs or nodes are plotted where each node contains one eight core CPU. In order to use all cores the number of OpenMP threads for each case is chosen to fill the nodes using the process explained in section 3.2. Since this is a strong scaling test, the case with the lowest cost is the most efficient one and linear scaling would result in a horizontal line. Similar to section 3.2 using a higher parallelization (i.e. node count) the cost increases

slightly. The case on 71 nodes can be conducted either using parallelization 60^2 with two OpenMP threads or parallelization 120^2 with eight OpenMP threads and both result in almost the same cost, which is different to the scaling in section 3.2 and is most likely due to the different hardware.

On Piz Daint the same version that resulted in a speed-up of around 1.3x on Titan is slower than the CPU version for all cases but the parallelization 60^2 on 71 GPUs. This difference between Titan and Piz Daint can be explained considering that both have the same Nvidia K20x GPUs but the CPUs on Piz Daint are more powerful. Using 71 GPUs the testcase can be executed either using parallelization 120^2 with 1 MPI subdomain per GPU or using parallelization 60^2 with 4 MPI subdomains per GPU. It is apparent that the latter is to prefer which is different to the CPU version where these two parallelizations show almost the same performance.

The blue lines indicate the GPU version with Fortran parameters set for *nxp*, *nyp* and *nzp*. While this requires recompiling to run the two different parallelizations (in contrast to both the CPU and the GPU version with variable *nxp*, *nyp* and *nzp*), it results in a significant speed-up with respect to the GPU version with variable *nxp*, *nyp* and *nzp*. The trend for both GPU versions in terms of scaling across nodes are similar and the speed-up in the best case is $\approx 1.5x$ with respect to CPU.

The porting to accelerators showed that for particular cases a significant speed up can be obtained. In order to see this speed up the code has to be recompiled every time the domain decomposition is changed. This is not a serious restriction though since for most cases the MPI subdomain size is kept at the optimum anyway.

Chapter 4

Resolution requirements of the fine scales and influence of boundary conditions

Before the results of the simulations can be used for an in-depth investigation it is important to test that a realistic flow is simulated. Since in this work turbulence details are investigated that have not been reported for LPTs in previous works, the validation is carried out in a more detailed way compared to other studies with a particular focus on turbulence parameters. Previous works investigating the flow through LPTs have shown that the mean flow solutions could be represented by their methods once a sufficient resolution was chosen. Given that the small scale flow details contain an amount of energy that might be orders of magnitudes smaller than the large flow scales, their contribution to the mean flow might be small. On the other hand the small scales are the important scales for some higher order statistical moments like the time mean of dissipation (Pope, 2000). To the authors knowledge neither of the previous works for real geometry LPT flows reported turbulence parameters depending on the small scales. Therefore the resolution requirements provided by these studies might not be sufficient for a reliable prediction of dissipation related quantities.

The mathematical description of the problem is comprised of the governing equations as stated in section 1.2.1. To obtain a solution the numerical methods with boundary conditions given in chapter 2 are applied. The governing equations as used in this work are widely considered to correctly represent the behaviour of flows present in LPTs. The underlying theory is therefore used in this work as well and no validation of the governing equations is conducted. In order to solve the equations numerically they are discretized and solved on a grid. The discretization algorithms used in this work have been used and validated for DNS of other types of flows in several works (Sandberg *et al.*, 2010, 2012; Sandberg & Jones, 2011) and, again, are not validated in this work.

In order to fully validate the method for LPT flows, the adequateness of boundary conditions, domain extent and the grid quality are presented. For a thorough validation experimental results are required which are available for one reference case and are used to validate the simulation against a "real-world" setup. However, the available data include only first order statistical quantities, namely the pressure distribution and total pressure loss. Assuming a turbulence cascading process where larger scales break down into smaller scales and the smallest scales only contain little energy (Pope, 2000), it is conceivable that a sufficient resolution of the smallest scales is not required to give correct first order statistics. Such considerations are the basis of implicit LES that have been shown to give good agreement with experiments (e.g. Hickel *et al.* (2006)). Hence, while an experimental validation using the available data is presented it does not suffice to assess the correct representation of the small scales. Therefore, it is only possible to show the grid independence of the solution using a grid convergence study which along with the general acceptance of the validity of the set of governing equations serves as a strong argument for the correctness of the solution.

As briefly discussed in chapter 1 for an accurate numerical approximation the combination of grid and numerical scheme has to be sufficient in order to resolve all relevant flow scales. The numerical scheme in this work is fixed such that only the grid has to be investigated. This is influenced by a few factors. First, since a metric transformation is used to map the physical problem onto a computational space it is required that these metrics terms are continuous in space except for at the block interfaces where a special treatment is applied (see chapter 2), a condition which is fulfilled by all grids used in this work.

Another factor that impacts the solution accuracy is orthogonality. Perfect orthogonality cannot be achieved in the full domain due to the non-orthogonal blade shape. The meshing strategy used in this work ensures perfect mesh orthogonality at the blade only which is deemed most important. Cases for which results in the wake are published (D1 to D3 defined in table 4.2) in addition also require a high mesh quality in the wake region which is achieved by placing cells with higher skewness outside of the wake region. Inside the wake region the maximum deviation from orthogonality is lower than 15 degrees where the maximum skewness in the full domain is around 25 degrees. This is illustrated in figure 4.1 where as an example the mesh non-orthogonality for a simulation of the case at $Re_{is} = 60,000$ on mesh D1 (for more details see table 4.2) is presented. The blue lines are streamlines illustrating the flow path. The flow enters the domain from the left and the streamlines turn around the blade until they exit at the lower bound of the figure. The two middle streamlines enclose the wake region. This can be seen by the regions of elevated turbulence kinetic energy depicted by the color filling in the figure. The green lines enclose regions where the angle between grid lines deviate by more than 15 degrees from orthogonality. It can be seen that only two small regions

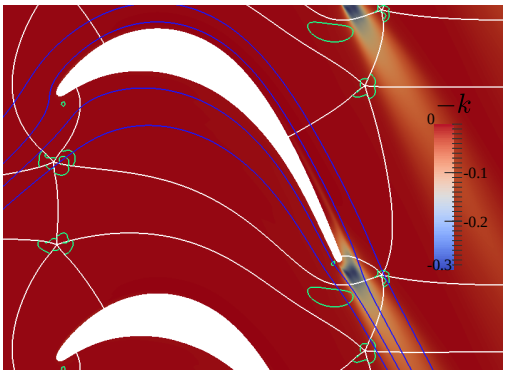

FIGURE 4.1: D1 grid quality: filled contour of turbulent kinetic energy; green contour lines enclose areas with a grid angle of larger than 15 degrees; blue lines represent streamlines.

show angle deviations of more than 15 degrees inside of the two innermost streamlines and neither of these regions is inside the wake.

4.1 Statistical convergence

Direct numerical simulations provide the time resolved three-dimensional flow field. For engineering applications though often performance parameters are investigated where the information of the simulations is post-processed. Particularly time averaged solutions are often considered and time spectra are investigated. In order to obtain a time averaged solution a constant mean value has to be approached ensuring that the simulation data is averaged over a sufficiently long time. With respect to time evolving simulations the averaging span is tried to be kept at a minimum owing to the linear increase in computational cost with run time. The averaging time span is mostly dominated by the lowest frequencies with substantial energy. In order to understand the extent of the required averaging time span the simulations are executed and the solutions averaged over various intervals are compared. Once two subsequent intervals of sufficient time show the same mean results the solution is considered time converged and referred to as statistically converged.

In this work the DNSs are initialized with the respective precursor 2d "DNS" which in general is not a solution of the three dimensional DNS, leading to a transient phase at the start. During this transient phase there is no time mean available and if the time averaging procedure is applied to this data the obtained results vary for different intervals. Hence, before starting to collect statistics first the end of the transient phase has to be reached which is assessed in two ways. The boundary conditions in these simulations are such that at the inlet the three momentum components and density are prescribed (compare from section 2.2). Hence, the inlet total energy is the only free component and if there is drift of a mean value a transient phase is still seen. In figure 4.2 time evolution of the total energy at the inlet for one point in the flow field is presented.

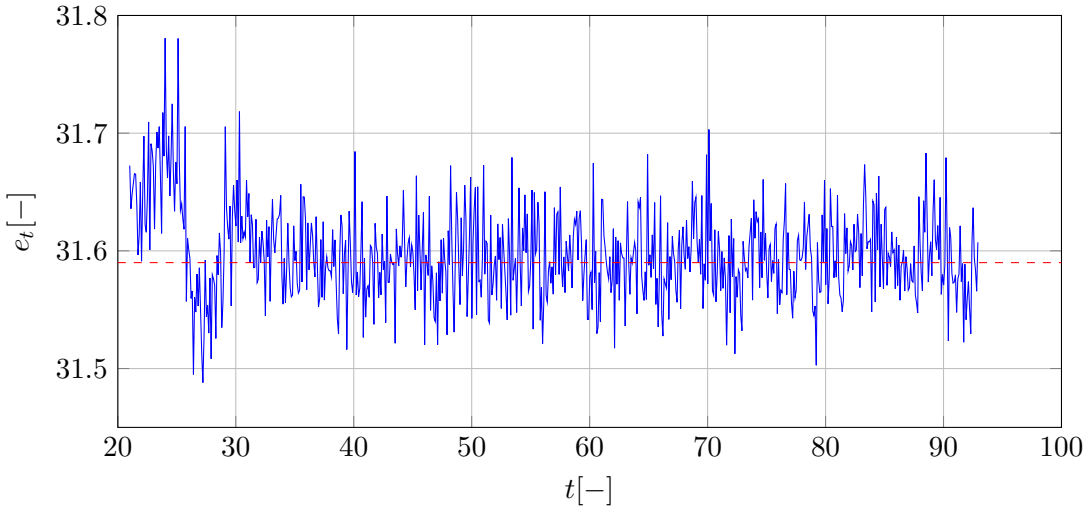

FIGURE 4.2: Time series of total energy (blue line) in the inlet region of the cascade at $(-0.3, 0.0)$ plotted over its mean value (read dashed line).

Since the transient characteristic of the flow is overlayed with turbulent fluctuations it is not clear where the actual end of the transient is. On the other hand it can be clearly seen that the changes in the time span between 20 and about 30 are of different nature compared to the changes after that point. In order to understand what data to use mean values are computed from different time intervals and compared. The transient phase is passed if two different intervals result in the same mean value. This is show in figure 4.3 and 4.4 where pitchwise profiles at a streamwise position of $x = 0.9$ are plotted. Three intervals of the same time evolving simulation are chosen and the mean values are compared with each other. A position close to the trailing edge is used since there spanwise coherent vortex shedding from the trailing edge interacts with vortex shedding from the separation bubble leading to the lowest frequency with significant energy. The first interval is chosen such that it extends past the transient phase between 23 and 39. The second interval extends from 40 to 53 and the third interval from 59 to 93. There are almost no differences between the three intervals in terms of Favre averaged mean flow velocity profiles as can be seen in figure 4.3. Looking at figure 4.4 it can be seen, though, that there are differences in all quantities between the first interval and the two almost equivalent other intervals. Hence, it can be concluded that the second and third interval are statistically converged whereas the first interval also contains part of the transient phase.

Given that for DNS simulations cost is of paramount importance it is crucial to keep the simulation time short and therefore the minimum required time for transient and for the collection of meaningful statistics is of interest. Conclusions generalized for different cases are difficult to obtain since the transient phase is affected by the initial condition. Further, the extent of the interval required for statistical convergence is dominated by low frequency phenomena containing significant energy. For this particular case the most important low frequency phenomenon are the vortex shedding in counterplay with

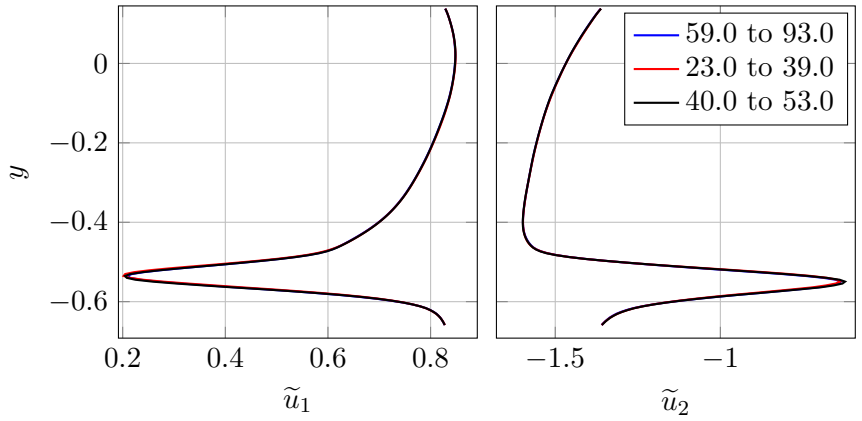

FIGURE 4.3: Statistical convergence test for the Favre averaged velocity components for a pitchwise profile at $x = 0.9$.

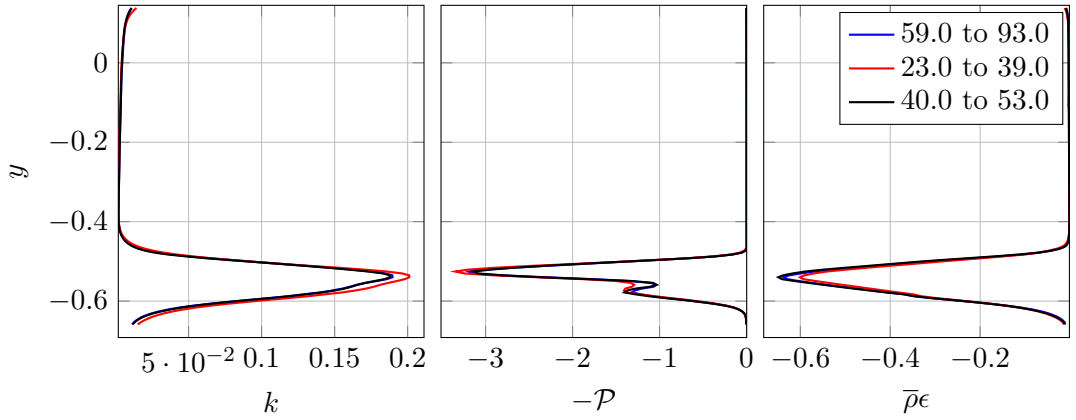

FIGURE 4.4: Statistical convergence test for TKE, production of TKE and dissipation of TKE for a pitchwise profile at $x = 0.9$.

the separation bubble. This process is severely influenced by both Reynolds number and background turbulence. On the other hand for the grid convergence study where the same flow conditions are used for several cases a guideline can be determined and 13 time units are used to collect statistics. For all other cases used in this work statistical convergence has been investigated in the same way as described above and only statistically converged results are presented. Even though not shown in plots it has been found that for shorter time spans statistical convergence was not achieved.

4.2 Grid convergence using conventional metrics

In this section the grid convergence study conducted is presented for both the $Re_{is} = 60,000$ and $Re_{is} = 100,000$ cases using pressure distribution around the blade, the wake loss and nondimensional wall units as usually performed for LPT DNS works. For both Reynolds numbers the same grid is used for cases with and without background turbulence. The grid convergence study is performed for the turbulent case at $Re =$

	G_1		G_2		G_3	
Block	n_ξ	n_η	n_ξ	n_η	n_ξ	n_η
1	288	192	336	288	576	384
2	288	48	336	96	576	96
3	144	192	216	288	288	384
4	144	240	216	360	288	480
5	144	240	216	360	288	480
6	48	240	96	360	96	480
7	144	192	216	288	288	480
8	288	192	360	288	576	480
9	288	48	360	96	576	96
Σ	274,176		581,760		1,179,648	
n_z	66		130		194	
Δd_{wall}	2.8×10^{-4}		1.5×10^{-4}		0.8×10^{-4}	
Σ_{3d}	18×10^6		72×10^6		200×10^6	

TABLE 4.1: Number of points for the 3 grids used for the grid refinement study at the blade

60,000 since resolving the background turbulence is expected to be the more challenging and also more realistic case bearing in mind that real engine configurations almost always experience background turbulence. At $Re = 100,000$ the clean simulation is considered in the grid convergence study. A subset of the results presented here has been published in Sandberg *et al.* (2015).

The general block setup is presented in figure 2.3. In this work two sets of grids have been used. Grids G1 to G3 are used to investigate the influence of the resolution on the flow around the blade. The points used for each block are summarized in table 4.1. In this table the number of grid points in each Block, the total number of points in the ξ-η plane Σ, the number of points in the spanwise direction n_z, the height of the wall next cell in normal direction Δd_{wall} and the total number of points for three-dimensional simulations are given. It can be seen that the spacing in the wall normal direction, Δd_{wall}, is roughly halved for each refinement level and the number of points in the spanwise direction is doubled from G_1 to G_2 and increased by another 50% from G_2 to G_3. The number of points around the blade is the sum of n_η for blocks 3, 4, 5 and 7 and results in 864, 1296 and 1824 for grids G_1 , G_2 and G_3, respectively. This results in an increase of points around the blade of about 50% for each refinement where the refinement is clustered in the adverse pressure gradient region on the suction side and close to the trailing edge on the pressure side where transition might occur.

As discussed in chapter 1 the target of this study is to conduct simulations of the T106A profile at two different Reynolds numbers that can be used to support the turbulence model development. For DNS simulations the grid used has to resolve the smallest scales while the domain is still large enough to allow for a correct representation of the flow. A grid convergence study is presented for the two Reynolds numbers considered separately.

4.2.1 Case at $Re_{is} = 60,000$

For the case at $Re = 60,000$ the baseline grid used is G_1 and the refined grid is G_2. In figure 4.5 the wall next cell size in nondimensional wall coordinates is presented. Wall

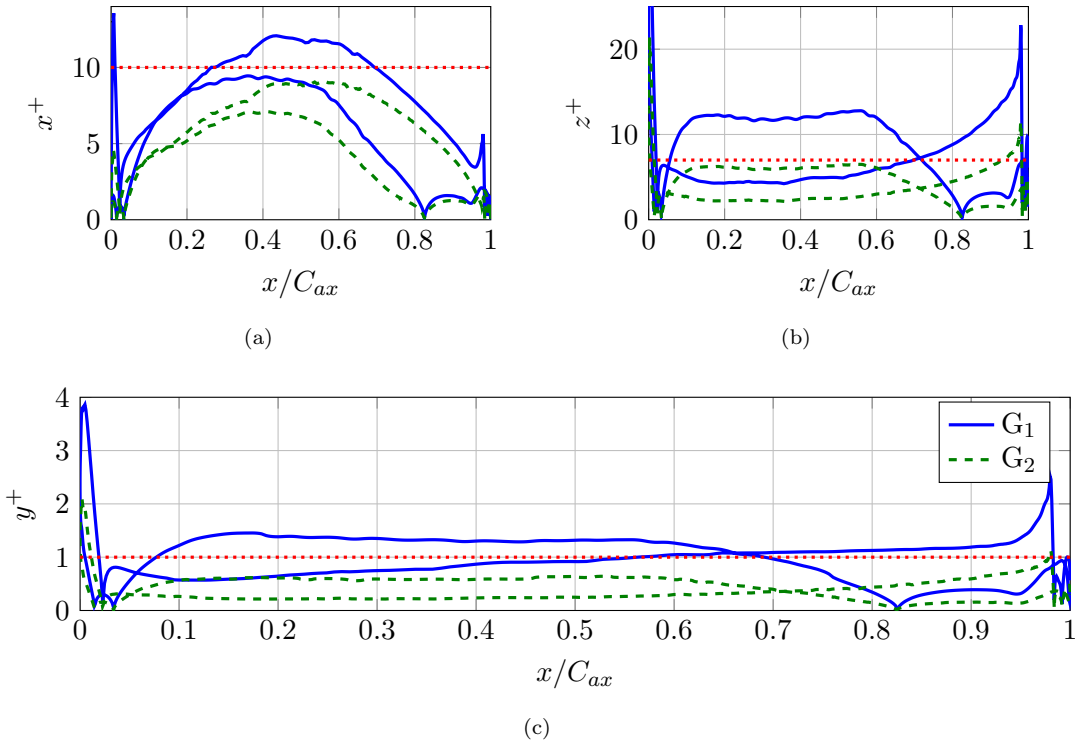

FIGURE 4.5: Wall next cell size in wall coordinates at $Re = 60k$; (a): tangential direction, (b): spanwise direction and (c): wall normal direction where the red-dotted line indicates the guideline value

coordinates are used to quantify the resolution of the wall. Considering the high wave number resolution of the compact schemes used in this work, guideline values for the three coordinates are $x^+ < 10$, $y^+ < 1$ and $z^+ < 7$ for turbulent boundary layers which are met by grid G_2 for most of the blade. Only in the vicinity of the leading and trailing edge the values are exceeded. Considering that in the $Re = 60k$ case the boundary layers are mostly laminar, grid G_1 was created slightly overrunning the guidelines. Note that the zeros of the nondimensional wall units along the axial chord indicate the positions of separation and reattachment. The leading edge separation bubble can be seen to be between 0.01 and 0.03 while the suction side separation starts at 0.83 and does not show reattachment until the trailing edge. It can be seen that both grids show similar separation zones.

In order to assess if grid convergence is achieved simulation results for both grids are compared in figure 4.6 for two commonly used parameters that are widely used to assess the accuracy of numerical simulations. The pressure distributions are virtually the same. Minor differences can be seen in the wake loss plot and could probably be improved by

continuing the simulation using G_2. This has not been done in light of the significant cost and since the current state of convergence already allows to draw the conclusions of interest in this work. In terms of the quantities assessed in this section grid G_1 is sufficient to resolve the flow.

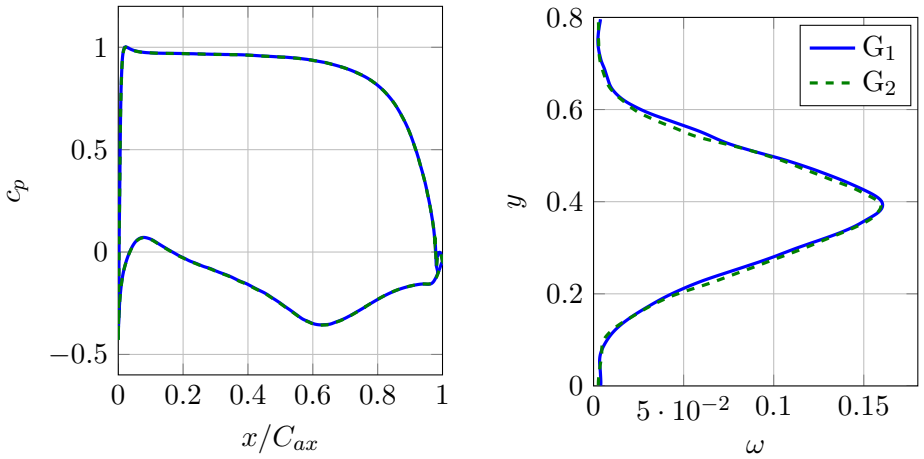

(b)

FIGURE 4.6: Pressure distribution around the blade (a) and wake loss (b) for both grids at $Re = 60k$

4.2.2 Case $Re = 100,000$

The baseline grid in the $Re = 100,000$ case is grid G_2 and the refined grid is G_3. Dimensionless wall coordinate plots for this case are presented in figure 4.7. For the $Re = 100k$ case the wall coordinates also follow the guidelines for most of the blade for the fine grid G_3 and compared to the $Re = 60k$ case the baseline grid is in better accordance with the guidelines particularly for the wall normal and spanwise directions. This increase in resolution accounts for the higher Re and thus possibly "more" transitional boundary layers. The results in terms of static pressure distribution about the blade and wake loss are presented in figure 4.8. The static pressure distributions about the blade are virtually the same and only minor differences can be observed in the wake losses. Also at the higher Reynolds number, the overall agreement is reasonable and discrepancies are expected to be due to an insufficiently long runtime for the finer grid G_3 due to the high cost of these simulations. However, the agreement is sufficient to use grid G_2 for simulations at $Re = 100k$.

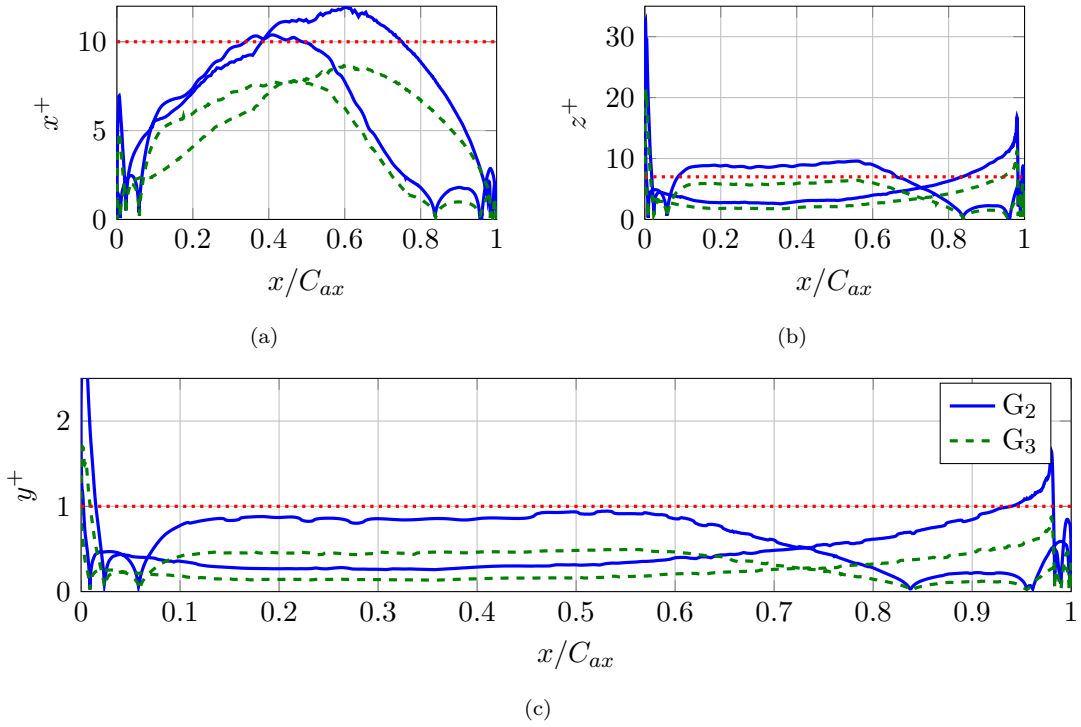

FIGURE 4.7: Wall next cell size in wall coordinates at $Re = 100k$; (a): tangential direction, (b): spanwise direction and (c): wall normal direction where the red-dotted line indicates the guideline value

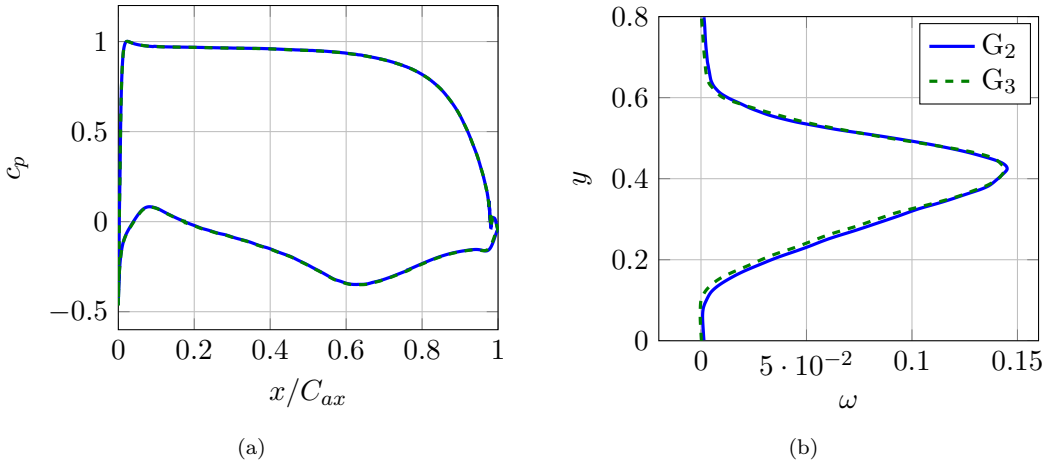

FIGURE 4.8: Pressure distribution around the blade (a) and wake loss (b) for both grids at $Re = 100k$

4.3 Grid convergence using turbulence characteristics in the wake

One of the targets of this study is to extract information useful for turbulence modelling from the simulations. In the previous section wake loss and blade pressure distribution have been used to assess the mean flow field and grid convergence was achieved in both

	D_1		D_2		D_3	
Block	n_ξ	n_η	n_ξ	n_η	n_ξ	n_η
1	240	180	480	360	832	320
2	240	60	480	120	832	512
3	120	180	240	360	256	320
4	120	300	240	600	256	834
5	120	300	240	600	256	834
6	60	300	120	600	512	834
7	120	180	240	360	256	768
8	240	180	480	360	1280	768
9	240	60	480	120	1280	512
Σ	248,400		993,600		3,463,168	
n_z	98		130		194	
Δd_{wall}	3.6×10^{-4}		2.5×10^{-4}		1.8×10^{-4}	
Σ_{3d}	24×10^6		129×10^6		672×10^6	

TABLE 4.2: Number of points for the 3 grids used for the grid refinement study of the turbulence quantities in the wake

cases with the coarsest grid used. For the mean flow the most energetic large scales are the major contributor which might be well resolved on the same grid where small scale phenomena like dissipation might still be under resolved. Hence, the grid convergence of all quantities presented in chapters 5 and 6 have been validated as well and in the following a grid convergence study for TKE, the production of TKE and the dissipation of TKE is presented. While TKE and production of TKE are dominated by large flow scales dissipation is expected to be severely influenced by the small flow scales. Therefore, dissipation of TKE serves as a more stringent measure of grid convergence. High values of turbulence only occur in the wake such that the grid convergence study is presented for the wake region.

First a second set of grids with increased resolution in the wake region is introduced. In table 4.2 the number of points for each block for the different grids used in this study are presented. For the numerical method used the smallest cells that are generally located at the blade surface dictate the time step of the simulation. Therefore, the findings of the grid refinement study around the blade are used reduce to the cost of this second refinement study which is of particular importance since the resolution of the downstream wake area results in substantial increase in cell count. Using the grid counts given in table 4.2 the grid spacing in the wake region for ξ and η direction is approximately 3.3×10^{-3}, 1.6×10^{-3} and 0.7×10^{-3} for grids grids D_1 , D_2 and D_3, respectively.

The results of the convergence study are presented in figure 4.9 at $x = 0.9$ directly downstream of the trailing edge and at $x = 1.1$ further downstream where the wake is already further mixed. Wake mixing and dissipation lead to a widening and decrease in the peak magnitude of TKE as illustrated in figure 4.9 (a) and (b) where the peak intensity has decreased by a factor of 4. The three grids show reasonable agreement

between each other, where at $x = 0.9$ the solution on D1 has slightly lower values and further downstream the magnitude of D3 is lower compared to the other two components. While the discrepancy of D1 might be due to a too coarse resolution the difference in D3 is expected to be due to statistical convergence. Conducting the simulation for longer time would have resulted in higher cost which was not deemed necessary since this is considered a satisfactory grid convergence for the investigations in this work.

In figure 4.9 (c) and (d) the production of TKE is presented where differences in the near trailing edge region mostly stem from the anisotropic contributions of the Reynolds stress. In the far field the D1 shows smaller values in the peak production but, again all three grids show reasonable agreement. Note that while the magnitude of TKE decreased by a factor of five between $x = 0.9$ and $x = 1.1$, the production of TKE reduced by a factor of 100.

Dissipation though shows a different behaviour where grids D2 and D3 show reasonable agreement while the magnitude of D1 is significantly smaller. At the near wake position the peak in dissipation of TKE is only about 60% of the corresponding value on the other grids and in the far wake the peak magnitude is about 30% smaller compared to the finer grids.

While for mean quantities and large scale turbulence quantities D1 give reasonable results, dissipation requires a higher resolution due to the importance of small scale physics. This is of particular interest since the resolution of the studies published in literature is similar to that of D1 or coarser considering that D1 was created to be at least as fine as in studies published in literature which was assessed in terms of the spacing at the wall, the number of points across the pitch, axial direction and along the blade.

Grid convergence in the wake region has not been tested for the case at $Re_{is} = 100,000$ due to the significantly increased costs. This is not considered as a problem since for wake flows the smallest scales are expected to scale with the inverse of Reynolds number. Hence, the required resolution has been extrapolated from the conclusions at $Re_{is} = 60,000$ and grid D3 is used for these simulations.

4.4 Influence of the Boundary Condition on the Simulation

In section 2.2 two types of inlet boundary conditions (BCs), characteristic and fixed inlet with sponge, have been described. Simulations with different BC choices at $Re_{is} = 60,00$ are compared revealing influence of the chosen BCs on the solution. In fact appropriately dealing with the fluctuations present at the inlet turns out to be an important factor of the computational setup.

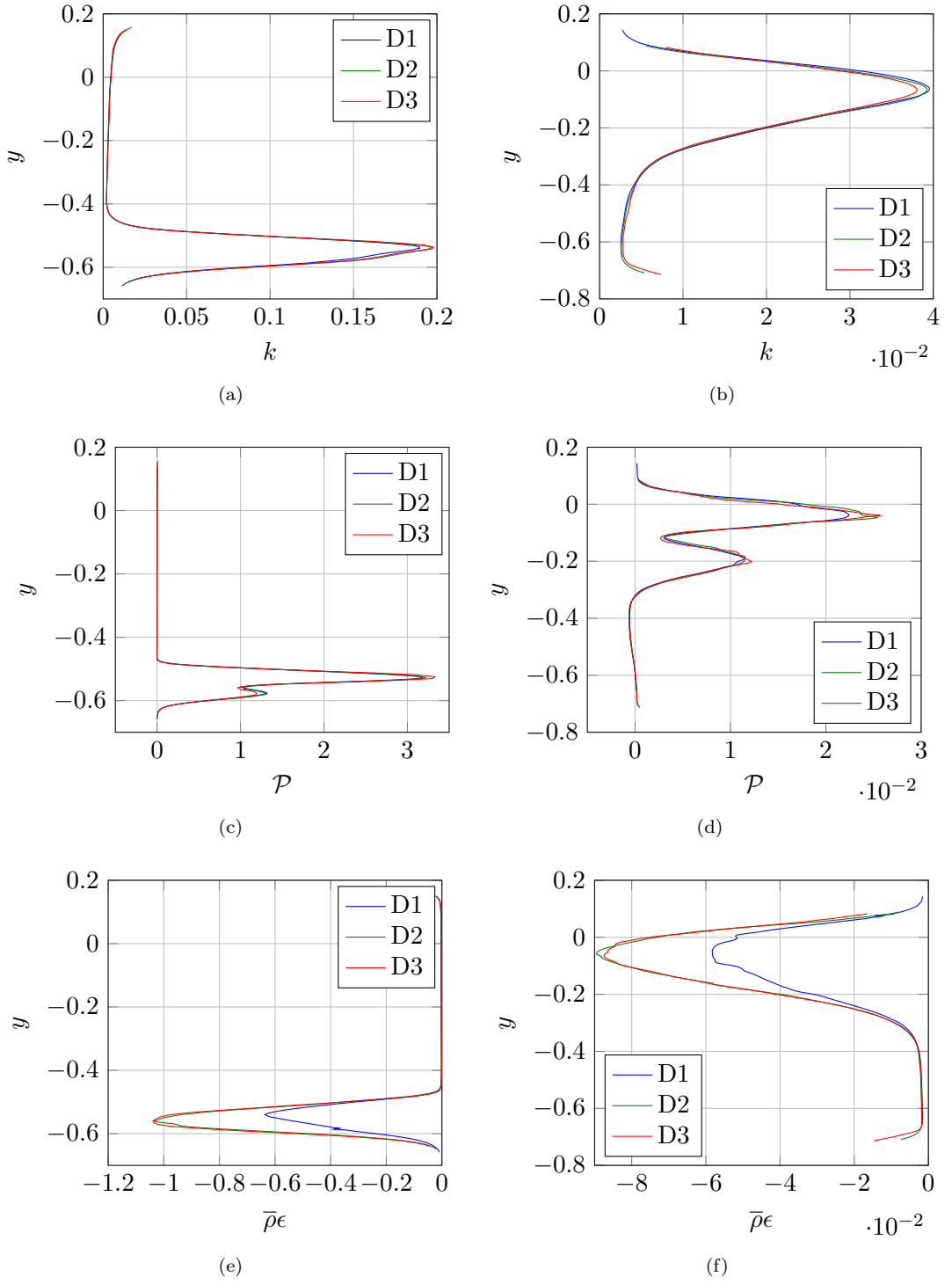

FIGURE 4.9: Grid convergence of TKE, its production and dissipation at $Re_{is} = 60,000$ at location $x = 0.9$ (left column) and $x = 1.1$ (right column).

In the following four cases are compared that are summarized in table 4.3. I1 is based on the characteristic inlet condition and the other three cases use a sponge. The most basic type of boundary conditions are fixed value boundary conditions where the boundary value is kept constant. In case of subsonic compressible simulations it can be shown

Case	Inlet BC	TI at inlet	TI at meas. pos.
I1	CBC with Lele corr.	none	? %
I2	fixed with sponge	none	0.28%
I3	fixed with sponge	1%	0.58%
I4	fixed with sponge	4%	1.8%

TABLE 4.3: Cases used to compare different inlets

that four variables are transported in the direction of the flow and one in the opposite direction (compare from section 2.2). Hence, considering the inlet one wave arrives at the inlet and if a fixed value is set a difference occurs leading to a reflection. The reflection might occur in all four flow variables transported into the domain. Hence, vortical reflections as well as dilatational reflections might be present. Since for fixed inlets the reflections can alter the flow behaviour they are not used in compressible DNS studies in general. Different approaches have been developed and tested and here CBCs and fixed inlet with sponges (see section 2.2) are used and compared. To understand the differences of the different inlet BCs on acoustic reflections, dilatation contours in the inlet region are compared in figure 4.10. Vortical reflections are presented in figure 4.11 and finally, to get a quantitative measure, time spectra are presented in figure 4.12.

First simulations with a CBC with a correction (Poinsot & Lele, 1992) at the inlet have been conducted. If the correction factor σ_{in} was set to the value suggested in the literature (0.25), a mean value drift occurred that could not be accepted. Therefore the two larger values 1 and 4 were used. Using $\sigma_{in} = 1$ acoustic waves appeared upstream of the blade as presented in figure 4.10 (a). Waves generated by the vortex shedding at the trailing edge approach the inlet and there they are in general inclined with respect to the inlet. The characteristic boundary approach is developed using one-dimensional considerations and hence expects waves approaching to be parallel to the inlet boundary. If a strongly inclined wave reaches the boundary as shown close to A1 it might cause a reflection and if this reflection is such that it results in a wave normal to the inlet it remains in the domain since in the pitchwise direction periodic boundaries are used. Every time such a wave hits the leading edge it wraps around it and a strong reflection is generated as indicated at point A2. This reflection interacts with the blade and might alter the flow solution. In order to suppress these undesired waves a higher value for σ_{in} of 4 was used which diminishes the waves but in this case vortical reflections are introduced (this case is not shown here).

Since with different levels of σ_{in} for CBCs no satisfactory solution could be obtained, an entirely different approach was tested where the boundary condition value was fixed but, in order to attenuate approaching waves, a sponge layer was introduced. Using this sponge layer no apparent acoustic or vortical structures have been introduced which can be seen by looking at figure 4.10 (b). The sponge layer though is clearly visible and close to its end a high dilatation region exists and even though in this snapshot its values are negative the sign changes with time. Importantly, this high dilatation region is confined

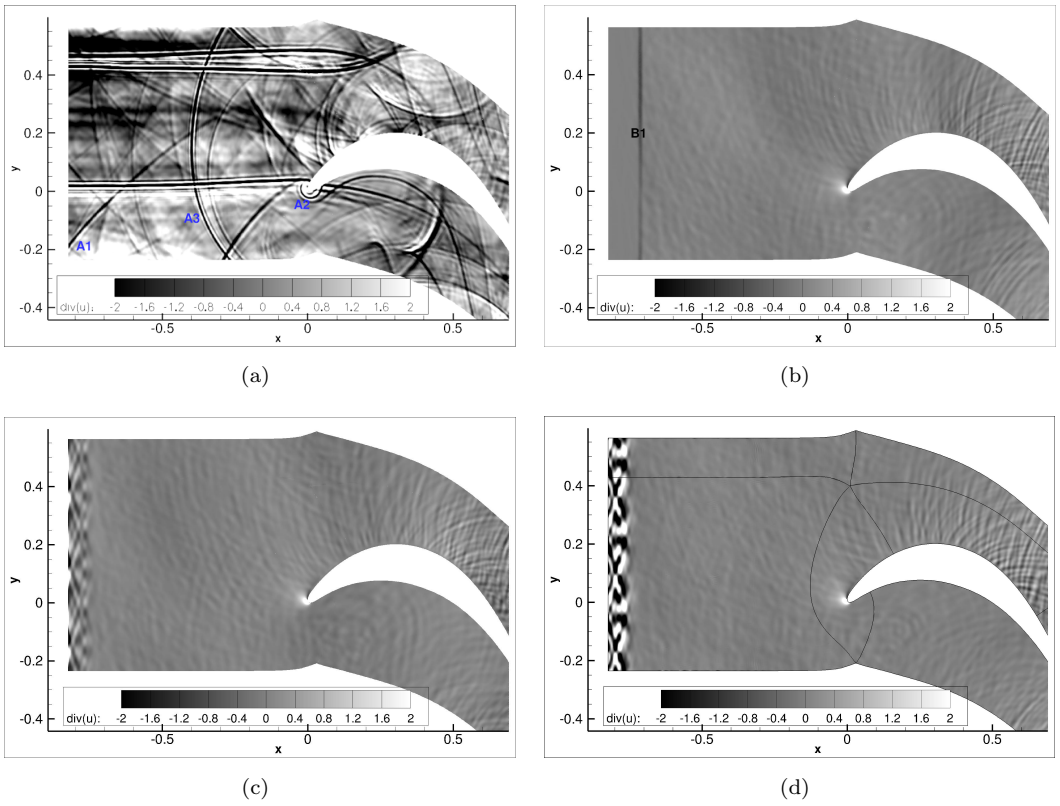

(a) (b)

(c) (d)

FIGURE 4.10: Dilatation in the inlet region for cases I1 (a), I2 (b), I3 (c) and I4 (d)

to the sponge and the waves still apparent closer to the blade are a result from the vortex shedding at the trailing edge and thus physical. Their magnitude is significantly smaller than in the case of using the CBC as discussed above. For cases I3 and I4 background turbulence is injected. Looking at their dilatation fields presented in 4.10 (c) and (d) only in the sponge region differences to the case with sponge and no additional turbulence presented in figure 4.10 (b) are apparent. Hence, the structures introduced are mostly vortical and leave the acoustic field almost unaltered. The differences in the sponge are expected since the background turbulence specified at the inlet is not divergence free. However, a small distance downstream of the sponge no apparent differences are observed such that this is not expected to be problem.

In figure 4.11 spanwise vorticity plots are presented for the four cases. Both the CBC using $\sigma_{in} = 1$ and the sponge case without background turbulence do not show vortical structures. In contrast the cases with background turbulence levels of 0.58% and 1.9% at the inlet measurement plane at $x = -0.3$ (cases I3 and I4, respectively) do show vortical structures. Particularly considering case I3 having almost the same inlet turbulence level as the experiment this shows that the clean cases I1 and I2 do not introduce vortical reflections of the smallest order considered. In fact in general the turbulence intensity in LPTs is of the order 4% (Halstead *et al.*, 1997*a*) and higher, so that both inlet conditions are satisfactory in terms of the vortical reflections introduced.

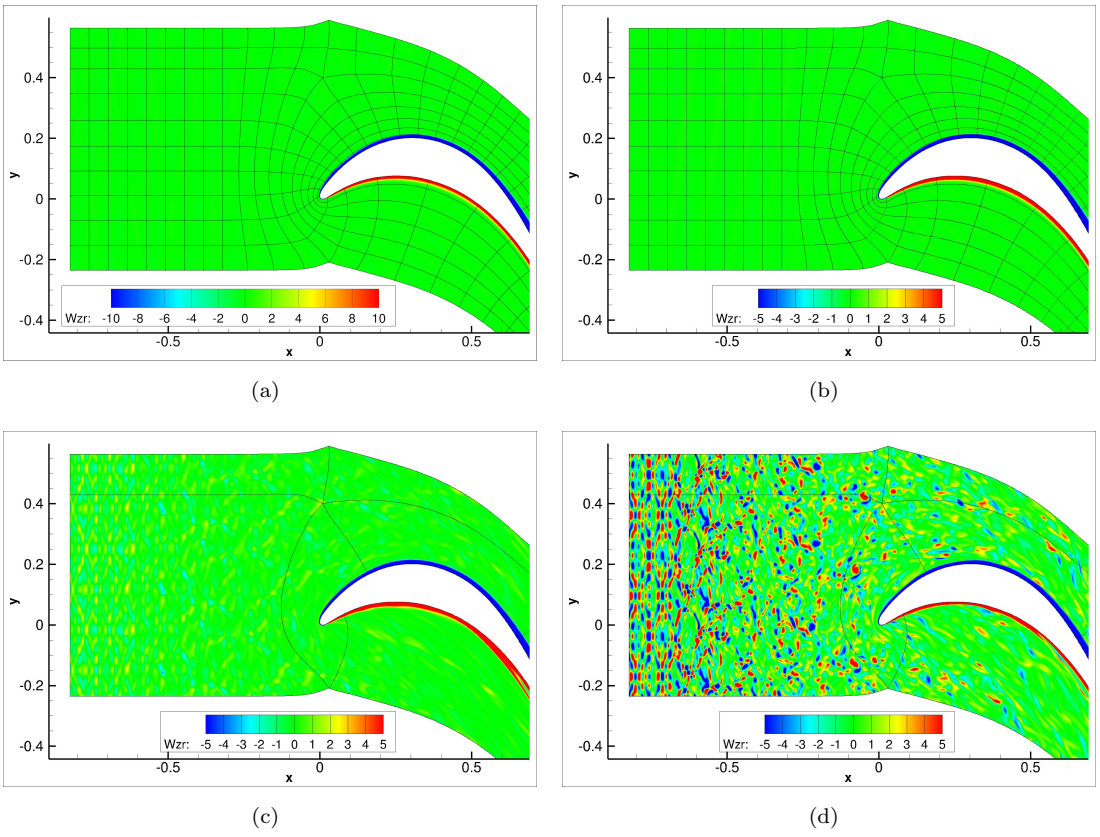

FIGURE 4.11: Spanwise vorticity in the inlet region for cases I1 (a), I3(b), I4 (c) and I5 (d)

In order to get a more quantitative understanding of the different inlet methods, time spectra of the kinetic energy of the velocity components are presented in figure 4.12 at a location of x=-.3 and y=0.0. For case I1 no monitor point was available but since this case displayed severe reflections the CBC at the inlet will not be used further in this study (more details later). Case I2 peaks at a Strouhal number of about 5.1 and at integer multiples in the streamwise and pitchwise velocity spectra. These frequencies can be related to the vortex shedding at the trailing edge. This is emphasized by the fact that the energy in the spanwise component at a Strouhal number of 5.1 is small indicating that the phenomenon is spanwise coherent, like the vortex shedding is in this case. If a low level of background turbulence is present as in case I3 the gaps between these peaks start to fill but it takes turbulence levels in excess of 1% to clearly cover the peaks caused by the acoustic waves. However, in this case a peak at the vortex shedding frequency is still apparent in the pitchwise velocity even though it is less clear than in the other cases. Hence, the flow is forced with turbulence like energy levels across all frequency. This discussion only focuses on energy content at certain frequencies and it might be that certain flow phenomena are more sensitive to acoustic signals. Hence, to be sure even higher levels might be required to overlay the acoustics which is important because in experiments only the turbulence intensities are reported in general and it is not clear to which extent these are related to acoustic or vortical phenomena.

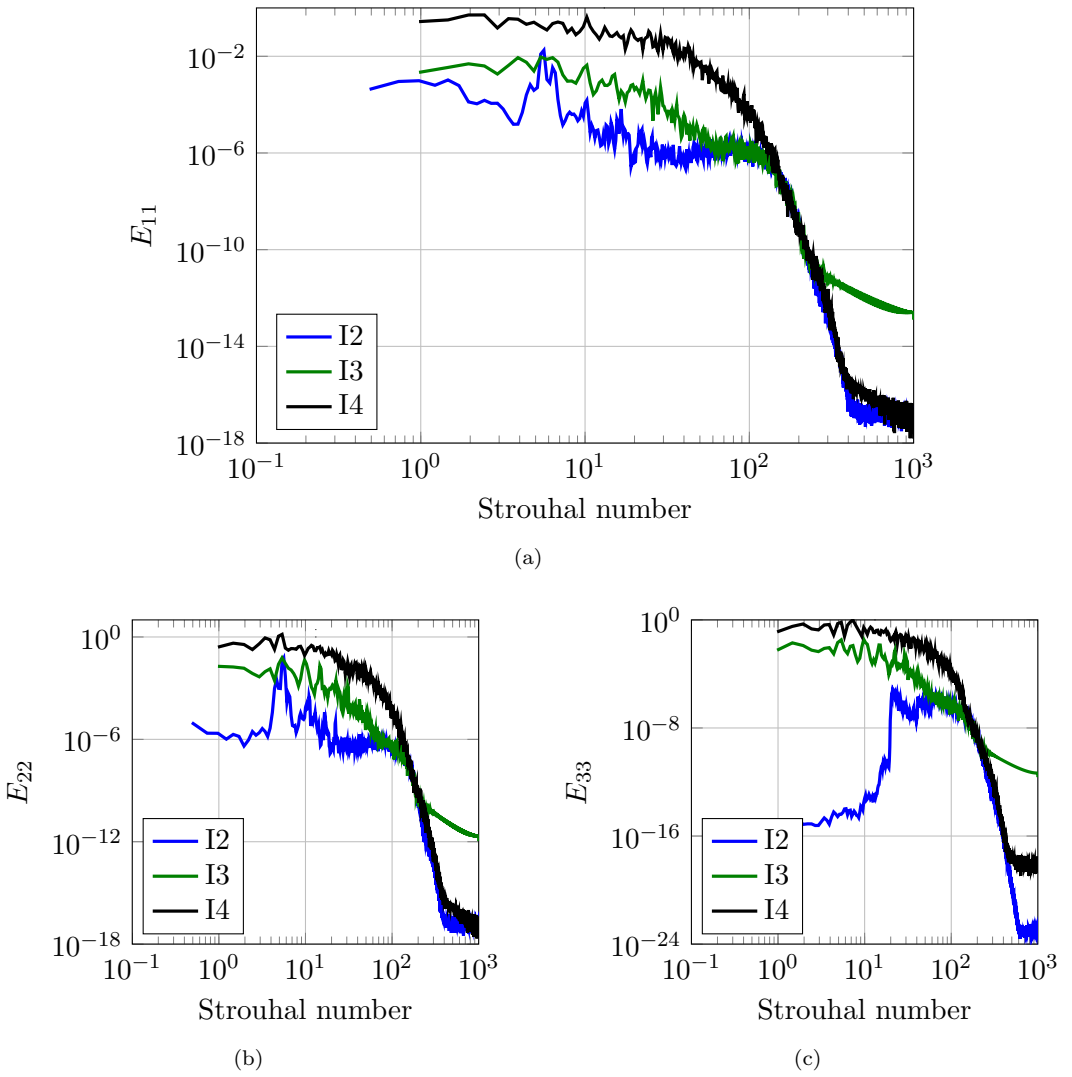

FIGURE 4.12: Time spectra of monitor point in the inlet regions for different cases of streamwise (a), pitchwise (b) and spanwise (c) velocity components at x=-.3 and y=0.0

In order to quantify the accuracy of wake losses and static pressure distribution simulations I1-I4 are compared to experimentally measured ones. The results are plotted in figure 4.13 and for the c_p distribution no significant differences between the various cases are observed. Only on the suction side close to the trailing edge minor changes are apparent if a close up of the trailing edge region is considered. This is not true for the wake losses where severe differences are apparent. From the experiment the absolute pitchwise position of the measurement was not clear such that the peak position of the experiment was adjusted to fit case I2. Hence, no conclusions on the absolute position can be made and only the shape of the wakes can be compared. The absolute position of the peak depends on the turning of the blade and thus on the outlet angle which for experiments and simulations agrees up to the accuracy provided in the experiment and is 63.2 degrees. Focussing on case I1 using a CBC at the inlet the wake is less deep and the peak is rounder compared to the experiment. This is generally a sign of higher dissipation which might be due to a more three dimensional wake. Higher fluctuation

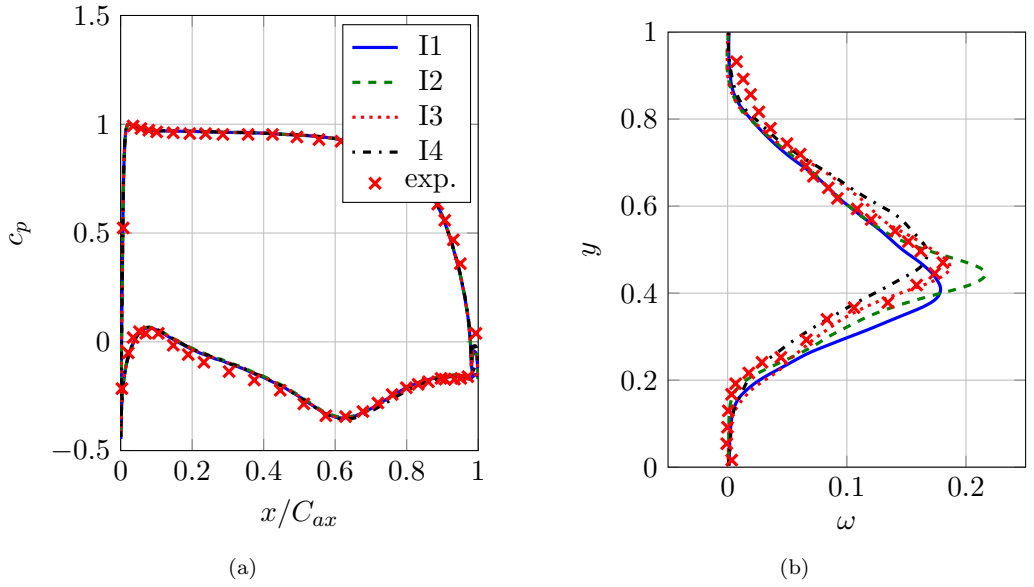

FIGURE 4.13: Static pressure coefficient around the blade (a) and Wake losses (b) for the cases I1 -I4

levels due to the reflections as discussed before are present from the inlet and seem to cause faster breakdown of the wake due to their interaction with the trailing edge flow separation and the wake. However, the discrepancy is only small. Case I2 shows the result for a case using a sponge and no background turbulence for which the velocity fluctuations at the inlet are smallest. However, this case also does not agree well with experiments. Comparing the fluctuation level at the inlet of the "clean" experiment to the "clean" simulation it is found that the amplitude in the experiment is higher. Therefore, case I3, a simulation with background turbulence resulting in about the same turbulence level at the inlet as the experiment was conducted and this simulation shows good agreement with the experiment.

Considering the results presented in this section the CBCs at the inlet used in this work are not used due to the unclear influence on the wake. Since the waves are impinging at a non-zero angle with respect to the inlet the one-dimensional theory used in deriving the CBC seems to fail. Using a method where the pitchwise variation along the inlet would be considered might solve the problem with the reflection but was not tested since simulations with fixed inlet and sponge provided good agreement with experiments if the correct level of velocity fluctuations were used. This is not straight forward, though, because the ratio of acoustic waves to the total fluctuation level in the experiments is not clear. Unless both acoustic and vortical fluctuations result in the same transition behaviour this is a source of uncertainty. Therefore, it is suggested to compare simulations and experiments for cases using a significant level of background turbulence. This has two important advantages: firstly at higher turbulence level most of the fluctuations are of vortical nature and thus the uncertainty in the "natural" fluctuations in the wind

tunnel is less important. Secondly, considering that the difference in turbulence level between I2 and I3 is 0.4% and between I3 and I4 it is 1.2% but the changes in the wake loss shape are smaller between the latter two cases any difference in fluctuation level is not so crucial. This does not allow for the investigation of the influence of small turbulence level without further investigations but since in a real engine the turbulence intensity is at higher levels anyway this should not be a limitation. If RANS are to be tested against DNS the same level of perturbations can be prescribed since this information can be extracted from DNS data. With respect to future experiment it is also suggested to record a detailed description of the fluctuation in terms of turbulence length scales and energy-frequency spectra. This allows for a more sophisticated evaluation of the accuracy of DNS and RANS studies.

A similar study has been performed for the oulet and it was concluded that zonal CBCs gave the best attenuation of reflections and thus are used in this work. The fluctuation approaching the trailing edge and wake region in general are small.

Chapter 5

Statistical Presentation of the Flow Fields

In this chapter the flow is investigated using established statistical methods. The idea is to present these results such that they can be used by a turbulence modeller or a user of such turbulence models to evaluate the performance of a particular model with respect to a dataset representative of an LPT flow at mid-span. Comparing the model term by term with the DNS data allows to understand which particular part of the model fails and where it has to be improved. Additionally the terms in the budgets of the transport equation of total energy and TKE represent the different mechanisms of energy transfer in the flow and are used to rate their importance.

The difference of this chapter to most LPT DNS publications in the past is in the reporting of detailed TKE budgets as given by equation (1.35). As discussed in chapter one, budgets have been reported for various canonical flows like in Mansour *et al.* (1988); Speziale *et al.* (1992); Rodi & Mansour (1993); Coleman *et al.* (2003); Hoyas & Jimenez (2008); Eitel-Amor *et al.* (2014). The flows in these studies are all characterized by the fact that significant local variations of the mean flow profile are restricted to one direction. Looking at zero pressure gradient boundary layers, for example, the most significant local changes are observed in the wall normal direction with minor changes in the streamwise direction and spatially homogenous mean flow in the spanwise direction. As a consequence the gradients of the time averaged flow field in the span and streamwise directions are small with respect to the wall normal ones. However, most of the budget terms depend on spatial gradients as can be seen in equation (1.35). Therefore, budgets of flows with no streamline curvature (one dominant direction of mean flow change) are dominated by contribution in one particular direction, e.g. the wall normal direction for a zero pressure gradient boundary layer. Hence, it is not clear how a turbulence model developed for such flows would behave in a more complex flow as present for an LPT midspan section. Due to the focus of the wake region the budgets obtained in this work

are compared to results published by Thomas *et al.* (2003) who focused on the early wake of a rectangular trailing edge.

LPT flows as considered in this work might feature separated flow regions as well as trailing edge vortex shedding. In light of these flow features the most relevant studies that reported TKE transport equation budgets were published for a flat plate boundary layer subjected to an adverse pressure gradient causing a separation bubble by Laurent *et al.* (2011) and a flat plate with a rectangular trailing edge where the focus is on vortex shedding by Yao *et al.* (2001). Both datasets represent incompressible flows and the flow about an LPT combines vortex shedding with separation. Hence, the presented dataset is more relevant for turbomachinery flows. This can be particularly useful since no generally accepted turbulence models exist. Hence, turbulence modellers or CFD users of established turbulence models can use the information provided in this chapter to understand the performance and deficiencies of their particular model of choice in more detail for a case much closer to their design space. On the other hand it should be noted that this dataset is based on a two dimensional mean flow and three dimensional phenomena present at endwalls are not represented.

In order to test the performance of a particular RANS model it is of interest to compare the prediction of this model with the actual terms obtained from DNS. In section 1.2.2 the Favre averaged equations have been presented and the terms requiring modelling have been highlighted. If the sum of these fluctuating terms in each Favre averaged equation is modelled correctly, an accurate simulation of the mean flow field can be expected. Therefore, following Pichler *et al.* (2015), the flow field is presented in detail. The basic idea is to present the dataset such that it can be used for turbulence model validation. To that end, data is presented along pitchwise profiles at three streamwise positions. Choosing three streamwise position allows to investigate if the turbulence mixing process is captured correctly and at these three particular positions also the mechanism leading to mixing in terms of turbulence kinetic energy are quantified. This is of particular interest since, as has been discussed in chapter 1, the wake is generated at the trailing edge and then undergoes mixing before it interacts with the downstream blade row. If the prediction of wake generation or mixing is inaccurate, the interaction with the downstream blade row cannot be predicted correctly.

The terms presented for the Favre averaged transport equations are summarized in table 5.1 where in the first column the variable name that will be used in the plots is written. The second column contains the governing relationship and the third column gives the name these terms are often addressed as in literature (e.g: Wilcox (1998)).

The table is divided into four sections by horizontal lines according to the equation each of the terms originates from. In the last column reference to the respective Favre averaged transport equation is provided. The first section contains the Reynolds stress (RS) and its divergence where only the latter appears in the transport equation of Favre

variable	formula	description	appearing in eqn.
τ_{ij}	$-\overline{\rho u_i'' u_j''}$	Reynolds stress (RS)	(1.18)
$m_{\tau,i}$	$\frac{\partial}{\partial x_j}\left(\tau_{ij}\right)$	diffusion of RS	
$e_{t,kin}$	$-\frac{\partial}{\partial x_j}\left(\overline{\rho}\widetilde{u}_j\frac{1}{2}\widetilde{u}_i\widetilde{u}_i\right)$	transport of kinetic energy	(1.19)
$e_{t,h}$	$-\frac{\partial}{\partial x_j}\left(\overline{\rho}\widetilde{u}_j\widetilde{h}\right)$	transport of enthalpy	
$e_{t,\widetilde{u}}$	$\frac{\partial}{\partial x_j}\left(\widetilde{u}_i t_{ij}\left(\widetilde{u}\right)\right)$	molecular stress work	
$e_{t,\tau}$	$\frac{\partial}{\partial x_j}\left(\widetilde{u}_i\tau_{ij}\right)$	RS Work	
$e_{t,u''}$	$\frac{\partial}{\partial x_j}\left[\overline{u_i''}t_{ij}\left(\widetilde{u}\right)+\widetilde{u}_i t_{ij}\left(\overline{u''}\right)\right]$	Favre diffusion	
$e_{t,\widetilde{T}}$	$\frac{\partial}{\partial x_j}\left(c_{th}\mu\frac{\partial\widetilde{T}}{\partial x_j}\right)$	mean heat flux	
$e_{t,T''}$	$\frac{\partial}{\partial x_j}\left(c_{th}\mu\frac{\partial\overline{T''}}{\partial x_j}\right)$	Favre heat flux	
$e_{t,h''}$	$-\frac{\partial}{\partial x_j}\left(\overline{\rho u_j'' h''}\right)$	turbulent heat flux	
$e_{t,TKE}$	$-\frac{\partial(\overline{\rho}\widetilde{u}_j k)}{\partial x_j}$	transport of TKE	(1.19) and (1.35)
$\mathcal{C}_1$	$-\frac{\partial}{\partial x_j}\left(\overline{\frac{\rho u_i'' u_i'' u_j''}{2}}\right)$	turbulent transport	
$\mathcal{C}_3$	$\frac{\partial}{\partial x_j}\left(\overline{t_{ij}\left(u''\right)u_i''}\right)$	molecular diffusion	
$\mathcal{P}$	$\overline{\rho}\tau_{ij}\frac{\partial\widetilde{u}_i}{\partial x_j}$	TKE production	(1.35)
$\overline{\rho}\epsilon$	$-\overline{t_{ij}\left(u''\right)\frac{\partial u_i''}{\partial x_j}}$	TKE dissipation	
Π	$\overline{p'\frac{\partial u_i''}{\partial x_i}}$	Pressure Dilatation	
$\mathcal{V}$	$\overline{u_i''\frac{\partial t_{ij}(\bar{u})}{\partial x_j}}$	viscous work	
$\mathcal{R}$	$-\overline{u_i''}\frac{\partial\overline{p}}{\partial x_i}$	pressure work	
$\mathcal{C}_2$	$-\frac{\partial}{\partial x_j}\left(\overline{p' u_i''}\delta_{ij}\right)$	pressure diffusion	

TABLE 5.1: Budgest of the transport equation of Favre averaged momentum, Favre averaged total energy and turbulence kinetic energy.

averaged momentum directly and as such the RS is not among the terms to be captured in this section. Since it is used in many turbulence models, though, it is reported as well. The second section contains all terms appearing only in the transport equation of Favre averaged total energy. In the third section terms are summarized that appear in both the transport equations of Favre averaged total energy and TKE and in the last section terms only present in the transport equation of TKE are collected. In order to validate RANS models it would be sufficient to only compare the modelling terms and the mean flow profiles since matching those would guarantee the correct representation of the flow field. Since it allows to discuss energy transfer mechanism, though, the full budgets and not only the terms requiring modelling are presented in the following for the transport equations of Favre averaged total energy and TKE.

5.1 Mean flow results

Before the quantities relevant for turbulence modelling are discussed the pressure distribution about the blade, wake loss profiles and the wall shear stress at the blade are presented in figures 5.1 and 5.2 since they are often used for performance assessment and flow investigations in other works. The results discussed in the following confirm the trends reported in literature. Note that the wall shear stress is positive in the clockwise direction around the blade (see figure 5.3) such that the mostly positive line is the suction side and the mostly negative line is the pressure side. Negative values for the suction side and positive values for the pressure side indicate regions with flow separations.

In figure 5.1 (a) the pressure distribution about the blade, given by

$$c_p = \frac{p_{t,in,mix} - p(x)}{p_{t,in,mix} - p_{out,mix}} \tag{5.1}$$

is presented. There are only minor differences on the pressure side (upper curves) for the cases at two different Reynolds numbers. On the suction side there are small differences close to the leading edge which seem to stem from a larger suction side separation for the $Re_{is} = 100,000$ case. The suction side leading edge separation is clearer in figure 5.2 (a) where the wall shear stress for both suction and pressure side is plotted. The most important differences between the $Re_{is} = 100,000$ case and the $Re_{is} = 60,000$ case are between the peak suction point and the trailing edge. In this region of deceleration the boundary layers might separate which manifests itself in a plateau in the pressure distribution. This is apparent for the $Re_{is} = 60,000$ case but less obvious for the $Re_{is} = 100,000$ case. This is confirmed by the wall shear stress plots looking at the trailing edge region as presented in 5.2 (b) where the separation occurs earlier and the negative wall shear stress is higher for the $Re_{is} = 60,000$. For both cases the separation does not show a reattachment where stronger vortex shedding for the $Re_{is} = 60,000$ case leads to higher peaks in the wall shear stress distributions around the trailing edge.

In figure 5.1 (b) the wake loss, given by

$$\omega = \frac{p_t(y) - p_{out,mix}}{p_{t,in,mix} - p_{out,mix}} \tag{5.2}$$

at $x = 1.26$ is presented for both cases. The wake shape is similar but the $Re_{is} = 60,000$ case shows a wider extent towards the suction side. Its peak location is slightly shifted to the positive y direction indicating a lower exit angle and less turning with respect to the $Re_{is} = 100,000$ case. Overall the losses of the $Re_{is} = 60,000$ are higher compared to the $Re_{is} = 100,000$ case which has been reported for various blades.

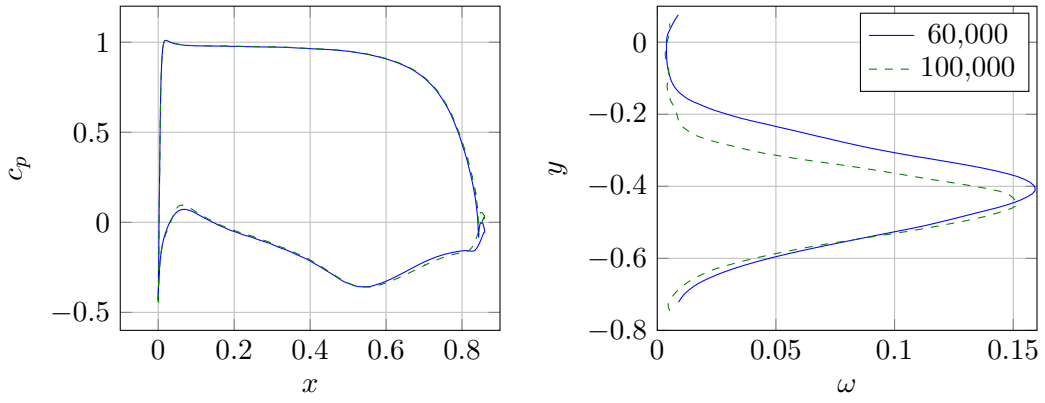

(a) (b)

FIGURE 5.1: Blade pressure and wake loss distribution for the simulations at $Re_{is} = 60,000$ and $Re_{is} = 100,000$.

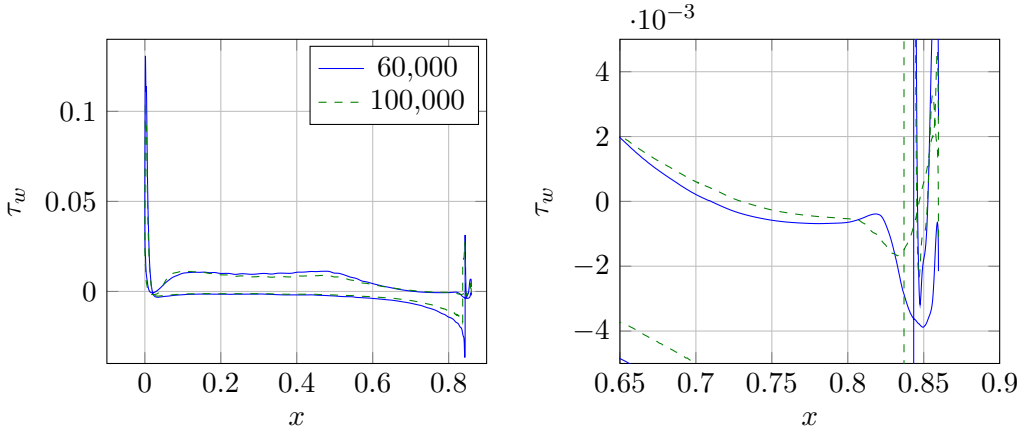

(a) (b)

FIGURE 5.2: Wall shear stress around the blade for the simulations at $Re_{is} = 60,000$ and $Re_{is} = 100,000$.

5.2 Favre averaged results

As mentioned above, turbulence models fail for various flows and to date no generally accepted turbulence model has been established. Therefore it is of interest to investigate the turbulent flow content. For the cases under investigation the most energetic turbulent flows are in the wake and in the boundary layers close to the trailing edge, as shown in figure 5.3 where TKE contours are presented. At the lower Reynolds number $Re_{is} = 60,000$ the levels of TKE in the near wake are higher. It is expected that this is related to the larger separation which due to a larger blockage mimics a "thicker" trailing edge that subsequently leads to a more intense vortex shedding. Further, the peak intensity is shifted downstream and is more local at the lower Reynolds number. Hence, even though both cases are fully separated, according to the wall shear stress profiles presented in figure 5.2, the case at $Re_{is} = 100,000$ is closer to transition and reattachment, as

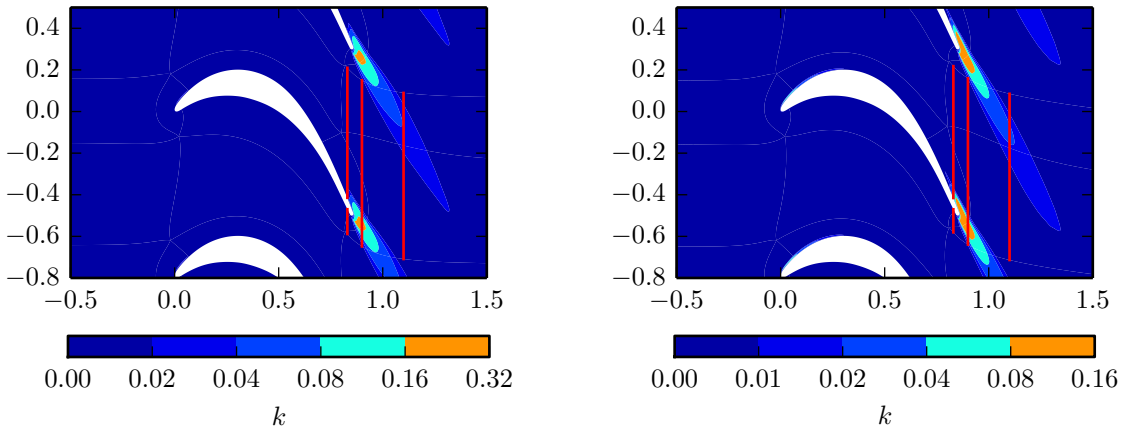

FIGURE 5.3: Turbulent kinetic energy plot for case $Re_{is} = 60,000$ (left) and case $Re_{is} = 100,000$ (right). Red lines indicate profiles at which detailed quantities are presented.

expected. Comparing with results for the rectangular trailing edge case by (Thomas *et al.*, 2003) the results in this work show asymmetry due to different states of the boundary layers on either side.

Further, both cases also show elevated TKE levels close to the leading edge where the leading edge separation takes place and the incoming turbulence interacts with the leading edge. It seems as if this effect is more pronounced in the $Re_{is} = 100,000$ case, but this is due to the lower contour level magnitudes and the actual magnitudes of TKE are similar in both cases. Turbulence mainly leads to an enhanced mixing of the wake and in order to capture this process three profiles are extracted at which the results are presented. The positions of these three pitchwise profiles are presented in figure 5.3 by the red vertical lines located at streamwise positions of 0.83, 0.9 and 1.1. High levels of TKE highlight the wake region such that the three profiles are located in the separation bubble upstream of the trailing edge ($x = 0.83$), in the vortex shedding region ($x = 0.9$) and in the further mixed wake ($x = 1.1$).

5.2.1 Near wake region

In figure 5.4 the mean flow profiles of the Favre averaged mean flow field are presented in the near wake at $x = 0.9$. Together with $\widetilde{u}_3 = 0$ these quantities comprise the mean flow field of the independent flow variables of the governing equations. The most distinct peaks occur around $y = -0.5$ and are related to the wake region where, similar to above, the peak location of the $Re_{is} = 100,000$ case is slightly shifted towards the pressure side due to a higher turning angle. For the $Re_{is} = 60,000$ case the mean flow profiles show a deeper wake, except for the static temperature profile which exhibits almost no difference at the wake position. In the density profile the negative peak around $y = -0.5$ is located downstream of the separated zone above the wake center. Apart from this low density

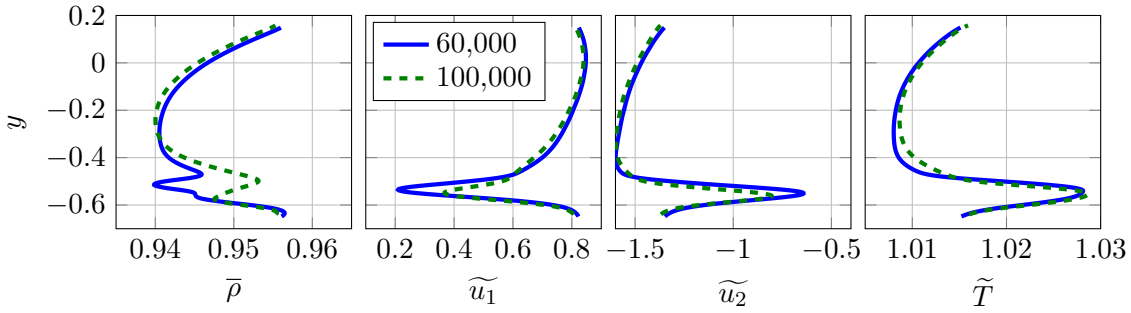

FIGURE 5.4: Mean flow profiles in the near wake at $x = 0.9$.

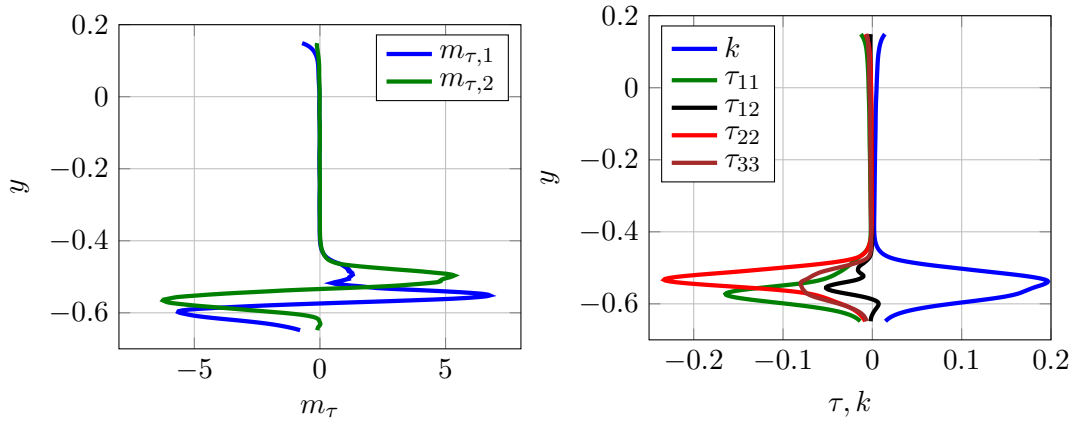

(a) (b)

FIGURE 5.5: Divergence of RS m_τ (a) and RS $\tau_i j$ (b) in the near wake at $x = 0.9$ at $Re_{is} = 60,000$.

peak the profile is similar to that of the $Re_{is} = 100,000$ case where the wake connects the lower density area on the suction side with the higher density area at pressure side.

To solve the Favre averaged momentum equations the divergence of velocity fluctuation correlations $\overline{\rho u_i'' u_j''}$ have to be modelled which is generally done by modelling them as stresses, the RS. The divergence of the RS ($m_{\tau,i}$) and the actual RS along with the TKE are presented in figure 5.5 and 5.6 for both cases, respectively. As expected the largest magnitudes are in the wake region. If these terms can be matched, a turbulence model would be expected to correctly predict the flow. Vortex shedding is more intense at $Re_{is} = 60,000$ due to the larger separation leading to a virtually thicker trailing edge. This is also reflected in the larger magnitude both of the divergence of the RS and the RS itself at the lower Reynolds number.

Budgets of the transport equation of Favre averaged total energy are presented in figure 5.7 for both cases. Since an LPT flow with a constant time mean is considered the budgets of the Favre averaged equations have to be balanced which has been tested for all budgets. In order to reduce the number of lines in the plots, terms appearing in both the transport equation of Favre averaged TKE and total energy are only plotted in

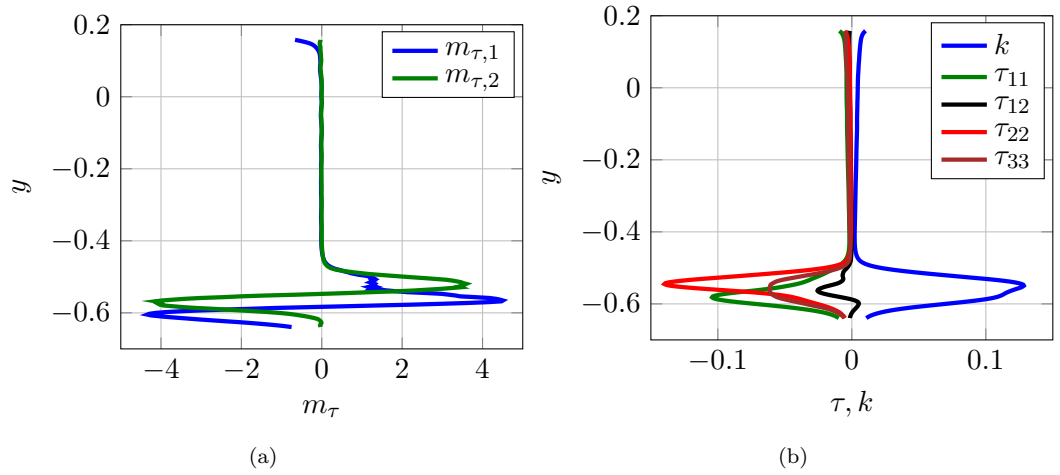

FIGURE 5.6: Divergence of RS m_τ (a) and RS $\tau_i j$ (b) in the near wake at $x = 0.9$ at $Re_{is} = 100,000$.

figure 5.8. Hence, summing up all terms in figure 5.7 does not result in zero but requires to add $e_{t,k}$, $\mathcal{C}_1$ and $\mathcal{C}_3$ from figure 5.8. This applies to all three locations plotted in the following.

These budgets are useful to understand the energy transfer in the flow and, therefore, along with presenting those to aid CFD users and turbulence modellers, the important mechanisms for spatial energy redistribution are discussed. Note that total energy is conserved in the flow such that only spatial redistribution but no sink or source terms appear in its transport equation. Each term represents a line in the plot and a positive contribution leads to an increase of total energy due to the particular mechanism and negative values to a reduction. Since a flow with a constant time mean is considered the budgets are balanced such that the sum of all terms is zero, i.e. the terms have to cancel each other out.

Again the wake is highlighted by the peaks around the center at approximately $y = -0.5$. Comparing both cases it is obvious that the magnitudes for the respective terms of case $Re_{is} = 60,000$ are higher, particularly in the wake region, which is due to the more intense vortex shedding leading to enhanced mixing in that region. Many RANS models for compressible flows are extensions of the incompressible versions for which the magnitudes of $e_{t,u''}$ and $e_{t,T''}$ are identically zero. Looking at the magnitude of these terms, this assumption appears to be appropriate for this particular flow. Further $e_{t,\widetilde{u}}$ and $e_{t,\widetilde{T}}$ are small but since both $\widetilde{u}_i$ and $\widetilde{T}$ are part of the Favre averaged solution those are generally still considered in the models.

The largest magnitudes are due to transport of kinetic energy ($e_{t,kin}$) and transport of enthalpy ($e_{t,h}$). In the passage those are the only two important terms. These terms are followed by the RS work ($e_{t,\tau}$) which is the largest quantity that has to be modelled. Its magnitude is only significant inside the wake but there it reaches more than 70% of the

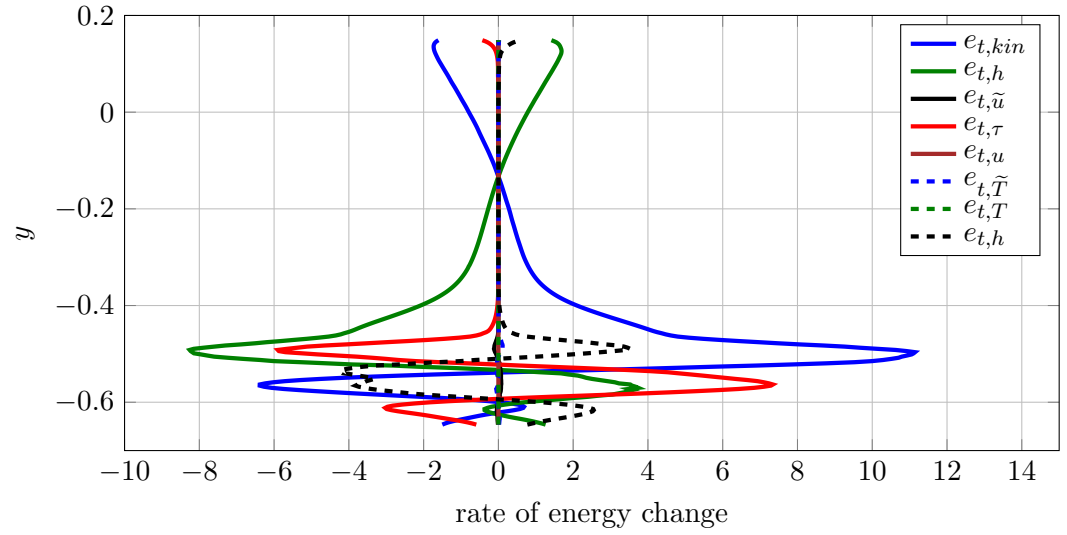

(a)

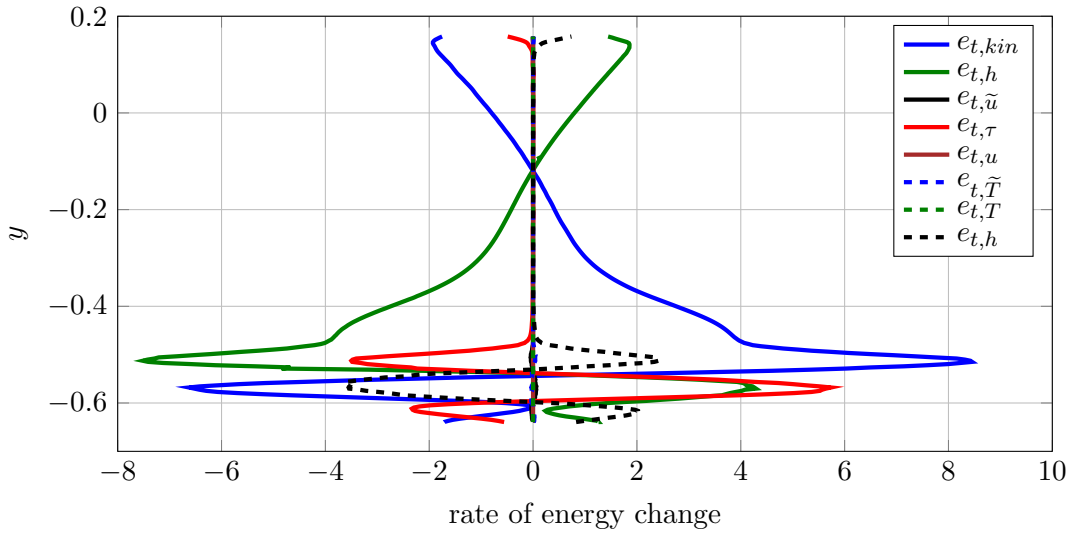

(b)

FIGURE 5.7: Favre averaged total energy budgets in the near wake ($x = 0.9$) for the simulations at $Re_{is} = 60,000$ (a) and at $Re_{is} = 100,000$ (b).

transport of kinetic energy. In addition also the turbulent transport of enthalpy ($e_{t,h''}$) followed by the transport of turbulent kinetic energy ($e_{t,k}$) are important and exceed 50% and 15%, respectively, with the extent of their contribution limited to the wake again. The ratios are fairly similar for both Reynolds numbers but the magnitudes for the higher Reynolds number are about 30% lower due to the aforementioned reasons.

In figure 5.8 the budgets of the transport equation of TKE for both Reynolds numbers are presented. The budgets indicate by which mechanisms TKE is altered in the flow field. In contrast to the transport equation of Favre averaged total energy it also contains sink and source terms that represent energy transfer to and from Favre averaged internal energy ($\overline{\rho}\epsilon$, Π and $\mathcal{C}_2$) and Fravre averaged mean kinetic energy ($\mathcal{P}$, $\mathcal{V}$ and $\mathcal{R}$). Again

positive terms lead to an increase and negative terms to a decrease of TKE and all terms are balanced since a time mean solution is considered. The magnitudes are about a factor of three smaller compared to the total energy budgets. Due to their low magnitudes the terms only appearing in the compressible equations, $\mathcal{V}$ and $\mathcal{R}$, can be neglected for both Reynolds numbers. In addition the pressure strain correlation, Π, also would be identically zero for incompressible flows and its magnitude is low, so that neglecting it, as done in many turbulence models, is not considered a problem. The final term with a negligible magnitude is the molecular transport of TKE $\mathcal{C}_3$.

Production $\mathcal{P}$ is the most important mechanism followed by the turbulent transport of TKE, $\mathcal{C}_1$, (often referred to as triple correlation) for both Reynolds numbers. The turbulent transport of pressure, $\mathcal{C}_2$, follows in terms of magnitude at the lower Reynolds number. While all the terms discussed so far are a factor of approximately 1.5 smaller at the higher Reynolds number, dissipation is only about 10% smaller at the higher Reynolds number. Looking at the large scales it was already discussed that the vortex shedding is more intense leading to a stronger interaction with the mean flow (production) and also turbulent transport of TKE and pressure ($\mathcal{C}_1$ and $\mathcal{C}_2$) seem to scale with larger flow scales in this particular case. In contrast dissipation (ϵ) mostly happens at the smallest scales (Pope, 2000). In the popular picture of turbulence introduced by Richardson, turbulence is mostly generated at the largest scales and then it cascades down. During this cascading process molecular viscosity becomes more important and leads to increasing dissipation of TKE such that dissipation becomes more important at smaller scales. Using this idea the dissipation at the current position is a result of processes responsible for the magnitudes of TKE further upstream and the time it takes for the large scales to break down into small scales. The onset of transition and the related TKE levels are larger further upstream at the higher Reynolds number but in particular the vortex shedding at the trailing edge revert the picture immediately downstream of the trailing edge. In addition the smallest scales in a flow scale with Reynolds number such that it might take more time for the larger scales to break down to levels where molecular viscosity is important which would lead to smaller dissipation at the higher Reynolds number. At this stage it is not clear which of these mechanisms is more important.

Kolmogorov (1941) reasoned that under certain circumstances turbulence is in a "quasi equilibrium" state where turbulence is dissipated at the same rate as it is produced. This idea was picked up by many turbulence modellers and is an essential part of many widely used turbulence models like many two equation models. It can be seen that this is clearly not the case at this position by comparing the production of TKE with the dissipation in figure 5.8 for both cases where in production is significantly greater than dissipation, similar to the work of (Thomas *et al.*, 2003) for the rectangular trailing edge case.

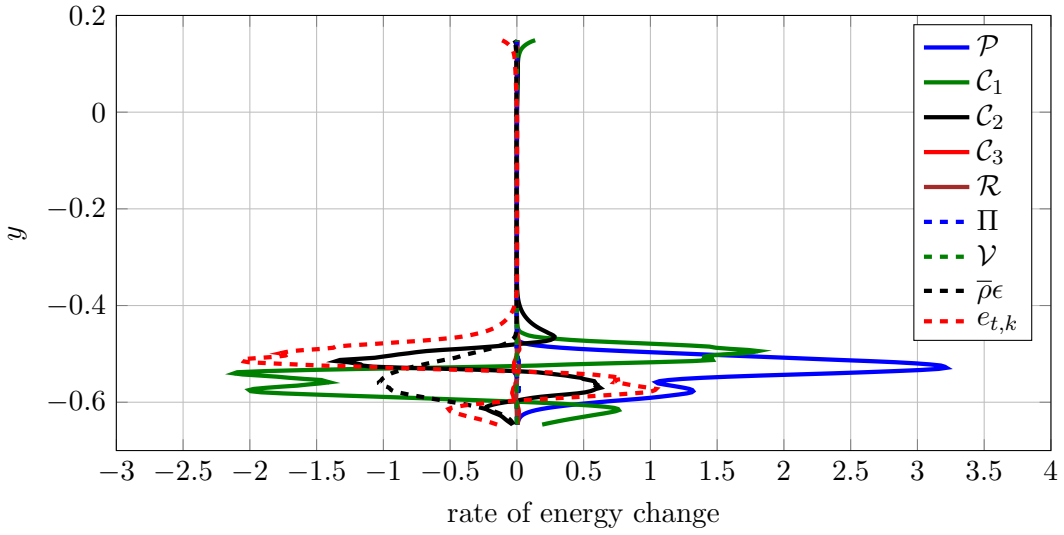

(a)

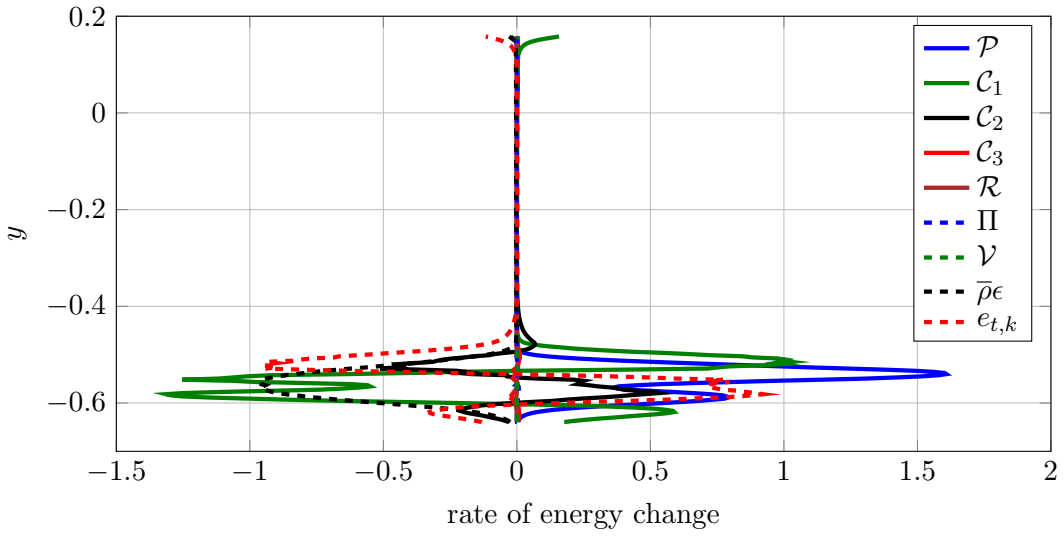

(b)

FIGURE 5.8: Favre averaged TKE budgets in the near wake ($x = 0.9$) for the simulations at $Re_{is} = 60,000$ (a) and at $Re_{is} = 100,000$ (b).

5.2.2 Developed wake

In the last section the flow at a profile in the most energetic turbulence region has been presented and now the flow in the further developed wake at $x = 1.1$ is discussed. The mean flow profiles are plotted in figure 5.9. Peaks in the profiles at $y = -0.1$ indicate the wake center where again the downward shift of the center is apparent for the case with the higher Reynolds number. Wake mixing, though, leads to a significant reduction of the wake deficit compared to the position immediately downstream of the trailing edge discussed in the previous section.

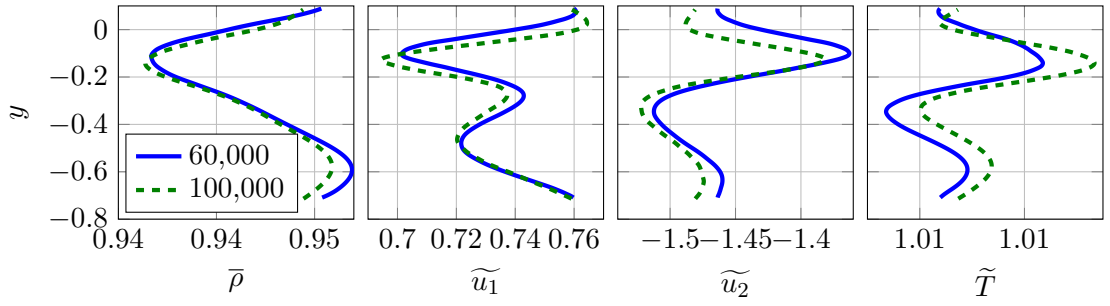

FIGURE 5.9: Mean flow profiles in the far wake at $x = 1.1$.

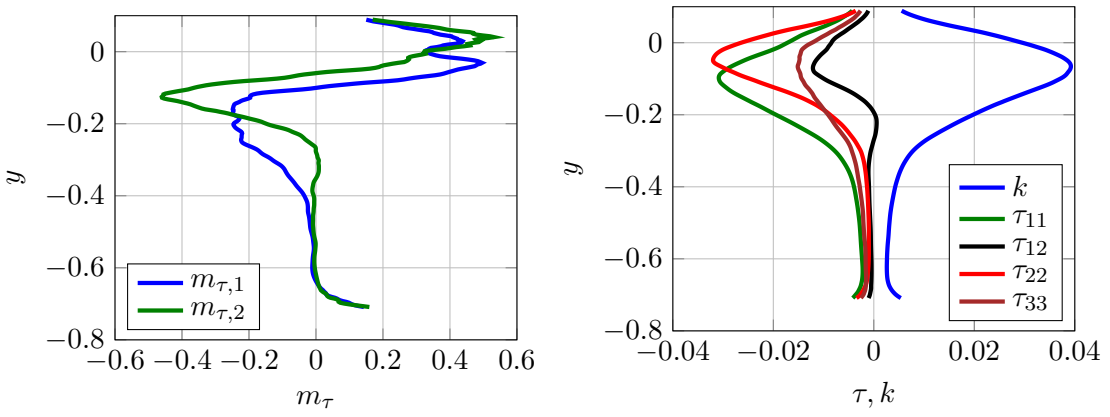

FIGURE 5.10: Divergence of RS(a) and RS (b) in the far wake at $x = 1.1$ at $Re_{is} = 60,000$.

To assess the performance of turbulence models again profiles of the divergence of the RS and the RS components are plotted in figure 5.10 and 5.11 at $Re_{is} = 60,000$ and $Re_{is} = 100,000$, respectively, for the further developed wake at $x = 1.1$. Compared to the profile close to the trailing edge the magnitudes of the divergence of the RS at both Reynolds numbers have already reduced by a factor of 10 and the RS and TKE by a factor of approximately 5 where the RS is more isotropic as would be expected considering other studies like Thomas *et al.* (2003). The low magnitudes of the RS at this position already lead to some wiggles in the plots of divergence of RS which are due to an insufficient statistical convergence and the already low magnitudes of the fluctuations.

Using figure 5.12 the energy transfer in the further developed wake at $x = 1.1$ is discussed. At this position the profiles of both cases are similar apart from and upward shift due to a different wake center position and the magnitudes of the turbulent contributions are higher at $Re_{is} = 60,000$. Comparing to the position close to the trailing edge the magnitudes have decreased significantly indicating weaker energy transfer. While close to the trailing edge the largest terms appear inside the wake region there are almost no differences at $x = 1.1$ between the wake and the surrounding flow in terms of the strength of the mechanisms. Even though the transport of mean kinetic energy $e_{t,kin}$ and

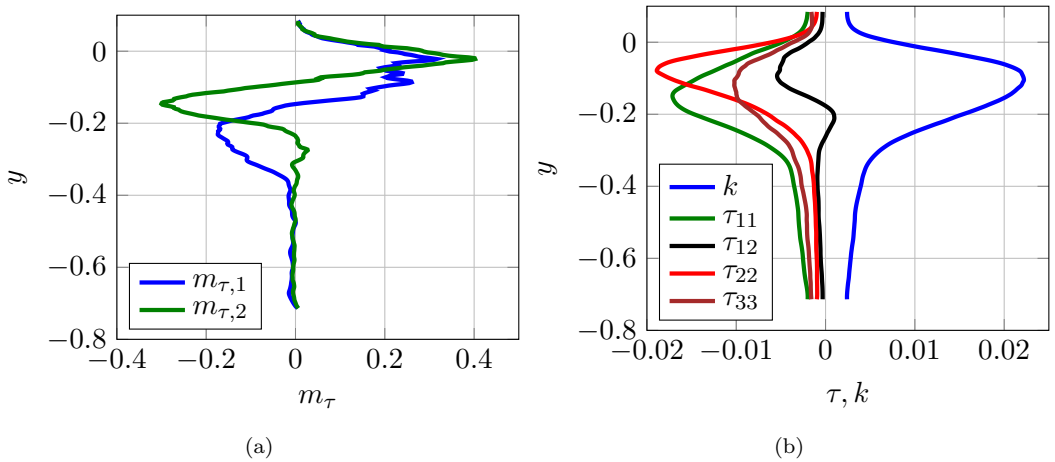

FIGURE 5.11: Divergence of RS(a) and RS (b) in the far wake at $x = 1.1$ at $Re_{is} = 100,000$.

enthalpy $e_{t,h}$ are still the most important mechanisms, in the wake region the turbulent mechanisms have increased in relative importance for both cases. In fact, in the wake the RS work is of the same order as the energy transfer mechanisms based on the mean flow field at the lower Reynolds number. The turbulent transport of heat $e_{t,h''}$ and the transport of turbulent kinetic energy $e_{t,k}$ follow in terms of their magnitudes.

Also at $x = 1.1$ the magnitudes of the time average of Favre fluctuations is small such that the energy transfer mechanisms given by the terms $e_{t,u''}$ and $e_{t,T''}$ are small again with respect to the other terms such that neglecting them in models seems plausible. In addition the molecular heat transfer ($e_{t,\tilde{T}}$) and viscous work ($e_{t,\tilde{u}}$) again have little influence on the energy transfer.

In figure 5.13 the budgets of the transport equation of TKE are presented for both cases at $x = 1.1$. Comparing the two cases the lower Reynolds number has larger magnitudes of all terms where most terms scale with a factor of two. The major exception is dissipation which is larger with respect to the other terms at $Re_{is} = 100,000$. Similar to the position close to the trailing edge mechanisms related to molecular transport of TKE ($\mathcal{C}_3$), pressure work ($\mathcal{R}$), viscous work ($\mathcal{V}$) and the pressure strain correlation (Π) are as expected small with respect to the others and neglecting them in a model also appears to be justified.

The dominating mechanism in both cases is the turbulent transport of TKE ($\mathcal{C}_1$) followed by dissipation of TKE. In contrast to the position immediately downstream of the trailing edge the importance of production ($\mathcal{P}$) is not the dominating mechanism but is smaller than the aforementioned contribution. As mentioned above several basic turbulence considerations assume a balance of production and dissipation of TKE which is clearly not the case. While at $x = 0.9$ production was larger than dissipation the situation is reversed now. Considering that the other terms representing energy transfer between mean kinetic energy, TKE and internal energy are negligible this means that along this

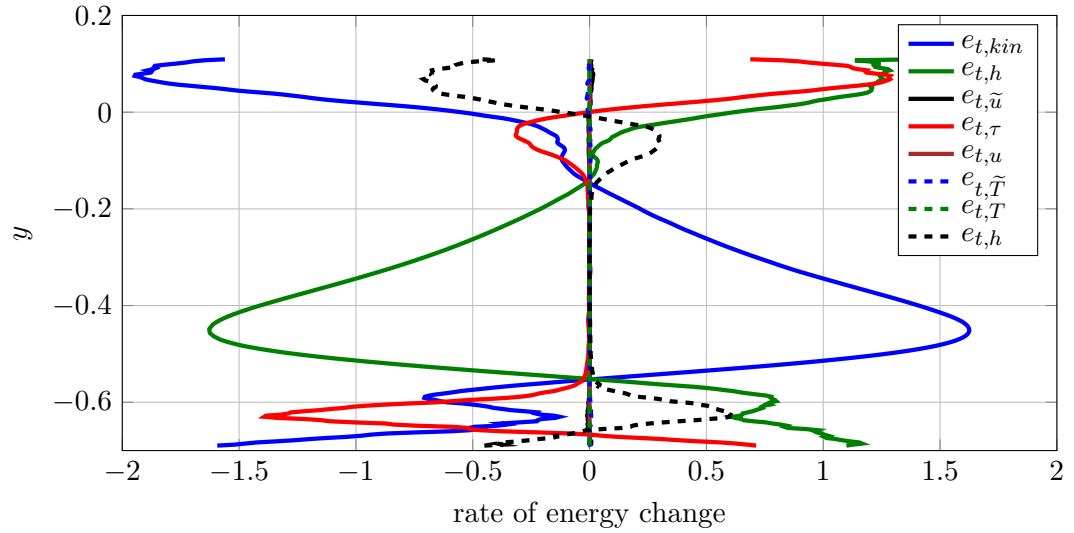

(a)

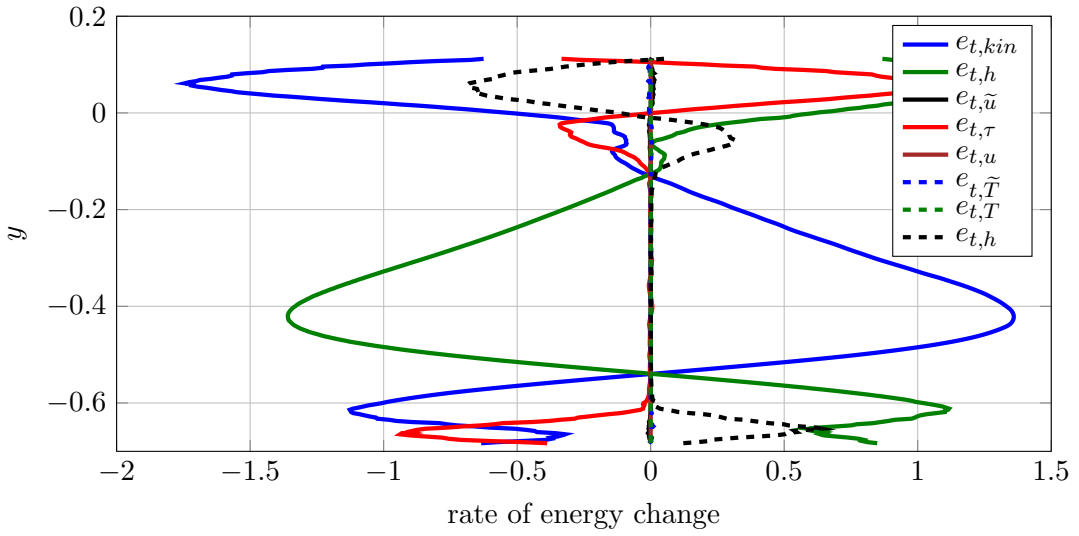

(b)

FIGURE 5.12: Favre averaged total energy budgets in the far wake ($x = 1.1$) for the simulations at $Re_{is} = 60,000$ (a) and at $Re_{is} = 100,000$ (b).

profile the flux from TKE to internal energy is larger than the flux from mean kinetic energy to TKE.

5.2.3 Separation bubble

On the suction side the flow is not turbulent before it separates and does not clearly reattach at both Reynolds numbers at the flow conditions prescribed. The pressure side is also not fully turbulent. Most of the investigations presented in this section are useful for fully turbulent investigations but for transitional flows different quantities seem to be more suitable since the low intermittency leads to low magnitudes of the

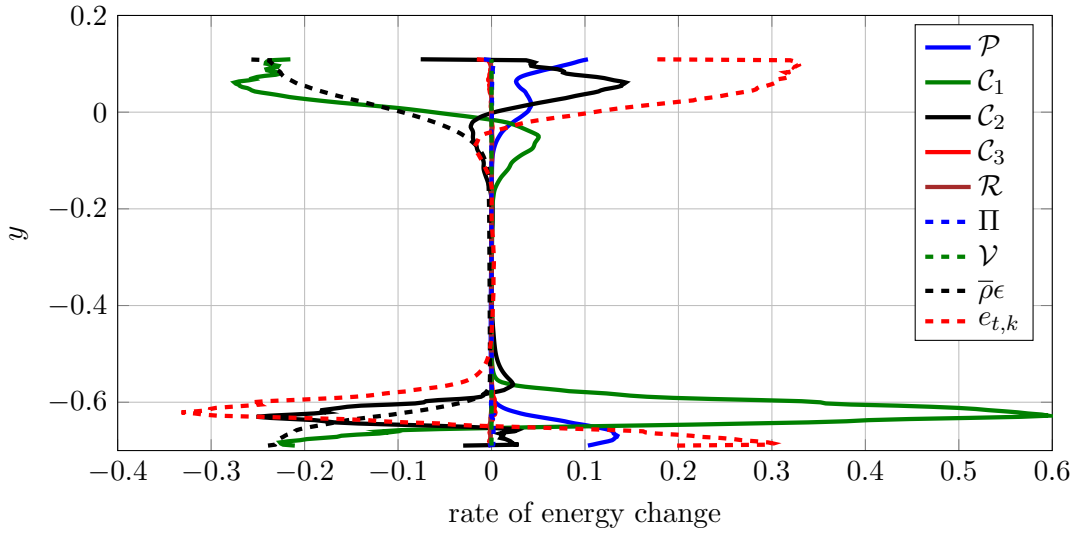

(a)

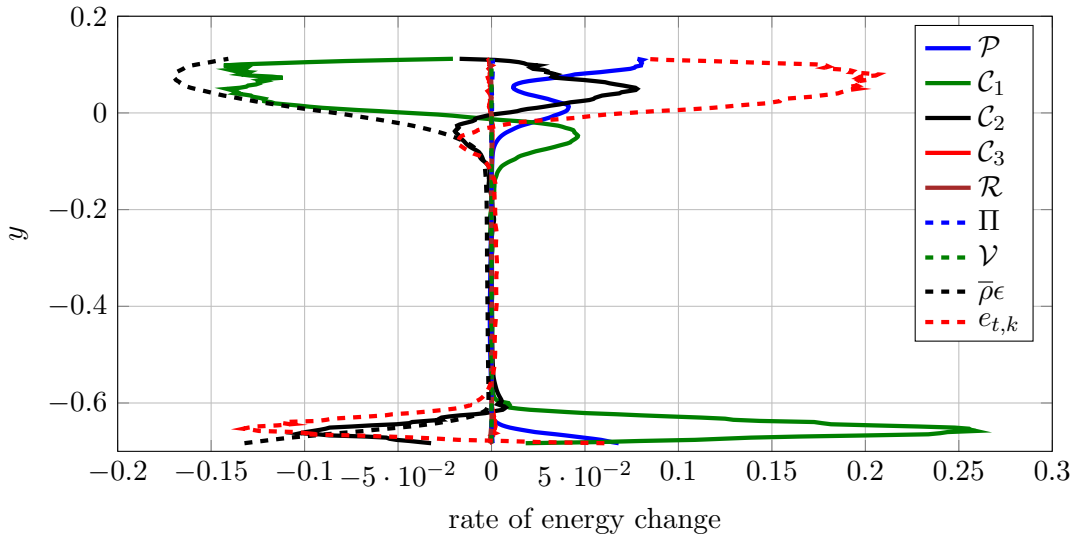

(b)

FIGURE 5.13: Favre averaged TKE budgets in the far wake ($x = 1.1$) for the simulations at $Re_{is} = 60,000$ (a) and at $Re_{is} = 100,000$ (b).

terms considered here. Therefore, at this position the terms reported might not help turbulence model development by themselves but are still considered important since they define the "inflow to the turbulent region".

Mean profiles presented in figure 5.14 serve as the first point of assessment. All profiles are split into two sections where the upper section represents the suction side part of the flow field and the lower one presents the pressure side profile. Towards the wall both profiles show steep decays of the velocity profile amplitude towards zero at the wall. Negative values in the streamwise velocity profile and positive values in the pitchwise velocity profile close to the suction side indicate the separation present at this location.

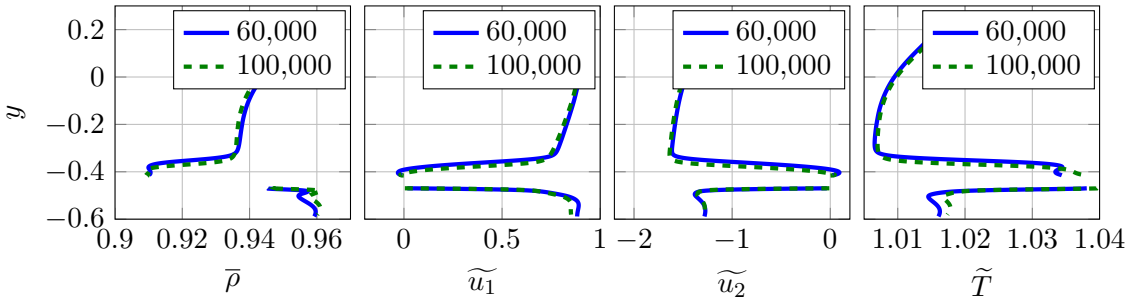

FIGURE 5.14: Mean flow profiles in the separation bubble close to the trailing edge at $x = 0.83$.

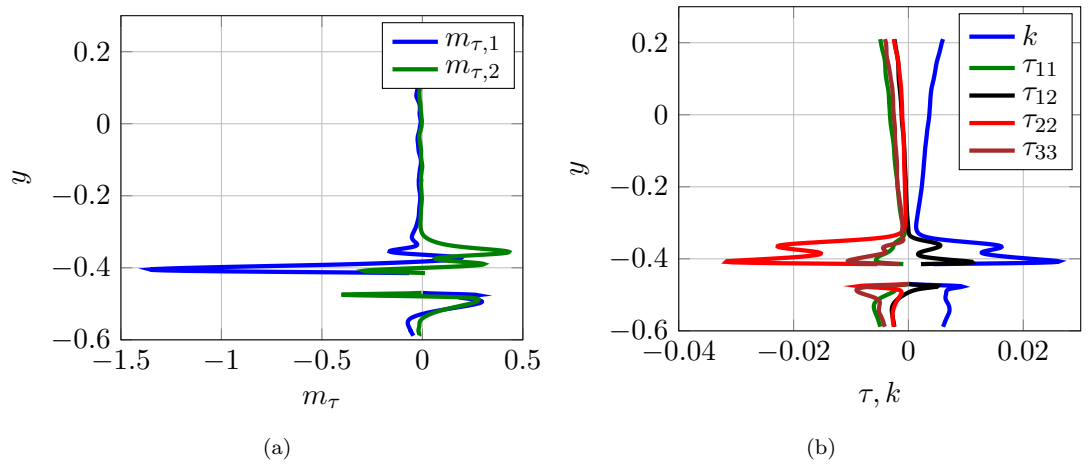

(a) (b)

FIGURE 5.15: Divergence of RS(a) and RS (b) in the near wake at $x = 0.9$ at $Re_{is} = 60,000$.

The mean flow profiles at both Reynolds numbers are similar except for inside the boundary layer.

Even though the flow is not "fully" turbulent, velocity fluctuations are present in the boundary layer, particularly in the separation bubble, such that the RS is not zero, as illustrated in figures 5.15 and 5.16 where the RS and its divergence are presented for both cases. As discussed above the separation bubble is wider in pitchwise direction at the lower Reynolds number which is also reflected in both the RS and its divergence, while the magnitudes are larger at the higher Reynolds number indicating stronger velocity fluctuations. In both cases the RS and its divergence are larger on the suction side even though they are still small compared to the position immediately downstream of the trailing edge.

Budgets of the Favre averaged transport equation at $x = 0.83$ are presented in figure 5.17. Similar to the downstream positions discussed above the higher Reynolds number case has smaller amplitudes. Over the majority of the pitch mean kinetic energy and enthalpy transport counteract each other. In the vicinity of the pressure side heat transfer and viscous work have significant amplitudes. While at the pressure side none of the "turbulent" terms is of significant magnitude, on the suction side in particular in

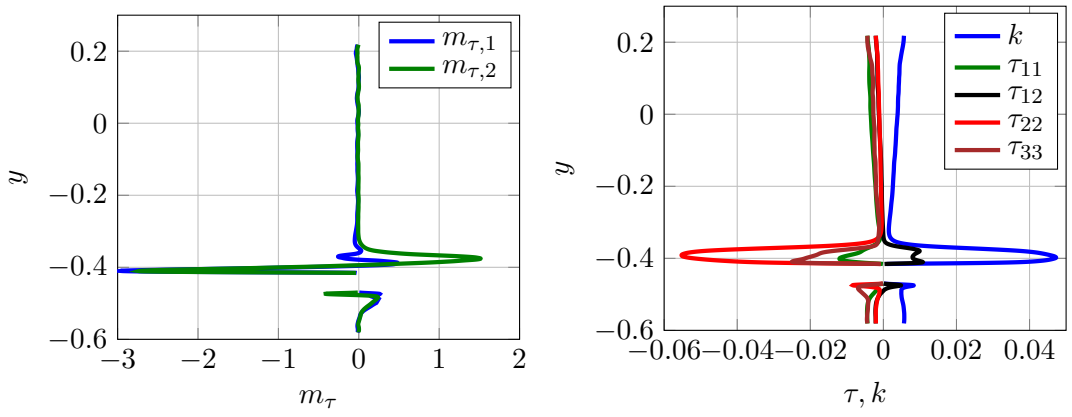

(a) (b)

FIGURE 5.16: Divergence of RS(a) and RS (b) in the near wake at $x = 0.9$ at $Re_{is} = 100,000$.

the separation bubble the terms depending on fluctuations have a none-zero contribution. However, the magnitudes of the terms depending on the fluctuating flow field are small at this position with respect to position immediately downstream of the trailing and are of the same order of magnitude as in the far wake.

In figure 5.18 budgets of the transport equation of TKE are presented. Only inside the boundary layers significant magnitudes are present. Note that the terms are larger in the $Re_{is} = 100,000$ case in contrast to most of the investigations above. This is probably related to are more progressed state in the separated transition process. The largest contribution is due to production of TKE, i.e. a net energy transfer from mean kinetic energy to TKE. Directly at the wall the viscous dissipation and molecular transport are large which is in agreement with boundary layer work. While turbulent transport was important in the wake, it is negligible at $x = 0.83$. A non-zero contribution is due to turbulent transport of pressure. All other terms are small at this position. The results are in qualitative agreement with results in Laurent *et al.* (2011) who also show a dominance of production ($\mathcal{P}$, advection of TKE ($\epsilon_{t,k}$) and $\mathcal{C}_\in$ in the separation bubble.

Results in this section, particularly in the wake where the turbulence statistics are largest, show qualitatively similar behaviour to the results by Thomas *et al.* (2003) who investigate a rectangular trailing edge. The major difference is in the boundary layers on the pressure side and the suction side leading resulting in asymmetric TKE budgets. Hence, the budgets presented in this work allow to develop a tailored turbulence model for LPT application based on a dataset in a typical Reynolds number range for LPTs using a geometry a turbine geometry. In addition these results allow to investigate the influence of compressibility at moderate Mach numbers as present in an LPT for the given flow. In the bubble the turbulence characteristics are similar to Laurent *et al.* (2011).

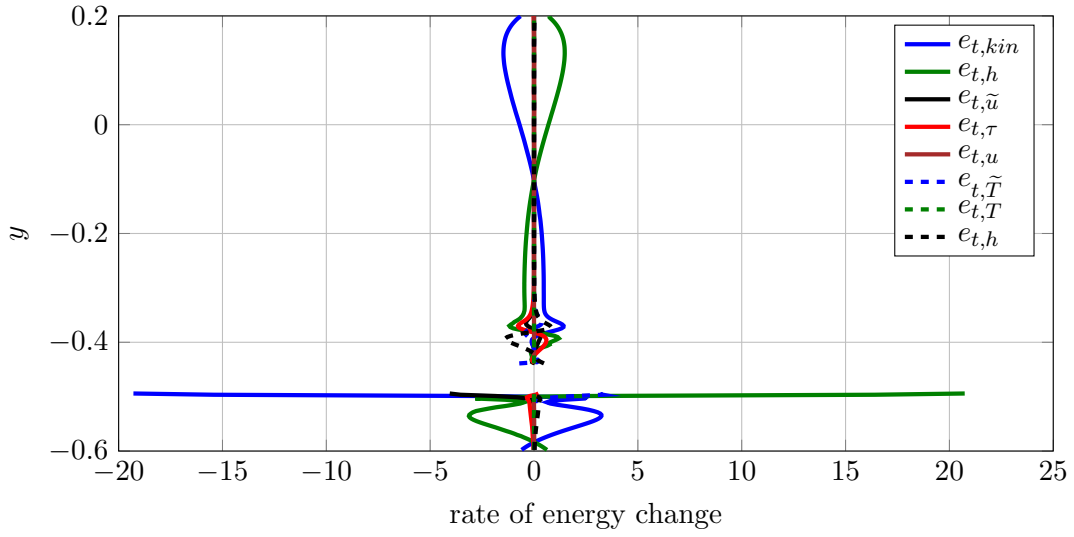

(a)

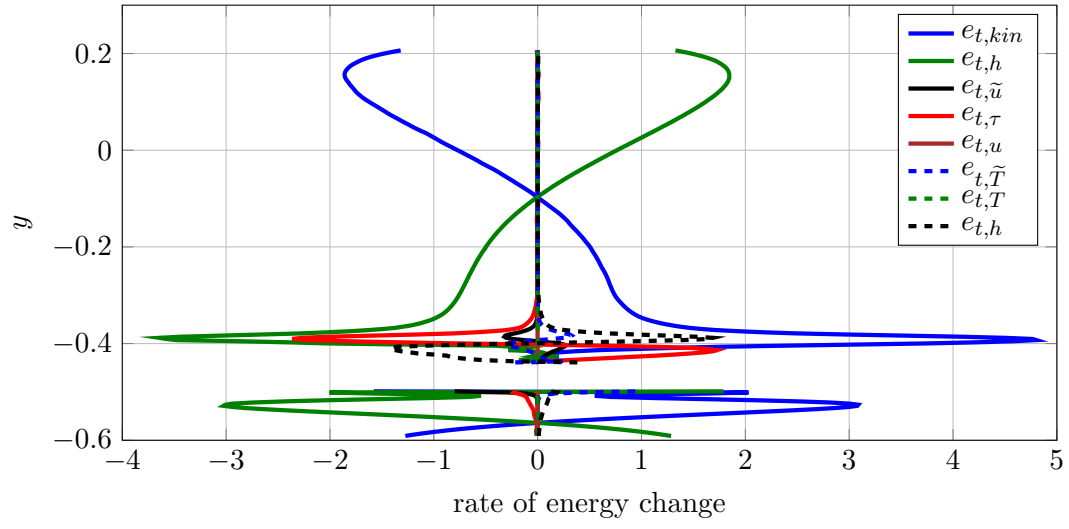

(b)

FIGURE 5.17: Favre averaged total energy budgets in the separation bubble close to the trailing edge ($x = 0.83$) for the simulations at $Re_{is} = 60,000$ (a) and at $Re_{is} = 100,000$ (b).

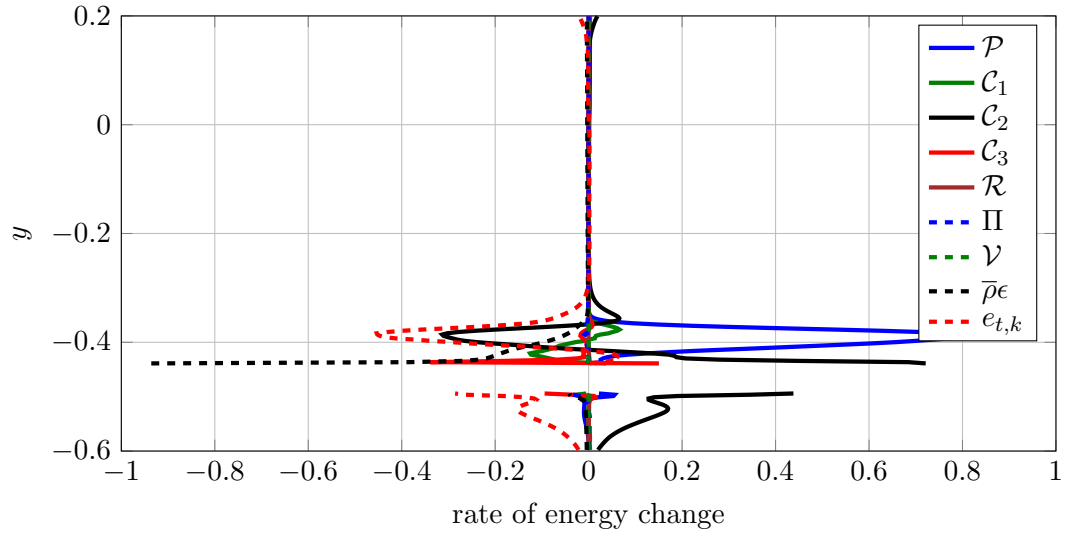

(a)

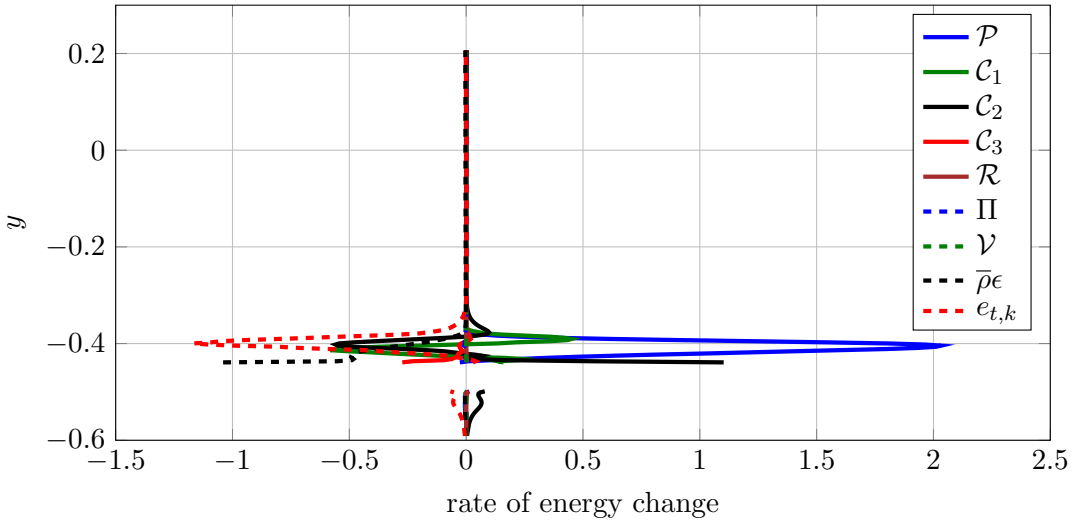

(b)

FIGURE 5.18: Favre averaged TKE budgets in the separation bubble close to the trailing edge ($x = 0.83$) for the simulations at $Re_{is} = 60,000$ (a) and at $Re_{is} = 100,000$ (b).

Chapter 6

Turbulence Characterization and Modelling

In literature Favre averaged approaches to obtain numerical predictions of flows through LPTs are wide spread. As discussed in chapter 1 these models only solve the mean flow equations where often the ensemble averaging is replaced by a time averaging. This averaging process results in terms that are solely governed by mean flow components and are part of the solution and terms that are influenced by the fluctuations of the flow field. Since the fluctuating part of the flow field is not solved for, models have to be applied to account for the effect of the fluctuating part on the Favre averaged flow field and, thus, close the system. To understand the accuracy of some selected models the prediction of these terms based on the DNS mean flow field are compared with the sampled quantities that have been presented in chapter 5. The results presented in this chapter have partly been published in Pichler *et al.* (2015) and in Michelassi *et al.* (2015).

6.1 Testing strategy

Before the results are presented the testing strategy is outlined. First the models that are used in this work are discussed and then error definitions to fully assess the different RANS models are introduced. Since the largest Reynolds stress components appear in the wake the focus in this chapter is on the wake region. Generally for studies of the wake the coordinate system is aligned with the wake center line and the direction perpendicular to the wake. In order to compare with these works a second coordinate system is introduced as indicated in figure 6.1. Both coordinate systems have the same spanwise direction (3), which is perpendicular to the plane presented. Coordinate system $1-2$ is the coordinate system that has been used throughout this work where 1 is the axial direction and 2 is the pitchwise direction. The "wake-aligned" coordinate system

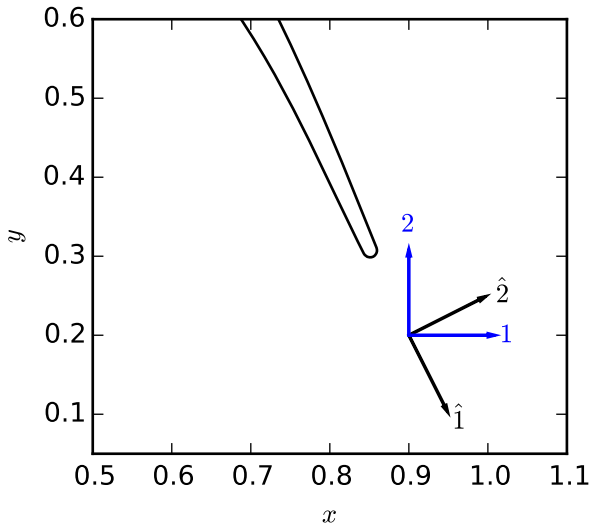

FIGURE 6.1: Coordinates systems used in this work.

$\hat{1}-\hat{2}$ is obtained by rotating the $1-2$ coordinate system by the outlet flow angle of 63.2 degrees in the clockwise direction about the 3 axis. To convert results between the two coordinate systems, standard transformation matrices are used for vectors and tensors.

6.1.1 Description of the models used in this work

First the models are defined by presenting a model for each term presented in table 5.1 depending on fluctuations. Currently, many Favre averaged predictions of LPT flow fields are obtained using one variant of the eddy-viscosity model relying on a linear coupling of the mean strain field and the Reynolds stress (RS) as introduced by Boussinesq (1877). It is based on an equivalence to the constitutive relationship for molecular stresses which is generally accepted as a valid approximation. The main difference between molecular motion and turbulence is in the significantly larger length and time scales of turbulence leading to substantial errors in several flows using a linear relationship (Wilcox (1998) and Pope (2000) for a more detailed discussion). Even though these models have substantial deficiencies they are widely used due to their robustness and simplicity. In practice these models are often tuned for a certain geometry and flow type resulting in a good agreement with experiments (e.g. Pacciani *et al.* (2011) and Sanders *et al.* (2011)). Applying these tailored models to a wide range of geometries and flow conditions outside of the calibration space can lead to substantial errors. Higher fidelity models using non-linear constitutive relationships or full RS models are becoming more popular, but still suffer from numerical difficulties and also require more development to be adapted to particular engineering applications (Franke *et al.*, 2005). Since the low pressure turbine community did not yet agree on a single preferred model, it is difficult to draw general conclusions on the major problems in "the model". In the following

the models used in the testing are presented where all the variables in the constitutive relationships are taken from DNS, including k and ϵ.

6.1.1.1 Assumptions used in all models

As mentioned above a model for each term containing fluctuations in the transport equations of Favre averaged total energy and Favre averaged momentum has to be provided. These terms are summarized in the top three sections of table 5.1. Given that many RANS models (also nonlinear models) use the transport equation of turbulence kinetic energy (eq. 1.35), it is used for all models discussed in this work requiring models for the terms in the bottom section in table 5.1.

Considering that terms depending on the time averages of the Favre fluctuations of velocity, $\overline{u''}$, and temperature, $\overline{T''}$, would be zero in the incompressible limit, it is generally assumed that terms multiplied by those can also be neglected at the low Mach numbers generally present in LPTs as has been discussed in chapter 5. Hence, the terms $e_{t,u''}$, $e_{t,T''}$ and $\mathcal{W}$ are also neglected. Similarly also the pressure dilatation term is zero for incompressible cases and, therefore, often assumed to be zero for compressible turbulence models at low Mach numbers and this assumption is used in this work as well.

For the Reynolds stress tensor only linear stress models based on the Boussinesq approximation are considered in this work. It is comprised of an isotropic and anisotropic contribution given by

$$\tau_{b,ij} = \underbrace{2\mu_t \left[\widetilde{S}_{ij} - \frac{1}{3}\widetilde{S}_{ii}\,\delta_{ij}\right]}_{\text{anisotropic}} - \underbrace{\frac{2}{3}\overline{\rho}k\delta_{ij}}_{\text{isotropic}} \tag{6.1}$$

as discussed in more detail in section 1.3.4. The isotropic part requires modelling of k which for all models used in this work is done by using the transport equation for k. Considering the anisotropic part the Favre averaged strain rate can be obtained from the mean flow solution but the turbulence viscosity has to be provided to fully define the RS model. However, there is no universally accepted governing relationship such that different approaches for computing μ_t are compared in this work and they will be defined in the next section for each model.

The diffusion terms $\mathcal{C}_1$ to $\mathcal{C}_3$ are generally modelled using the gradient diffusion hypothesis defined as (Wilcox, 1998)

$$C_{gd} = \frac{\partial}{\partial x_j}\left[\left(\mu + \frac{\mu_t}{\sigma_k}\right)\frac{\partial k}{\partial x_j}\right], \tag{6.2}$$

where the common value of 1.0 for the constant σ_k for $k-\epsilon$ models is used. Note that in contrast to Wilcox (1998), who neglects the pressure diffusion, $\mathcal{C}_2$, C_{gd} is also used

to model $\mathcal{C}_2$, providing results that are in better agreement as will be shown later. This might be an artefact of the tuning of the parameters to mean flow results such that the missing contribution by not using model for $\mathcal{C}_2$ is counteracted by a larger contribution of C_{gd}.

The final term that requires modelling is dissipation and a transport equation can be derived for it. However, the contributions in this equation are dominated by higher order moments of the fluctuations and their derivatives and, therefore, by the small scale information. Due to the limited availability of measurement data of higher order moments the existing models the terms in the equations are not linked to the respective terms in the transport equation of ϵ but are based on more abstract physical considerations (Wilcox, 1998). Dissipation can also be obtained by modelling the transport equation the turbulence frequency (ω) which is the second popular approach. Together with their derivatives and combinations like the shear stress transport model (Menter, 1994) they comprise the majority of dissipation modelling. However, due to the missing link between the model and the budgets of the transport equation of ϵ a direct evaluation of the terms cannot be performed and, therefore, no assessment of the terms in these transport equations is performed.

6.1.1.2 Model specific assumptions - turbulence viscosity

In the previous section widely used modelling assumptions have been presented and these assumptions are used in many works published in literature. However, the turbulence viscosity is defined in different ways for specific models and several studies adjust the standard parameter constants to better match experiments. If a "different" constant resulted in a better match than either the parameter identified by the model developers was wrong or it is not a constant and a more general model would have to be applied. Assessing the universality of model requirements would require a larger database which is not available in this work. Therefore, the difference between the models tested is how the turbulence viscosity is defined, which is outlined in the following.

Standard $k-\epsilon$: The first turbulence viscosity formulation used in this work is the wide spread approach based on dimensional arguments that appears in many two equation models like the $k-\epsilon$ model, the $k-\omega$ model and their derivatives. Essentially the turbulence viscosity is given by

$$\mu_{t,k\epsilon} = c_\mu \overline{\rho} \frac{k^2}{\epsilon}, \tag{6.3}$$

where c_μ is a proportionality coefficient and for the $k-\epsilon$ model the standard value of 0.09 is used. Considering that $\epsilon = \omega k$ a similar equation holds for the $k-\omega$ model. The major difference between these two models is in the transport equation for either ϵ

or ω. Since DNS values are used the errors are equivalent for both models. Note that turbulence models are generally calibrated to give best results in comparison with mean profiles. Hence, it is conceivable that the turbulence viscosity predicted by a model gives a smaller error than the one using DNS results (Wilcox, 1998) for k and ϵ. Therefore, care has to be taken using the viscosity defined from DNS results because this viscosity does not represent a lower bound for that error and actual turbulence models might perform better. However, since the calibration depends on a particular flow, this cannot be expected to hold in general and would suggest that something is not correct in the underlying physical modelling assumptions.

Minimum RS error: In chapter 1 a turbulence viscosity yielding a minimum error in the Reynolds has been defined as

$$\mu_{t,\tau} = \frac{1}{2} \frac{\sum_{k=1}^{3} \sum_{l=1}^{3} \widetilde{S}^*_{kl} \tau^*_{kl}}{\sum_{k=1}^{3} \sum_{l=1}^{3} \widetilde{S}^{*2}_{kl}}, \tag{6.4}$$

where * denotes the anisotropic (deviatoric) components of the tensors. This turbulence viscosity uses the RS obtained from DNS and is not obtained from physical understanding. Rather it is the result of the minimization of the error in the RS and this dependence on the RS prevents its use in RANS models where the RS is the solution and cannot be used as an argument. Still it is useful since it serves as an indicator for the best possible performance of linearmodels and indicates the improvement potential of other models. However, it is the divergence of the RS that is responsible for the turbulent mixing and not the RS directly such that it is not guaranteed that $\mu_{t,\tau}$ yields the smallest error in the RANS model.

Minimum Error in the shear component of the Reynolds stress: Minimizing the error in the Reynolds stress does not necessarily lead to a minimum error in Reynolds stress models. Considering a turbulent boundary layer for example the spatial distributions in the streamwise and spanwise direction are almost uniform such that a model predicting them wrong would not lead to an error in the divergence as long as it predicts it equally wrong in these directions. Hence, improving the prediction of the wall normal gradients and in particular the shear component might be beneficial. Therefore, some works focus on the accurate prediction of the shear component of the Reynolds stress. This relies on small spatial variations of the Reynolds stress which cannot be expected to hold for the large spatial variations in the trailing edge region. Nevertheless, optimizing for the shear component only might help since shear is an important

mechanisms in that area. Therefore, a third turbulence viscosity, given by

$$\mu_{t,sh} = \frac{1}{2}\frac{\hat{\tau}^*_{12}}{\hat{S}^*_{12}}, \tag{6.5}$$

is used. Note that wake aligned quantities are used to optimize in the wake normal direction. Due to $\hat{S}^*_{12}$ being in the denominator, $\mu_{t,sh}$ tends towards infinity for non-zero values $\hat{\tau}^*_{12}$ if $\hat{S}^*_{12}$ approaches zero. The idea of this optimization is to allow a larger error in the other RS components since those are assumed to cause less error to the mean. In order to prevent numerical difficulties a limiter of ± 0.005 for $\mu_{t,sh}$ is used. Similar issues would arise for $\mu_{t,opt}$ in case all anisotropic strain rates would approach zero at the same location, which however, is less likely such that no limiter is used for $\mu_{t,opt}$.

6.1.2 Testing framework

To fully test the influence of a turbulence model all terms requiring modelling have to be assessed. Note that all testing performed in this work is so called "a priori" testing and as such only tests the errors in the prediction of the modelled term. However, in many flow studies the mean flow field (e.g. ρ, $\vec{u}$, T) is the target and the analysis presented here does not directly give the error in the solution as will be discussed in more detail later. These have been presented above and in the following the corresponding errors for each term are introduced. For all terms that are considered negligible in standard models no error is defined and the magnitude of these terms presented in chapter 5 directly gives the error. First the modelling error in each component of the RS is defined as

$$\zeta_{m,ij} = \tau_{ij} - \tau_{m,ij}, \tag{6.6}$$

along with its magnitude

$$\zeta_m = \left|\left|\sum_{j=1}^{3}\sum_{i=1}^{3}\zeta^2_{m,ij}\right|\right|. \tag{6.7}$$

In addition the relative error is defined as

$$\zeta_{r,m} = \frac{\zeta_m}{\left|\left|\sum_{j=1}^{3}\sum_{i=1}^{3}\tau^2_{ij}\right|\right|}. \tag{6.8}$$

Relative and absolute errors allow to understand the error in the Reynolds stress, hence, the quantity that is model However, the actual error appearing in each component of the Favre averaged momentum equation is given through

$$\xi_{m,i} = \frac{\partial}{\partial x_j}\left(\tau_{ij} - \tau_{b,ij}\right), \tag{6.9}$$

Name	Re_{is}	TI
T1	60,000	0.2%
T2	60,000	3.8%
T3	100,000	0.2%
T4	100,000	3.8%

TABLE 6.1: Cases used to compared linear stress-strain models

where the modelled $\tau_{b,ij}$ depends on the choice of μ_t. Hence, the distribution of the RS in space is more important rather than the exact amplitude. Furthermore the modelled RS introduces an error in the Favre averaged total energy equation given by

$$\chi_{\tau,m} = \frac{\partial}{\partial x_j}\left(\widetilde{u}_i \tau_{ij} - \widetilde{u}_i \tau_{m,ij}\right). \tag{6.10}$$

In this work for all turbulence models discussed TKE is modelled using the Favre averaged transport equation for TKE. The error in production of TKE is quantified as

$$\chi_{\mathcal{P}} = \overline{\rho}\left(\tau_{ij} - \tau_{m,ij}\right)\frac{\partial \widetilde{u}_i}{\partial x_j}. \tag{6.11}$$

Finally, the error in the diffusion terms in the transport equation of TKE modelled by the gradient diffusion hypothesis results in

$$\chi_{\text{diff}} = \frac{\partial}{\partial x_j}\left[\overline{u_i'' t_{ij}\left(u''\right)} - \overline{p' u_i''}\delta_{ij} - \overline{\rho u_j'' \frac{1}{2} u_i'' u_i''}\right] - \frac{\partial}{\partial x_j}\left[\left(\mu + \frac{\mu_t}{\sigma_k}\right)\frac{\partial k}{\partial x_j}\right]. \tag{6.12}$$

6.2 Global investigations of the Reynolds stress error

In the following the errors in the Reynolds stress resulting from the use of different models are presented. Since the actual Reynolds stress and not its influence on the transport equations in this section $\mu_{t,opt}$ (representing the least error in the RS) is compared to $\mu_{t,k\epsilon}$ (representing a popular physical model) to understand the improvement potential of the latter in terms of the error in the Reynolds stress. Results for the cases presented in table 6.1 are available at two different Reynolds numbers and turbulence intensities. These four cases allow to investigate the influence of both Reynolds number and turbulence intensity on the Reynolds stress modelling error. First detailed results for case T2 are presented and then trends with respect to the other cases are shown. T2 is the case at lower Reynolds number with background turbulence intensity. To obtain $\mu_{t,k-\epsilon}$ the constant c_μ is set to the generally used value of 0.09. In figure 6.2 the errors previously defined for the Reynolds stresses are presented. The absolute minimum error of the RS is presented in figure 6.2 (a) which is the lower limit of all turbulence models. The largest errors occur within two regions that are close to the leading edge (point 1) and close to the trailing edge (point 2). Since it is a case with background turbulence, turbulence is present in the whole domain. The elevated error regions of the absolute error, obtained

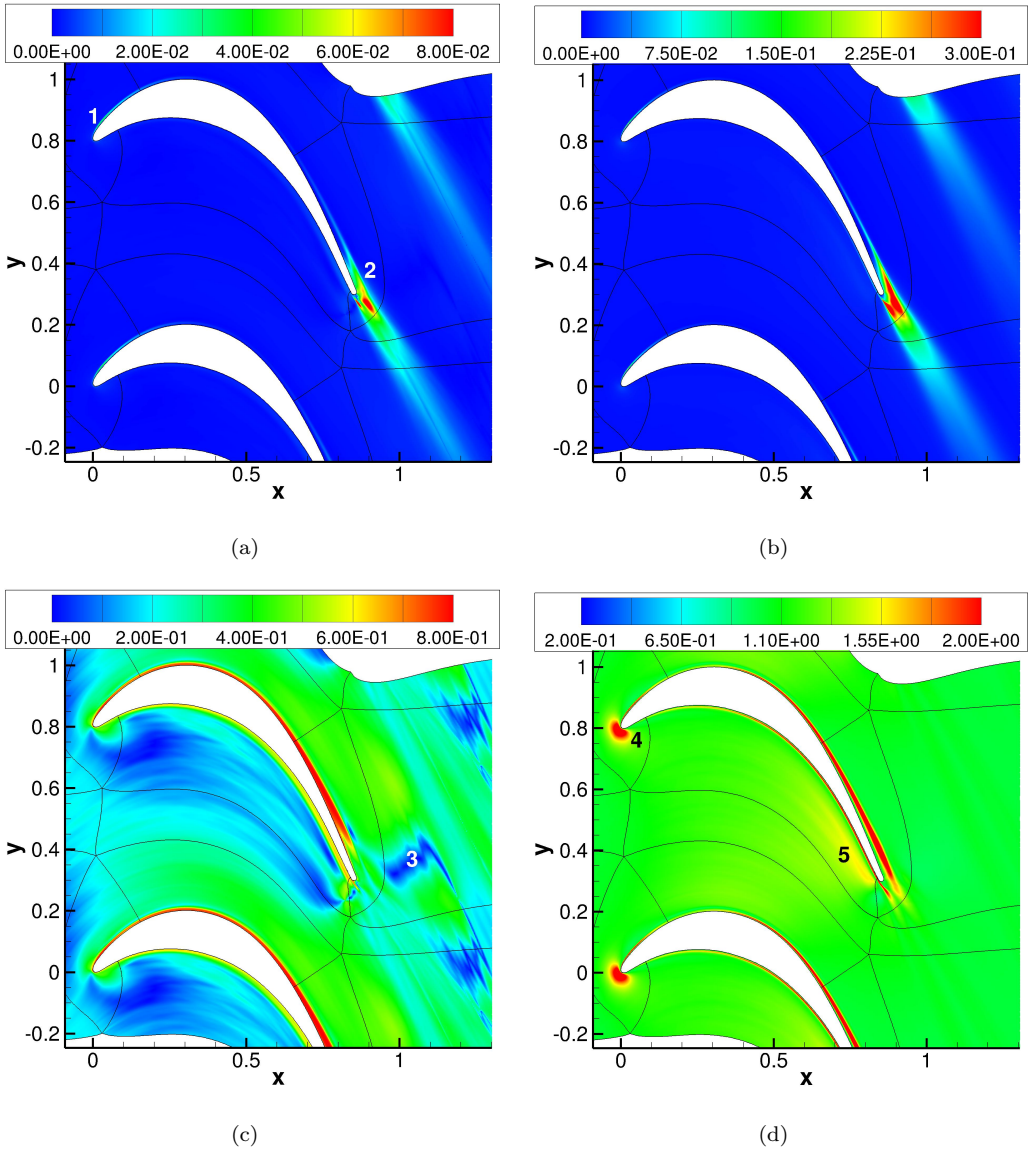

FIGURE 6.2: Error using linear turbulence models for case T2: (a) absolute minimum error ζ_{min}, (b) absolute error $\zeta_{k-\epsilon}$ using $\mu_{t,k-\epsilon}$, (c) relative minimum error $\zeta_{r,min}$ and (d) relative error $\zeta_{r,k-\epsilon}$ using $\mu_{t,k-\epsilon}$

using $\mu_{t,k-\epsilon}$ and presented in figure 6.2 (b), are confined to the same regions as for the absolute error using $\mu_{t,opt}$. However, the distribution changes slightly and the suction side error increases with respect to the pressure side error. The most notable difference is in the error magnitude being significantly higher (the contour levels are scaled by a factor of 3). The absolute errors indicate where most of the error is introduced but a low error does not necessarily mean an increased model validity. This is apparent by looking at the figures 6.2 (c) and (d) showing the relative error using $\mu_{t,opt}$ and $\mu_{t,k-\epsilon}$, respectively. The relative error shows the relation of the error to the Reynolds stress norm, i.e. if the error is unity the error is of the order of the Reynolds stress itself. Comparing the relative errors with the respective absolute errors the picture changes completely. The maximum absolute error region close to the trailing edge is not apparent at all in the

case of $\mu_{t,opt}$ and of slightly lower magnitude as the error in the boundary layer in case of $\mu_{t,k-\epsilon}$. Note, the problem with the relative error definition is that the error can be large even though almost nothing has to be modelled since the Reynolds stress itself is small. This is illustrated by both relative errors showing a complete invalidity of linear stress-strain modelling in the mostly laminar boundary layer. Therefore, the relative error is not considered alone but only used to comment on the validity of the Reynolds stress model in regions where the absolute error is high. Further, as mentioned above, turbulence models are calibrated using experimental data so that they might perform better than indicated by $\mu_{t,k-\epsilon}$. On the other hand in RANS solver both k and ϵ have to be modelled such that the performance could also be worse. The plots presented here show the error that would occur with correctly predicted k and ϵ.

First the general flow field is discussed before the focus is shifted to points 1-5 indicated in figure 6.2. In the inlet region both the absolute and the relative errors are small. The mean strain rates are small and any turbulence anisotropy would strongly depend on history effects. Hence, since the injected background turbulence is almost isotropic no anisotropy has to be modelled leading to small errors. In general, though, it cannot be expected that the Reynolds stress tensor of the incoming turbulences strongly depending on upstream behaviour is nearly isotropic such that general comments in this region are difficult to make.

The mean strain rates in the vane originate mainly from the potential flow and the absolute error still is small across the whole blade passage. In the relative error, it appears as if the error increases while turbulence is convected downstream which would comply with expectations. The Boussinesq approximation is based on the analogy with the modelling of molecular stress by a linear relationship to the strain rate, that is giving good results of the molecular stress for many flows (inlcuding LPTs). By contrast linear stress-strain models often fail for turbulence which is attributed to their longer time and length scales (Wilcox, 1998) so that they take longer to adapt to the strain field (often referred to as history effects). Since the anisotropic strain field is inhomogeneous in the blade passage the Reynolds stresses convected to this position have a different anisotropy and, therefore, a larger relative error. Once the turbulence leaves the inhomogeneous strain field it is higher than at the inlet. Since it is expected that the flow returns to isotropy further downstream this error is also expected to decay.

Linear stress-strain models of Reynolds stresses use simplified assumptions that do not hold for certain regions and do result in errors. In order to improve modelling it is therefore of interest to better understand which mechanisms are violated. As mentioned earlier, the Reynolds stress is the spatial derivative of the single-point single-time velocity correlation. In the following at points 1 and 2 as highlighted in figure 6.2, which have shown significant errors in modelling, the flow is investigated in light of

- Cause of the velocity fluctuations (component, structures) to understand what has to be modelled
- Composition of isotropic and anisotropic part of the Reynolds stress
- Validity of linear relationship and optimum $\mu_{t,opt}$
- Magnitude of error for separate components

Point 1 is considered by looking at a streamline going through the point with coordinates (0.01338952,0.04610836). While it is assumed that the boundary layer is laminar close to the leading edge, the flow above it is not and this is where the major error occurs. This area is of particular interest since the receptivity of the boundary layer is higher close to the leading edge as discussed in section 1.3.3 such that a wrong prediction of turbulence in this area might have an impact on the prediction of a transition model. The profile along a streamline is extracted since it allows to compare with other research where often the flow is parallel to one of the axis in the mean sense and the discussion considers the flow to be aligned with the streamline parallel and normal directions. Further, this means that the mean convection (in contrast to the turbulent transport) is along the streamline such that no mean convection to or from the streamline occurs. This helps to simplify the analysis in terms of budgets of transport equations. Nevertheless this means the actual shape of the streamline considered in general is more complex. It also should be noted that along the streamline mean quantities might change significantly over a short distance which for various simple canonical cases like fully developed channel and pipe flows is not the case and only more complex flows including stagnation points or flows past bluff bodies and airfoils show similar behaviour.

The streamline chosen is presented in figure 6.3 (a) and passes through the high error region at the inlet as depicted by point 1 in figure 6.2 (a). The annotations in the plot give the length along the streamline l and the line is colored by $\zeta_{\tau,min}$. In figure 6.3 (b) instantaneous flow structures around point 1 are presented using iso-surfaces of the Q-criterion at a level of 50 showing the orientation of the structures close to the leading edge. The development of the non-zero Reynolds stress components (solid lines) and their separation in anisotropic parts (dashed lines) and isotropic parts $2/3\rho k$ (dash-dotted lines) are plotted over the length along the streamline as presented in figure 6.4. All quantities in figures 6.4 to 6.6 are transformed so that the 1 direction is aligned with the streamline and the 2 direction is normal to the streamline and to the spanwise 3 direction. From figure 6.2 (a) it can be seen that the leading edge position is at $l \sim 0.08$ and the highest error region is around $l = 0.15$.

Focusing on the leading edge first ($l \sim 0.08$), in each of the Reynolds stress components (solid lines) a negative peak is apparent around the leading edge but not at the same point. In figure 6.3 (a) the positions of the negative peaks in each component are

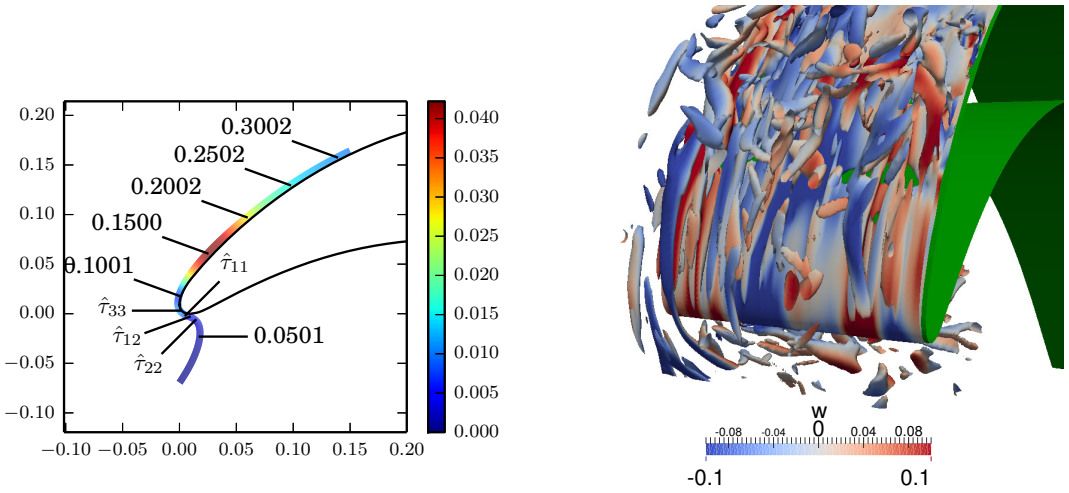

(a) (b)

FIGURE 6.3: Streamline colored by $\zeta_{\tau,min}$ (a) and instantaneous flow structures visualized by the second invariant of the velocity gradient tensor $Q = 50$ colored by the spanwise component of velocity (b) for case T2 at point 1 as indicated in figure 6.2

denoted by $\hat{\tau}^*_{ij}$ to allow for better orientation. Up to $l = 0.05$ the stress tensor is mostly isotropic indicated by the almost equal normal components being of the same order as $2/3\rho k$ and the significantly smaller shear stress component. While approaching the leading edge region, initially the normal components perpendicular to the streamline τ_{22} and τ_{33} are decreasing in amplitude and the streamwise normal stress component increases in amplitude. On the approach towards the blade surface the negative peak of τ_{22} is reached and then decays in amplitude which is expected to be due to the vicinity of the wall and the therefore smaller fluctuation amplitude normal to the wall (i.e. $\tau_{22} = \overline{-\rho u_2' u_2'}$ decays). This restriction does not apply to the spanwise fluctuations, resulting in a further decrease of τ_{33} until it reaches its peak at the leading edge and starts decaying along the suction side. At this stage the exact mechanisms responsible for this behaviour are not clear. Since close to a leading edge there is a stagnation point with an associated strain field around it, this strain in conjunction with the Reynolds stresses will lead to production of Reynolds stresses. But this cannot be the only source since the biggest increase in magnitude is in τ_{33} but the production of τ_{33} only depends on mean velocity gradients being zero by definition. It is expected that the reorientation and wrapping of the free-stream turbulence close to the leading edge as shown in figure 6.3 (b) leads to this decrease. Turbulence structures approaching from the inlet are generally randomly orientated but due to their convection they are wrapped around the leading edge leading to thinner more elongated structures. The decomposition of the normal stress components results in only a moderate increase in magnitude in turbulence kinetic energy compared to the increase in magnitude of the anisotropic stress components. Past the leading edge all Reynolds stress components but τ_{11} decay. Close to the leading edge also τ_{11} starts decaying but then a large increase is apparent a short distance downstream of the leading edge. This increase is expected to be due to the leading edge separation

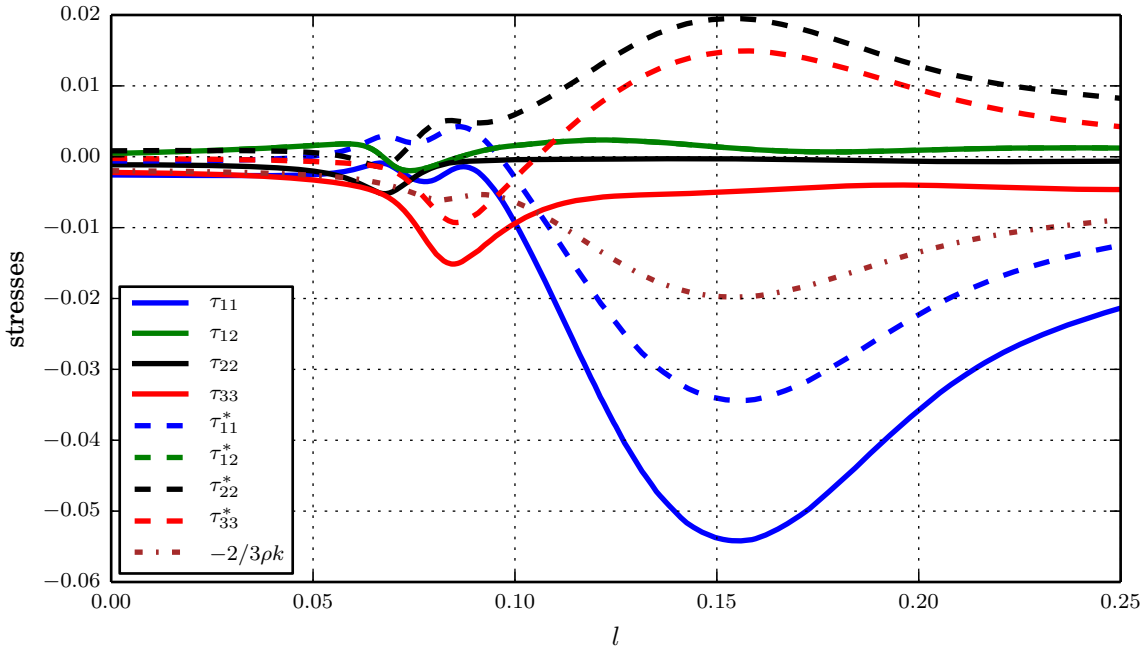

FIGURE 6.4: Components of Reynolds stress and anisotropic part of the Reynolds stress at point 1.

bubble. In terms of the decomposition in anisotropic and isotropic parts the decrease of only one normal components of the Reynolds stress results in an increase in magnitude of the turbulence kinetic energy at a third of the rate of the normal component. Since the other two normal components remain at the same level the rate of change in turbulence kinetic energy directly results in a change of the anisotropic parts in these components.

Using linear stress strain models the anisotropic parts are modelled using the traceless strain rates. The components of both tensors are plotted in figure 6.5 along with $\mu_{t,opt}$ depending only on the two tensors as given by equation 6.4. Note that by definition the shear component τ_{12} is equivalent to the anisotropic shear component τ^*_{12} such that the two lines fall on top of each other. In order for the linear relation to be valid at each point one scalar value would have to give the ratio between the strain and the respective stress component. In the inlet region the anisotropic stress and anisotropic strains are small and the actual model contribution is negligible. All strain rates but S^*_{33} experience significant peaks around the leading edge which is expected due to the flow field being close to a stagnation point. In an incompressible flow S^*_{33} would be identical to zero since the dilatation is zero and in the compressible case the S^*_{33} component is one third of the dilatation. Past the leading edge the anisotropic shear strain is significantly greater than the anisotropic normal strains. Hence, a linear stress strain model would give a significantly higher shear stress as well. This is in contrast to the anisotropic stress components where actually the normal components are clearly larger than the

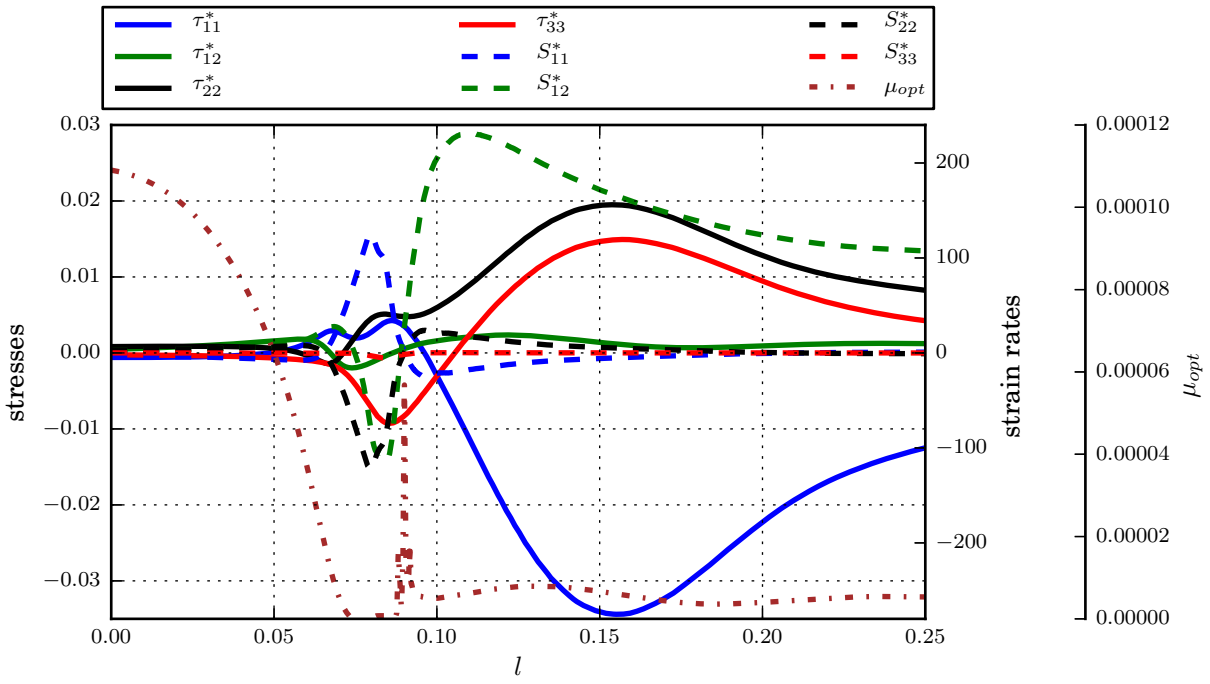

FIGURE 6.5: Components of anisotropic part of the Reynolds stress and anisotropic part of strain rate along with the turbulence viscosity resulting in the minimum error with a linear turbulence model at point 1.

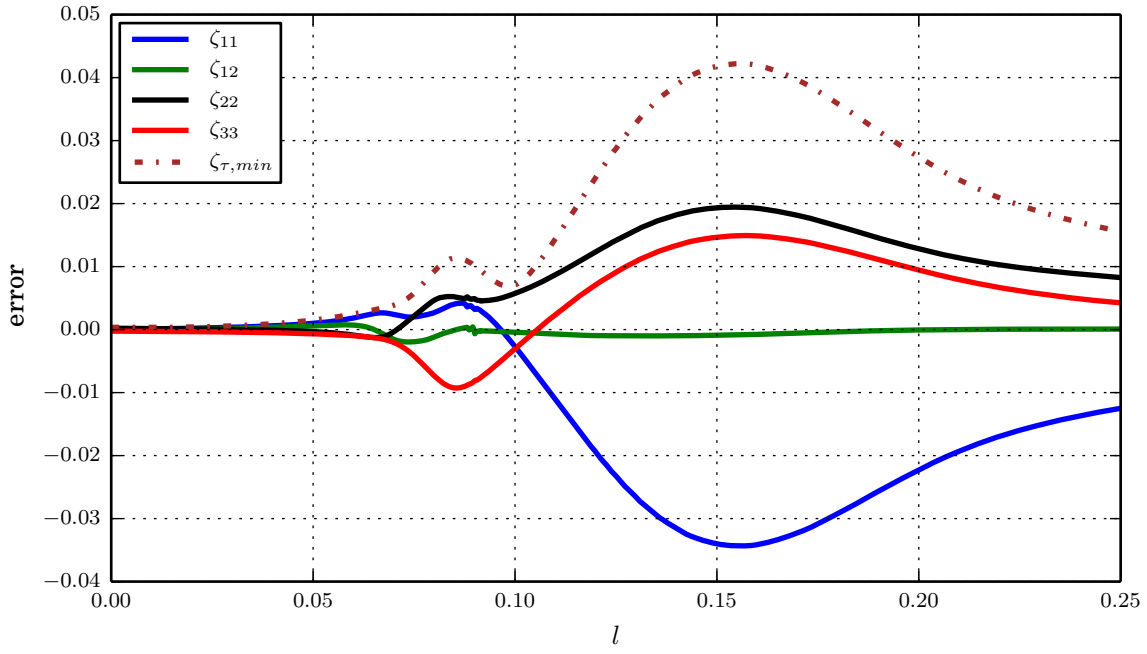

FIGURE 6.6: Minimum error in each component of the Reynolds stress due to modelling with a linear turbulence model at point 1.

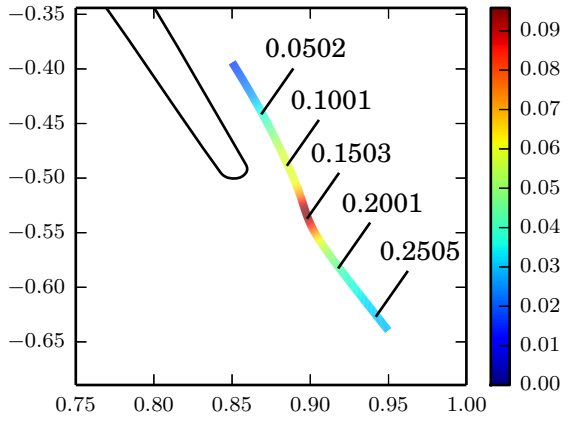

FIGURE 6.7: Streamline going though point 2 as shown in figure 6.2 (a)

shear component. As a consequence $\mu_{t,opt}$ (indicating the linear relation between the two anisotropic tensors as discussed earlier) reduces from the start of the streamline to the end of it even though the fluctuations increase which is somewhat contradictory considering that it is a turbulence quantity.

In figure 6.6 the difference of the simulated Reynolds stress and the linearly modelled one as given in equation 6.7 is plotted. The modelling of the anisotropic shear stress is captured well by the model using $\mu_{t,opt}$ which is expected simply for the fact that the anisotropic shear strain is significantly larger than the others and $\mu_{t,opt}$ is optimized to get this correct. Any larger value of $\mu_{t,opt}$ might model the normal stresses better but results in an increase of the error in the shear component. This results in the errors in the other components being similar to the actual stress. Hence, the normal components are completely miss-predicted. Most of the modelling discrepancy seems to be due to the separation zone.

The analysis only focuses on the local error and thus no direct conclusions on the global influence are possible. Generally speaking, though, it should be mentioned that due to the favourable pressure gradient downstream of the leading edge and the low Reynolds number, most of the fluctuations might decay to a level to low to cause transition. On the other hand this region is important for receptivity in terms of bypass transition. Hence, even small errors might be amplified.

Point 2 is located in the trailing edge region and again for this point a streamline going through the maximum error region is discussed in the following. In figure 6.7 similar to the previous discussion a streamline colored by $\zeta_{\tau,min}$ through the error region is shown where the labels along the line indicate the length along the streamline. In figure 6.8 the stress components in a coordinate system aligned with the streamline direction, the direction perpendicular to the streamline and perpendicular to the spanwise direction

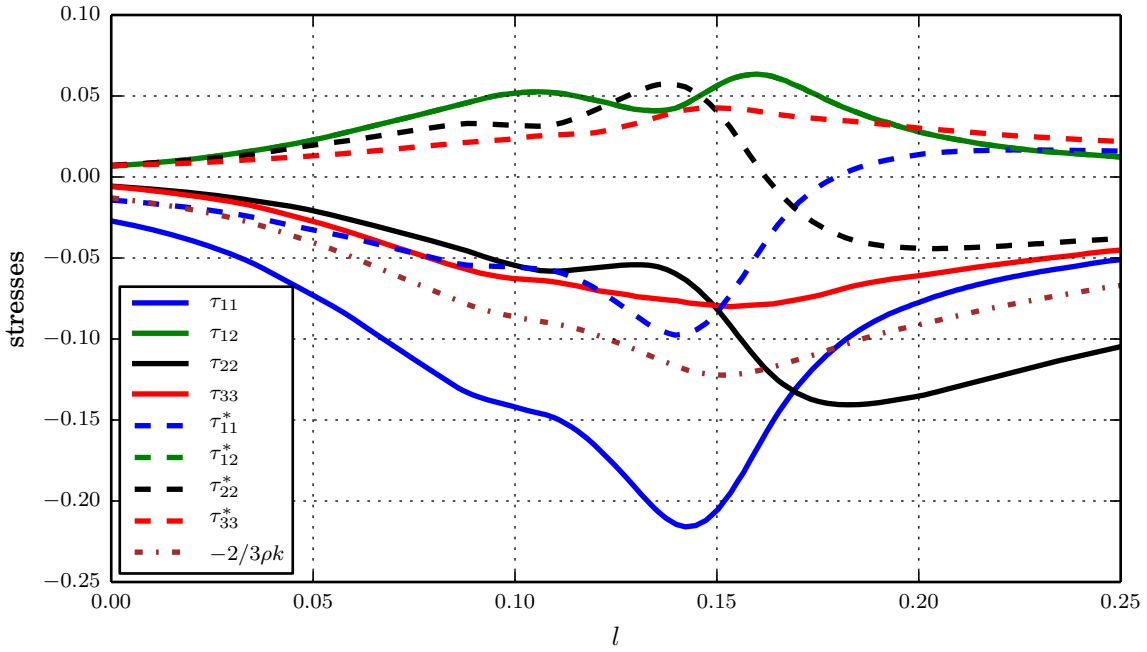

FIGURE 6.8: Components of Reynolds stress and anisotropic part of the Reynolds stress at point 2

and the spanwise direction are plotted. The flow at the trailing edge is influenced by both the open separation bubble and the vortex shedding. Along the streamline all stress components are mainly increasing in magnitude up to the maximum error position where the increase in τ_{11} is slightly greater than in the other components. The increase in magnitude is both in the isotropic and anisotropic parts where the isotropic part increases at a higher rate. Throughout the whole domain the isotropic part is greater than each anisotropic component such that the modelling of it is more important. Nevertheless, the anisotropic parts are significant and the modelling error might lead to significant errors in the solution. From the maximum error point on, all components but τ_{22} decrease in magnitude. The increase in τ_{22} is most likely due to a different alignment of the coordinate system with respect to the wake center line so that what seems to be an additional increase in magnitude is only due to the coordinate transformation (also resulting in stronger than expected decrease in τ_{11}). To understand the validity of linear stress-strain models the anisotropic stress and strain tensors are compared in figure 6.9. Compared to the leading edge region around point 1, here the anisotropic stress and strain components do mostly have at least the same sign (except for the spanwise component where the anisotropic strain is almost 0 again) indicating a better alignment of the two tensors. In the boundary layer the shear strain component is the major component similar to the leading edge. However, past the trailing edge it decays and at the end of the domain it is zero. Generally speaking, except for the spanwise component, the alignment improves with downstream distance from the

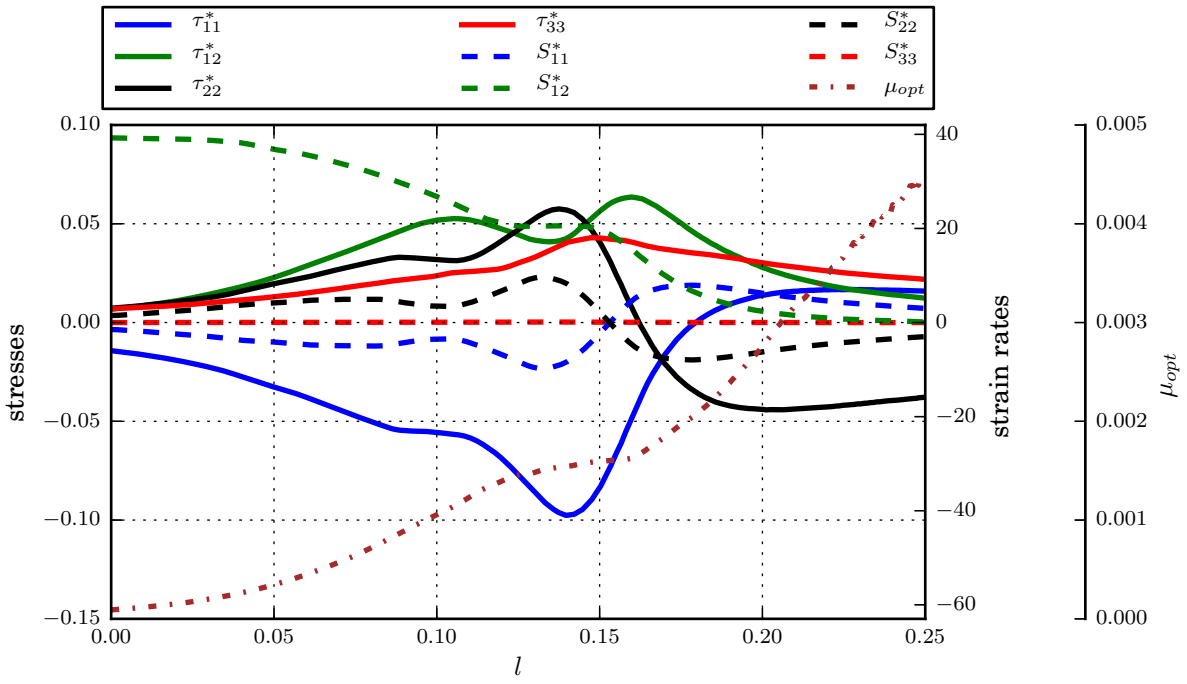

FIGURE 6.9: Components of anisotropic part of the Reynolds stress and anisotropic part of strain rate along with the turbulence viscosity resulting in the minimum error with a linear turbulence model at point 2

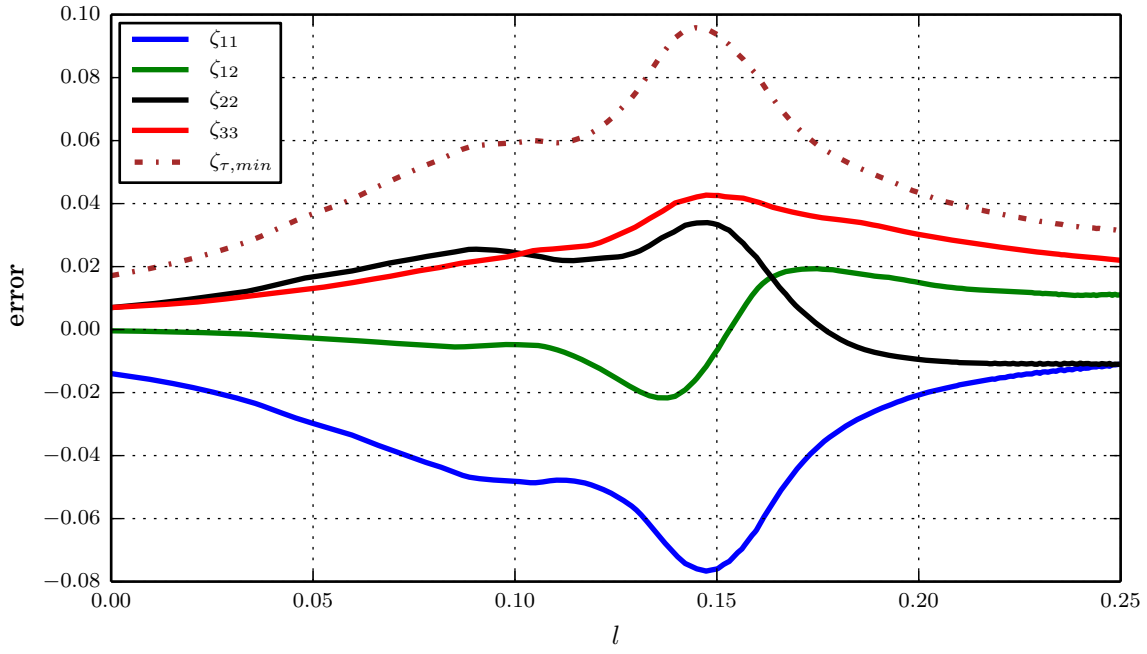

FIGURE 6.10: Minimum error in each component of the Reynolds stress due to modelling with a linear turbulence model at point 2

trailing edge which is expected due to the further developed wake and the break up of the spanwise coherent vortices shed at the trailing edge. This also results in an increase of the turbulence viscosity $\mu_{t,opt}$ that initially in the boundary layer is almost zero.

The error made using a linear model in the region around point 2 is plotted in figure 6.10. Similar to the leading edge region around point 1 the error seems to scale with the absolute magnitude. This confirms the conclusions made earlier discussing the relative error, that the model validity is equally poor for this flow and in regions with higher Reynolds stress the absolute error is largest in amplitude. Compared to the leading-edge region, though, the model is able to better predict the individual stress components and the alignment seems to be better. Comparing the error with the actual stress component it is found that at the end of the domain on average about 50% of the anisotropic stress is computed correctly. In terms of global influence it is expected that such a model would not be able to correctly predict the wakes, which has been reported in literature several times. However, further investigations are required to identify the processes and flow mechanisms that are not modelled appropriately by looking at budgets of the Reynolds stress transport equations.

Looking at figure 6.2 a few more regions are noteworthy to be mentioned. The relative error using $\mu_{t,opt}$ in figure 6.2 (c) shows variations around point 3 leading to a decreased error compared to the surrounding field. In this area the strain rates are small such that small changes in the strain lead to a zero crossing in the dominant error term. Hence, the smaller absolute errors are not related to a better model validity. Point 4 shows the well known phenomena of the $k-\epsilon$ model, that the strain field around a stagnation point results in unrealistically increased estimate of the Reynolds stresses, which is generally dealt with by limiters of the turbulence viscosity. That limiting the turbulence leads to no notable increase in error can be seen in figure 6.2 (c) where the only difference to the k-ϵ model is in the definition of the turbulence viscosity. In this case the turbulence intensity is adjusted intrinsically through the definition leading to no apparent increased error in this region. Finally, around point 5 a larger error region can be seen in figure 6.2 (d) which is expected to be due to the alignment of the vortices as reported by Wu & Durbin (2001*b*), resulting in higher anisotropy.

Comparing the absolute errors introduced through Reynolds stress modelling for a case with at higher Reynolds number (T4) shows a similar global picture but the error magnitudes are decreased. This is expected to be due to more three-dimensional flow and the therefore better validity of the modelling assumptions. Cases with no additional background turbulence (T1 and T3) do not show absolute Reynolds stress modelling errors in the inlet region around point 1. This is expected since in these cases the flow is mostly laminar and no turbulence has to be modelled. In the wake region at the trailing edge the error is increased which is attributed to more coherent structures due to the vortex shedding at the trailing edge and therefore a less three dimensional wake.

6.3 Detailed model assessment in the wake region

While in the last section the focus was on the Reynolds stress and relating its modelling error to physical considerations, in this section a detailed examination of the actual influence on the transport equation as can be done with the data provided in chapter 5 is presented. In the last chapter it was suggested to compare the predictions of turbulence models in a RANS solver on a term by term basis to DNS data. No RANS simulations are conducted in the scope of this work and the assessment of turbulence models is based on DNS mean flow predictions. As will be discussed in the following there are important differences between assessing the performance of a turbulence model based on a RANS flow field and a DNS mean flow field. Similar to chapter 2 where a vector equation for the instantaneous equations was developed also the mean flow equations can be transformed to a vector equation using the mean flow solution vector given by $\vec{\widetilde{q}} = [\overline{\rho}, \overline{\rho}\widetilde{u}_1, \overline{\rho}\widetilde{u}_2, \overline{\rho}\widetilde{u}_3, \overline{\rho}\widetilde{e}_t]^T$ where each component of the vector equation is given by

$$\frac{\partial}{\partial t}\widetilde{q}_i + \frac{\partial}{\partial x_j}\left(\widetilde{u}_j \widetilde{q}_i\right) = S_i + M_i \,. \tag{6.13}$$

The r.h.s. terms of eqns. (1.18)-(1.19) are grouped such that S_i contains all terms depending on mean quantities only. The term M_i is comprised of the terms dependent on unknown fluctuations that have to be modelled (in blue, eqns. (1.18)-(1.19)). In case that a model is not appropriate a modelling error $M_{i,e}$ would be introduced. Since the equation still has to be balanced a different solution $\hat{q}_i$ is obtained. However, the source term S_i is a function of the solution vector q_i such that it will differ between the solutions q_i and $\hat{q}_i$ leading to the source error $S_{i,e}$

$$\frac{\partial}{\partial t}\widetilde{\hat{q}}_i + \frac{\partial}{\partial x_j}\left(\widetilde{\hat{u}}_j \widetilde{\hat{q}}_i\right) = (S_i + S_{i,e}) + (M_i + M_{i,e}). \tag{6.14}$$

The difference between the solutions $\widetilde{q}_i$ and $\widetilde{\hat{q}}_i$ is the mean flow error $\delta_i = \widetilde{\hat{q}}_i - \widetilde{q}_i$. Substituting δ_i into eqn.(6.14) and subtracting it from eqn.(6.13) a transport equation for this error can be derived resulting in

$$\frac{\partial \delta_i}{\partial t} + \frac{\partial\left(\widetilde{u}_j \delta_i\right)}{\partial x_j} = S_{i,e} + M_{i,e} - \frac{\partial}{\partial x_j}\left(\left(\widetilde{q}_i + \delta_i\right)\left(\widetilde{u}_j - \widetilde{\hat{u}}_j\right)\right). \tag{6.15}$$

From eqn. (6.15) it is apparent that the interaction of the modelling error $M_{i,e}$ and the mean flow error δ_i is not straight forward. Published work focusing on a direct assessment of the modelling error $M_{i,e}$ through collection of budgets of various transport equations mostly focused on canonical cases having two or three homogeneous or slowly varying spatial directions, where the accumulation of the error is easier to understand. However, the situation is less clear for more complex flows where the propagation of the mean error cannot easily be deduced directly, as in LPT flows. Comparing RANS results with experiments on the other hand directly provides the mean flow error δ_i, but its relation

to the modelling error M_i, particularly in a quantitative manner, is less clear. Since the gap between modelling error and mean flow error is quite complex for LPT flows both mean flow and turbulence modelling quantities are reported at various streamwise profiles.

Another important difference between mean flow and modelling error is that the modelling error $M_{i,e}$ is local, i.e. only comprised of local quantities. If the correct mean flow is known it can be used to understand the local error imposed by the modelling assumptions. On the other hand the error in the mean flow prediction δ_i is the solution of the transport equations 6.15 and as such contains the error generated at the particular position, but also all the error transported to the position under consideration. Therefore, it is less clear where the actual error does originate from. Hence, purely local considerations are not possible for the mean flow error. A local error definition though is helpful in the context of turbulence model development since it directly points to the error source.

6.4 Turbulence viscosity and RS results from the use of different models

In this section the error in the Reynolds stress model at $x = 0.9$ is discussed, i.e. at the same location at which the budgets have been presented in chapter 5. First the turbulence viscosities defined in the previous section are plotted in figures 6.11. Per definition $\mu_{t,opt}$ leads to the smallest error in the RS such that any difference in $\mu_{t,k\epsilon}$ and $\mu_{t,sh}$ would result in additional errors in the RS as defined in equation 6.7. Over a small section on the pressure side portion of the wake $\mu_{t,k\epsilon}$ closely resembles $\mu_{t,opt}$, but in general there are large differences between the two definitions and the overall agreement between those two is considered poor. The shear stress optimized turbulence viscosity $\mu_{t,sh}$ is mostly larger than the other two definition where the limiter is in use for a significant portion of the pitch. Note that outside the wake optimizing for the shear component as such is difficult to justify since it depends on the orientation of the coordinate system which is not apparent to choose outside of the wake. However, the magnitudes of the anisotropic RS is small such that the model development is most important in the wake. Hence, the results of this study are still considered important.

In figure 6.12 (a) - (d) the anisotropic RS from DNS is compared to linear RS models using the turbulence viscosities discussed above. Since there is zero strain in the 3 direction all linear models for component $\hat{\tau}^*_{33}$ regardless of the turbulence viscosity by default will fail to predict a non-zero RS as present in the DNS. The shear component $\hat{\tau}^*_{12}$ is best matched by the shear optimized turbulence viscosity $\mu_{t,sh}$ which, except for zero anisotropic shear strain gives correct results. However, all other components are significantly over predicted and the zero crossing close to the center of the wake results in

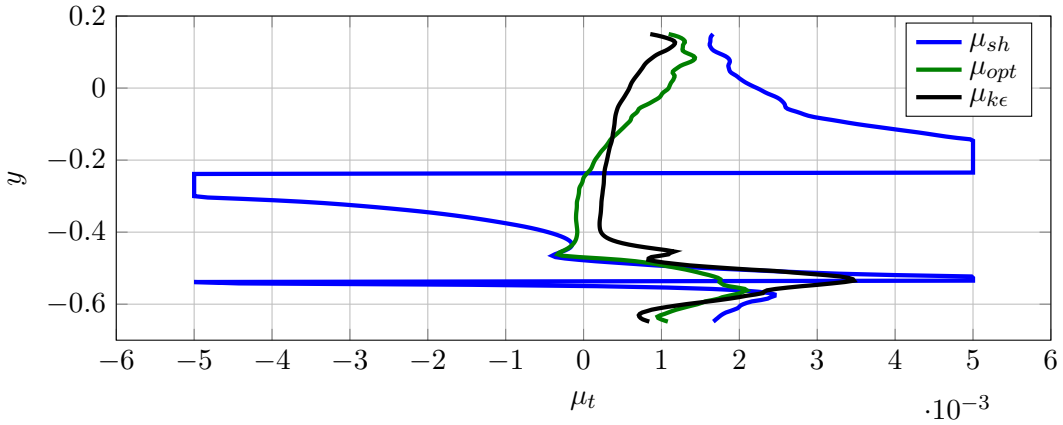

FIGURE 6.11: Turbulence viscosity according to the definitions used in this work immediately downstream of the trailing edge ($x = 0.9$) for the simulation at $Re_{is} = 60,000$.

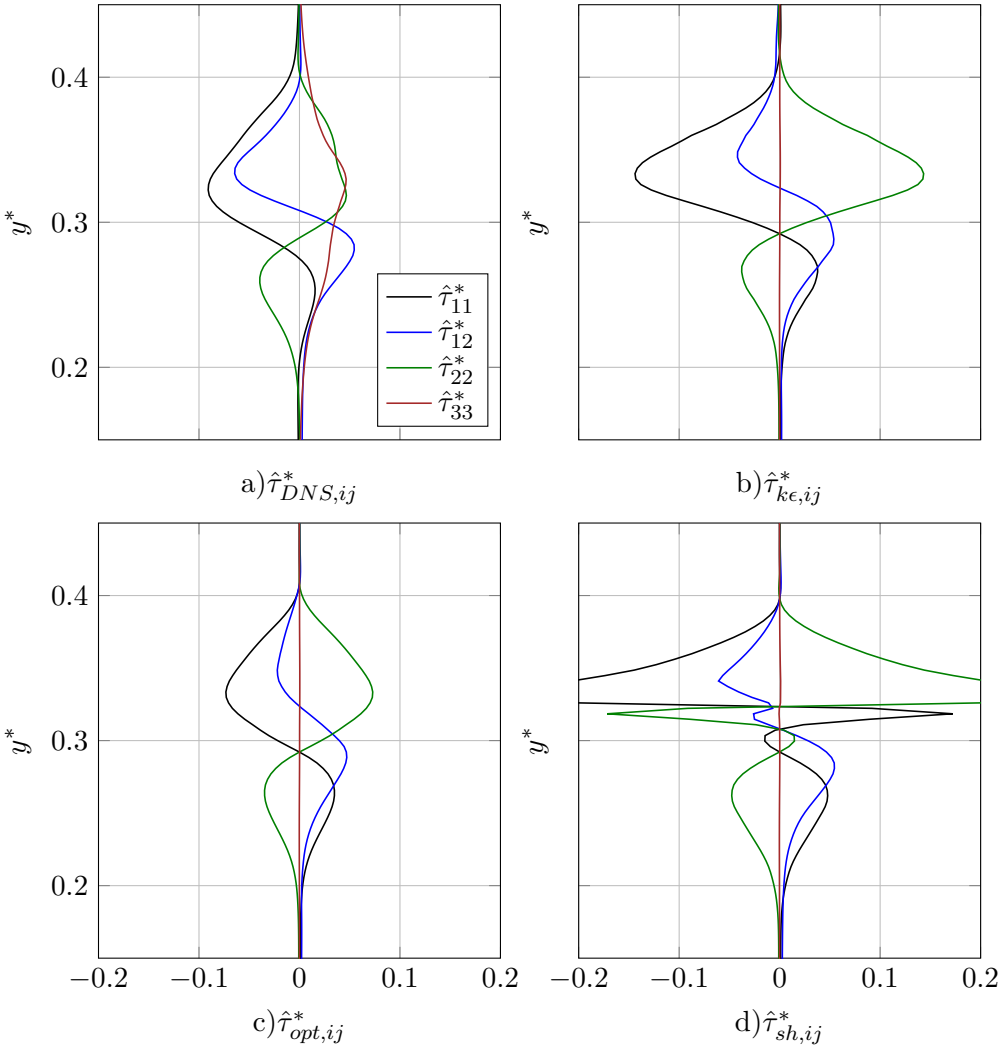

FIGURE 6.12: Comparison of anisotropic parts of the Reynolds stress from DNS (a) and the Reynolds stress computed using the $k\epsilon$ model (b), the optimized turbulence viscosity (c) and the shear stress optimized turbulence viscosity (d) immediately downstream of the trailing edge ($x = 0.9$) for the simulation at $Re_{is} = 60,000$.

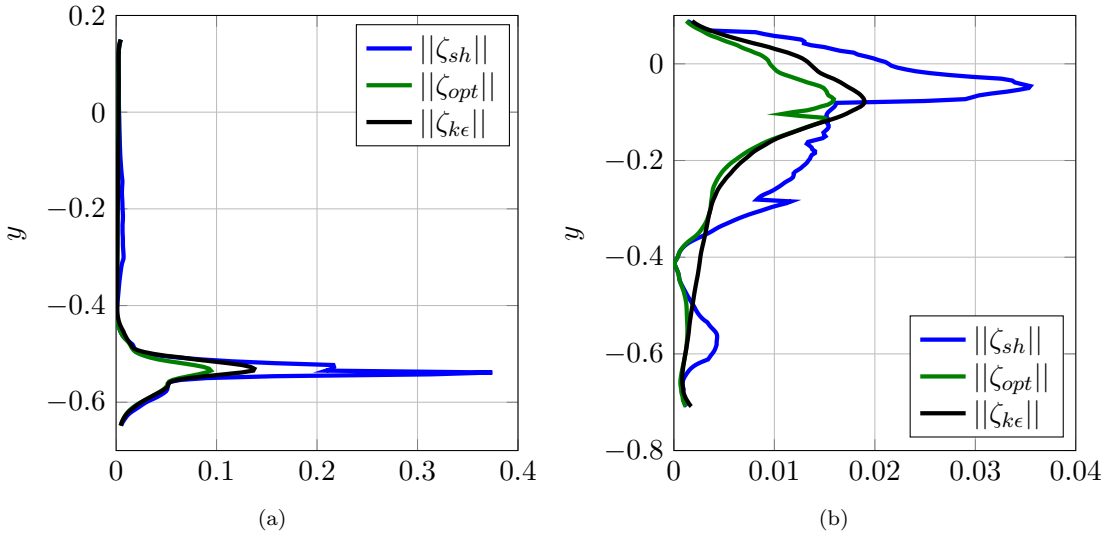

FIGURE 6.13: Reynolds stress modelling error at $x = 0.9$ (a) and $x = 1.1$ (b) for the simulations at $Re_{is} = 60,000$.

a significant peak in the profiles of $\hat{\tau}^*_{sh,11}$ and $\hat{\tau}^*_{sh,22}$. The optimized turbulence viscosity is the best compromise to match all components but still has significant deviation from the DNS results. The physically based $\mu_{t,k\epsilon}$ mostly predicts larger anisotropic RS with respect to $\mu_{t,opt}$ inside the wake region which is considered to be more important due to the higher RS values. Overall the suction side portion of the wake shows larger deviations for all models than the pressure side portion, indicating a stronger missalignment in that area. In general, $\mu_{t,k\epsilon}$ is closer to $\mu_{t,opt}$ compared to $\mu_{t,sh}$ holds also at the other locations discussed in chapter 5 but for conciseness are not plotted here.

6.4.1 Modelling errors in the wake

In figure 6.13 the error occuring in the Reynolds stress is presented in the near wake (a) and the further developed wake (b). As expected the results follow the conclusions from the previous paragraph where the smallest errors are achieved by using $\mu_{t,opt}$ and since $\mu_{t,k\epsilon}$ is closer to $\mu_{t,opt}$ than $\mu_{t,sh}$ also the errors of the $k-\epsilon$ model are smaller. Even though the ranking of the errors due to the three turbulence viscosity specifications is same in the further developed wake the differences between $\mu_{t,opt}$ and $\mu_{t,ke\epsilon}$ have decreased and there is little margin for improvement of $\mu_{t,k\epsilon}$ at this position.

In order to assess the performance of the different turbulence viscosities in terms of their influence on the transport equation of Favre averaged momentum, the error introduced in those in the near and further developed wake is plotted in figure 6.14, respectively for case T2. While the optimized turbulence viscosity indeed shows an improvement in the near wake, in the further developed wake there are sections where it performs better and worse. Like in the near wake the suction side leg is improved by using $\mu_{t,opt}$ but on the pressure side leg the performance is worse with a high peak. As discussed

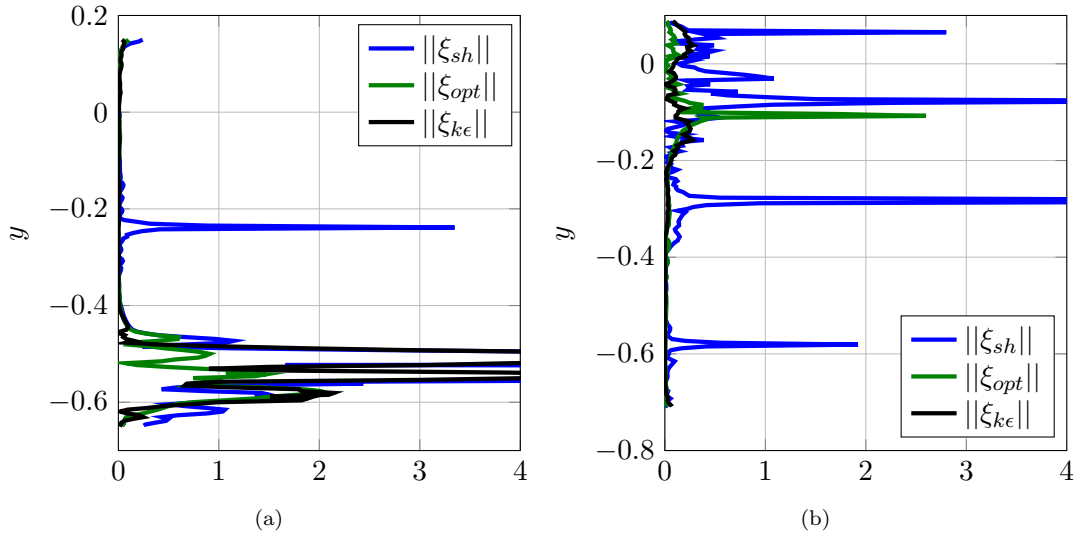

FIGURE 6.14: Modelling error in the divergence of the Reynolds stress at $x = 0.9$ (a) and $x = 1.1$ (b) for the simulations at $Re_{is} = 60,000$.

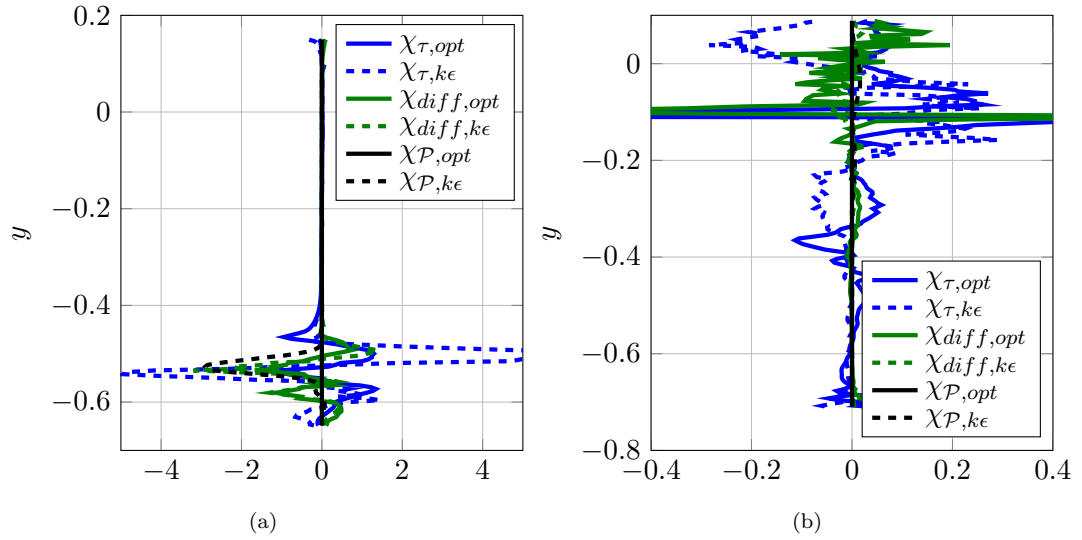

FIGURE 6.15: Modelling error in the transport equations of Favre averaged energy at $x = 0.9$ (a) and $x = 1.1$ (b) for the simulations at $Re_{is} = 60,000$.

above not the RS but its divergence enters the Favre averaged equations and therefore the spatial derivatives are important. Looking at the figure 6.13 (b) again it can be seen that the optimized profile shows a minimum at around y=-0.1. Large spatial changes in the RS lead to this minimum but these large spatial changes lead to larger derivatives direction inheriting large diffusion. This leads to a significant error in the divergence of the RS. The shear optimized turbulence viscosity shows several peaks related to zeros in the anisotropic shear strain rate and overall is significantly worse at both positions compared to the other two turbulence viscosities.

Finally the errors in the modelling of the transport equations of total energy and TKE are discussed. Again the performance of $\mu_{t,sh}$ is significantly worse and is not plotted

in figure 6.15 (a) and (b) for the near and further developed wake, respectively. The processing applied to obtain the error terms amplifies minor changes in the variables extracted from the time averaged simulation solution leading to visible noise in the profiles presented in figure 6.15. This is a particular issue if the magnitudes of the terms are small as in figure 6.15 (b) and there in particular $\chi_{diff,opt}$. However, the noise is smaller then the actual magnitudes such that the results still allow to rate the performance of the models discussed. As expected the error in the RS work χ_τ follows the conclusions of the RS errors discussed above. In the near wake a better performance compared to the physically inspired $\mu_{t,k\epsilon}$ is present and in the far wake both have their respective regions of strength. The error in the diffusion term, χ_{diff} is slightly smaller compared to the error in the RS work and also here the performance of $\mu_{t,opt}$ is better in the near wake and in the far wake its performance is better on the suction side leg while it has a similar performance for most of the pressure side compared to $\mu_{t,k\epsilon}$ and also suffers from peaks as discussed for ξ_{opt}. For production the situation is slightly different, as the error for the optimized case is almost zero. Indeed using $\mu_{t,opt}$ would result in zero error in the incompressible case. By contrast there is a nonzero error when using $\mu_{t,k\epsilon}$, however, it is smaller compared to the error in diffusion and RS work.

Chapter 7

Summary and Conclusions

Lowering the fuel consumption and improving the performance is of paramount importance in gas turbine design, both for aircraft engines and power generation. During all design stages it is important to assess different designs and rate their performance in terms of predefined parameters. Even though these parameters have been defined and research has revealed many physical processes and has given designers important tools to obtain these parameters, the accuracy of prediction methods, in particular if new concepts have to be assessed, is still not satisfactory. In this work several steps have been made that are intended to be of use to improve these design tools, which are summarized in the following.

The basic idea was to conduct direct numerical simulations (DNS) of LPTs in order to obtain additional insight into the flow dynamics. In the past mostly incompressible DNS of LPTs have been conducted and the focus of these studies has been on showing the superior prediction capability with respect to other models such as RANS. In addition, large scale turbulence physics were discussed and several important features of the flow have been revealed. However, none of these works focused on fine scale turbulence properties, in particular their higher order statistics. Therefore, this was chosen as the topic of the current work.

DNSs need to resolve small as well as large scales, resulting in grids with a large number of points. In order to solve these in a reasonable time frame a highly parallel optimized numerical method has to be used. The numerical method has been discussed in chapter 2 and is based upon HiPSTAR, which was previously used for DNS of various canonical flow cases as well as flows about airfoils. In terms of functionality, in addition to the available code base particularly new boundary conditions had to be developed as well as an efficient parallel treatment of the points where five grid blocks neighbour.

In addition to an accurate numerical method, computational performance is paramount and, therefore, computational performance has been improved as outlined in chapter

3. One of the major developments is an efficient turbulence generation method which for larger length scales and higher Reynolds numbers leads to a 30% reduction in run time. In addition tweaks to the message passaging interface (MPI) calls lead to a 10-15% speed up with respect to the original code. Due to the advent of graphics processing units (GPU) for numerical computations the code was ported to exploit some of the worlds largest computers. Comparing the performance of the NVIDIA Kepler K20x to an AMD Operton on the Oak Ridge leadership computing facility's cluster Titan, a speed up of more than 2x has been achieved. This was realized by using the OpenACC framework, which required to identify the parallel regions and limit the data transfer between CPU and GPU.

One of the key targets of the study was to collect data to help turbulence modelling, namely budgets of the Favre averaged transport equations of momentum, total energy and TKE. Since some of these quantities that were collected are based on the smallest scales of the flow, and none of the previous studies published in literature provided information on appropriate grid resolution to resolve the small scales, a thorough validation was conducted in chapter 4. While the mean flow quantities and terms dominated by large scales showed grid convergence for meshes of similar size as used in previously published studies, quantities related to dissipation in particular required a more refined grid.

Another important aspect was the validation of the boundary conditions, particularly at the inlet and outlet. For compressible simulations acoustic waves convect through the flow field. When they approach boundaries they are reflected. These are artificial reflections (in reality they would propagate out of the domain) that may alter the flow as has been shown in chapter 4. While characteristic boundary conditions that are widely used in external flows failed to sufficiently reduce spurious reflections, introducing a sponge layer successfully prevented reflections. The influence of fluctuations on the loss has been discussed when the simulations were compared against experiments. Simulations with similar background turbulence level as the experiment showed good agreement but conducting a "clean" simulation with no additional background turbulence lead to a significantly thinner and deeper wake. This is of interest since the experiment was conducted without a turbulence generation grid and the data provided does not allow to understand the energy spectra. It was suggested to conduct experiments at higher background turbulence level overlaying any acoustic signals and provide energy spectra to allow for better assessment of the accuracy of simulations. Overall boundary layer separation length and losses showed similar variations with Reynolds number and background turbulence as published in various other works. The simulation setup developed in this work has been used for other work published since then.

To help turbulence modellers and to give CFD users a reference to test their model of choice, budgets of the transport equations have been presented in chapter 5. Comparing the models term by term this dataset allows to understand the weaknesses of the model

of interest. In addition, the energy transfer in the wake region was discussed and the importance of the mechanisms was discussed. It was shown that in the near wake production of TKE exceeds dissipation while the opposite happens in the developed wake. Energy transfer mechanisms only comprised of first order statistics are more important than mechanisms due to second order statistics (i.e. turbulence) even though particularly in the wake turbulent mechanisms reach more than 60% of the mean convection in the near wake and are close to mean values in the further developed wake. The higher Reynolds number case shows lower levels of TKE in the near wake wake which was related to a smaller separation and the therefore smaller virtual trailing edge thickness leading to a less intense vortex shedding. This is also reflected in the stronger turbulence kinetic energy dynamics in the near wake except for dissipation being related to the smaller scales and, therefore, not directly influenced by the vortex shedding at this position.

Next linear turbulence models have been reviewed. A rational of how the testing of RANS models in this work relates to approach published in many LPT works, where RANS models were assessed in terms of their influence of the error in the mean, was presented. It was shown that the approach chosen in this work is able to pinpoint where the modelling errors are made but cannot directly be used to understand the influence of the modelling error on the mean flow field (a priori testing). However, it cannot give the error in the mean flow field. Three different turbulence models were investigated, all of them based on the Boussinesq approximation (linear coupling of Reynolds stress and strain) and only varying in the definition of the turbulence viscosity. In order to understand the improvement potential of standard models a standard $k-\epsilon$ model was compared with one version where DNS results were used to optimize the turbulence viscosity to minimize the error in the anisotropic Reynolds stess components or of the shear component only, respectively. It was shown that the performance of the shear optimized version was worse compared to the $k-\epsilon$ model. Optimizing for the full anisotropic Reynolds stress tensor was beneficial in the near wake region, particularly on the suction side leg of the wake. However, there is still a large error remaining in the fully optimized case such that the linear stress strain relationship fails. In the further developed wake there was almost no improvement of the optimized model such that it was suggested to use more sophisticated nonlinear approaches.

The global error picture revealed that the linear turbulence model fails with significant absolute error in the near wake and to a smaller extent close to the leading edge at the suction side. The latter error is related to the deformation of the inlet turbulence in the presence of the wall exhibiting a large favourable pressure gradient. Hence, it is only present for cases with inlet turbulence. The high absolute magnitude of the error in the near wake is due to the large Reynolds stress magnitude and not due to particularly bad modelling by the linear turbulence model compared to other positions, as was revealed by relative error plots. However, a linear relation will always result in an error in flow

regions exhibiting such characteristics, even when a turbulence viscosity is used resulting in the smallest possible error. Hence, only improving the prediction of the turbulence viscosity is not sufficient and nonlinear relationships are other constitutive relationships for the Reynolds have to be used.

7.1 Future work

In this work the wake generation and its mixing process downstream without the presence of a downstream blade row have been simulated and analysed. Wake generation and early mixing, though, is only the first step in the interaction with the next blade row which is crucial for the performance of low pressure turbines and other parts of engines. Therefore, the logical next step is to extend the analysis to the convection of the wake through the next blade row and then to the influence of the wake on transition of the subsequent blade row. This is expected to highlight the problems of current turbulence models and again give the designer a dataset for model validation. Simulations incorporating wakes generated by bars have already been presented in Michelassi *et al.* (2015), based on based on a further extension of the numerical setup presented here. Initial results for the assessment of RANS models for cases with upstream moving bars have also been presented in Michelassi *et al.* (2015).

With respect to issues of linear modelling issues it has been shown that an improvement potential of current approaches is in improving the predictions of the turbulence viscosity but even in case of the best eddy-viscosity model substantial errors will remain. Therefore, the analysis should be extended to non-linear models, in particular explicit algebraic Reynolds stress models (EARSM) and full Reynolds stress models. The analysis in this work has shown the importance of the different terms in the TKE equation and it is expected that the same terms are important for Reynolds stress modelling as well with the exception of the pressure strain correlation which is known to be dominated by the anisotropic contributions.

Another important aspect is to include end walls. Even though more than 60% of the losses are generally attributed to the primary profile loss sources (2D) and, therefore most important, there are still 40% resulting from different sources where the mean flow field has a three dimensional character. Hence, applying the analysis of this work to full three dimensional configurations would be beneficial.

Appendix A

Nondimensionalization

In section 1.2.1 the nondimensionalized governing equations are introduced and here the relations between the dimensional and nondimensional equations are presented. This is of particular importance since the solutions obtained from the numerical simulations (being in nondimensional space) have to be compared to measurements (being in dimesional space). First the equations are nondimensionalized and the reference values with their relations are identified. This will show that the nondimensional governing equations depend on the following dimensionless products Re_∞, Ma_∞ and Pr_∞. Then all other equations used in this work will be transformed to their nondimensional form.

Nondimensionalization of the Governing equations

In this section the nondimensionalization is executed and the results are summarized in the next section. To obtain nondimensional quantities every physical quantity is decomposed in a reference value (index "∞") and the nondimensional quantity such that varialbe q is decomposed into

$$q^* = q_\infty q. \tag{A.1}$$

where the star represents a dimensional representation.

Continuity Equation

Decomposing the quantities in the Continuity equation yields:

$$\frac{\partial\left(\rho_\infty \rho\right)}{\partial\left(t_\infty t\right)} + \frac{\partial}{\partial\left(L_\infty x_i\right)}\left(\rho_\infty \rho u_\infty u_i\right) = 0 \tag{A.2}$$

Since the reference quantities are constant, they can be put in front of the differentiation. Further both sides are dived by the rho_∞ and u_∞ and multiplied by L_∞ in order to get rid of the reference quantities in the second term of the equation leading to:

$$\frac{L_\infty}{u_\infty t_\infty}\frac{\partial \rho}{\partial t} + \frac{\partial}{\partial x_i}(\rho u_i) = 0 \tag{A.3}$$

It is desireable to also get no reference quantities ahead of the first term and this is achieved by setting

$$t_\infty = \frac{L_\infty}{u_\infty} \tag{A.4}$$

and eventually the nondimensional continuity equation is obtained.

$$\frac{\partial \rho}{\partial t} + \frac{\partial}{\partial x_i}(\rho u_i) = 0 \tag{A.5}$$

Momentum Equation

Rearranging of the Momentum equation in a similar way to the continuity equation and using equation (A.4) yields:

$$\frac{\partial}{\partial t}(\rho u_i) + \frac{\partial}{\partial x_j}(\rho u_j u_i) = -\frac{p_\infty}{\rho_\infty u_\infty^2}\frac{\partial p}{\partial x_i} + \frac{1}{Re_\infty}\frac{\partial}{\partial x_j}\left(2\mu s_{ij} - \frac{2}{3}\mu\frac{\partial u_k}{\partial x_k}\delta_{ij}\right) \tag{A.6}$$

where

$$Re_\infty = \frac{\rho_\infty u_\infty L_\infty}{\mu_\infty} \tag{A.7}$$

is the reference Reynolds number. Further, defining

$$p_\infty = \rho_\infty u_\infty^2 \tag{A.8}$$

the factor ahead of the first term on the right hand side of equation (A.6) is unity and such diminishes. Eventually the nondimensional momentum equations yield

$$\frac{\partial}{\partial t}(\rho u_i) + \frac{\partial}{\partial x_j}(\rho u_j u_i) = -\frac{\partial p}{\partial x_i} + \frac{1}{Re_\infty}\frac{\partial}{\partial x_j}\left(2\mu s_{ij} - \frac{2}{3}\mu\frac{\partial u_k}{\partial x_k}\delta_{ij}\right) \tag{A.9}$$

Energy Equation

Applying the same decomposition to the energy equation yields

$$\begin{aligned}&\frac{\rho_\infty u_\infty^2}{t_\infty}\frac{\partial}{\partial t}\left[\rho\left(e + \frac{1}{2}u_i u_i\right)\right] + \frac{\rho_\infty u_\infty^3}{L_\infty}\frac{\partial}{\partial x_j}\left[\rho u_j\left(h + \frac{1}{2}u_i u_i\right)\right] \\ &= \frac{\mu_\infty u_\infty^2}{L_\infty^2}\frac{\partial}{\partial x_j}(u_i t_{ij}) - \frac{\mu_\infty T_\infty}{L_\infty^2}\frac{\partial}{\partial x_j}\left(-\frac{\mu c_p}{Pr}\frac{\partial T}{\partial x_j}\right)\end{aligned} \tag{A.10}$$

In this decomposition specific internal energy and specific enthalpy are nondimensionalized by the kinetic energy (i.e. $e^* = u_\infty^2 e$). Dividing both sides by $\rho_\infty u_\infty^3 L_\infty^{-1}$ and assuming that the Prandtl number is constant (i.e $Pr = Pr_\infty$) yields

$$\begin{aligned} &\frac{\partial}{\partial t}\left[\rho\left(e+\frac{1}{2}u_i u_i\right)\right] + \frac{\partial}{\partial x_j}\left[\rho u_j\left(h+\frac{1}{2}u_i u_i\right)\right] \\ &= \frac{1}{Re_\infty}\frac{\partial}{\partial x_j}\left(u_i t_{ij}\right) - \frac{c_{p,\infty} T_\infty \mu_\infty}{\rho_\infty L_\infty u_\infty^3 Pr_\infty}\frac{\partial}{\partial x_j}\left(-\mu\frac{\partial T}{\partial x_j}\right) \end{aligned} \tag{A.11}$$

Using reference Mach number $Ma_\infty = {}^{u_\infty}/_{a_\infty}$ with $a_\infty = \sqrt{(\gamma-1)\, c_p T_\infty}$ eventually one obtains the nondimensional energy equation:

$$\begin{aligned} &\frac{\partial}{\partial t}\left[\rho\left(e+\frac{1}{2}u_i u_i\right)\right] + \frac{\partial}{\partial x_j}\left[\rho u_j\left(h+\frac{1}{2}u_i u_i\right)\right] \\ &= \frac{1}{Re_\infty}\frac{\partial}{\partial x_j}\left(u_i t_{ij}\right) - \frac{1}{(\gamma-1)\, Re_\infty Pr_\infty M_\infty^2}\frac{\partial}{\partial x_j}\left(-\mu\frac{\partial T}{\partial x_j}\right) \end{aligned} \tag{A.12}$$

Identified Nondimensional Variable

In this section a summary of the relations of nondimensional variables and their dimensional counterparts is presented. It can be used to convert variables from dimensional into nondimensional space and back. In the above derivation several reference quantities and its dependence among each other was developed. Six independent variables and flow properties have been obtained and are summarized in table A.1. Using the

Physical Quantity	**Reference Value**
Length	L_∞
Density	ρ_∞
Velocity	U_∞
Temperature	T_∞
Isentropic exponent	γ

TABLE A.1: Independent dimensional-nondimensional variables

relations obtained in the previous section the dependent variables can be related to the independent ones as presented in table A.2 The final three lines in the table are the quantities that are required for the simulations. In order to compare with experiments the

Equation in nondimensional form

If the nondimensional representation of the variables is used each equation has to be transformed to its nondimensional form. This is performed in the following for several

Physical Quantity	**Reference Value**
Time	$t_\infty = {}^{L_\infty}/_{U_\infty}$
Pressure	$p_\infty = \rho_\infty U_\infty^2$
Energy	$e_\infty = U_\infty^2$
Enthalpy	$h_\infty = U_\infty^2$
Stress	$\tau_\infty = \rho_\infty U_\infty^2$
Speed of sound	$c_\infty = \sqrt{(\gamma - 1)\, c_{p,\infty} T_\infty}$
Viscosity	$\mu_\infty = \mu(T_\infty)$
Reynolds Number	$Re_\infty = \frac{\rho_\infty U_\infty L_\infty}{\mu_\infty}$
Mach Number	$Ma_\infty = \frac{U_\infty}{c_\infty}$
Prandtl Number	$Pr_\infty = \frac{c p_\infty \mu_\infty}{\kappa_\infty}$

TABLE A.2: Dependent dimensional-nondimensional variables and their definitions

equations. For the a few equations the nondimensionalization is presented and then only the results are compared in a table.

Equation of state, inner energy and enthalpy

The equation of state in dimensional for is defined as

$$p' = \rho' T' R \tag{A.13}$$

Replacing the specific gas constant with the specific heat at constant pressure changes c_p and the isentropic exponent given by

$$R = c_{p,\infty} \frac{\gamma - 1}{\gamma}, \tag{A.14}$$

decomposing it into reference values and nondimensional variable (as given in table A.1) and collecting all reference values in on fraction the following expression is obtained

$$p = \frac{(\gamma - 1)\, p, \infty T_\infty}{\gamma u_\infty^2}\, \rho T. \tag{A.15}$$

The nominator in the fraction is the reference speed of sound squared which with the reference velocity squared in the denominator yield the reference Mach number and thus the equation of state in nondimensional form follows as

$$p = \frac{\rho T}{\gamma M_\infty^2}\,. \tag{A.16}$$

Similar the inner energy e can be nondimensionalized starting from

$$e' = \frac{c_{p,\infty}}{\gamma} T' \tag{A.17}$$

after decomposing and collecting the reference values one obtains

$$e = \frac{c_{p,\infty} T_\infty}{\gamma u_\infty^2} \frac{\gamma - 1}{\gamma - 1} T \tag{A.18}$$

where the fraction with $\gamma - 1$ in both nominator and denominator is added to identify the reference Mach number in the nominator and thus the equation for internal energy in nondimensional form reads as

$$e = \frac{T}{\gamma \left(\gamma - 1\right) M_\infty^2}. \tag{A.19}$$

Similar the enthalpy equation can be obtained as

$$h = \frac{T}{\left(\gamma - 1\right) M_\infty^2}. \tag{A.20}$$

Between the three equations that have been derived in this section the relation

$$\rho e = \frac{\rho T}{\gamma \left(\gamma - 1\right) M_\infty^2} = \frac{p}{\left(\gamma - 1\right)} = \frac{\rho h}{\gamma} \tag{A.21}$$

holds which can be easily seen by comparing equations A.16, A.18 and A.20. In table A.3 the dimensional equations along with the nondimensional ones are presented.

name	dimensional form	nondimensional form	eqn.
speed of sound	$a' = \sqrt{c_{p,\infty} \left(\gamma - 1\right) T'}$	$a = \frac{\sqrt{T}}{M_\infty}$	
speed of sound	$a' = \sqrt{\gamma \frac{p'}{\rho'}}$	$a = \sqrt{\gamma \frac{p}{\rho}}$	
isentropic relation p	$\frac{p'_t}{p'} = \left[1 + \frac{\gamma-1}{2} M'^2\right]^{\frac{\gamma}{\gamma-1}}$	$\frac{p_t}{p} = \left[1 + \frac{\gamma-1}{2} M^2\right]^{\frac{\gamma}{\gamma-1}}$	
isentropic relation T	$\frac{T'_t}{T'} = \left[1 + \frac{\gamma-1}{2} M'^2\right]$	$\frac{T_t}{T} = \left[1 + \frac{\gamma-1}{2} M^2\right]$	
isentropic relation ρ	$\frac{\rho'_t}{\rho'} = \left[1 + \frac{\gamma-1}{2} M'^2\right]^{\frac{1}{\gamma-1}}$	$\frac{\rho_t}{\rho} = \left[1 + \frac{\gamma-1}{2} M^2\right]^{\frac{1}{\gamma-1}}$	
blade pressure	$c_p = \frac{p'_{t,in} - p'(s)}{p'_{t,in} - p'_{out}}$	$c_p = \frac{p_{t,in} - p(x)}{p_{t,in} - p_{out}}$	

TABLE A.3: Formulas in dimensional and nondimensional space

Appendix B

Reynold stress related derivations

B.1 Derivation of Reynolds stress transport equations for compressible flows

In order to obtain the Reynolds stress transport equation (RSTE) for Reynolds stress component $\tau_{ij} = \overline{\rho u_i'' u_j''}$ the relation

$$\tau_{ij} = \overline{u_i'' \mathcal{N}(u_j) + u_j'' \mathcal{N}(u_i)} \tag{B.1}$$

is constructed where the operator $\mathcal{N}(u_i)$ is the Navier Stokes operator (in primitive variable form) given by

$$\mathcal{N}(u_i) = \underbrace{\rho \frac{\partial u_i}{\partial t}}_{1} + \underbrace{\rho u_k \frac{\partial u_i}{\partial x_k}}_{2} + \underbrace{\frac{\partial p}{\partial x_i}}_{3} - \underbrace{\frac{\partial t_{ik}}{\partial x_k}}_{4} \tag{B.2}$$

with the viscous stresses defined as

$$t_{ik} = \frac{2\mu}{\mathrm{Re}} \left[\frac{1}{2} \left(\frac{u_i}{x_k} + \frac{u_k}{x_i} \right) - \frac{1}{3} \frac{u_p}{x_p} \delta_{ij} \right]. \tag{B.3}$$

The derivation of equation B.1 is carried out for each term of equation B.2 defined by an underbrace separately for better readability and then the terms are combined. Treating the first term only and substituting the Favré average for the velocity one obtains equation B.4. Next the property $\overline{a+b} = \overline{a} + \overline{b}$ is applied and the terms being zero are identified yielding equation B.5. Using partial integration results in equation B.6 and finally in order to obtain the time derivative of the Reynolds stress density is

also integrated which has to be corrected by the additional term in equation B.7.

$$\overline{u_i''\rho\frac{\partial u_j}{\partial t}+u_j''\rho\frac{\partial u_i}{\partial t}}=\overline{u_i''\rho\frac{\partial}{\partial t}\left[\widetilde{u_j}+u_j''\right]+u_j''\rho\frac{\partial}{\partial t}\left[\widetilde{u_i}+u_i''\right]} \tag{B.4}$$

$$=\underbrace{\overline{u_i''\rho\frac{\partial\widetilde{u_j}}{\partial t}}}_{=0}+\overline{u_i''\rho\frac{\partial u_j''}{\partial t}}+\underbrace{\overline{u_j''\rho\frac{\partial\widetilde{u_i}}{\partial t}}}_{=0}+\overline{u_j''\rho\frac{\partial u_i''}{\partial t}} \tag{B.5}$$

$$=\overline{\rho\frac{\partial u_i''u_j''}{\partial t}} \tag{B.6}$$

$$=\frac{\partial\overline{\rho u_i''u_j''}}{\partial t}-\overline{u_i''u_j''\frac{\partial\rho}{\partial t}}=\frac{\partial\tau_{ij}}{\partial t}-\overline{u_i''u_j''\frac{\partial\rho}{\partial t}} \tag{B.7}$$

For the second term the derivation has the following form

$$\overline{u_i''\rho u_k\frac{\partial u_j}{\partial x_k}+u_j''\rho u_k\frac{\partial u_i}{\partial x_k}}=\overline{u_i''\rho\left(\widetilde{u_k}+u_k''\right)\frac{\partial}{\partial x_k}\left[\widetilde{u_j}+u_j''\right]+u_j''\rho\left(\widetilde{u_k}+u_k''\right)\frac{\partial}{\partial x_k}\left[\widetilde{u_i}+u_i''\right]}$$

$$=\underbrace{\overline{u_i''\rho\widetilde{u_k}\frac{\partial\widetilde{u_j}}{\partial x_k}}}_{=0}+\underbrace{\overline{u_i''\rho\widetilde{u_k}\frac{\partial u_j''}{\partial x_k}}}_{a_1}+\overline{u_i''\rho u_k''\frac{\partial\widetilde{u_j}}{\partial x_k}}+\underbrace{\overline{u_i''\rho u_k''\frac{\partial u_j''}{\partial x_k}}}_{b_1}$$

$$+\underbrace{\overline{u_j''\rho\widetilde{u_k}\frac{\partial\widetilde{u_i}}{\partial x_k}}}_{=0}+\underbrace{\overline{u_j''\rho\widetilde{u_k}\frac{\partial u_i''}{\partial x_k}}}_{a_2}+\overline{u_j''\rho u_k''\frac{\partial\widetilde{u_i}}{\partial x_k}}+\underbrace{\overline{u_j''\rho u_k''\frac{\partial u_i''}{\partial x_k}}}_{b_2}$$

$$=\underbrace{\frac{\partial\overline{\rho u_i''u_j''}\widetilde{u_k}}{\partial x_k}-\overline{u_i''u_j''\frac{\partial\rho\widetilde{u_k}}{\partial x_k}}}_{a=a_1+a_2}+\overline{\rho u_i''u_k''}\frac{\partial\widetilde{u_j}}{\partial x_k}+\overline{\rho u_j''u_k''}\frac{\partial\widetilde{u_i}}{\partial x_k}+\underbrace{\frac{\partial\overline{\rho u_i''u_j''u_k''}}{\partial x_k}-\overline{u_i''u_j''\frac{\partial\rho u_k''}{\partial x_k}}}_{b=b_1+b_2}$$

$$=\frac{\partial\overline{\rho u_i''u_j''}\widetilde{u_k}}{\partial x_k}+\overline{\rho u_i''u_k''}\frac{\partial\widetilde{u_j}}{\partial x_k}+\overline{\rho u_j''u_k''}\frac{\partial\widetilde{u_i}}{\partial x_k}+\frac{\partial\overline{\rho u_i''u_j''u_k''}}{\partial x_k}-\overline{u_i''u_j''\frac{\partial\rho u_k}{\partial x_k}}$$

$$=\frac{\partial\tau_{ij}\widetilde{u_k}}{\partial x_k}+\tau_{ip}\frac{\partial\widetilde{u_j}}{\partial x_k}+\tau_{jk}\frac{\partial\widetilde{u_i}}{\partial x_k}+\frac{\partial\overline{\rho u_i''u_j''u_k''}}{\partial x_k}-\overline{u_i''u_j''\frac{\partial\rho u_k}{\partial x_k}} \tag{B.8}$$

First the Favré decomposition is substituted, the terms are expanded and the zero terms are identified. Then terms a_1 and a_2 are transformed to a by factoring out $\rho\widetilde{u_p}$ and integrating the resulting bracket and finally integrating such that the first term in a is obtained (being the transport term in RSTE) which has to be corrected by the second term. Also terms b_1 and b_2 are transformed in a similar way. In the last step $u_i''u_j''$ is factored out from the second terms in a and b and combining the two resulting derivatives yields the last term in equation B.8.

The third term follows straight forward as

$$\overline{u_i''\frac{\partial p}{\partial x_j}+u_j''\frac{\partial p}{\partial x_i}}=\overline{u_i''\frac{\partial\overline{p}}{\partial x_j}}+\overline{u_j''\frac{\partial\overline{p}}{\partial x_i}}+\overline{u_i''\frac{\partial p'}{\partial x_j}}+\overline{u_j''\frac{\partial p'}{\partial x_i}}$$

$$=\overline{u_i''\frac{\partial\overline{p}}{\partial x_j}}+\overline{u_j''\frac{\partial\overline{p}}{\partial x_i}}+\overline{\frac{\partial u_i''p'}{\partial x_j}}-\overline{p'\frac{\partial u_i''}{\partial x_j}}+\overline{\frac{\partial u_j''p'}{\partial x_i}}-\overline{p'\frac{\partial u_j''}{\partial x_i}} \tag{B.9}$$

The viscous stress can be decomposed as

$$\begin{aligned} t_{ik}(u) &= \frac{\partial}{\partial x_k}\left[\frac{2\mu}{\mathrm{Re}}\left[\frac{1}{2}\left(\frac{\partial u_i}{\partial x_k}+\frac{\partial u_k}{\partial x_i}\right)-\frac{1}{3}\frac{\partial u_p}{\partial x_p}\delta_{ik}\right]\right] \\ &= \frac{\partial}{\partial x_k}\left[\frac{2\mu}{\mathrm{Re}}\left[\frac{1}{2}\left(\frac{\partial \widetilde{u_i}}{\partial x_k}+\frac{\partial \widetilde{u_k}}{\partial x_i}\right)-\frac{1}{3}\frac{\partial \widetilde{u_p}}{\partial x_p}\delta_{ik}\right]\right]+\frac{\partial}{\partial x_k}\left[\frac{2\mu}{\mathrm{Re}}\left[\frac{1}{2}\left(\frac{\partial u_i''}{\partial x_k}+\frac{\partial u_k''}{\partial x_i}\right)-\frac{1}{3}\frac{\partial u_p''}{\partial x_p}\delta_{ik}\right]\right] \\ &= t_{ik}(\widetilde{u})+t_{ik}(u'') \end{aligned} \tag{B.10}$$

The last term is obtained by substituting the Favré decomposed viscous stress into it and then integrating the fluctuating velocity in terms a and b as

$$\begin{aligned} \overline{u_j''\frac{\partial t_{ik}(u)}{\partial x_k}}+\overline{u_i''\frac{\partial t_{jk}(u)}{\partial x_k}} &= \overline{u_j''}\frac{\partial t_{ik}(\widetilde{u})}{\partial x_k}+\overline{u_i''}\frac{\partial t_{jk}(\widetilde{u})}{\partial x_k}+\underbrace{\overline{u_j''}\frac{\partial t_{ik}(u'')}{\partial x_k}}_{a}+\underbrace{\overline{u_i''}\frac{\partial t_{jk}(u'')}{\partial x_k}}_{b} \\ &= \overline{u_j''}\frac{\partial t_{ik}(\widetilde{u})}{\partial x_k}+\overline{u_i''}\frac{\partial t_{jk}(\widetilde{u})}{\partial x_k}+\underbrace{\frac{\partial}{\partial x_k}\overline{u_j''t_{ik}(u'')}-\overline{t_{jk}(u'')\frac{\partial u_i''}{\partial x_k}}}_{a} \\ &\quad+\underbrace{\frac{\partial}{\partial x_k}\overline{u_i''t_{jk}(u'')}-\overline{t_{ik}(u'')\frac{\partial u_j''}{\partial x_k}}}_{b} \end{aligned} \tag{B.11}$$

Collecting the terms together then yields the Reynolds stress transport equations

$$\begin{aligned} \frac{\partial \tau_{ij}}{\partial t}+\frac{\partial \tau_{ij}\widetilde{u_k}}{\partial x_k} &= \underbrace{-\tau_{ik}\frac{\partial \widetilde{u_j}}{\partial x_k}-\tau_{jk}\frac{\partial \widetilde{u_i}}{\partial x_k}}_{P_{ij}}\underbrace{-\frac{\partial \overline{\rho u_i''u_j''u_k''}}{\partial x_k}}_{T_{1,ij}} \\ &\quad+\underbrace{\overline{u_i''}\frac{\partial \overline{p}}{\partial x_j}+\overline{u_j''}\frac{\partial \overline{p}}{\partial x_i}}_{R_{ij}}+\underbrace{\overline{\frac{\partial u_i''p'}{\partial x_j}}+\overline{\frac{\partial u_j''p'}{\partial x_i}}}_{T_{2,ij}}\underbrace{-\overline{p'\frac{\partial u_i''}{\partial x_j}}-\overline{p'\frac{\partial u_j''}{\partial x_i}}}_{\Pi_{i,j}} \\ &\quad+\underbrace{\overline{u_j''}\frac{\partial t_{ik}(\widetilde{u})}{\partial x_k}+\overline{u_i''}\frac{\partial t_{jk}(\widetilde{u})}{\partial x_k}}_{\mathcal{V}_{ij}}+\underbrace{\frac{\partial}{\partial x_k}\overline{u_j''t_{ik}(u'')}+\frac{\partial}{\partial x_k}\overline{u_i''t_{jk}(u'')}}_{T_{3,ij}} \\ &\quad\underbrace{-\overline{t_{jk}(u'')\frac{\partial u_i''}{\partial x_k}}-\overline{t_{ik}(u'')\frac{\partial u_j''}{\partial x_k}}}_{\epsilon_{ij}} \end{aligned} \tag{B.12}$$

where the last terms in equations B.7 and B.8 give the continuity equation and thus cancel out.

Appendix C

T106 Blade coordinates used in this work

x	y
0.000000000000000	0.008844902761512
0.000454880713449	0.006014533877828
0.001314099838853	0.003891757215065
0.002779826582190	0.002122776662763
0.004144468722537	0.001061388331381
0.005761822370357	0.000404338411955
0.007732972128636	0.000050542301494
0.009754664188411	0.000000000000000
0.012180694660140	0.000303253808966
0.014606725131869	0.000808676823910
0.017386551714058	0.001718438250808
0.020065293693259	0.002880911185178
0.025978742968099	0.006065076179323
0.039271368261114	0.014050759815431
0.052614535855624	0.021985901150045
0.065351195832202	0.029011281057760
0.078239482713262	0.035733407156509
0.090521261976390	0.041646856431349
0.102954668144001	0.047155967294234
0.114731024392187	0.051957485936197
0.126659007544854	0.056304123864712
0.138081567682579	0.060044254175294
0.149554670121797	0.063380046073922
0.160623434149061	0.066159872656111

Continued on next page

Table C.1 – continued from previous page

x	y
0.171742740477819	0.068585903127840
0.182609335299105	0.070557052886120
0.193475930120392	0.072224948835434
0.204190898037195	0.073539048674287
0.214956408255494	0.074600437005669
0.225620833870802	0.075308029226590
0.236285259486111	0.075863994543027
0.257361399209258	0.076167248351994
0.277982658218954	0.075560740734061
0.287939491613343	0.074903690814635
0.297896325007731	0.074044471689231
0.307499362291658	0.073033625659344
0.317051857274092	0.071668983518996
0.335449255018036	0.068232107017380
0.353644483556004	0.063885469088865
0.373861404153747	0.058123646718509
0.393673986339534	0.051704774428726
0.413132772414861	0.044527767616527
0.432338846982716	0.036592626281913
0.441891341965149	0.032296530654893
0.451241667741605	0.027697181218907
0.460794162724038	0.022693493370966
0.470245573103482	0.017487636317047
0.479899152688905	0.011826898549679
0.489401105369843	0.005913449274840
0.499206311859748	-0.000505423014944
0.508809349143676	-0.007177006812198
0.518614555633581	-0.014354013624397
0.528318677520496	-0.021733189642573
0.538427137819367	-0.029718873278681
0.548383971213755	-0.037957268422261
0.557885923894695	-0.046347290470324
0.567236249671151	-0.054888939422870
0.576889829256572	-0.064037095993348
0.586341239636017	-0.073336879468310
0.595792650015461	-0.082990459053732
0.605041891188928	-0.092846207845130
0.614240590060901	-0.103005210445496

Continued on next page

Table C.1 – continued from previous page

x	y
0.623237119726896	-0.113315839950344
0.640825840646932	-0.134543606577974
0.657757511647541	-0.156377880823536
0.673880505824241	-0.178717578084041
0.689194823177030	-0.201309986852017
0.703700463705910	-0.224003480222983
0.717346885109386	-0.246595888990959
0.730235171990447	-0.268986128552959
0.742264239746103	-0.290972029703004
0.753585715280839	-0.312401965536611
0.764199598594653	-0.333124309149296
0.774105889687547	-0.353088518239566
0.783355130861014	-0.372193508204433
0.791997864416549	-0.390186567536424
0.800034090354151	-0.407118238537032
0.807514350975316	-0.422786352000282
0.814388103978549	-0.437190907926174
0.820604807062354	-0.450230821711718
0.826215002528228	-0.461805008753925
0.831117605773180	-0.471862926751302
0.835312616797212	-0.480303491100859
0.838698950997333	-0.487126701802597
0.841276608373546	-0.492231474253527
0.842944504322859	-0.495516723850660
0.844258604161712	-0.497386789005951
0.845977042412520	-0.498903058050782
0.847341684552868	-0.499711734874692
0.848807411296205	-0.500116073286647
0.850374222642529	-0.500368784794118
0.852749710812764	-0.500267700191129
0.855024114380010	-0.499509565668714
0.856742552630818	-0.498246008131355
0.858107194771166	-0.496578112182042
0.859168583102548	-0.494606962423761
0.859674006117491	-0.492484185760998
0.859572921514502	-0.490310866796741
0.859067498499559	-0.488188090133978
0.857702856359211	-0.484801755933857

Continued on next page

Table C.1 – continued from previous page

x	y
0.855630621997943	-0.479545356578444
0.852800253114258	-0.472570518972223
0.849312834311148	-0.463877243115194
0.845168365588611	-0.453617155911839
0.840417389248141	-0.441790257362160
0.835059905289740	-0.428447089767650
0.829095913713406	-0.413739280032793
0.822525414519140	-0.397666828157588
0.815449492309930	-0.380381361046518
0.807767062482788	-0.361933421001079
0.799579209640702	-0.342373550322763
0.790784849180685	-0.321802833614560
0.781535608007217	-0.300271813177965
0.771679859215818	-0.277932115917460
0.761318687409475	-0.254884826436034
0.750401550286695	-0.231180487035181
0.738928447847476	-0.206869640016397
0.726899380091820	-0.182204996887151
0.714314347019725	-0.157085473044456
0.701122806329697	-0.131814322297279
0.687375300323233	-0.106391544645617
0.673021286698837	-0.080968766993957
0.658060765456507	-0.055647073945285
0.642443194294751	-0.030578092404085
0.626118030912074	-0.005913449274840
0.617728008864012	0.006216703083806
0.609135817609971	0.018195228537968
0.600341457149953	0.030022127087647
0.591344927483958	0.041646856431349
0.582146228611986	0.053018874267579
0.572694818232541	0.064188722897831
0.563091780948613	0.075105860020612
0.553185489855719	0.085719743334427
0.543026487255354	0.095979830537781
0.532614773147517	0.105936663932169
0.521950347532208	0.115489158914602
0.510982668107933	0.124637315485080
0.499812819477681	0.133280049040615

Continued on next page

Table C.1 – continued from previous page

x	y
0.488339717038462	0.141568986485689
0.476714987694759	0.149251416312831
0.464787004542092	0.156478965426524
0.452757936786436	0.163150549223779
0.440476157523307	0.169367252307584
0.428042751355696	0.175027990074952
0.415407175982107	0.180183304827377
0.402670516005529	0.184782654263363
0.389731686822974	0.188826038382912
0.376641230735937	0.192363999487517
0.363399147744415	0.195345995275683
0.350005437848411	0.197721483445918
0.336460101047923	0.199490463998220
0.322813679644448	0.200703479234085
0.309116715939478	0.201259444550523
0.295318667631518	0.201158359947534
0.281520619323559	0.200450767726613
0.267722571015601	0.199136667887760
0.253975065009136	0.197165518129480
0.240227559002671	0.194537318451774
0.226581137599195	0.191353153457630
0.213035800798707	0.187511938544058
0.199642090902703	0.183064216012555
0.186298923308194	0.178009985863119
0.173208467221156	0.172349248095752
0.160269638038600	0.166132545011946
0.147583520363518	0.159359876611702
0.135049029592918	0.152031242895021
0.122767250329789	0.144197186163396
0.110637097971144	0.135807164115333
0.098810199421464	0.126962261353820
0.087084385474774	0.117510850974376
0.075661825337050	0.107705644484471
0.064239265199326	0.097192845773645
0.053170501172062	0.086326250952359
0.042051194843304	0.074600437005669
0.031386769227995	0.062520826948518
0.020570716708203	0.049228201655502

Continued on next page

Table C.1 – continued from previous page

x	y
0.010411714107837	0.035430153347543
0.007682429827142	0.031235142323512
0.005205857053919	0.026837962093503
0.003335791898627	0.022895662576943
0.001718438250808	0.018801736155900
0.000758134522415	0.015314317352790
0.000101084602989	0.011725813946691
0.000000000000000	0.008844902761512

TABLE C.1: T106 blade coordinates where the pitch of the T106A is 0.799

Bibliography

Adumitroaie, V, Ristorcelli, J R & Taulbee, D B 1999 Progress in Favr{é} Reynolds stress closures for compressible flows. *Physics of Fluids* **11** (9), 2696.

Anderson, J D 1995 *Computational Fluid Dynamics, The Basics with Applications*. McGraw-Hill.

Archer Web Team 2015 Best practice guide. http://archer.ac.uk/documentation/best-practice-guide/arch.php.

Bijak-Bartosik, E, Elsner, W & Wysocki, M 2009 Evolution of the wake in a turbine blade passage. *J. Theor. Appl. Mech* **47** (1), 41–53.

Binder, A., Förster, W., Kruse, H. & Rogge, H. 1985 An Experimental Investigation Into the Effect of Wakes on the Unsteady Turbine Rotor Flow. *Journal of Engineering for Gas Turbines and Power* **107**, 458.

Boussinesq, J 1877 Théorie de l'écoulement tourbillant. *Mem. Pre. par. div. Sav.* **23**.

Cicatelli, G & Sieverding, Ch 1997 The effect of vortex shedding on the unsteady pressure distribution around the trailing edge of a turbine blade. *Journal of turbomachinery* **119** (October 1997).

Coleman, G. N., Kim, J. & Spalart, P. R. 2003 Direct numerical simulation of a decelerated wall-bounded turbulent shear flow. *J. Fluid Mech.* **495**, 1–18.

Coull, John D. & Hodson, Howard P. 2011 Unsteady boundary-layer transition in low-pressure turbines. *Journal of Fluid Mechanics* **681** (1), 370–410.

Coull, J. D. & Hodson, H. P. 2012 Predicting the Profile Loss of High-Lift Low Pressure Turbines. *Journal of Turbomachinery* **134** (2), 1–14.

Coull, J. D., Thomas, R. L. & Hodson, H. P. 2010 Velocity Distributions for Low Pressure Turbines. *Journal of Turbomachinery* **132** (4).

Cumpsty, N a. & Horlock, J H 2006 Averaging Nonuniform Flow for a Purpose. *Journal of Turbomachinery* **128** (1), 120.

Denton, J D 1993 The 1993 IGTI Scholar Lecture: Loss Mechanisms in Turbomachines. *Journal of Turbomachinery* **115** (4), 621.

Denton, J. D. 2004 *Axial Turbine Design*. University of Cambridge, lecture notes for Cambridge Turbomachinery Course.

Dring, R. P., Joslyn, H. D., Hardin, L. W. & Wagner, J. H. 1982 Turbine Rotor-Stator Interaction. *Journal of Turbomachinery* **104**, 729.

Durbin, P., Zaki, T. & Liu, Y. 2009 Interaction of discrete and continuous boundary layer modes to cause transition. *International Journal of Heat and Fluid Flow* **30** (3), 403–410.

Edwards, Tom, Centre, Cray & Sandberg, Richard 2010 Parallelising HiPSTAR using OpenMP. http://www.hector.ac.uk/coe/pdf/HiPSTAR_FinalReport_July2010.pdf.

Eitel-Amor, Georg, Örlü, Ramis & Schlatter, Philipp 2014 Simulation and validation of a spatially evolving turbulent boundary layer up to Re{_}\theta=8300. *International Journal of Heat and Fluid Flow* **47**, 57–69.

Ferziger, J H 1998 *Numerical Methods for Engineering Application*. Wiley.

Franke, Martin, Wallin, Stefan & Thiele, Frank 2005 Assessment of explicit algebraic Reynolds-stress turbulence models in aerodynamic computations. *Aerospace Science and Technology* **9** (7), 573–581.

Frigo, Matteo & Johnson, Steven G. 2011 FFTW - manual. http://www.fftw.org/fftw3.pdf.

Gao, Shian, Voke, Peter R. & Gough, Tim 1997 Turbulent Simulation of a Flat Plate Boundary Layer and Near Wake. In *Direct and Large Eddy Simulation II*, pp. 115–124.

Gerrard, J. H. 1966 The mechanics of the formation region of vortices behind bluff bodies. *Journal of Fluid Mechanics* **25** (02), 401.

Giesing, J. P. 1968 Nonlinear Interaction of Two Lifting Bodies in Arbitrary Unsteady Motion. *Journal of Fluids Engineering* **90** (3), 387–394.

Giles, M B & Reguly, I 2014 Trends in high-performance computing for engineering calculations. *Philosophical Transactions of the Royal Society A* **372:201303**.

Granet, Victor, Vermorel, Olivier & Gicquel, Laurent 2010 Comparison of nonreflecting outlet boundary conditions for compressible solvers on unstructured grids. *AIAA journal* **48** (10), 2348–2364.

Gross, Andreas & Fasel, Hermann F 2008 Multi-block Poisson grid generator for cascade simulations. *Mathematics and Computers in Simulation* **79** (3), 416–428.

Guezennec, Nicolas & Poinsot, Thierry 2009 Acoustically Nonreflecting and Reflecting Boundary Conditions for Vorticity Injection in Compressible Solvers. *AIAA Journal* **47** (7), 1709–1722.

Halstead, D. E., Wisler, D.C., Okiishi, T. H., Walker, G. J., Hodson, H. P. & Shin, H. W. 1997*a* Boundary Layer Development in Axial Compressors and Turbines: Part 1 Composite Picture. *Journal of Turbomachinery* **119**, 114.

Halstead, D. E., Wisler, D.C., Okiishi, T. H., Walker, G. J., Hodson, H. P. & Shin, H. W. 1997*b* Boundary Layer Development in Axial Compressors and Turbines: Part 3 of 4 - Turbines. *Journal of Turbomachinery* **119** (April).

Hannemann, K. & Oertel, H. 1989 Numerical simulation of the absolutely and convectively unstable wake. *Journal of Fluid Mechanics* **199**, 55.

Heskestad, Gunnar & Olberts, D R 1960 Influence of Trailing-Edge Geometry on Hydraulic-Turbine-Blade Vibration Resulting From Vortex Excitation. *Journal of Engineering for Power* **82** (2), 103–109.

Hickel, Stefan, Adams, Nikolaus a. & Domaradzki, J. Andrzej 2006 An adaptive local deconvolution method for implicit LES. *Journal of Computational Physics* **213** (1), 413–436.

Hillewaert, Koen, de Wiart, Corentin Carton, Verheylewegen, Guillaume & Arts, Tony 2014 Assessment of a high-order discontinous Galerkin mehtod for DNS of transition at low Reynolds number in the T106C high lift low Pressure turbine. In *Proceedings of the ASME turbo Expo - GT2014-26739*, pp. 1–12.

Hodson, H. P. 2004 *Blade to Blade Flowfields and Blade Surface Boundary Layers in Axial Turbomachines*. University of Cambridge, lecture notes for Cambridge Turbomachinery Course.

Hodson, Howard P. & Howell, Robert J. 2005 Bladerow Interaction, Transition, and High-Lift Aerofoils in Low-Pressure Turbines. *Annual Review of Fluid Mechanics* **37** (1), 71–98.

Hoyas, Sergio & Jimenez, Javier 2008 Reynolds number effects on the Reynolds-stress budgets in turbulent channels. *Physics of Fluids* **20** (10), 101511.

Jacobs, Robert G & Durbin, Paul a. 1998 Shear sheltering and the continuous spectrum of the OrrSommerfeld equation. *Physics of Fluids* **10** (8), 2006.

Jeong, J & Hussain, F 1995 On the identification of a vortex. *J. Fluid Mech.* **258**, 69–94.

Jimbo, Tomohiko & Biswas, Debasish 2010 A high-order LES turbulent model to study unsteady flow characteristics in a Low Pressure Turbine. In *Proceedings of the*

3rd Joint US-European Fluids Engineering Summer Meeting (FEDSM-ICNMM2010-30450), pp. 1–9.

Kalitzin, G, Wu, X & Durbin, P A 2003 DNS of fully turbulent flow in a LPT passage. *International Journal of Heat and Fluid Flow* **24** (4), 636–644.

Kármán, Th V 2013 On the mechanism of the drag a moving body experiences in a fluid (translation of original paper). *Progress in Aerospace Sciences* **59**, 13–15.

Kennedy, C A, Carpenter, M H & Lewis, R M 2000 Low-storage, explicit Runge-Kutta schemes for the compressible Navier-Stokes equations. *Applied Numerical Mathematics* **35**, 177–219.

Kennedy, C A & Gruber, Andrea 2008 Reduced aliasing formulations of the convective terms within the Navier-Stokes equations for a compressible fluid. *J. Comp. Phys.* **227**, 1676–1700.

Kim, J W & Lee, D J 2000 Generalized Characteristic Boundary Conditions for Computational Aeroacoustics. *AIAA Journal* **38** (11), 2040–2049.

Kim, J W & Lee, D J 2003 Characteristic Interface Conditions for Multiblock High-Order Computation on Singular Structured Grid. *AIAA Journal* **41** (12), 2341–2348.

Kim, J W & Sandberg, R D 2012 Efficient Parallel Computing with Compact Finite Difference Schemes. *Computer and Fluids* **58** (1), 70–87.

Klebanoff, PS, Tidstrom, KD & Sargent, LM 1962 The three-dimensional nature of boundary-layer instability. *J. Fluid Mech* **12** (1), 1–34.

Klein, M, Sadiki, A & Janicka, J 2003 A digital filter based generation of inflow data for spatially developing direct numerical or large eddy simulations. *J. Comp. Phys.* **186** (2), 652–665.

Kolmogorov, A N 1941 The Local Structure of Turbulence in Incompressible Viscous Fluid for Very Large Reynolds Numbers. *Dokl. Akad. Nauk SSSR* **40** (4).

Laurent, C., Mary, I., Gleize, V., Lerat, A. & Arnal, D. 2011 DNS database of a transitional separation bubble on a flat plate and application to RANS modeling validation. *Computers & Fluids* **61**, 21–30.

Lee, Myoingkyu & Moser, Rober D 2014 Direct numerical simulation of turbulent channel flow up to Reτ 5200. *ArXiv* , arXiv: arXiv:1410.7809v2.

Levesque, John & Wagenbreth, Gene 2011 *High Performance Computing*. Boca Raton: CRC Press.

Levesque, John M., Sankaran, Ramanan & Grout, Ray 2012 Hybridizing S3D into an exascale application using OpenACC: An approach for moving to multi-petaflops and beyond. In *International Conference for High Performance Computing, Networking, Storage and Analysis, SC*.

Luo, Hualing, Qiao, Weiyang & Xu, Kaifu 2009 Passive control of laminar separation bubble with spanwise groove on a low-speed highly loaded low-pressure turbine blade. *Journal of Thermal Science* **18** (3), 193–201.

Mansour, N. N., Kim, J. & Moin, P. 1988 Reynolds-stress and dissipation-rate budgets in a turbulent channel flow. *Journal of Fluid Mechanics* **194**, 15–44.

Marxen, Olaf, Lang, Matthias, Rist, Ulrich, Levin, Ori & Henningson, Dan S. 2009 Mechanisms for spatial steady three-dimensional disturbance growth in a non-parallel and separating boundary layer. *Journal of Fluid Mechanics* **634**, 165.

Matsuura, K. 2006 Large-eddy simulation of compressible transitional cascade flows with and without incoming free-stream turbulence. *JSME International Journal Series B* **49** (3).

Mayle, R E & Dullenkopf, K 1991 More on the Turbulent-Strip Theory for Wake-Induced Transition. *Journal of Turbomachinery* **113** (3), 428.

Medic, Gorazd & Sharma, Om P 2012 Large-Eddy Simulation of Flwo in a Low-Pressure Turbine Cascade. In *Proc. ASME Turboexpo GT2012-68878*, pp. 1–10.

Menter, F R 1994 Two-equation eddy-viscosity turbulence models for engineering applications. *AIAA J.* **32** (8), 1598–1605.

Meyer, R X 1958 The Effect of Wakes on the Transient Pressure and Velocity Distributions in Turbomachines. In *Transactions of the ASME*.

Michalek, Jan, Monaldi, Michelangelo & Arts, Tony 2012 Aerodynamic Performance of a Very High Lift Low Pressure Turbine Airfoil (T106C) at Low Reynolds and High Mach Number With Effect of Free Stream Turbulence Intensity. *Journal of Turbomachinery* **134** (6), 061009.

Michelassi, Vittorio, Chen, Li-Wei, Pichler, Richard & Sandberg, Richard 2015 Compressible Direct Numerical Simulation of Low-Pressure Turbines -Part II: Effect of Inflow Disturbances. *Journal of Turbomachinery* **137** (7).

Michelassi, Vittorio., Wissink, Jan. & Rodi, Wolfgang. 2003 Analysis of DNS and LES of flow in a low pressure turbine cascade with incoming wakes and comparison with experiments. *Flow, turbulence and combustion* **69**, 295–330.

Mills, N J 1996 The biomechanics of hip protectors. *Proceedings of the Institution of Mechanical Engineers. Part H, Journal of engineering in medicine* **210** (4), 259–266.

Mittal, R & Venkatasubramanian, S 2001 Large-eddy simulation of flow through a low-pressure turbine cascade. *AIAA Paper* pp. 1–9.

Moore, Gordon E. 1965 Cramming more components onto integrated circuits. *Proceedings of the IEEE* **38** (1), 82–85.

Muldoon, Frank & Acharya, Sumanta 2006 Analysis of k and epsilon Budgets for Film Cooling Using Direct Numerical Simulation. *AIAA Journal* **44** (12), 3010–3021.

Okajima, Atsushi 1982 Strouhal numbers of rectangular cylinders. *Journal of Fluid Mechanics* **123**, 379.

Okajima, A 1990 Numerical simulation of flow around rectangular cylinders. *Journal of Wind Engineering and Industrial Aerodynamics* **33**, 171–180.

Pacciani, R., Marconcini, M., Arnone, a. & Bertini, F. 2011 An Assessment of the Laminar Kinetic Energy Concept for the Prediction of High-Lift, Low-Reynolds Number Cascade Flows. *Proceedings of The Institution of Mechanical Engineers, Part A-Journal of Power and Energy* **225** (7), 995–1003.

Parker, R 1968 Pressure Fluctuations Due to Interaction between Blade Rows in Axial Flow Compressors. *Proceedings of the Institution of Mechanical Engineers* **183**.

Parker, R & Watson, JF 1972 Interaction effects between blade rows in turbomachines. *Proceedings of the Institution of Mechanical Engineers* **186** (21).

Pichler, R, Sandberg, R D, Michelassi, V & Bhaskaran, R 2015 Investigation of the accuracy of rans models to predict the flow through a low-pressure turbine. In *Proceedings of the ASME - GT2015-43446*, pp. 1–14.

Poinsot, T J & Lele, S K 1992 Boundary Conditions for Direct Simulations of Compressible Viscous Flows. *J. Comp. Phys.* **101** (1), 104–129.

Pope, S B 2000 *Turbulent Flows*. Cambridge University Press.

Prosser, R 2005 Improved boundary conditions for the direct numerical simulation of turbulent subsonic flows. I. Inviscid flows. *Journal of Computational Physics* **207** (2), 736–768.

Rodi, W. & Mansour, N. N. 1993 Low Reynolds number k ϵ modelling with the aid of direct simulation data. *Journal of Fluid Mechanics* **250**, 509–529.

Rogers, Michael M 2002 The evolution of strained turbulent plane wakes. *Journal of Fluid Mechanics* **463**, 53–120.

Rudy, D H & Strikwerda, J C 1980 A Nonreflecting Outflow Boundary Condition for Subsonic Navier-Stokes Calculations. *J. Comp. Phys.* **36**, 55–70.

Sandberg, R.D., Sandham, N.D. & Suponitsky, V. 2012 DNS of compressible pipe flow exiting into a coflow. *International Journal of Heat and Fluid Flow* **35**, 33–44.

Sandberg, R D & Jones, L E 2011 Direct numerical simulations of low Reynolds number flow over airfoils with trailing-edge serrations. *J. Sound and Vibration* **330** (16), 3818–3831.

Sandberg, Richard D., Michelassi, Vittorio, Pichler, Richard, Chen, Liwei & Johnstone, Roderick 2015 Compressible Direct Numerical Simulation of Low-Pressure Turbines -Part I: Methodology. *Journal of Turbomachinery* **137** (5).

Sandberg, R D, Suponitsky, V & Sandham, N D 2010 Direct numerical simulation of a canonical compressible nozzle flow. *DLES 8,* .

Sanders, Darius D, OBrien, Walter F, Sondergaard, Rolf, Polanka, Marc D & Rabe, Douglas C 2011 Predicting Separation and Transitional Flow in Turbine Blades at Low Reynolds NumbersPart I: Development of Prediction Methodology. *Journal of Turbomachinery* **133** (3), 31011.

Sarkar, S 2007 Effects of passing wakes on a separating boundary layer along a low-pressure turbine blade through large-eddy simulation. *Proceedings of the Institution of Mechanical Engineers, Part A: Journal of Power and Energy* **221** (4), 551–564.

Sarkar, S 2008 Identification of Flow Structures on a LP Turbine Blade Due to Periodic Passing Wakes. *Journal of Fluids Engineering* **130** (6), 61103.

Sarkar, S. 2009 Influence of Wake Structure on Unsteady Flow in a Low Pressure Turbine Blade Passage. *Journal of Turbomachinery* **131** (4), 041016.

Schlichting, Hermann 1979 *Boundary Layer Theory*, 7th edn. McGraw-Hill.

Schmitt, François G. 2007 About Boussinesq's turbulent viscosity hypothesis: historical remarks and a direct evaluation of its validity. *Comptes Rendus Mécanique* **335** (9-10), 617–627.

Smith, L. H. 1966 Wake Dispersion in Turbomachines. *Journal of Fluids Engineering* **88** (3), 688–690.

Spalart, Phillippe R, Shur, M. L., Strelets, M. Kh. & Travin, A. K. 2014 Direct Simulation and RANS Modelling of a Vortex Generator Flow. In *Proceeding of ETMM10 - Marbella*.

Speziale, C G, Abid, R & Anderson, E C 1992 Critical evaluation of two-equation models for near-wall turbulence. *AIAA J.* **30** (2), 324–331.

Stieger, R D & Hodson, H P 2005 The Unsteady Development of a Turbulent Wake Through a Downstream Low-Pressure Turbine Blade Passage. *Journal of Turbomachinery* **127** (2), 388.

Tabor, G.R. & Baba-Ahmadi, M.H. 2010 Inlet conditions for large eddy simulation: A review. *Computers and Fluids* **39** (4), 553–567.

Thomas, T G, Yao, Y F & Sandham, N D 2003 Structure and Energetics of a Turbulent Trailing Edge Flow. *International Journal of Comuters & Mathematics* **46** (4), 671–680.

Thompson, J., Soni, B. & Veatherill, N. 1999 *Handbook of Grid Generation*. Boca Raton: CRC Press.

Thompson, K W 1987 Time Dependent Boundary Conditions for Hyperbolic Systems. *J. Comp. Phys.* **68**, 1–24.

TITAN Web Team 2015 Titan Accelerated Computing Guide. https://www.olcf.ornl.gov/support/system-user-guides/accelerated-computing-guide/#2617.

Toebes, G. H. & Eagleson, P. S. 1961 Hydroelastic Vibrations of Flat Plates Related to Trailing Edge Geometry. *Journal of Basic Engineering* **83** (4), 671.

Top500 2015 Top500. www.top500.org.

Touber, E & Sandham, N D 2009 Large-eddy simulation of low-frequency unsteadiness in a turbulent shock-induced separation bubble. *Theor. Comp. Fluid Dyn.* **23** (2), 79–107.

Tucker, P G 2011 Computation of unsteady turbomachinery flows: Part 2 LES and hybrids. *Progress in Aerospace Sciences* **47** (7), 546–569.

Wilcox, D C 1998 *Turbulence Modeling for CFD*, 2nd edn. DCW Industries.

Wissink, J 2003 DNS of separating, low Reynolds number flow in a turbine cascade with incoming wakes. *International Journal of Heat and Fluid Flow* **24** (4), 626–635.

Wissink, J G & Rodi, W 2006 Direct numerical simulation of flow and heat transfer in a turbine cascade with incoming wakes. *J. Fluid Mech.* **569**, 209–247.

Wu, Xiaohua & Durbin, Paul 2001*a* Evidence of longitudinal vortices evolved from distorted wakes in a turbine passage. *Journal of Fluid Mechanics* **446**, 199–228.

Wu, X & Durbin, P A 2001*b* Evidence of longitudinal vortices evolved from distorted wakes in a turbine passage. *J. Fluid Mech.* **446**, 199–228.

Wu, Xiaohua, Jacobs, Robert G., Hunt, Julian C. R. & Durbin, Paul a. 1999 Simulation of boundary layer transition induced by periodically passing wakes. *Journal of Fluid Mechanics* **398**, 109–153.

Xie, Zheng-Tong T & Castro, Ian P. 2008 Efficient Generation of Inflow Conditions for Large Eddy Simulation of Street-Scale Flows. *Flow, Turbulence and Combustion* **81** (3), 449–470.

Yao, Y. F., Savill, a. M., Sandham, N. D. & Dawes, W. N. 2002 Simulation and modelling of turbulent trailing-edge flow. *Flow, Turbulence and Combustion* **68** (4), 313–333.

Yao, Y. F., Thomas, T. G., Sandham, N. D. & Williams, J. J R 2001 Direct numerical simulation of turbulent flow over a rectangular trailing edge. *Theoretical and Computational Fluid Dynamics* **14** (5), 337–358.

You, Donghyun, Mittal, Rajat, Wang, Meng & Moin, Parviz 2006 Analysis of stability and accuracy of finite-difference schemes on a skewed mesh. *Journal of Computational Physics* **213** (1), 184–204.